Université Catholique de Louvain
Ecole Polytechnique de Louvain
Institute of Condense Matter and Nanosciences
Division of Bio and Soft Matter

Synthesis and thermo-rheological properties of thermoplastic elastomers based on hydrogen-bonded hard segments

Ashwinikumar Sharma

Jury members:

Prof. Evelyne Van Ruymbeke (UCLouvain), supervisor

Dr. Carel Fitié (DSM BV, Netherlands), co-supervisor

Prof. Jacques Devaux (UCLouvain), chairperson

Prof. Jean-François Gohy (UCLouvain), secretary

Prof. Charles-André Fustin (UCLouvain)

Dr. Wilco Appel (DSM BV, Netherlands)

Prof. Guilhem Baeza (INSA Lyon, France)

Prof. Pavlik Lettinga (Forschungzentrum Jülich, Germany)

Thesis submitted in fulfilment of the degree
of Doctor in Engineering Sciences

Louvain-la-Neuve 2019

Abstract

Polyesteramide (PEA) segmented copolymers represents an interesting class of thermoplastic elastomers (TPEs), containing of two different segments termed as hard segment (HS) and soft segment (SS). Chemically, SSs are polyether units having low T_g, which provides flexibility to the polymer chain, whereas HSs are short amide units, which can self-associate via hydrogen bonding and form a physical crosslinked network. The thermodynamic incompatibility between the SS and HS results in a two-phase morphology and sets the interesting properties of these copolymers. For example, they show the physical property of rubbers at room temperature, such as softness, flexibility and resilience, while at high temperature, the HS domains melt, making the segmented copolymers processable like thermoplastics. Thus, this temperature dependence of the HS domains allows the transition from a processable melt to a solid, rubber-like object, and vice versa. This last one can be tuned by playing with the chemical chain composition, type of the HSs (monodisperse or polydisperse) and the extent of phase separation, which strongly affects the copolymer properties and make them suitable for different applications in automotive, electric and consumer product industries.

This thesis aims to synthesize well-defined amide-based PEAs of equal molar mass, but containing different HS concentrations (0, 5, 10, 15 and 20wt%) and to study their properties in order to understand in depth the role of HS density on morphology, thermal and viscoelastic properties. Parallel to this, it also aims to study the effect of polymer chain architecture, by synthesizing and studying PEAs with same HS density but with a dumbbell architecture. The structure-property relationship is established based on various experimental techniques like small-angle and wide-angle X ray scattering, DSC, FTIR, FSC and shear rheology. The results show that the final properties of the samples like high-temperature stability, temperature independent plateau modulus, or improved low-temperature flexibility are strongly dependent on their microstructure, which is largely influenced by the chemical composition, HS density, SS entanglements, thermal history, cooling conditions (fast or slow) and external parameters like time and temperature. Hence, the systematic study offers many possibilities for engineering these materials to meet the required behavior.

Table of Contents

List of acronyms

ATRP	Atom transfer radical polymerization
COPE	Copolymer esters
$CDCl_3$	Deuterated Chloroform
DSC	Differential Scanning Calorimetry
DMA	Dynamic Mechanical Analysis
DMI	Dimethyl isophthalate
DMT	Dimethyl terephthalate
DAB	1,4-Diaminobutane
DOT	Dioctyl terephthalate
EPDM	Ethylene propylene diene monomers
Et_2O	Diethyl ether
Et_3N	Triethylamine
FTIR	Fourier-Transform Infrared Spectroscopy
FSC	Fast Scanning Calorimetry
GPC	Gel permeation chromatography
HS	Hard Segment
HSs	Hard Segments
HFIP	Hexafluoroisopropanol
ISR	Intermediate Segregation Limit
LCP	Liquid-crystal polymer
LAOS	Large -amplitude oscillatory shear
MD	Monodispersed

MeOH	Methanol
MeCN	Acetonitrile
NMR	Nuclear Magnetic Resonance
NMP	N-methyl-pyrrolidone
OCEMs	Original equipment manufacturers
ODT	Order-Disorder Transition
PEA	Polyesteramide
PEAs	Polyesteramides
PEG	Polyethylene glycol
PA66	Polyamide 66
PPG	polypropylene glycol
PDMS	Polydimethyl siloxane
PTMO	Poly(tetramethylene oxide)
PCL	Polycaprolactone
PEBA	Poly(ether-block- amide)
ROP	Ring-opening polymerization
RAFT	Reversible addition-fragmentation chain transfer polymerization
SSL	Strong Segregation Limit
SAXS	Small Angle X-ray Scattering
SANS	Small-Angle Neutron Scattering
SBS	Polystyrene-polybutadiene-polystyrene
SS	Soft Segment
SSs	Soft Segments
SIS	Styrene-Isoprene-Styrene
SBC	Styrene block copolymers

TPE	Thermoplastic Elastomer
TMS	Tetramethylsilane
TPEs	Thermoplastic Elastomers
TPOs	Thermoplastic Polyolefins
TPV	Thermoplastic Vulcanizates
TLC	Thin-layer chromatography
THF	Tetrahydrofuran
TEM	Transmission Electron Microscopy
TPU	Thermoplastic polyurethane
(U)SAXS	(Ultra) Small Angle X-ray Scattering
WSL	Weak Segregation Limit

Chapter 1: **Introduction to Thermoplastic Elastomers (TPEs)**

Abstract

This introductory chapter briefly produces an overview of segmented copolymers or TPEs, mainly focusing on their different classes based on the chemical composition. These segmented copolymers show phase separated domains due to thermodynamic incompatibility of the different blocks, providing material thermoplastic and elastomeric properties. Furthermore, if the hard segments can crystallize or associate via supramolecular interactions such as hydrogen bonding, hard segment domains with different morphologies can be obtained, depending on these interactions as well as on the sample composition. Thus, depending on the different types of soft segments and hard segments present in the segmented copolymer, various morphologies can be obtained, as discussed in this chapter. Due to tunable properties, TPEs have a wide range of applications. Global market growth also shows a significant increase in consumption in the future.

1.1 Introduction to block copolymers

Block copolymers are a particular class of copolymers, in which different monomers units are grouped into blocks by covalent bond along the polymer chain.[1] Block copolymers containing two distinct monomers A and B can have various architectures, which can be controlled by the synthesis techniques. For example, it is possible to prepare linear diblock (AB), triblock (ABA), multiblock or segmented copolymers $(AB)_n$ as well as star multi-blocks $(AB)_nX$ copolymers. When a third monomer is added, linear block copolymers ABC, ACB and BAC can also be prepared.[2-5] Figure 1.1 shows some examples of synthesized architectures of block copolymers as represented by Hamley.[1]

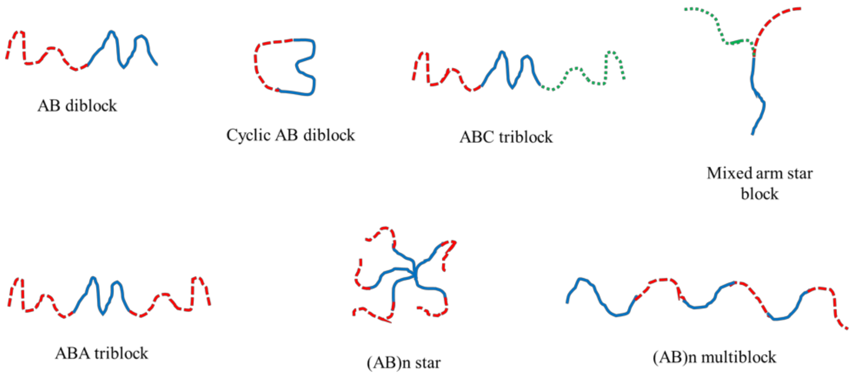

Figure 1.1: Block copolymers architecture.[1]

Generally, the method of choice for the synthesis of diblock and triblock copolymers is living polymerization or anionically reactive polymers, which ensures a narrow molecular weight distribution. The synthesis strategy used for the preparation of multiblock copolymers involves the synthesis of the individual A and B chains with functional groups such as hydroxyls and carboxyl's at both ends. The functionalized chains are subsequently subjected to step-growth polymerization for the preparation of the multiblock copolymer.[1]

Two competing effects govern the thermodynamics of block copolymer melts. At high temperature, the chains are homogeneously mixed, as in any polymer melt. On cooling or decreasing temperature, the tendency for the blocks to segregate is enhanced as the enthalpic process of demixing is favored, which is accompanied by a reduction in entropy as the chain configuration becomes more constrained. This tendency of blocks to segregate on lowering the temperature leads to a process called microphase separation.[1,2] The phase behavior of block copolymers has been studied over decades and is relatively well understood.[6-9] This process of segregation of chains is driven by an unfavorable mixing enthalpy and a small mixing entropy, while the covalent bonds connecting the blocks preventing macroscopic phase separation.[10,12] The extent of microphase separation depends on the total degree of polymerization N, the Flory-Huggins parameter χ and the volume fraction of the constituent blocks f (f_A and f_B, $f_A = 1 - f_B$). The Flory-Huggins parameter χ is inversely proportional to temperature, which reflects the interaction energy between different segments. On the other hand, the configurational entropy contributes to the Gibbs energy and is proportional to the degree of polymerization N. Therefore the segregation product χN determines the degree of microphase separation and when the product χN exceeds a critical value $(\chi N)_{ODT}$ (ODT = order-disorder transition), the block copolymers microphase separates into a periodically ordered structure, with typical length scale of ~ 5 – 500 nm.[1,2,10,11] The structure thus formed depends on the copolymer architecture and composition. Depending on the value of χN, three different regimes for the segregation can be observed: The weak limit (WSL) with $\chi N \leq 10$; the intermediate region (ISR) with $10 < \chi N \leq 50$ and the strong segregation limits (SSL) for $\chi N \to \infty$. In the bulk, the majority block is segregated from the minority block forming regularly shaped and well-organized nanodomains. The shape of the segregated domains in a block is governed by the volume fraction of the minority block, f, and its incompatibility. At a volume fraction of ≈

20%, the minority block forms a body-centered cubic spherical phase in the matrix of the majority block. It changes to the hexagonally packed cylinder at a volume fraction of ≈ 30%. Alternating lamellae are formed at approximately equal volume fraction for the two blocks. At a volume fraction of ≈ 38%, the minority block forms gyroid or perforated morphology at moderate and high incompatibility, respectively.[10-13] Figure 1.2 shows the equilibrium morphologies and phase diagram in the case of asymmetric diblock copolymers.[1] It is possible to predict the structure of a copolymer due to advances in the theory of block copolymer melt, in all regimes for a given χ, N, f and segment length, a. The self-consistent field theory provides a unified mean-field picture, with simpler limiting theories for weak and strong segregation regimes.

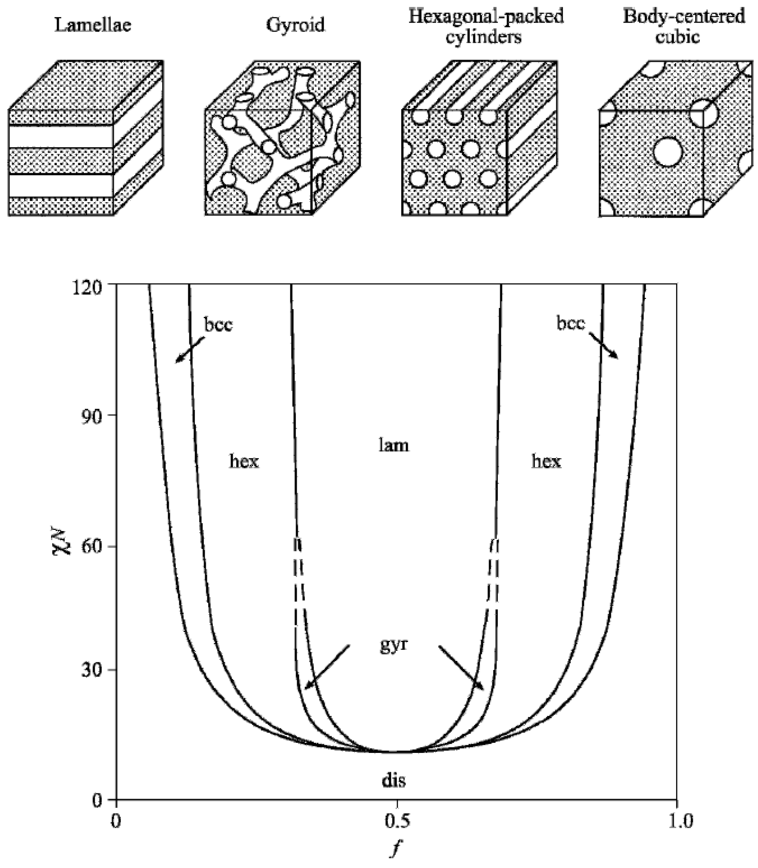

Figure 1.2: Phase diagram along with equilibrated morphologies, calculated using self-consistent mean field theory (SCF) for a symmetric diblock copolymer. The region of stability for disordered (dis), lamellar (lam), gyroid (gyr), hexagonal (hex) and body-centered cubic (bcc) phase are indicated.[14,15]

While the equilibrated morphologies of block copolymer melts are well defined, their structure can deviate from the equilibrated one if they are trapped upon vitrification. The mechanisms underlying the glass transition are like those of the constituent homopolymers.[1,13] In a system with one or both components of a block copolymer can crystallize, a profound structural dynamic change can take place. The fundamental process in crystallization is the change in conformation of the block, i.e. the adoption of an extended or a folded structure rather than a coiled configuration found in the melt or solution.[1,12,13] Crystallization taking place from the melt state often leads to a lamellar structure, with an arrangement/order depending on the cooling conditions from the melt. On the other hand, crystallization from semi-dilute and concentrated solutions can lead to the formation of a liquid crystalline phase such as the cubic phase of spherical micelles, a hexagonal phase of rod-like micelles or a lamellar phase. In addition to the formation of extended or folded chains, crystallization may also lead to gross orientation changes of chains. For example, chain folding with stems parallel to the lamellar interface has been observed for block copolymers containing poly(ethylene), while tilted structures are formed by the other crystalline block copolymers. The kinetics of crystallization has been studied in detail and appears to be largely like the crystallization dynamics of homopolymers.[13]

There is no comprehensive theory for crystallization in block copolymers that can account for the configuration of the polymer chain, i.e. the extent of chain folding, whether tilted or oriented parallel or perpendicular to the lamellar interface. The self-consistent field theory that has been applied in a restricted model seems to be the most promising approach.[1,2]

The characterization techniques like Small-Angle X-ray Scattering (SAXS), Small-Angle Neutron Scattering (SANS), rheology, Transmission Electron Microscopy (TEM) and Atomic Force Microscopy (AFM) are widely used to study the microphase separation and morphologies of block copolymers.[5,10,11]

To summarize, the nano and microphase separation in block copolymers are highly governed by the chain composition, architecture, fluctuation effects and cooling procedure. While it is well understood in case of diblock copolymers, the phase separation morphology becomes more complex for triblock and multiblock copolymers like thermoplastic elastomers, where crystallization of HS results into a complex morphology.

1.2 Thermoplastic Elastomers

Thermoplastic elastomers (TPEs) represent an interesting class of materials, which combine both thermoplastic and elastomeric properties.[16] They can be classified into different categories based on the polymer chain composition and different types of monomers used. TPEs are roughly classified into three main groups: the largest group consisting of an ABA triblock copolymer, like polystyrene-polybutadiene (SBS) block copolymers. In these materials, the crosslinking takes place due to the formation of glassy domains of polystyrene, that are embedded in the rubbery polybutadiene phase.[12] The second group consists of thermoplastic polyolefins (TPOs), blended with an elastomer, for example, a blend of polypropylene and EPDM rubber. The third group composed of multiblock copolymers, which usually consist of short glassy or crystalline hard segment (HS) and long amorphous soft segment (SS).[17,18] The typical arrangement of HS and SS in the polymer chain is shown in Figure 1.3.

Figure 1.3: Schematic representation of segmented copolymer.

In last few decades, these types of elastomers have developed a lot. In 1937,[19] a breakthrough occurred with the discovery of diisocyanate polyaddition reaction, which was applied to produce polyurethane fibers and elastomeric polyurethane by I. G. Farben. The development of polyurethanes continued until the late 1960s, including the commercialization of polyurethane TPEs, which was introduced by B.F. Goodrich, Mobay and Upjohn in USA, and by Bayer A.G. and Elastogran in Europe.[22] Further research at DuPont eventually led to the invention of elastic linear copolyesters, prepared by melt-copolymerized polymers via melt-ester exchange method.[20,21] Styrene-diene block copolymers were first developed by Shell using anionic block copolymerization of styrene with butadiene (S-B-S) and styrene with isoprene (S-I-S), which became available in 1966 followed by a wide range of TPEs in the 1970s.[23]

Thus, segmented copolymers are the $(A\text{-}B)_n$ type alternating each other, in which A and B segments are short and numerous. These A and B segments of different physical characteristics are covalently linked and termed as hard segment (HS) and soft segment (SS). Thermoplastic and elastic behavior of these polymers can be explained by their multiphase structure, which is a consequence of the chemical nature and incompatibility between the hard (rigid) and soft (flexible) segments. The sequential arrangement and nature of the segments play thus an important role in determining the copolymer properties. Most segmented copolymers exhibit a two-phase structure, at service temperatures. The SS component is rubbery while the HS is a glassy or semicrystalline nature. TPEs consist of materials with both thermoplastic and elastomeric properties: They show the physical property of conventional rubbers at room temperature, such as softness, flexibility and resilience, whereas, in contrast to convention rubbers, they can be processed as thermoplastics.[22] Indeed, at high temperature, the HS domains, which play the role of physical cross-links, melts and the segmented copolymers can flow. Thus, the temperature dependence of the HS domains allows the transition from a processible melt to a solid, rubber-like object, and vice versa. This transition is rapid and reversible. This allows processing thermoplastic elastomers using conventional plastics techniques, such as injection molding or extrusion. On the contrary, thermoset elastomers involve the vulcanization process, which is a chemical process causing the natural rubber or related polymer to form networks by chemical, permanent cross-links. This process is slow and irreversible.

1.3 Associating and supramolecular interaction in segmented TPE’s

Supramolecular chemistry refers to the domain beyond that of molecules and focuses on the chemical systems made up of a discrete number of assembled molecular subunits. Supramolecular chemistry examines the weaker and reversible non-covalent interactions between molecules. These interactions include hydrogen-bonding, metal-coordination, hydrophobic forces, van der Waals forces, $\pi - \pi$ interactions and electrostatic effects.[25,26] As stated earlier, most of TPEs are known to show associating interactions, as HSs include highly polar groups, which forms physical crosslinks and results into microphase separated morphologies. Therefore, amide containing segmented copolymer systems represent an interesting class of thermoplastic elastomers, in which HS can associate via supramolecular interactions such as hydrogen bonding. Usually, the SSs are composed of low T_g oligomeric sequence like poly(ethylene glycol) (PEG), poly(propylene glycol) (PPG), poly(dimethyl siloxane) (PDMS), poly(tetramethylene oxide) (PTMO), or polyester.[27-29] These SS provides flexibility to the chain, while their incompatibility with the HS promotes microphase separation. Figure 1.4a lists few of these SSs with molecular weight of about 2000 g.mol^{-1} along with their structures, T_g and T_m values.[26]

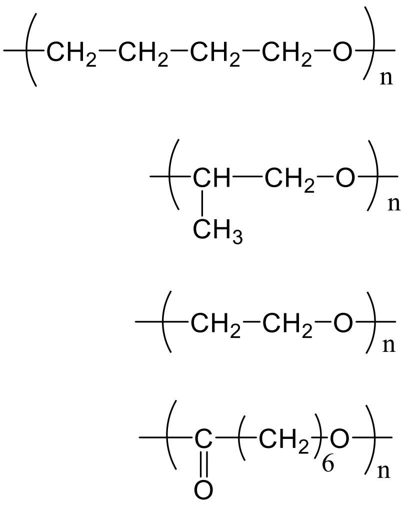

	T_g (°C)	T_m (°C)
PTMO	-65	28 - 40
PPO	-61	-
PEO	-48	50 - 53
PCL	-50	36 - 48

Figure 1.4a: Chemical structure of the SSs used in the synthesis of TPEAs.

On the other hand, HSs capable of associating into nano-domains acting as physical crosslinks are generally urethanes,[30,31] urea,[32,33] imides,[34,35] amides[36] and esters or a combination of two or more of these functionalities.[37] However, in addition to the nature of these HS, other parameters such as their aromaticity, symmetry, number of hydrogen bonding groups, molecular weight and number of repeating units play an important role in determining the physical properties of a copolymer.[38,39] Thus, the interplay of all these factors provides possibility of tuning the physical properties of many different segmented copolymers. To promote as the association of hydrogen bonding groups, several studies have shown that the amide group leads to one of the strongest intermolecular interactions. Based on group contribution method calculations, it was shown that the cohesive energy density of hydrogen bonding for urea, amide, urethane and imide are 2079, 1862, 1385 and 980 J/cm^3 respectively, while the hydrogen bonding energy of the amide groups is equal to 32.5 KJ.mol^{-1}.[40]

Therefore, the type of interactions can be elaborated considering (AB)$_n$ type segmented copolymer where ‘A’ is a thermoplastic crystalline HS and ‘B’ is an elastomeric/soft phase at service temperatures. Polystyrene-polybutadiene-polystyrene (SBS) triblock polymers marketed under the trademark “Kraton®”, shows thermodynamic incompatibility between the polystyrene HS and polybutadiene SS, which results in the formation of separate polystyrene phase. The physical entrapment of the polystyrene chain ends in these glassy domains immobilizes the polybutadiene segments and in fact, crosslinks the elastomer. At temperature above the T_g of polystyrene, the glassy phase softens and flows, converting the material to a viscous liquid which can be readily processed. However, at ambient temperature, these polystyrene domains are hard and act as physical cross-links, tying the elastomer chains together in a three-dimensional network and the polymer again behaves like a covalently cured elastomer. The other example is of polyetheresters TPE commercialized by Dupont derived from terephthalic acid, tetramethylene glycol and polytetramethylene oxide (PTMO) under the trade name Hytrel®.[24]

On the other hand, TPUs (a subcategory of TPEs) marketed for the first time under the trade name Estane®, Texin® and Pellethane® by Goodrich, Mobay and Upjohn respectively, shows microphase separation strongly dependent on the hydrogen bond formation between the urethane linkages. These segmented copolymers consist of either polyester or polyether SS alternating with urethane HS, because of the basic thermodynamic incompatibility of the segments, localized microphase separation occurs, leading to the well-organized domain structure.[24] The amide, urea, urethane and imide functionality possesses strong hydrogen bonding characteristics that are well-suited for the formation of strong physical crosslinks necessary for enhanced physical properties of segmented copolymers. Therefore, the final properties of the material are strongly influenced by the extent of the microphase separation and morphological characteristics of the HS domains. PEBAX® first commercialized by Arkema is another example, these TPEs contain polyamide HS and polyether SS interconnected by ester linkage.[41] These copolymers exhibit a complex morphology induced by microphase separation and a high degree of HS crystallization. Figure 1.4b shows a different type of HS, which exhibit hydrogen bonding in TPEs.

Moreover, ionic bonding also results in the formation of a network structure. This was well illustrated with butadiene-methacrylic acid copolymers containing small quantities of ionic salt which bound together forming clusters, involving the carboxylate anion attached to the elastomeric backbone and cations dispersed throughout the bulk polymers.

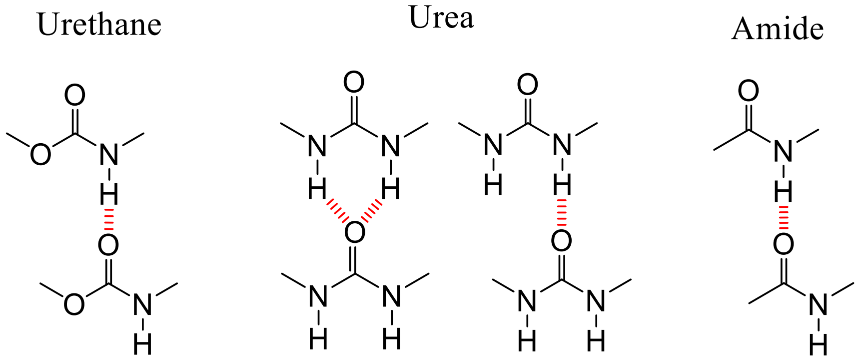

Figure 1.4b: Inter-chain hydrogen bonding observed in urethane, urea and amide HS based TPEs.

It is clear from the above examples that the intermolecular interaction plays an important role in increasing the extent of phase separation and obtaining the better mechanical properties of TPEs. However, the overall mechanical properties of the material not only depend on the intermolecular interaction but also depends upon the relative volume fractions of soft and hard phases, and on the intrinsic properties of each of the phases. Which in turn depend on details of molecular packing of the constituents within the phases, including the density of hydrogen bonds.

1.4 Morphology of segmented TPE's

As mentioned in section 1.1, the morphology of segmented multi-block or di-block copolymer is determined by the phase separation between the HS and SS, and the possible crystallization of the HSs. As in all semicrystalline solid polymers, the polymer properties do not depend directly on the molecular structure but also on the supramolecular structure or so-called morphology, which in turn depends on both, the molecular structure of the polymer and on the sample history. The inherent incompatibility of the two copolymer segments with physical crosslinking inter-molecular interactions results in the formation of a microphase-separated morphology. Factors necessary to generate a microphase separation include the overall degree of polymerization (N), volume fraction of the segments (f), and Flory-Huggins interaction parameter (χ). Microphase-separated morphologies consist of amorphous, semi-crystalline, or a combination of both HS microdomains dispersed throughout the soft polymer matrix. Since the commercialization of TPEs, a large research development took place, in order to understand the influence of the chain structure and crystallization on the morphology of segmented TPEs.

Crystallizable TPEs without hydrogen bonding - Cella, Seymour and Wegner proposed several morphological models, based on the behavior of copolyester TPE systems. Based on the experimental results, Cella[42] concluded that these materials possess a two-phase morphology consisting of continuous and interpenetrating crystalline and amorphous regions. It is the incorporation of the HS into crystallites that are responsible for the development of properties like those of conventionally cured elastomers. The crystalline phase consists of thin lamellae interconnected by short length tie molecules like one found in semicrystalline homopolymers. The high melting temperatures of these crystallites make the polymer suitable for even high-temperature applications which can be withstand by thermoplastic elastomers having hydrogen bonding mechanisms of intermolecular association. However, Seymour et al.[43] considered a model more analogous to common semicrystalline thermoplastics than to a block-copolymer system which undergoes microphase separation. With the use of small angle light scattering and polarized light microscopy, the authors concluded that the copolyesters crystallize in a spherulitic superstructure with chain folding. According to this model, the soft phase is embedded between radial crystalline fibrils of spherulites consisting of the HS. The amorphous phase is a mixture of the SS and non-crystalline HS showing a single glass transition region.

Later, Wegner[44,45] studied the segmented copoly(ether ester)s based on PBT (HS) and PTMO (SS) and concluded that these material crystallize to form supramolecular structures similar to that of observed for homopolymers e.g. such as spherulites or networks built up of individual lamellae. Such spherulitic superstructure was also found in segmented thermoplastic urethane systems. According to the author, the type of structure formed is highly dependent on the crystallization process rather than the chain structure. The most important parameter was found to be the supercooling ($\Delta T = T_m - T_c$), and how the crystallization was carried out, isothermally or under rapid quenching, shear-flow or by annealing from the glassy state. The only morphological feature which seems to have some relation to the molecular architecture of the chains was the thickness of the crystalline core of the lamellae.

***Crystallizable TPEs with hydrogen bonding* -** In hydrogen bonding segmented copolymers like PEBAX®, which is poly(ether-block-amide) (PEBA) copolymer consist of linear chains of hard polyamide covalently linked to soft polyether segment. Microphase separation occurs through HS crystallization into crystalline regions. The long ribbon-like polyamide crystalline regions provide copolymer mechanical strength upon mechanical deformation. Atomic force microscopy (AFM) and small angle X-ray scattering (SAXS) analysis have revealed the formation of nanofibrils oriented in the direction of an applied strain, which acts as the load bearing nanostructures that dominates the mechanical properties.[46]

Finally, the phase separation, morphology and properties of the non-hydrogen bonded segmented copolymers depends on the polymer chain composition, nature of HS and SS, SS molecular weight (SS molecular weight decreases, the phase mixing increases) and processing conditions. In addition to the above-mentioned factors, for hydrogen bonded segmented copolymers, the ability, strength and number of hydrogen bonding groups play an important role in determining the thermal and mechanical properties. The extent of crystallinity that the hydrogen bonding HS possesses also significantly affects the thermo-mechanical properties, therefore hydrogen bonded TPEs are highly tunable materials. This scenario can be further explained with an example based on the nature of HS i.e. uniform and non-uniform.

Harrell in 1969,[47] was the first to investigate the behavior of uniform (monodispersed) and non-uniform (polydispersed) HS in non-hydrogen bonding polyurethanes, followed by Ng et al.[48] and Eisenbach.[49] It was concluded that the HSs of uniform length crystallize faster and better than non-uniform length. Harrell observed that polymers with uniform urethane segments break at a higher strain than polymers with non-uniform urethane segments. Miller et al.[50] compared segmented copolymers with a narrow length distribution of the HS and SS showing high break strain as compared to polymers with broad segment length distributions. In the past, article by Gaymans et al.[51] showed that the segmented copolymers with short A-segments (HS) may crystallize in their extended form. If the segments are monodispersed (MD) in length, they stack neatly and form crystals of uniform thickness, without a partial crystalline interphase layer that is present in copolymers with polydisperse A-segments (Figure 1.5). Copolymers with these monodisperse segments have well-defined crystallite structures in which the crystallites are dispersed in a matrix phase of the B-segments. In such well-defined copolymer systems, structure-property relationships can be more easily studied. Also, these semi-crystalline materials present a very interesting combination of physical and engineering properties (see chapter 2, section 2.4).

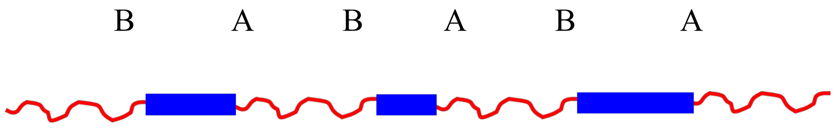

Polydisperse HS

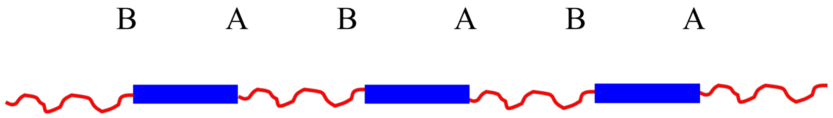

Monodisperse HS

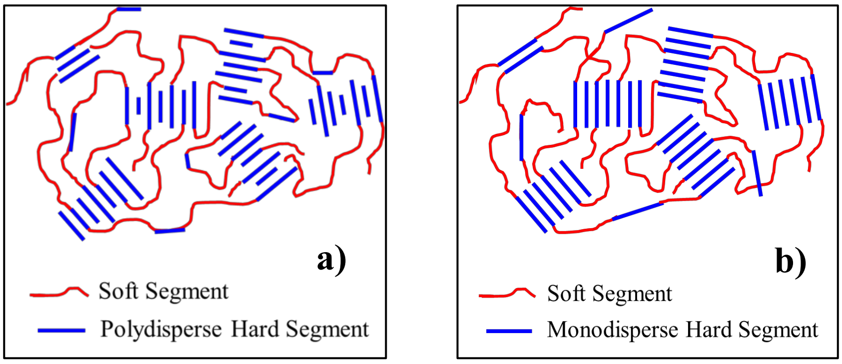

Figure 1.5: Phase-separated morphology in segmented copolymers; a) with polydisperse HS; b) with monodisperse HS.

Some studies were performed to understand the influence of the polydispersity of the SSs on the overall properties of thermoplastic elastomeric polyurethanes. Harrell and Copper[52] evaluated this effect by synthesizing segmented copoly(ether urethane)s with PTMO (SS) pre-polymer of low polydispersity (PDI = 1.1) and high polydispersity (PDI = 1.7). A slight increase in the property like strength and strain at break was observed upon lowering the polydispersity of the soft segments.

1.5 Application of TPE’s

Depending on the chemical nature of the polymer chain, the type of intermolecular interaction, and the extent of phase separation, the segmented copolymers are used in the various industrial area, such as automotive and consumer products. Furthermore, the market research report from Grand View Research shows expected an increase in consumption of TPEs globally in coming years.[53] Increasing consumption across various applications such as footwear, consumer goods, electronics, and construction has been instrumental in the global market growth over the last few years.[21] Increasing demand in automotive component manufacturing is expected to be a major factor driving the global industry growth over the time period. Regulatory intervention by environmental agencies aimed at carbon emission reduction through an increase in fuel efficiency has forced major automotive original equipment manufacturers (OEMs) to incorporate plastics as a substitute to metals and alloys. Increasing consumer preference for high performance and lightweight passenger cars has been driving plastics innovation in automotive manufacturing. Figure 1.6 shows the thermoplastic elastomers market volume by product (Kilo Tons) in Europe.

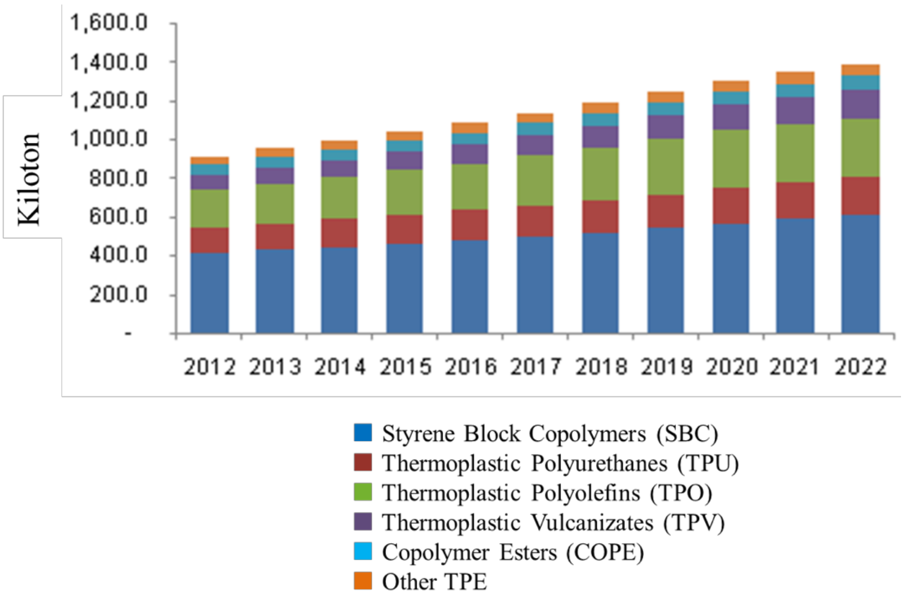

Figure 1.6: Europe thermoplastic elastomers market volume by product, 2012 - 2022 (Kilo Tons).[53]

Thermoplastic elastomers exhibit superior physical and chemical properties compared to thermoset plastics, thus gaining preference in terms of application. High substitution rate of TPU & TPO as an alternative to ethylene propylene diene monomer (EPDM) in construction materials is expected to complement global industry demand over time. Table 1 shows the properties and applications of TPEs based on chemical composition.

Table 1: Properties and applications of TPEs based on the chemical composition.[54]

Type of TPEs	Properties	Applications
Thermoplastic Styrene based	Wide hardness range and good heat and weathering resistance	Toys, dustcovers, mats, interior and exterior parts of cars, seals, grips for tools
Thermoplastic Olefins	Good heat resistance, excellent ozone resistance and some oil resistance	Different components in cars, electrical products, hoses, seals
Thermoplastic Polyurethane	Excellent wear resistance, load-bearing capacity and good oil resistance	Shoe soles, wheels, hoses
Thermoplastic Polyesters	High tear strength, abrasion resistance, low compression set and resistance to hot oils	Components in cars, hoses, tubes, wheels, bellows
Thermoplastic polyamides	Good mechanical strength, low-temperature flexibility and resistance to oxidation	Components in cars, hoses, tubes, wheels, bellows

1.6 Objectives of this work

This introductory chapter gives a brief overview of different types of segmented copolymers i.e. TPEs, their possible morphologies and their main properties. As it has been described, the thermodynamic incompatibility between the SS and HS results in a two-phase morphology and sets the interesting properties of these copolymers. These properties depend on the extent of phase separation, which is highly influenced by the polymer chain composition, and the type and amount of HS (hydrogen bonded or non-hydrogen bonded, monodisperse or polydisperse) which form the supramolecular structures by phase separation, crystallization or molecular association. Furthermore, the morphology of TPEs is becoming complex and highly tunable when the HSs are capable of forming hydrogen bonding. Their complexity and tunability depend on the number of hydrogen bonding group in an HS unit, on the strength of the hydrogen bonds and on the length of HS units. Moreover, it is very evident that the dispersity of HS plays an important role in the mechanical and thermal properties of TPEs.

Therefore, the aim of this thesis is to synthesize well-defined TPEs with supramolecular, amide-based HSs. In particular, we would like to synthesize and study the properties of segmented copolymers of equal molar mass, but containing different HS concentrations (0, 5, 10, 15 and 20wt%), in order to understand the role of HS density on the resulting properties.

Besides the synthesis, a key objective of this thesis is to understand the influence of HS concentration, thermal history and deformation on the phase separation and crystallization processes, which themselves influence the morphology of the crystallites and the viscoelastic properties of the TPEs. Hence, we would like to establish the structure-property relationship for TPEs, which eventually can lead to improve or optimize properties such as high-temperature stability, temperature independent plateau modulus over a wide range of temperature, or improved low-temperature flexibility with fast and complete crystallization.

Parallel to this, this thesis also aims to study the effect of polymer chain architecture, by synthesizing and studying the TPEs with dumbbell architecture based on similar HS and SS system as that of segmented TPEs (see Figure 1.7).

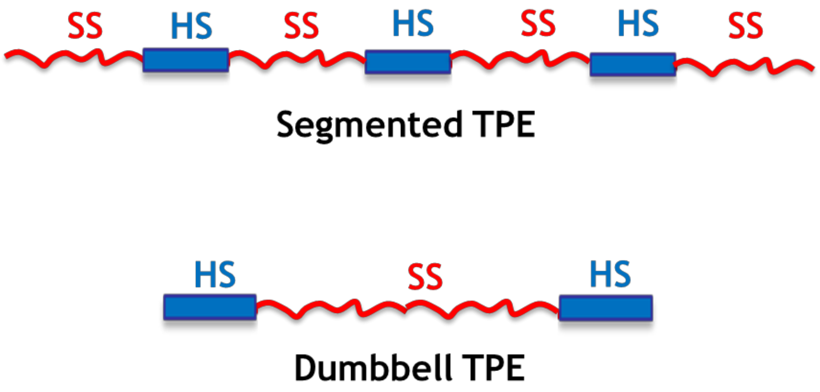

Figure 1.7: Different polymer chain architecture of synthesized polyesteramide TPEs.

In this set of samples, monodisperse HS concentration was systematically varied to 3, 5 and 20wt%. With such architecture, modifying the HS density results in obtaining copolymers with different molar masses. The key idea behind this work is to understand the influence of both the position of HS and the total length of the copolymer on the properties. We would like to investigate its effect on phase separation and crystallization, as well as on its stability to temperature. On the other hand, we would like to study the role of SS entanglements and how these ones affect the low-temperature viscoelastic properties. Therefore, based on a comparative study, we intend to understand in detail the structure/property relationship of these materials.

1.7 Outline of thesis

Chapter 2 – Introduces a specific class of TPEs, the thermoplastic poly(esteramides), with a detailed literature review. Various amide-based HS and ether-based soft segment copolymer systems are discussed. In these systems, the role of segment length, type of segment and their effect on properties are highlighted, with the objective to give insights on how one can engineer the properties of TPEs for the required application.

Chapter 3 – Here, we describe the synthesis of monodisperse T4T HSs along with the synthesis of segmented and dumbbell (T4T-PTMO) TPE with varying HSs concentration via polycondensation method. Synthesized copolymers are characterized using NMR, DSC, FTIR and GPC confirming the structure and other physiochemical properties.

Chapter 4 – In this chapter, we study the segmented copolymer samples using DSC, WAXS and (U)SAXS techniques in order to investigate the packing of the T4T units, their crystallites shape, orientation the growth mechanism from melt state. This study allows us to understand the key parameters and control the multiscale structure of segmented copolymers as per applications.

Chapter 5 – From a processing point of view, Fast Scanning Calorimetry (FSC) technique is used to investigate the crystallization behavior of segmented TPEs. The FSC measurements is a very powerful technique to help us to understand the formation of perfect T4T ribbon-like structures and imperfect ‘baby-ribbon’ structures. We show how these structures can be controlled based on the cooling rate, the isothermal time, the temperature and the chain mobility. Therefore, these results provide us with new insights for the control of the thermo-mechanical properties of these systems, useful in the design of new applications.

Chapter 6 – A systematic rheological investigation of segmented TPEs is carried out to understand the effect of chain composition and thermal history as a function of time, frequency and strain amplitude over a broad temperature range. Moreover, a statistical model is introduced in order to analyze the composition of the segmented copolymers. This allows us to understand the influence of the HSs density and their association probability on the fraction of SSs trapped between associated HSs and on the level of the high and low-frequency moduli of the material. In this chapter, we show how large flow can induce irreversible changes in the sample, depending on temperature.

Chapter 7 – A comparative study on thermo-mechanical and rheological properties of dumbbell versus segmented TPEs is proposed, based on rheometry and FSC. It is expected that at the same fraction of HSs, the dumbbells architectures display enhanced chain mobility but lower connectivity between the molecules. Therefore, we would like to understand the consequence of these effects on melting temperature, on their crystallization, and on the morphologies of the HS domains.

Chapter 8 – In this chapter, we propose a summary of the main results found in the previous chapters and discuss how they could be helpful for improving the properties of TPEs in further applications as conclusions and perspectives.

1.8 References

1) Hamley, Ian W., and Ian W. Hamley. The physics of block copolymers. Vol. 19. Oxford: Oxford University Press, 1998.
2) Lodge, Timothy P. "Block copolymers: past successes and future challenges." Macromolecular chemistry and physics 204.2 (2003): 265-273.
3) Pochan, Darrin J., et al. "Morphologies of microphase-separated A2B simple graft copolymers." Macromolecules 29.15 (1996): 5091-5098.
4) Uhrig, David, and Jimmy W. Mays. "Synthesis of combs, centipedes, and barbwires: poly (isoprene-graft-styrene) regular multigraft

copolymers with trifunctional, tetrafunctional, and hexafunctional branch points." Macromolecules 35.19 (2002): 7182-7190.

5) Bates, Frank S., and G. H. Fredrickson. "Block copolymers-designer soft materials." Physics today 52 (2000).

6) Leibler, Ludwik. "Theory of microphase separation in block copolymers." Macromolecules 13.6 (1980): 1602-1617.

7) Bates, Frank S. "Polymer-polymer phase behavior." Science 251.4996 (1991): 898-905.

8) Fredrickson, Glenn H., and Frank S. Bates. "Dynamics of block copolymers: Theory and experiment." Annual Review of Materials Science 26.1 (1996): 501-550.

9) Klok, H-A., and Sébastien Lecommandoux. "Supramolecular materials via block copolymer self-assembly." Advanced Materials 13.16 (2001): 1217-1229.

10) Feng, Hongbo, et al. "Block copolymers: Synthesis, self-assembly, and applications." Polymers 9.10 (2017): 494.

11) Lazzari, Massimo, Guojun Liu, and Sébastien Lecommandoux, eds. Block copolymers in nanoscience, chapter 1, p-1-6. John Wiley & Sons, 2007.

12) Abetz, Volker, and Peter FW Simon. "Phase behaviour and morphologies of block copolymers." Block copolymers I. Springer, Berlin, Heidelberg, 2005. 125-212.

13) Kim, Jin Kon, and Chang Dae Han. "Phase behavior and phase transitions in AB-and ABA-type microphase-separated block copolymers." Polymer Materials. Springer, Berlin, Heidelberg, 2009. 77-145.

14) Matsen, Mark W., and Michael Schick. "Stable and unstable phases of a diblock copolymer melt." Physical Review Letters 72.16 (1994): 2660.

15) Matsen, MARK W., and Frank S. Bates. "Unifying weak-and strong-segregation block copolymer theories." Macromolecules 29.4 (1996): 1091-1098.

16) Deleens, G., Foy, P. and Marechal, E. Eur. Pol. Journal 1977, 13, 337.
17) Coleman, D. "Block copolymers: copolymerization of ethylene terephthalate and polyoxyethylene glycols." Journal of Polymer Science 14.73 (1954): 15-28.
18) Witsiepe, W. K. "Segmented Polyester Thermoplastic Elastomers." ABSTRACTS OF PAPERS OF THE AMERICAN CHEMICAL SOCIETY. 1155 16TH ST, NW, WASHINGTON, DC 20036: AMER CHEMICAL SOC, 1972.
19) Legge, Norman R. "Thermoplastic elastomers." Rubber Chemistry and Technology 60.3 (1987): 83-117.
20) Mark, H. F. Encyclopedia of polymer science and technology; 3 ed.; Wiley-Interscience: New York, 2001.
21) Niesten, M. Ph.D. Thesis, University of Twente (Enschede), 2000.
22) Holden, G., 'Understanding thermoplastic elastomers', Carl Hanser, Munich (2000).
23) Holden, G., Bishop, E. T. and Legge, N. R. J. Pol. Sci. C 1969, 26, 36.
24) Legge, Norman R. "Thermoplastic elastomers, a comprehensive review." Hanser-Verlog (1987).
25) Miller JA, Lin SB, Hwang KKS, Wu KS, Gipson PE, Cooper LS. Properties of polyetherpolyurethane block copolymers: effects of hard segment length distribution. Macromolecules 1985;18:32–44.
26) Gaymans, Reinoud J. "Segmented copolymers with monodisperse crystallizable hard segments: Novel semi-crystalline materials." Progress in polymer science 36.6 (2011): 713-748.
27) Fang, Jianhua, et al. "Positron annihilation properties of copolyimides and copolyamides with microphase-separated structures." Journal of Polymer Science Part B: Polymer Physics 38.9 (2000): 1123-1132.
28) Okoroafor, E., and J. Rault. "Cryodilation of thermoplastic PEBA elastomers." Journal of Polymer Science Part B: Polymer Physics 29.11 (1991): 1427-1436.

29) Tavernier, Bruno, et al. "Effect of thermomechanical history on the crystallization of poly (ether-block-amide)." Polymer Engineering & Science 48.12 (2008): 2418-2425.

30) Korley, LaShanda T. James, et al. "Effect of the degree of soft and hard segment ordering on the morphology and mechanical behavior of semicrystalline segmented polyurethanes." Polymer 47.9 (2006): 3073-3082.

31) Pukánszky Jr, Béla, et al. "Nanophase separation in segmented polyurethane elastomers: Effect of specific interactions on structure and properties." European Polymer Journal 44.8 (2008): 2431-2438.

32) Jewrajka, Suresh K., et al. "Polyisobutylene-based segmented polyureas. I. Synthesis of hydrolytically and oxidatively stable polyureas." Journal of Polymer Science Part A: Polymer Chemistry 47.1 (2009): 38-48.

33) Tang, Donglin, et al. "Well-defined Biobased Segmented Polyureas Synthesis via a TBD-catalyzed Isocyanate-free Route." Macromolecular rapid communications 32.17 (2011): 1379-1385.

34) June, Stephen M., et al. "Photo-Reactive Polyimides and Poly (siloxane imide) s as Reversible Polymeric Interfaces." The Journal of Adhesion 86.10 (2010): 1012-1028.

35) Xi, Kai, et al. "Polyimide–polydimethylsiloxane copolymers for low-dielectric-constant and moisture-resistance applications." Journal of applied polymer science 113.3 (2009): 1633-1641.

36) Krijgsman, J., D. Husken, and R. J. Gaymans. "Synthesis and characterisation of uniform bisester tetra-amide segments." Polymer 44.23 (2003): 7043-7053.

37) June, Stephen M., Philippe Bissel, and Timothy E. Long. "Segmented block copolyesters using click chemistry." Journal of Polymer Science Part A: Polymer Chemistry 50.18 (2012): 3797-3805.

38) Sheth, Jignesh P., et al. "Role of chain symmetry and hydrogen bonding in segmented copolymers with monodisperse hard segments." Polymer 46.18 (2005): 7317-7322.

39) Sheth, Jignesh P., et al. "Structure–property behavior of poly (dimethylsiloxane) based segmented polyurea copolymers modified with poly (propylene oxide)." Polymer 46.19 (2005): 8185-8193.
40) Yilgor, Iskender, and Emel Yilgor. "Structure-morphology-property behavior of segmented thermoplastic polyurethanes and polyureas prepared without chain extenders." Polymer Reviews 47.4 (2007): 487-510.
41) Deleens, G. "A new generation of thermoplastic elastomers, the polyether block amides." SPE ANTEC. 1981.
42) Cella, Richard J. "Morphology of segmented polyester thermoplastic elastomers." Journal of Polymer Science: polymer symposia. Vol. 42. No. 2. New York: Wiley Subscription Services, Inc., A Wiley Company, 1973.
43) Seymour, R. W., J. R. Overton, and L. S. Corley. "Morphological characterization of polyester-based elastoplastics." Macromolecules 8.3 (1975): 331-335.
44) Wegner, G., et al. "Structure and properties of segmented polyether-esters. II. Crystallization behavior of polyether-esters with random distribution of hard segment length." Die Angewandte Makromolekulare Chemie: Applied Macromolecular Chemistry and Physics 74.1 (1978): 295-316.
45) Zhu, Li-Lan, and Gerhard Wegner. "The morphology of semicrystalline segmented poly (ether ester) thermoplastic elastomers." Die Makromolekulare Chemie: Macromolecular Chemistry and Physics 182.12 (1981): 3625-3638.
46) Hatfield, Galen R., et al. "Characterization of structure and morphology in two poly (ether-block-amide) copolymers." Macromolecules 26.24 (1993): 6350-6353.
47) Harrell LJ. Segmented polyurethanes. Properties as function of segment size and distribution. Macromolecules 1969;2:607–12.
48) Ng, H.N., Allegrazza, A.E., Seymour, R.W., Cooper, S.L., Polymer, 14, 255 (1973).

49) Eisenbach, C.D., Baumgartner, M., Gunter, G. in ‘Advances in Elastomer and Rubber Elasticity, proc. Symposium’, J. Lal and J. E. Mark Eds., Plenum Press, New York, 51 (1985).
50) Miller JA, Lin SB, Hwang KKS, Wu KS, Gipson PE, Cooper LS. Properties of polyetherpolyurethane block copolymers: effects of hard segment length distribution. Macromolecules 1985;18:32–44.
51) Gaymans, Reinoud J. "Segmented copolymers with monodisperse crystallizable hard segments: Novel semi-crystalline materials." Progress in polymer science 36.6 (2011): 713-748.
52) Harrell, L. L. "Segmented Polyurethanes: Properties as a Function of Segment Size and Distribution." Block Polymers. Springer, Boston, MA, 1970. 213-224
53) Grand view research, Inc., Jan 2016.
54) Drobny, Jiri George. Handbook of thermoplastic elastomers. Elsevier, 2014., Chapter 15 (pp. 281-315

Chapter 2: **Thermoplastic Polyesteramides (TPEAs)**

Abstract

This chapter focuses on segmented thermoplastic poly(esteramide)s consisting of amide moiety as crystallizable units, which ensure the toughness, whereas ether SS provides the softness or elastomeric properties to the material. Furthermore, the role of SS length and use of SS chain extender's in order to obtain low modulus elastomeric properties are discussed. Similarly, the effects of HS length on thermo-mechanical and flow properties are summarized. Based on these observations, this chapter provides insights into the selection of the HS and SS system from an application point of view.

2.1 Polyesteramides

Polyesteramide (PEA) segmented copolymers are the well-known class of thermoplastic elastomers.[1] PEAs form a versatile class of polymers, which are used in a broad range of applications (see chapter 1). Chemically, PEAs consist of long, flexible and low T_g polyether SS and short amide HS.[2] Their ability to self-associate via hydrogen bonding helps the HSs to aggregate and form rigid physical crosslinks.[2] In addition, the amide HS are incompatible with the soft SS, which induces microphase separation, crystallization or liquid-liquid demixing.[3] The ordered arrays, which are formed by the crystallized HSs, give good mechanical stability to the material and can lead to the reinforcement of the sample.[1] The HSs which do not crystallize or aggregate into HS domains are dissolved in the amorphous SS. This incomplete phase separation leads to an increase in the glass transition temperature of the SS, which is undesired for the low-temperature flexibility and elasticity of the material. By playing with the composition of the copolymer, PEAs exhibit a large range of tunable properties. It can be demonstrated with an example of segmented PEAs comprising different ester to amide ratios synthesized by melt polycondensation of a preformed bisamide-diol, 1,4-butanediol and dimethyl adipate.[5] The melt transitions of these copolymers can be tuned depending on the HS content from 63 ^{o}C to 140 ^{o}C for 10 to 85 mol% of HSs and so can the T_g of the flexible ester SS (-45 to -5 ^{o}C). By increasing the HS content from 10 to 85 mol% the elastic modulus can be tuned from 70 to 524 MPa, the stress at break from 8 to 28 MPa. However, while the strain at break was decreased from 820 to 370%. It can be concluded that the incorporation of well-defined amide HSs in the poly(butylene adipate) backbone results in improved thermal and mechanical properties compared to the homopolymer poly(butylene adipate). Thus, the properties of PEAs can be tuned for specific applications by varying the HS content; type of HS and SS combination as mentioned in section 2.5 of this chapter.

Among the polyether SS incorporated into PEAs, the most used and studied SS is the PTMO (poly (tetramethylene oxide)), which have low T_g and provides good flexibility as well as elastomeric properties to the material at low temperature. PTMO SSs of different molecular weight and functionalities are commercially available.[6]

Commonly used amide HS in PEAs are based on two and a half (TxTxT) units of nylon (Tx), or similarly, assembles one and a half (TxT) units, where 'T' stands for terephthalic unit and the 'x' represents the number of methylene groups between two amide bonds (spacer length) as shown in Figure 2.1, except for aramide HS, which assembles one and a half repeating unit of poly(phenylene terephthalamide), an aromatic polyamide.[7] The use of monodisperse amide units as HS is advantageous since polydisperse HSs impart poor phase separation and so the thermo-mechanical properties, as described in section 2.4. In addition, monodisperse amide HSs with allows reaching higher copolymer melting temperatures and less degradation during the melt synthesis and/or processing.[6]

a)

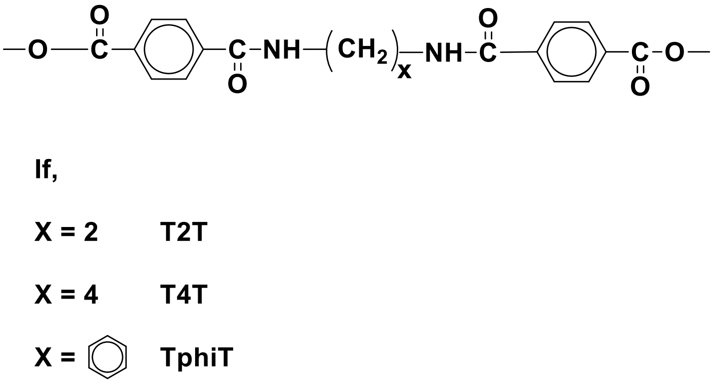

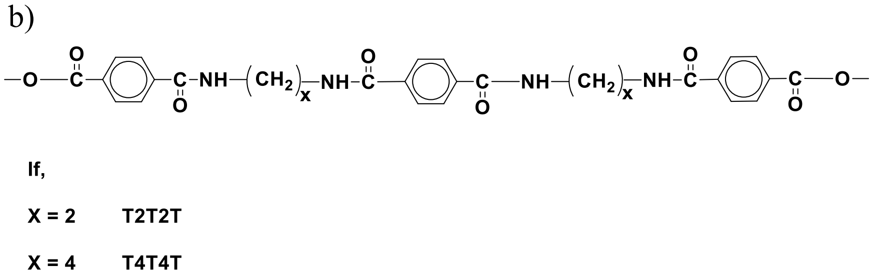

Figure 2.1: a) Structure of TxT di-amide HS and b) Structure of TxTxT tetra-amide HS.

Above the melting point of the crystalline phase, PEAs are homogenous, and their melt processing is possible. Upon cooling, the phase separation is restored by crystallization of the amide HS and the material regains its elastomeric properties.[8] Since the amorphous phase and the crystalline phase have a different chemical structure, the T_g/T_m ratio can have a value lower than $^2/_3$, which is common for pure semicrystalline thermoplastics.[9]

PEAs can be synthesized using polymerization techniques like ring-opening polymerization (ROP), reversible addition-fragmentation chain transfer polymerization (RAFT), atom transfer radical polymerization (ATRP) and polycondensation. Due to the simplicity of the technique, PEAs are generally synthesized using polycondensation methods, such as melt polycondensation, interfacial polymerization, solution polycondensation or solid state polycondensation.

The extent of phase separation and thermo-mechanical properties of PEAs are not only dependent on the type of HS used, but also on the HS length, for example, di-amide versus tetra-amide. Other important parameters for the phase separation and properties of PEAs are the dispersity and purity of the HS. Apart from this, the length of SS unit is also one of the key factors, which affect the sample properties since higher molecular weight PTMO and other SSs can crystallize, leading to temperature dependent rubbery plateau modulus. To overcome this problem, different types of chain extenders are often used during the synthesis, which results in relatively high SS molar mass, as well as in a temperature independent rubbery plateau modulus. Such chemical chain extenders help us to find a good balance between the modulus and the elastic properties of these materials. Therefore, it is important to know and understand the effect of these factors on the properties of PEAs, as discussed in the following sections.

2.2 Effect of SS length

The influence of the SS length was studied by Gaymans et al.[9] on PEAs composed of monodisperse di-amide T4T HS and PTMO SS. In this study, the authors varied the SS length in a systematical way, ranging from 250 g.mol^{-1} to 2900 g.mol^{-1}, in order to study the influence of SS length on the thermo-mechanical properties of these PEAs. Figure 2.2 shows the structure of T4T-PTMO system with varying SS length.

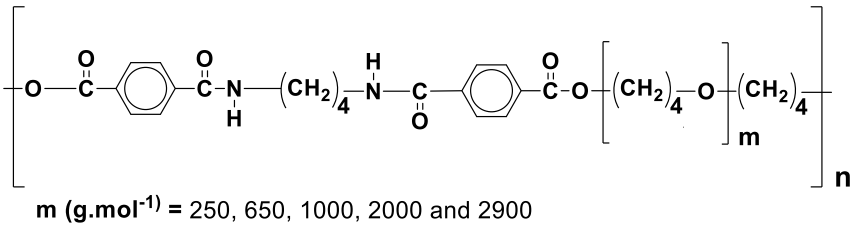

Figure 2.2: Chemical structure of di-amide T4T HS copolymerized with PTMO SS.

Varying the molar mass of the SS had a large impact on both thermal properties (see Section 2.2.1) and mechanical properties (see Section 2.2.2) of the samples.

2.2.1 Thermal properties

Conventional DSC data measured upon a heating rate of 20 ^{o}C.min^{-1} over a wide range of temperatures (-50 to 220 °C), revealed that two melting transitions occur at a low (-15 ^{o}C) and high temperature respectively. The high-temperature transition was attributed to the melting of T4T HS crystals and the low-temperature transition to the melting of crystalline PTMO SS. Both high-melting temperature T_m and crystallization temperature T_c was found to decrease with increasing SS lengths. PEAs with T4T-PTMO$_{2900}$ had a melting temperature of 83 °C in comparison with T4T-PTMO$_{250}$ with 185 ^{o}C. This strong decrease in melting temperature with increasing SS length was surprising, as monodisperse HSs were used in this study and the melting temperatures should not depend on the SS lengths. The authors concluded that the decrease in the melting temperature was not due to the difference of hard domain lamellar thickness, but it was due to the reduced lateral crystallite size or due to a 'solvent' effect of the amorphous phase when the density of SS unit is increased.

For these segmented polymers with uniform lengths, the degree of undercooling, $\Delta T = T_m - T_c$, was very small (9 - 20 °C), in comparison to the one of the fastest crystallizing polymer i.e. PBT with ΔT value of 36 °C.[9,10] Furthermore, no influence of the SS length was found in the value of ΔT. Very low ΔT values suggest fast crystallization kinetics and ordering in the melt for these materials, however, based on polarized light microscopy, no liquid-crystal polymer (LCP) behavior was observed.

The low-temperature melting transition associated with SS melting was completely absent for T4T-PTMO$_{250}$ sample as compared to higher M_w SS, which are able to crystallize. The increase in SS melting temperature with their length is shown in Figure 2.3. As it can be seen, longer PTMO segments can, of course, better crystallize and form thicker lamellar crystals, being less hindered by the HSs.

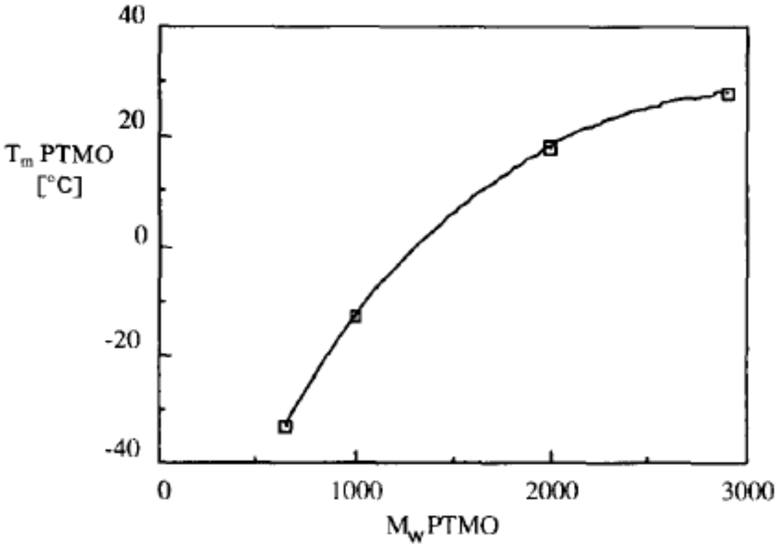

Figure 2.3: Melting temperatures of the crystalline PTMO fraction as a function of PTMO segment lengths in the T4T-PTMO copolymer system.

2.2.2 Mechanical properties

Dynamic Mechanical Analysis (DMA) was used to determine the elastic modulus in the low-strain limit as a function of temperature. Where comparing the T4T-PTMO$_{250}$ with other copolymers, a shift of the second-order transition from ~40 °C to -60 °C was observed. The occurrence of the two transitions at low temperatures indicates the presence of two amorphous phases, which differ in compositions, one being almost pure PTMO (the glass transition of PTMO lies at -84 °C), while the other being richer in HSs. In T4T-PTMO$_{2000}$ and T4T-PTMO$_{2900}$, the start of the rubbery plateau is shifted upwards to about 10 °C and an additional shoulder is observed at the end of the glass transition, as shown in Figure 2.4.

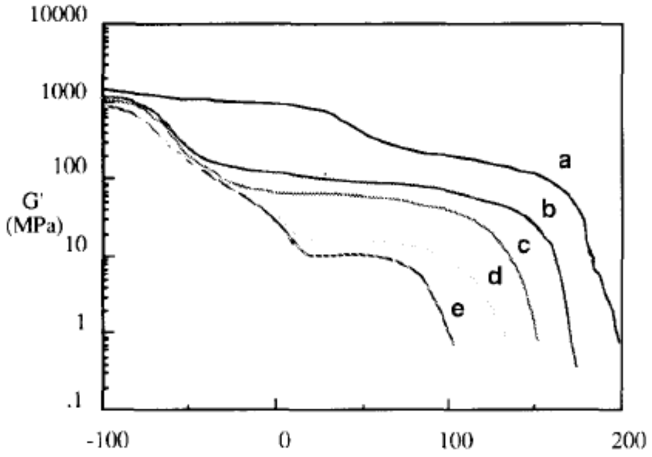

Figure 2.4: Storage modulus (G′) as a function of temperature for : a) T4T-PTMO$_{250}$; b) T4T-PTMO$_{650}$; c) T4T-PTMO$_{1000}$; d) T4T-PTMO$_{2000}$; e) T4T-PTMO$_{2900}$.

Such delay of the transition between glass region and rubbery plateau along with shoulders are unwanted as far as applications of PEAs are concerned. It can be further illustrated in Figure 2.5, which represents the measurement of flexural modulus over a wide range of temperatures. The plot can be divided into three distinct regions. First, at very low temperatures, i.e. below the glass transition of the elastomeric phase, where both the phases are hard, and the material is stiff and brittle. Second, above the glass transition of the elastomeric phase, the material softens and is elastic, with properties similar to the ones of a conventional vulcanized rubber. As the temperature increases, the modulus stays relatively constant i.e. region referred to as rubbery plateau, until the point where the hard phase softens or melts. At this point, the material enters the third region and becomes liquid-like. It is clear from the Figure 2.5 that the service temperature or temperature independent rubbery plateau lies in between the T_g of the elastomeric phase (lower service temperature) and the T_g or Tm of the hard phase (upper service temperature). Therefore, the melting of the SS interferes with the service temperature and properties of the polymer as well. However, the exact values depend on the service conditions of the final product, for example on the stress applied. In order to avoid temperature dependency of modulus over the required temperature range, the crystallization or melting of SS also needs to be avoided. Hence SS chain extenders are used to obtain good elastomeric properties at low temperature without SS melting.[12]

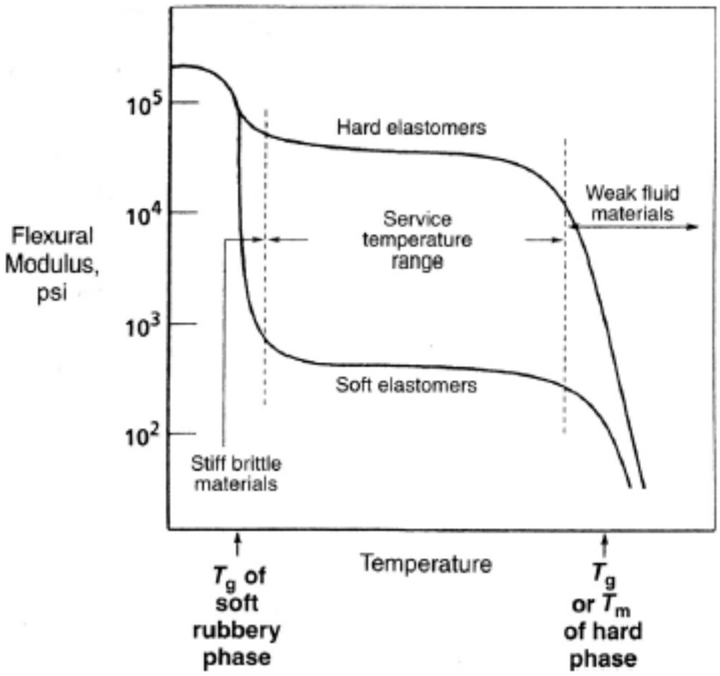

Figure 2.5: Stiffness of typical thermoplastic elastomers as a function of temperature.[12]

Complementary to DSC observations, the upward shift of rubbery plateau observed in Figure 2.4 is associated with the melting of PTMO crystals. The temperature at which flow occurs, DSC endotherms were related to the melting of the hard domains. The relationship between the observed glass transition temperature and the M_w of the SSs is shown in Figure 2.6. The steep rise in T_g between

$PTMO_{650}$ and $PTMO_{250}$ is due to the reduced mobility of a short chain between crystalline segments. It is clear from this data that for high M_w SS, change in T_g is very low.

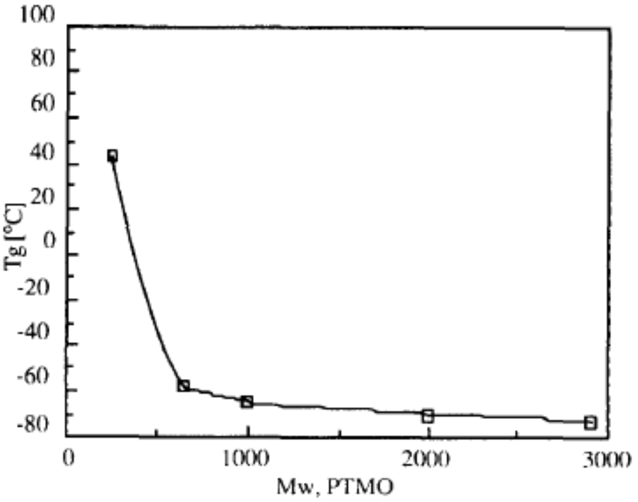

Figure 2.6: Glass transition temperature as a function of the PTMO segment length in the T4T-PTMO system.

Stress-strain measurements also reveal different drawing properties as well as possible flow-induced crystallization of these copolymers, as shown in Figure 2.7. For copolymer T4T-$PTMO_{650}$ and T4T-$PTMO_{1000}$ the stress reaches a plateau level, whereas for T4T-$PTMO_{2000}$ and T4T-$PTMO_{2900}$ much more elastomeric characteristics are observed with low initial moduli and a sigmoidal curve with strain at break exceeding 1000%. The final breaking stress is observed to be several times larger than the stress at the inflection point, and the overall behavior can be attributed to strain-induced crystallization, as confirmed by X-ray diffraction. While the crystallization of PTMO occurs in samples of T4T-$PTMO_{2000}$ and T4T-$PTMO_{2900}$ during stretching, T4T-$PTMO_{650}$ and T4T-$PTMO_{1000}$ samples did not show any sign of induced crystallization in wide-angle X-ray diffraction WAXD studies. This again confirms that high molar mass PTMO segments crystallize more easily than shorter SS.

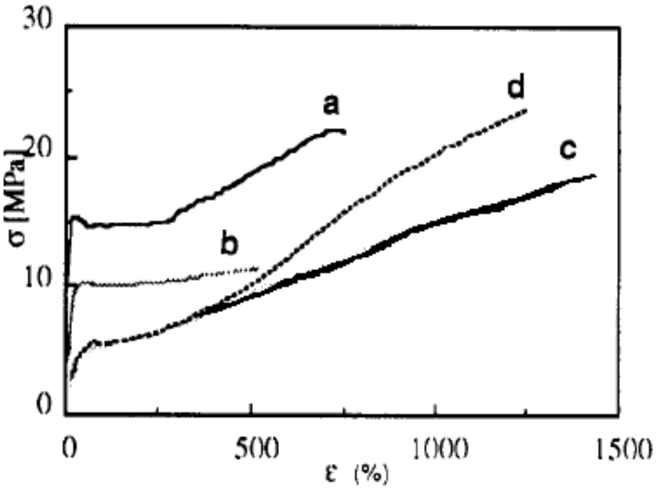

Figure 2.7: Stress-strain curves of the copolymers: a) T4T-PTMO$_{650}$; b) T4T-PTMO$_{1000}$; c) T4T-PTMO$_{2000}$; d) T4T-PTMO$_{2900}$.

2.3 SSs with chain Extenders

As it is evident from the previous section, SS like PTMO crystallizes strongly with an increase in M_w from 250 to 2900 g.mol^{-1}. Certainly, the SS melting temperature around room temperature is to be avoided, as it interferes and affects the thermal and mechanical properties at the intended service temperature. But in order to have low modulus and high elasticity, SSs should have a high M_w, while without crystallizing. Therefore, crystallization of SSs like PTMO and PEO are usually suppressed by copolymerizing these segments with a chain extender unit, known as structure-disturbing groups, which can reduce the structural regularity.[13-15] These extenders are generally ester groups such as terephthalic,[16,17] or isophthalic[18] as shown in Figure 2.8 (a). Long ether segments containing structure-disturbing groups can be obtained by reacting short ether segments with terephthalic or diisocyanate groups to long SS units, as shown in Figure 2.8 (b). In the past, SS lengths of PTMO_{1000} and PEO_{600} was increased to 9000 and even to 20,000 g.mol^{-1} by keeping the samples completely amorphous or keeping the melting temperature below the room temperature.[17-19] Consequently, the DMI-extended pre-polymer shown in Figure 2.8 (b) is a liquid at room temperature and the corresponding DMI-extended copolymers demonstrate a T_g of few degrees higher than that of the pure SS.[20] PTMO and PEO extended with terephthalic groups also showed an SS T_g that are only 5 °C higher. Thus, by incorporating disturbing groups or chemical extenders in the crystallizable SS, long chain SSs can be obtained either in an amorphous state or with the SS melting temperature being lower than the room temperature.

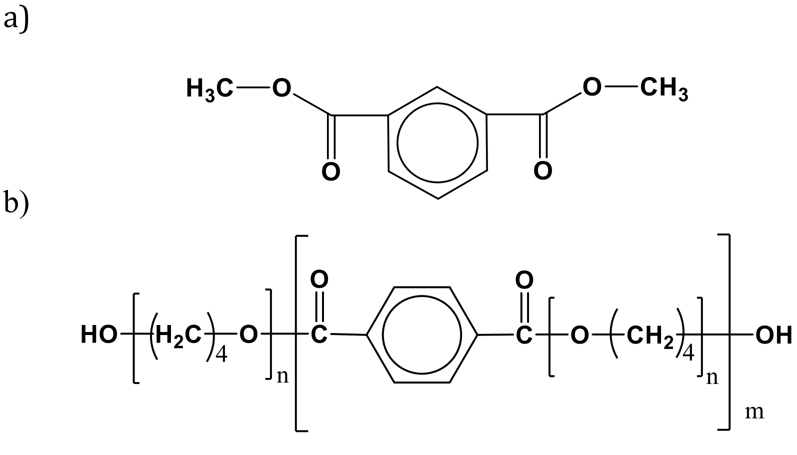

Figure 2.8: a) Chemical structure of Dimethyl isophthalate (DMI) and b) PTMO SS extended with dimethyl terephthalate (DMT).

2.4 Effects of HS dispersity

The structure of the HSs exerts a strong effect on the phase separation and consequently on the physical properties of the copolymer. Therefore, the dispersity of HS plays an important role in describing the final properties of the amide-based HS copolymers. In the past, van der Schuur et al.[16] compared monodisperse and polydisperse crystallizable amide HSs in copolymers based on poly(propylene oxide) (PPO) SSs. The author concluded that the copolymers with monodisperse amide HSs had higher moduli, higher melting temperatures, and lower compression as compared to their polydisperse counterparts irrespective of flexible SS. Similar study was done by Gaymans,[21] to understand how the properties of segmented copolymers are dependent on the dispersity of HSs. Gaymans and coworkers studied the copolymer system with monodisperse T6A6T crystallizable amide HSs and PTMO SS, where the tetra-amide HSs (T6A6T) were based on adipic acid (A), terephthalic acid (T), and hexamethylene diamine (6). This monodisperse HS system displays a rapid crystallization, a good phase separation, a high modulus, a high melting temperature and a temperature-independent rubbery modulus. Along with this, a copolymer system with a varying polydispersity of the amide HSs was studied by mixing uniform di-amide (T6T) with tetra-amide (T6A6T) and hexa-amide (T6A6A6T). The T6A6T concentration in the copolymers was varied while maintaining the average amide length at four amide groups. In this way, the weight percentage of crystallizable HSs was kept constant so that the degree of hydrogen bonding remains constant. Indeed, the polydispersity of the HSs was the only parameter that was varied as represented in Figure 2.9.

The thermo-mechanical and elastic properties of the copolymers were studied using DSC, DMTA and compression set techniques.

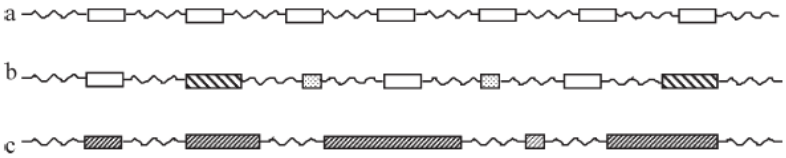

Figure 2.9: PTMO-T6A6T segmented copolymers (a) with monodisperse HSs; (b) mixture of monodisperse HSs and (c) polydisperse HSs.[21]

2.4.1 Thermal properties

The melting and crystallization behavior of the copolymers was studied at the cooling and heating rate of 20 °C.min^{-1} by DSC. The thermograms are presented in Figure 2.10, two peaks were observed during the heating cycle; one around 0 °C corresponding to the melting of crystalline PTMO, the second around 180 °C corresponding to the melting of the amide HSs. Upon cooling, the HSs crystallize around 165 °C and upon further cooling, the crystallization of PTMO was observed at -10 °C. With increasing HS dispersity, the melting and crystallization peaks of the HSs were found to get broader, on further increase melting and crystallization peak were not even visible. However, the melting temperatures were almost the same. The crystallization temperature of PTMO SS was influenced and found to slightly decrease with an increased polydispersity. As a result of the changes in the crystallization temperature of the PTMO SS, the resulting supercooling $\Delta T = (T_m - T_c)$ was increased (See Table 1). Also, the ΔH_m of the crystalline PTMO phase was increased, suggesting an increased degree of crystallinity of the PTMO SS. However, with the polydisperse HSs, the PTMO T_m and crystallinity was lower. It was unclear for the authors, why the PTMO melting temperature and crystallinity changed with polydispersity.

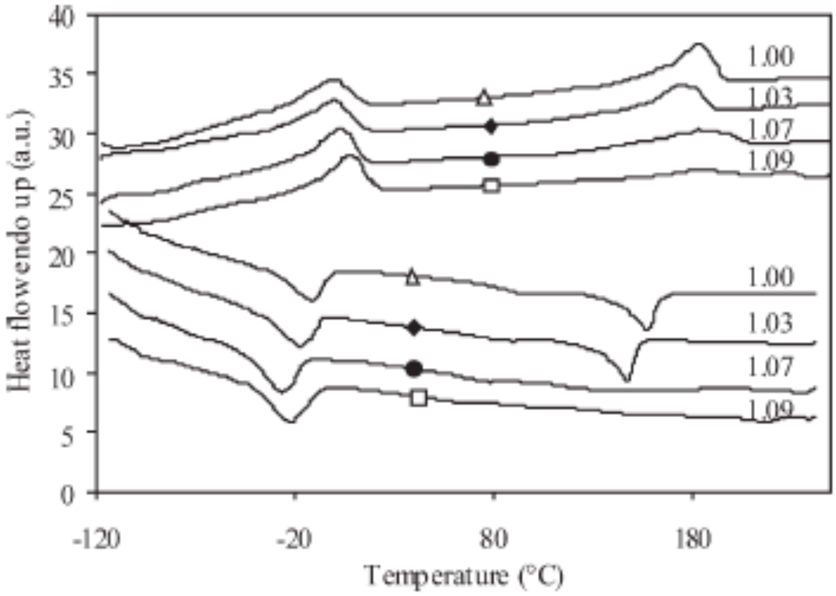

Figure 2.10: DSC thermograms for segmented copolymers based on PTMO and amide HSs with varying amide HS polydispersity: Δ - 1.00; ♦ - 1.03; ● - 1.07; □ - 1.09.

Table 1: DSC measurements for copolymers with varying amide HS polydispersity.

Polydispersity HS	**PTMO SS**			**Amide HS**			**Xc (%)**
	T_m (°C)	**T_c (°C)**	**ΔT (°C)**	**T_m (°C)**	**T_c (°C)**	**ΔT (°C)**	
1.0	-1	-1	0	183	164	19	93
1.01	-2	-13	11	180	163	17	89
1.03	0	-6	6	174	154	20	83
1.04	-1	-17	16	182	159	23	75
1.07	3	-13	16	190	165	25	65
1.09	8	-7	15	184	154	30	24
1.2	6	-33	39	-	-	-	-

The polydispersity of HS was also found to exert an effect on thermal behavior. The melting temperature seemed to be little affected, but the crystallization temperature decreased and so as the melting enthalpy. The supercooling $(T_m - T_c)$ increased with an increasing polydispersity of the copolymer (Table 1). These results suggested that copolymers with a higher polydispersity of the HSs crystallized more slowly and that their degree of crystallinity was lower. For the copolymer with polydisperse amide segments, no melt and crystallization transitions of the amide phase were observed. This was probably due to the wide variation in HS length resulting in very broad transitions. It can be concluded that for copolymers with an increasing polydispersity, the amide segment crystallization was slower, and the crystallinities were lower.

2.4.2 Dynamic Mechanical Thermal Analysis

Thermal mechanical properties of the copolymers were studied by means of DMTA; plots are shown in Figure 2.11. The glass transition of the PTMO SS was low and was not affected by the increasing polydispersity of the hard segment, suggested that the low amount of HS in the PTMO was low. Moreover, both the storage and loss modulus curves show a shoulder at 10 ^{o}C due to the melting of the PTMO. It was evident that the copolymer with monodisperse hard segments had a relatively high storage modulus at room temperature ($G'_{25\,^{o}C}$), which changed little with the polydispersity. The loss modulus curve showed a small broad peak was observed between 60 and 110 ^{o}C, suggesting the presence of a small amount of material melting at a lower temperature.

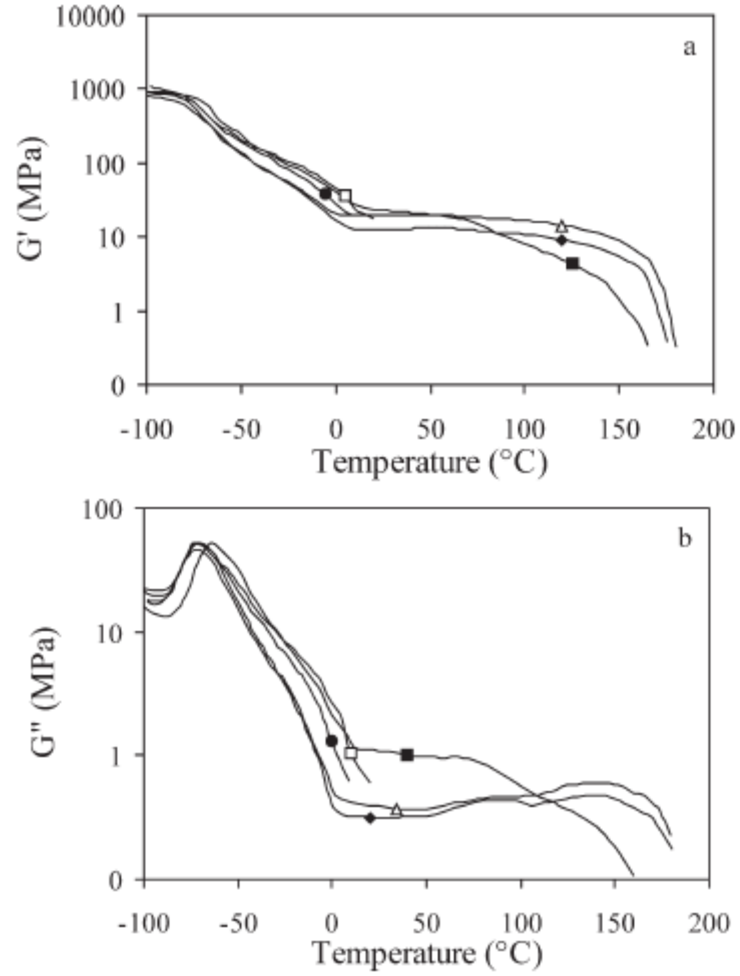

Figure 2.11: (a) Storage and (b) loss modulus as a function of temperature for PTMO-T6A6T copolymers with varying PDI: Δ - 1.00; ♦ - 1.03; ● - 1.07; □ - 1.09; ■ - 1.20.

The tan δ at room temperature was low and the values increased with an increasing polydispersity of the HSs (see Table 2). This suggests that the dynamic behavior at low strains was excellent but decreased with increasing polydispersity. The temperature dependence of the storage modulus in the rubbery regime ($\Delta G'$) was low (0.3% ^{o}C^{-}

^{1}) for monodisperse HSs copolymer but shows a significant increase to 1.1% °C^{-1} with an increase in the polydispersity of the HSs. The flow temperature (T_{fl}) was observed at about 180 °C, however, polydisperse copolymer had a lower T_{fl}. The values of T_{fl} from the DMTA measurements corresponded well with the T_m as measured with DSC (Table 1). At T_{fl}, the polydisperse copolymer was not fully molten, due to the very broad melting transition of the copolymer. The elasticity of segmented copolymers was quantified by means of compression set, at 25% compression at room temperature ($CS_{25\%}$). A low compression set value for monodisperse HS polymer corresponding to a good elastic behavior of copolymer as compared to copolymers with polydisperse HS, which shows high compression set value.

Table 2: Mechanical properties of segmented copolymers as a function of polydispersity.

Polydispersity of HS	$G'_{25\,^oC}$ (MPa)	tan $\delta_{25\,^oC}$	T_{flow} (°C)	$CS_{25\%}$ (%)
1.0	20	0.019	180	14
1.01	14	0.022	180	14
1.03	13	0.023	175	14
1.04	14	0.022	180	15
1.07	19	0.029	185	17
1.09	17	0.038	185	18
1.2	23	0.047	165	31

Thus, segmented copolymers with monodisperse HSs were found to have superior properties as compared to their counterparts with polydisperse HSs. Even small changes in the polydispersity of the HS had an effect on the modulus value, temperature dependence of the modulus, crystallization temperature, rate of crystallization and elastic behavior.

2.5 Effects of HS length

As explained above, controlling the HS dispersity is important in order to achieve temperature independent mechanical properties. Moreover, whereas the SS length and corresponding extenders play an important role in obtaining elastomeric properties at room temperature, the characteristics of HSs determine the final melting point and high-temperature properties. In this section, we illustrate the effect of HS length on thermo-mechanical properties.

2.5.1 Di-amide HS of uniform lengths

The di-amide segments (TxT) contains a one-and-a-half repeating unit of nylon x, T; except for aramide HS, which contains a one-and-a-half repeating unit of poly(phenylene terephthalamide), an aromatic polyamide. In the notation, ‘T’ stands for a terephthalic unit and the ‘x’ represents the number of methylene groups between two amide bonds (spacer length) as shown in Figure 2.1 (a). Polymers based on di-amide HS with even number of methylene groups were extensively studied by Gaymans et. al.,[22,23,8] as they are capable of forming good crystal packing enhanced with the short HS length as compared to the tetra-amide HSs. In this perspective, various systems containing T2T, T4T and TΦT HSs combined with PTMO SS were studied to understand the effect of spacer group (with even number of the methylene group in di-amide) on the thermo-mechanical and flow properties.

2.5.1.1 Thermal properties

PEA based on $PTMO_{650}$ was synthesized using various di-amide HSs, such as T2T, T4T and TΦT.[29] Comparative melting and crystallization temperatures of such copolymers are reported in Table 3. HSs (T2T, T4T and TΦT) along with dimethyl moiety do not show any specific correlation between their melting temperature and their length. HS based on TΦT display the highest melting temperature of 375 °C. It is expected that the corresponding copolymers could show a similar trend, however, T2T-PTMO$_{650}$ copolymer was found to have the lowest T_m, due to the smaller lamellar thickness and partial crystallization of T2T. A similar trend was observed for the crystallization temperatures (T_c) from 137 to 238 °C for TΦT- PTMO$_{650}$ copolymer.

Table 3: Thermal properties of a copolymer of PTMO$_{650}$ with different di-amide HSs.

Amide Segment	**Di-amide T_m (°C)**	**Copolymer T_m (°C)**	**T_c (°C)**	**ΔT (°C)**	**T_g (°C)**	**T_{fl} (°C)**	**G′ (at 25 °C) (MPa)**
T2T	315	163	137	26	-51	158	77
T4T	265	179	160	19	-51	170	116
TΦT	375	266	238	28	-58	247	118

The undercooling $\Delta T(T_m - T_c)$ values are lower than 30 °C, which means that the crystallization of these copolymers is fast irrespective of the type of HSs. The T2T–PTMO polymers have a relatively low melting temperature; this is partly due to the short length of the T2T units (1.7 nm).[22] However, when T2T HSs length was increased using 1,2 ethanediol, the copolymer showed extremely rapid crystallization even after losing the uniformity of the T2T HSs, due to increase in HS length. Therefore, the fast crystallization of T4T-PTMO copolymers allows complete crystallization and short injection molding cycles. Based on such observations, authors refer that the good phase separation and properties can be achieved with a crystallizable unit length of 2 nm.[22]

2.5.1.2 Dynamic mechanical behavior

Being a more sensitive technique, DMA analysis can give additional information about the melting of the PTMO crystalline phase, compared to the DSC. The T_g of T2T and T4T-PTMO copolymer was measured at -51 °C indicating that a small amount of HSs are present in the polyether phase. The rubbery plateaus were found to start at very low temperature for all the samples. As already mentioned, the storage modulus of a rubbery plateau is dependent on the crystallinity and lamellar packing of the crystalline phase. By comparing the storage modulus measured at 25 °C for the three samples, the large difference is observed (see Table 3), increasing from 77 MPa for T2T to around 117 MPa for T4T and TΦT HSs. Again, this suggests that a better packing of crystallites and a complete crystallization of copolymers take place with T4T and TΦT HSs.

The flow temperatures (T_{fl}) for all these copolymers were found to be very sharp and narrow but highly dependent on the type of di-amide HS. This sharp and narrow flow behavior was due to the uniform thickness of the lamellae. The flow temperature and storage modulus of the rubbery plateau are highly dependent on the HS content in the copolymers and is independent of the type of the HS.

2.5.2 Tetra-amide HS of uniform lengths

As already mentioned, tetra-amide HSs (TxTxT) are based on two and a half units of nylon x, T, where ‘T’ stands for a terephthalic unit and the ‘x’ represents the number of methylene groups between two amide bonds (spacer length) as shown in Figure 2.1 (b). D. Husken et al.[24] studied the effect of the methylene length of the tetra-amide HS on the thermal and elastic properties by using a $(PTMO_{1000}\text{-}T)_{6000}$–TxTxT system. In this work, a poly(tetramethylene oxide), PTMO of M_w = 1000 g.mol^{-1} was extended with terephthalic units to M_w = 6000, (denoted as $(PTMO_{1000}\text{-}T)_{6000}$). In this way, crystallization of the long

SS was avoided. The major outcomes of this work are described in the following sections.

2.5.2.1 Thermal properties

DSC results obtained at a heating rate of 20 ºC.min^{-}1 show that the melting temperature of the tetra-amide segments decreases when the number of methylene groups in between the diamide increases. The segments with an odd number of methylene groups in the diamine had a lower melting temperature and melting enthalpy than the segments with an even number of methylene units. These 'odd' segments have a weak packing of the chains in the crystal structure. This observation is in agreement with the general trend observed for polyamides i.e. the melting temperature decreases when the diamine unit is more flexible.

In particular, for PTMO–TxTxT segmented copolymers system, the cooling curve at 20 ºC.min^{-1} for uniform T4T4T, T6T6T and T8T8T segments showed two peaks, which was unusual. The first peak was attributed to the crystallization of the TxTxT segments. The second peak, which had a smaller area, was attributed to a crystalline transition, suggesting that the segmented copolymers had a liquid crystalline behavior.[24] However, no liquid crystalline behavior of the segmented copolymers was observed with optical microscopy combined with cross-polarizer owing to the low concentrations of the HSs.[25]

As expected, the observed melting temperature of copolymers decreases with increasing number of methylene groups in the diamine as an odd-even effect. For an odd number of methylene groups in the diamine, the melting temperature and melting enthalpy were lower. The crystallinity of these copolymers was determined by using the melting enthalpy of the TxTxT-dimethyl segments (see Table 4). The segmented copolymers with an odd number of methylene groups had lower crystallinity compared to the even number of methylene groups, which was probably due to a weak packing of the crystals.

Table 4: Thermo-mechanical properties of $(PTMO_{1000}\text{-}T)_{6000}$-TxTxT segmented copolymers.

Copolymer with HS	TxTxT (wt%)	T_m (°C)	T_c (°C)	ΔT (°C)	T_g (°C)	G′ 25 °C (MPa)
T2T2T	7.0	-	-	-	-61	6
T3T3T	7.4	182	146	36	-64	3
T4T4T	7.8	224	184/224 [a]	<5	-62	5
T6T6T	8.57	202	136/196 [a]	6	-62	6
T7T7T	8.96	172	121	51	-65	3
T8T8T	9.34	194	117/173[a]	21	-64	5

[a]Among the two observed crystallization peaks, the value of the second maximum crystallization peak is labeled.

The undercooling $\Delta T\ (T_m - T_c)$ for the PTMO–TxTxT segmented copolymers were found to be relatively small especially for the T6T6T segmented copolymer. There was no visible trend between the type of TxTxT segments and the values of the undercooling. Furthermore, the undercooling values of the PTMO–TxTxT copolymers were lower than the commercial materials like Arnitel and Desmopan.[26]

2.5.2.2 Dynamic mechanical behaviors

Due to the use of terephthalic chain extender, $PTMO_{1000}$ exhibits a glass transition temperature close to the T_g of the PTMO homopolymer, which is around -86 °C.[27] Therefore it manifest that the terephthalic extender group does not disturb the mobility of the amorphous phase, nor any TxTxT HS was dissolved in the PTMO phase.[28] The shear modulus of these PEAs as a function of temperature shows a small shoulder in the temperature range of -50 to -10 °C and was assigned to a small amount of crystalline PTMO. For all the segmented polymers the flex temperature or the rubbery plateau onset was between 7 to 11 ºC, irrespective of odd-even methylene group effect of HS. The shear modulus, at 25 ºC, was observed to be around 6 MPa for polymers made with an even number of methylene groups, whereas for an odd number of methylene groups it was slightly lower, equal to 3 MPa, as shown in Figure 2.12.

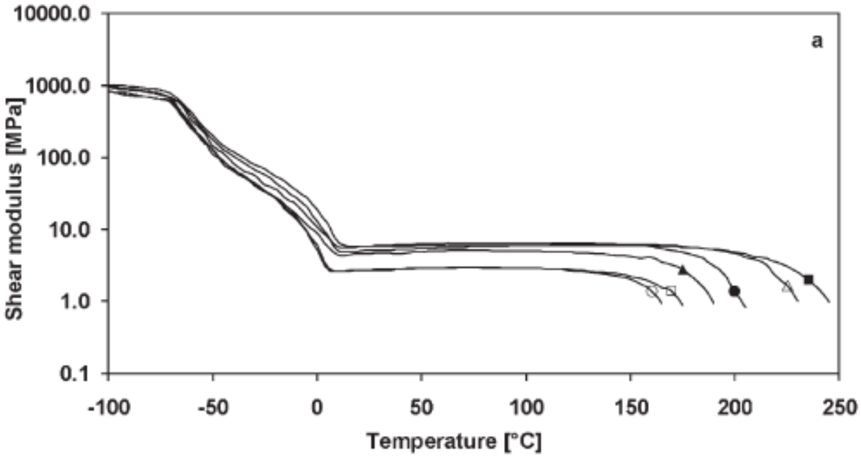

Figure 2.12: Shear modulus for (PTMO$_{1000}$-T)$_{6000}$-TxTxT segmented copolymers: (■) T2T2T, (Δ) T4T4T, (●) T6T6T, (▲) T8T8T, (□) T3T3T, (O) T7T7T.

The rubbery plateau modulus is mainly dependent on the crystallinity of the copolymers; odd-numbered TxTxT segments had low shear modulus due to weak chain packing. The rubbery plateau for all the PTMO–TxTxT copolymers is temperature independent with the sharp melting transition as compared to copolymers with polydisperse HS lengths, which shows a decrease in modulus with temperature. The low-temperature dependence of the modulus is due to the uniform length of the tetra-amide segments, due to which all the crystals melt in a narrow temperature range. Figure 2.13 show the flow temperatures of the segmented copolymers with different TxTxT segments as a function of the number of methylene groups in the diamine. It is clear from Figure 2.13 that the flow temperature decreases with increasing the diamine length ‘x’. Furthermore, a strong odd-even effect is observed. The flow temperatures measured by DMA and the melting temperatures measured by DSC are nearly identical.

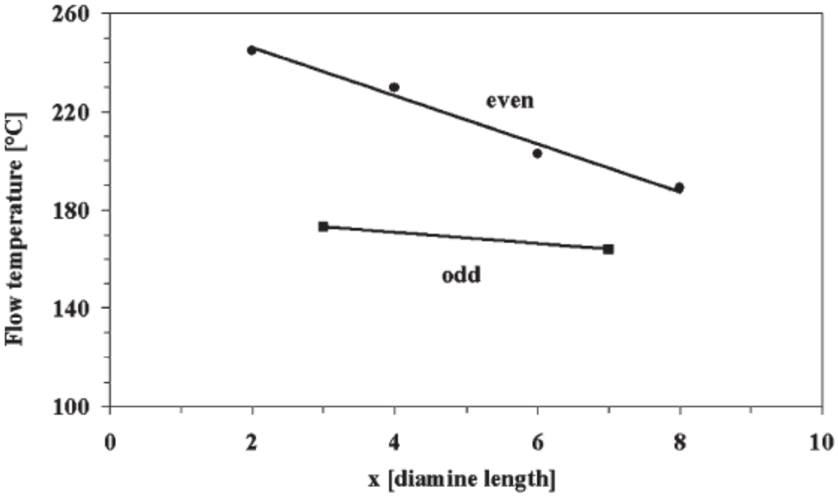

Figure 2.13: Flow temperatures of $(PTMO_{1000}\text{-}T)_{6000}$-TxTxT segmented copolymers as a function of the number of methylene groups in diamine (x).

2.6 Summary

Among the various classes of TPEs, PEAs represent an important class, due to their wide range of applications. A two-step synthesis is generally used to synthesize these PEA, starting from the synthesis of the monodisperse, well defined HSs and then the copolymerization of SS and HS via polycondensation. Amide-based HSs can aggregate and crystallize to form rigid physical crosslinks, which comes to reinforce the sample and therefore, give strong mechanical properties to the material. The structural regularity of the amide unit facilitates good thermo-mechanical properties. Furthermore, their fast crystallizing nature allows short cycle times for various processing techniques without post-processing curing. Above the melting point of the crystalline phase, PEAs are homogenous and melt processing is possible. Upon cooling, the phase separation is restored by crystallization of the amide HS and the material regains its elastomeric properties. In this respect, high M_w SS are ideal as they provide good flexibility and temperature independent rubbery plateau at low temperature. However, SS crystallization should be avoided in order to obtain good flexibility at low temperatures. Therefore, chain extender molecules are used as defects along the chain, to prevent crystallization of the high M_w SSs. On the other hand, amide HSs show an odd-even effect of the number of methylene groups (x) in between the two amide units on the high-temperature properties. HSs with even number of spacer ‘x’ have good properties while ‘odd’ segments show weak packing of the chains in the crystal structure. As far as length of HS is concerned, short HS length (di-amides) shows good phase separation and faster crystallization than tetra-amide.

2.7 References

1) Deleens, G., Foy, P. and Marechal, E. Eur. Pol. Journal 1977, 13, 337.
2) Gaymans, R. J., and J. L. De Haan. "Segmented copolymers with poly (ester amide) units of uniform length: synthesis." Polymer 34.20 (1993): 4360-4364.
3) Van Der Schuur, Martijn, et al. "Structure–property relations of segmented block copolymers with liquid–liquid demixed morphologies." Polymer 46.11 (2005): 3616-3627.
4) Holden, G., and N. R. Legge. "Styrenic thermoplastic elastomers." Thermoplastic elastomer’(Hanser Publisers, New York, 1996, (1996).
5) Lips, P. A. M., et al. "Synthesis and characterization of poly (ester amide) s containing crystallizable amide segments." Polymer 46.19 (2005): 7823-7833.

6) Gaymans, Reinoud J. "Segmented copolymers with monodisperse crystallizable hard segments: Novel semi-crystalline materials." Progress in polymer science 36.6 (2011): 713-748.

7) Gaymans, R. J. "The synthesis and some properties of nylon 4, T." Journal of Polymer Science: Polymer Chemistry Edition 23.5 (1985): 1599-1605.

8) Van Hutten, P. F., R. M. Mangnus, and R. J. Gaymans. "Segmented copolymers with polyesteramide units of uniform length: structure analysis." Polymer 34.20 (1993): 4193-4202.

9) Gaymans, R. J., and J. L. De Haan. "Segmented copolymers with poly (ester amide) units of uniform length: synthesis." Polymer 34.20 (1993): 4360-4364.

10) Van Bennekom, A.; Gaymans, R., Amide modified polybutylene terephthalate: structure and properties. Polymer 1997, 38 (3), 657-665.

11) Gaymans, R.; De Haan, J., Segmented copolymers with poly (ester amide) units of uniform length: synthesis. Polymer 1993, 34 (20), 4360-4364.

12) Jiri George Drobny; Handbook of thermoplastic elastomers; Elseevier, 2014, Chapter 1 (pp 1-10).

13) Versteegen, Ron M., et al. "Properties and morphology of segmented copoly (ether urea) s with uniform hard segments." Macromolecules 39.2 (2006): 772-783.

14) Husken, D., and R. J. Gaymans. "Water vapor transmission of poly (ethylene oxide)-based segmented block copolymers." Journal of applied polymer science 112.4 (2009): 2143-2150.

15) Arun, Araichimani, and R. J. Gaymans. "Hydrophilic poly (ethylene oxide)–aramide segmented block copolymers." European polymer journal 45.10 (2009): 2858-2866.

16) van der Schuur, Martijn, Jan de Boer, and Reinoud J. Gaymans. "Structure-property relations of poly (propylene oxide) block

copolymers with monodisperse and polydisperse crystallisable segments." Polymer 46.22 (2005): 9243-9256.

17) Biemond, G. J. E., Jan Feijen, and R. J. Gaymans. "Poly (ether amide) segmented block copolymers with adipic acid based tetraamide segments." Journal of applied polymer science 105.2 (2007): 951-963.

18) Krijgsman, J., D. Husken, and R. J. Gaymans. "Synthesis and properties of thermoplastic elastomers based on PTMO and tetra-amide." Polymer 44.25 (2003): 7573-7588.

19) Niesten, M. C. E. J., J. W. Ten Brinke, and R. J. Gaymans. "Segmented copolyetheresteraramids with extended poly (tetramethyleneoxide) segments." Polymer 42.4 (2001): 1461-1469.

20) Husken, Debby, Jan Feijen, and Reinoud J. Gaymans. "Segmented Block Copolymers with Terephthalic-Extended Poly (ethylene oxide) Segments." Macromolecular chemistry and physics 209.5 (2008): 525-534.

21) Biemond, G. J. E., Jan Feijen, and R. J. Gaymans. "Influence of polydispersity of crystallizable segments on the properties of segmented block copolymers." Polymer Engineering & Science 48.7 (2008): 1389-1400.

22) Bouma, Krista, Geertje A. Wester, and Reinoud J. Gaymans. "Polyether-amide segmented copolymers based on ethylene terephthalamide units of uniform length." Journal of applied polymer science 80.8 (2001): 1173-1180.

23) Niesten, M. C. E. J., Jan Feijen, and R. J. Gaymans. "Synthesis and properties of segmented copolymers having aramid units of uniform length." Polymer 41.24 (2000): 8487-8500.

24) Husken, D., J. Krijgsman, and R. J. Gaymans. "Segmented block copolymers with uniform amide segments." Polymer 45.14 (2004): 4837-4843.

25) Antoun, S., R. W. Lenz, and J-I. Jin. "Liquid crystal polymers. IV. Thermotropic polyesters with flexible spacers in the main chain."

Journal of Polymer Science: Polymer Chemistry Edition 19.8 (1981): 1901-1920.

26) Tang, Weiming, et al. "Segmented polyurethane elastomers with liquid crystalline hard segments. 1. Synthesis and phase behavior." Macromolecules 27.10 (1994): 2814-2819.

27) Dreyfuss, P., M. P. Dreyfuss, and G. Pruckmayr. "Tetrahydrofuran polymers." Wiley-Interscience, Encyclopedia of Polymer Science and Engineering. 16 (1989): 649-681.

28) Deschamps, A. A., Dirk W. Grijpma, and Jan Feijen. "Phase separation and physical properties of PEO-containing poly (ether ester amide)s." Journal of Biomaterials Science, Polymer Edition 13.12 (2002): 1337-1352.

29) Bouma, K., et al. "Polyesteramides based on PET and nylon 2, T Part 3. Properties." Polymer 41.11 (2000): 3965-3974.

Chapter 3: **Synthesis of well-defined T4T-PTMO copolymers**

Abstract

In this chapter, the synthesis route towards poly(tetramethylene oxide) (PTMO) based poly(esteramide)s (PEA)s with monodisperse di-amide (T4T) HSs is explained. The di-amide T4T segment is based on two terephthalic (T) units and a 1,4-diaminobutane in between terephthalic units. The first step was the synthesis of T4T-dioctyl HSs from dioctyl terephthalate (DOT) and 1,4-diaminobutane (DAB). In the second step, segmented copolymers were synthesized by condensation polymerization. In this set of segmented copolymers, the concentration of di-amide HSs was systematically varied from 0 wt% to 20 wt% in order to study the effect of H-bonding density on the properties of the copolymers. The synthesized copolymers were characterized by ^{1}*H-NMR, DSC, GPC and temperature dependent FT-IR.*

Secondly, a 'dumbbell' version of the poly(tetramethylene oxide) based poly(esteramide)s with monodisperse di-amide (T4T) HSs was synthesized, in which the HSs are only located at both extremities of the chain. To achieve this, mono-functional T4T-mono-octyl HSs were synthesized first, followed by a condensation polymerization with PTMO. Similarly, as for the segmented copolymers, the concentration of di-amide HSs in these dumbbell copolymers was systematically varied from 3 wt%, 5 wt% and 20 wt%. The composition of these copolymers was checked by ^{1}*H-NMR, DSC and GPC.*

3.1 Introduction

As explained in Chapter 2, thermoplastic polyesteramides (PEAs) are material of great interest due to their temperature independent properties, ease of processing,[1] thermo-mechanical and viscoelastic properties which can be controlled by varying the type and the size of the crystallizable and amorphous phases.

From literature, it is known that these materials can be made from a wide choice of HS and SSs. Therefore, these materials can be engineered to exhibit specific properties depending on the application. Among various SSs, PTMO is often used as flexible SS as it has low T_g, good hydrolytic stability and elastomeric properties at low temperatures.[2] Moreover, phase separation is key and HS length is one of the important factors which plays an important role in deciding the extent of phase separation. Research has shown that high phase separation can be achieved with an optimum HS length of 2 nm.[3] In that respect, the high-temperature properties are also dependent on the HS type and length and therefore the choice of HS becomes crucial. PEAs containing short HS showed good crystal packing and fast crystallizing nature in comparison to tetra-amide HSs.[4,5] Therefore, the short length HSs like di-amide becomes more advantageous. But still, the choice of spacer length [x= $(CH_2)_2$, $(CH_2)_4$, $(CH_2)_6$] with even number of methylene group among di-amide HSs remain important. T2T di-amide HS containing copolymers have low melting temperature and low storage modulus, due to small lamellar thickness.[3] On the other hand uniform T4T segments form perfect and stable lamellae, resulting in a temperature independent rubbery plateau.[4] In addition, T4T segment containing copolymers have a melting temperature that makes them easy to process, which makes these materials interesting from an industrial point of view.

Therefore, in this work, we focused on segmented copolymers based on PTMO SS and T4T di-amide HSs. For their synthesis, terephthalic based chain extenders were used during polycondensation to obtain high M_w of PTMO which provides low modulus and a high elasticity; while keeping a low crystallinity of PTMO. The concentration of HSs or hydrogen bonding density was varied from 0 to 20 wt.%. Moreover, dumbbell architecture copolymers based on the same HS and SS system were synthesized, to understand the effect of chain architecture and increased number of SS entanglements on thermal and rheological properties.

3.2 Synthesis of segmented PEAs

Several methods can be employed for the synthesis of segmented PEAs. Though condensation polymerization is the important one, the synthesis can be carried out in solution or via an interfacial technique. Sometimes a combination of two methods may be required.[6] The polymerization can also be carried out in one or two steps and in one or two pots. Thus, the choice of method depends on the nature of the starting material, each of them having its advantages and drawbacks. Furthermore, in this work, it was important to ensure the monodispersity of the di-amide HSs in order to obtain good phase separation and properties. Therefore, this section provides an overview of the synthesis of monodisperse di-amide HS and PEA copolymers containing monodisperse HSs.

3.2.1 Monodisperse HS synthesis

There are various methods to synthesize the preformed monomers; it is advantageous to form the amide linkage first and then ester linkage during the polymerization step to avoid the side reaction of amide group like transamidation reaction. Some of the developments and methods to obtain di-amide monodisperse HSs have been described in the literature. In particular:

Williams et al.[7] carried out the synthesis of PEAs based on 1,6-hexanediol and *N*,*N'*-bis(*p*-carbomethoxybenzoyl) hexanediamine (T6T-dimethyl). This bisesterdiamide was prepared from 4-

methoxycarbonyl benzoyl chloride and 1,6-hexanediamine.[8] The half acid chloride ester was added dropwise to a 1,6-hexanediamine/pyridine solution at the room temperature. After the addition was completed, the mixture was poured into ice water slurry. The product was recrystallized from ethanol to obtain pure di-amide segments.

Goodman and Starmer[9] prepared similar bisesterdiamides by reacting 4-ethoxycarbonyl benzoyl chloride with 1,6- hexanediamine. A solution of ethoxycarbonyl benzoyl chloride in toluene was added dropwise to a mixture of 1,6-hexanediamine in water and toluene. Then, sodium hydroxide solution was added dropwise in water. After the reaction was completed, the precipitate was washed with hot water. Butanol was used for recrystallization to obtain pure bisesterdiamide.

Ciceri et al.[10] synthesized T2T-dimethyl from dimethyl terephthalate (DMT) and 1,2-diaminoethane using lithium methanolate as a catalyst. The reaction was carried out in a solvent mixture of toluene and methanol (65 to 70 °C) over a period of 5 hours. Dimethyl formamide was used for recrystallization to obtain the pure T2T-dimethyl diamide.

A lithium-catalyzed synthesis for T6T-dimethyl was reported by Snam Progetti.[10] Starting materials were 1,6-hexanediamine and dimethyl terephthalate (DMT) dissolved in a methanol/toluene mixture at 65 °C. The catalyst, $LiOCH_3$, was added in a relatively large amount. An excess of DMT with respect to diamine was used to avoid further reaction of the T6T-dimethyl. The product was washed with toluene and twice with hot methanol. The bisesterdiamide was obtained without further purification.

Gaymans et al.[11] and van Bennekom[12] synthesized T4T-dimethyl (*N*,*N'*-bis(*p* carbomethoxybenzoyl)butanediamine) in a similar way as the T6T-dimethyl described by Snam Progetti (shown in Figure 3.1). However, they used a smaller excess of DMT over 1,4-butanediamine (DAB) and a lower lithium concentration. These conditions were shown to be as effective as the larger excess used by

Snam Progetti. A pure product was obtained after recrystallization from hot N-methyl-2-pyrrolidone.

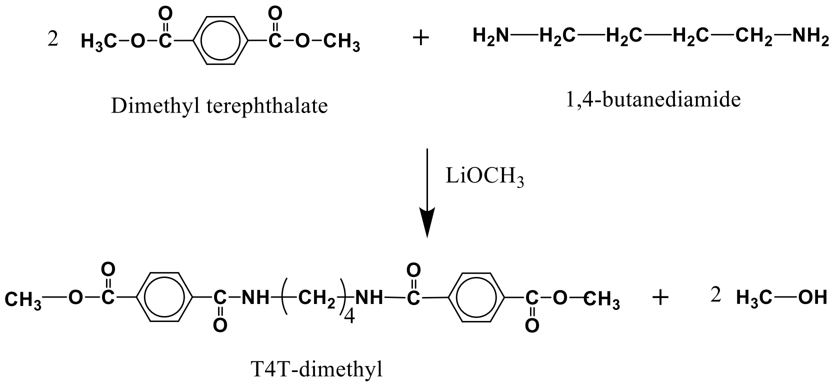

Figure 3.1 (a): Synthesis of T4T-dimethyl (di-amide) HS from dimethyl terephthalate (DMT) and 1,4-butane di-amide (DAB).

The synthesis of the T4T is obtained by selective precipitation of the bisamide and the use of an excess of DMT. The precipitation and the excess of DMT are important aspects of the reaction that allows for a high selectivity towards the bisamide T4T-dimethyl formation, as shown in Figure 3.1 (a). The authors assumed that the reaction starts with the formation of intermediate T4. This product precipitates partly and dissolves again to react with DMT to give T4T-dimethyl, which subsequently precipitates from the reaction mixture as the reactivity of both amine end groups was considered to be equal and one end group does not influence the reactivity of the other end group. Systematic representation of the reaction path is shown in the equation below.

$$\text{DMT} + \text{DAB} \rightarrow \text{T4}$$
$$\text{T4} + \text{DMT} \rightarrow \text{T4T} \qquad (1)$$

T4T-dimethyl precipitates from the reaction mixture and further reaction is limited. But other reactions may take place, as shown below.

$$\text{T4} + \text{DAB} \rightarrow \text{4T4} \qquad (2)$$
$$\text{T4} + \text{T4} \rightarrow \text{T4T4} \qquad (3)$$

$$\text{4T4} + \text{DMT} \rightarrow \text{T4T4} \qquad (4)$$
$$\text{T4T} + \text{DAB} \rightarrow \text{T4T4} \qquad (5)$$
$$\text{T4T} + \text{T4} \rightarrow \text{T4T4T} \qquad (6)$$
$$\text{T4T4} + \text{DMT} \rightarrow \text{T4T4T} \qquad (7)$$

T4 can be partially soluble in the reaction mixture. The solubility of T4 not only determines the rate of reaction for T4T but also for reactions (2) and (3). 4T4 (2) formation is low as compared to (1), if the concentration of DAB is low compared to DMT, therefore excess of DMT is taken and DAB is added dropwise. Reaction (3) is also slow compared to (1), if the concentration of the soluble T4 is low compared to DMT. Reaction (4) is not as important as the reaction (2) hardly takes place. Reaction (5) and (6) are dependent on the solubility of T4T-dimethyl, which is very low and therefore result in a low occurrence of these reactions. Again, if a significant excess of DMT is used, all the DAB reacts with DMT in reaction (1) and reaction 5 becomes even more unlikely Reaction (7) depends on (3), (4) and (5), which are already unlikely. Moreover, the poor solubility of the T4T4 limits the formation of T4T4T even further, which makes reaction (7) very unlikely. The other di-amide HSs like T2T and T6T can be synthesized similarly by using the respective diamine.[13]

3.2.2 Polyesteramide copolymer synthesis

Segmented PEAs with monodisperse di-amide HSs are synthesized from the purified bisesterdiamide as a starting material. Then through polycondensation reaction with hydroxyl functionalized SS, one can obtain the segmented PEA copolymers. PEAs are synthesized in a one-pot polymerization method like an interfacial, solution or melt polycondensation. SS often have hydroxyl end-groups, and the coupling with the acid or ester functionalized HS thus occurs by means of esterification or by a transesterification reaction. The polyamide and the polyether segments are usually incompatible, phase separation often occurs and the reaction between the reactive chain-ends can only take place at the interface.[25] Castaldo et al.[26] used reactive functional groups like acid halides to accelerate such reactions to synthesize PEEA based on PA66 and PEO. On the other hand, in solution polymerization, the application of solvent is required when the solubility or melting point of the monomers and/or the polymer is too high for bulk conditions. The reaction takes place in the presence of esterification catalyst such as tetraisopropyl orthotitanate as shown in Figure 3.1 (b).[3]

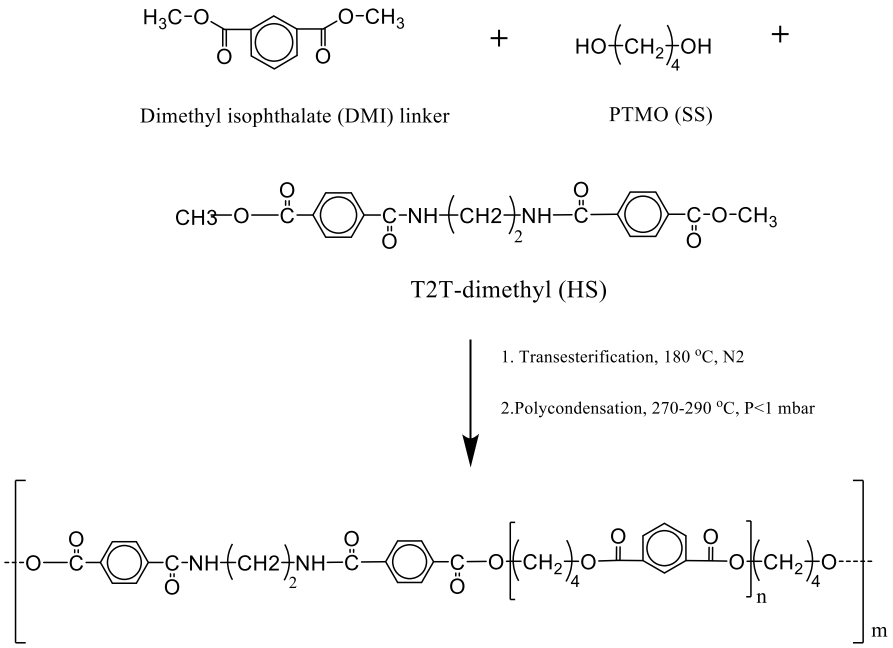

Figure 3.1 (b): Schematic representation of polycondensation reaction to obtain T2T HS based PEAs.

The polycondensation reaction takes place between T2T-dimethyl HS and PTMO SS along with the DMI as chain extender to avoid the crystallization of the SSs. First, the transesterification reaction takes place at 150 to 220 °C at atmospheric pressure in the presence of *N-methyl-pyrrolidone* (NMP) solvent, followed by the polycondensation reaction at 260 to 290 °C under vacuum. During the transesterification step, methanol is formed and distilled off, whereas NMP is removed during the polycondensation step. Various catalyst systems can be used to enhance the rate of transesterification and polycondensation. For transesterification step, calcium, manganese, cobalt acetates, etc. are used whereas polycondensation catalysts are based on antimony, germanium and titanium.

From a synthesis perspective, the challenge is to prepare PEA samples via a solvent-free melt polycondensation method. In the past, the amide HS like T4T-dimethyl ester has been used for the synthesis of polyesteramides. However, the melting temperature of T4T-dimethyl ester HS is around 260 °C and performing condensation polymerization at such high temperature may lead to the degradation of polyether SS, which is a disadvantage. To avoid this, generally, a solution polycondensation technique is used to perform transesterification reaction followed by melt polycondensation. In this method removing the high boiling point solvent after transesterification becomes difficult and makes the process expensive and the use of a solvent for melt polycondensation of high melting HS should be avoided. To overcome such issue during polymerization, in this work T4T-diethylhexyl ester HSs are used instead of T4T-dimethyl ester HS. Due to the presence of two, 2-ethylhexyl bulky groups T4T HSs have a much lower melting temperature (around 125 °C compared to 257 °C for the T4T-dimethyl),[24] therefore, melt polymerization can be done at regular temperatures. Moreover, after the transesterification, 2-ethylhexanol is obtained as a by-product, which has a boiling point of 184 °C and can easily be removed by distillation. Therefore, during this work ethylhexyl ester, HSs are used, which allow for a solvent-free melt polycondensation method in the synthesis of PEAs.

3.2.3 Materials

1,4-Diaminobutane (DAB), acetone and acetonitrile were purchased from Sigma Aldrich, dioctyl terephthalate (bis-(2-ethylhexyl) terephthalate) (DOT) was purchased from Eastman

Chemicals, poly(tetramethylene oxide) (PTMO) with an M_n of 650 and 250 g.mol^{-1} were purchased from BASF chemicals, Irganox© 1330 was purchased from Ciba. Sodium ethoxide (21 wt% in ethanol) with Acroseal© was purchased from Acros, Belgium. All chemicals were used as received. Sodium ethoxide 21% in ethanol was used to prepare sodium 2-ethylhexoxide 1 molar solution by replacing the ethanol by 2-ethyl hexanol using a distillation setup.

3.2.4 Synthesis of monodisperse T4T-dioctyl HSs

DAB (30 g, 0.34 mol) and DOT (574 g, 1.46 mol) were introduced in a round bottom flask equipped with stirrer and nitrogen inlet. Then, 61 cm^3 Sodium ethyl hexoxide solution (1 M) was added and the reaction was carried out for 24 h at room temperature under a nitrogen atmosphere. The reaction mixture was subsequently quenched using 10 mL of water. The T4T-dioctyl was precipitated using 2 L of acetone and filtered. The crude T4T-dioctyl ~250 g was recrystallized from 500 mL hot acetonitrile and washed thrice with 50 mL acetonitrile. The purified T4Tdioctyl was finally dried overnight in a vacuum oven at 65 ^{o}C.

3.2.5 Melt polycondensation - PTMO$_{650}$/DOT/PTMO$_{250}$ (0wt% T4T-(PTMO$_{650}$/DOT/PTMO$_{250}$)) copolymer

The reaction was carried out in a glass vessel reactor with a nitrogen inlet, distillation setup and mechanical stirrer. The reactor was loaded with PTMO$_{650}$ (58.98 g, 0.0907 mol), PTMO$_{250}$ (22.69 g, 0.0907 mol), DOT (64.44 g, 0.1649 mol), Irganox 1330 antioxidant (0.25 g, 0.0003 mol) and Titanium catalyst (0.057 g, 0.0037 mol) and heated to 240 ^{o}C under a reduced pressure of 500 mbar. Subsequently, the pressure was decreased to 10 mbar over a period of 2.5 h. With increasing viscosity of the melt, the stirring rate was gradually reduced from 400 RPM to 100 RPM. The pressure was further reduced to 10 mbar in next 3 h, with gradually reducing the stirring rate to 12 RPM. Then, the system was put under full vacuum (1 mbar) pressure for 1 h.

The polymerization was stopped at a torque of approximately 25 Ncm at 12 RPM to attain a high molecular weight polymer. The synthesized polymer was then removed from the reactor, quenched in water and finally dried overnight in a vacuum oven at 65 °C. Extended PTMO sample was prepared as a reference sample with the same molar mass as that of other samples but with 0% HSs. A similar procedure was used for 5, 10, 15 and 20 wt% HS (T4T) copolymer synthesis, an example for 5 wt% HS is given below.

3.2.6 Melt polycondensation of 5 wt% T4T-($PTMO_{650}$/DOT/$PTMO_{250}$) copolymer

The reaction was carried out in a glass vessel reactor with a nitrogen inlet, distillation setup and mechanical stirrer. The reactor was loaded with T4T-dioctyl (8.31g, 0.0136 mol), $PTMO_{650}$ (57.22 g, 0.0880 mol), $PTMO_{250}$ (22.04 g, 0.0880 mol), DOT (57.19 g, 0.1462 mol), Irganox 1330 antioxidant (0.25 g, 0.0003 mol) and Titanium catalyst (0.057 g, 0.0037 mol) and heated to 240 °C under a reduced pressure of 500 mbar. Subsequently, the pressure was decreased to 10 mbar over a period of 2.5 h. With increasing the viscosity of the melt, the stirring rate was gradually reduced from 400 RPM to 100 RPM. The pressure was then reduced to 10 mbar during 3 h, by gradually reducing the stirring rate to 12 RPM. The system was then put under full vacuum (1 mbar) pressure for 1 h. The polymerization was stopped at a torque of approximately 25 Ncm at 12 RPM to attain a high molecular weight polymer. The synthesized polymer was then removed from the reactor, quenched in water and finally dried overnight in a vacuum oven at 65 °C. Similarly, the procedure was followed for 10, 15 and 20 wt% T4T HS copolymer synthesis by adjusting the amounts of the ingredients as shown below.

Table 1: List of reactants with the amount in grams and moles used for the synthesis of 10, 15 and 20%HS samples.

Reactants	**10%HS**		**15%HS**		**20%HS**	
	(g)	(mol)	(g)	(mol)	(g)	(mol)
T4T-dioctyl	16.62	0.0272	24.93	0.0409	33.24	0.0545
PTMO$_{650}$	55.47	0.0853	53.71	0.0826	51.95	0.0799
PTMO$_{250}$	21.33	0.0853	20.66	0.0826	57.70	0.0799
DOT	49.94	0.1270	42.69	0.1093	35.44	0.0907

3.3 Characterization techniques

3.3.1 Nuclear Magnetic Resonance (NMR)

^{1}H-NMR spectra were recorded using a Bruker spectrometer at 300 MHz. Deuterated chloroform ($CDCl_3$) was used as a solvent along with small amount of trifluoroacetic acid (TFA) to weaken the hydrogen bonds in the samples. Tetramethylsilane (TMS) was used as the reference peak for ^{1}H-NMR analysis.

3.3.2 Gel Permeation Chromatography (GPC)

Gel permeation chromatography was performed on the different samples obtained, with a Viscotek GPC Max from Malvern (UK) equipped with a Viscotek Triple Detector Array 302 including ultra-violet (UV), refractive index (RI), differential viscometer (DV) and right-angle light-scattering (RALS) detector. The synthesized PEA samples were dissolved in HFIP at a concentration of 1.5 mg.mL^{-1}, filtered with 0.2 mm Teflon filters, and injected at a rate of 0.8 mL.min^{-1}. The temperature of both the column and the detector was kept constant at 35 °C.

3.3.3 Differential Scanning Calorimetry (DSC)

DSC thermograms were recorded on a Mettler Toledo DSC821e equipped with the STARe software. Calibration of an instrument was performed using Indium and Tin standards, covering the wide temperature range required for measuring the synthesized PEA copolymers (-90 to 300 °C). Polymer samples were dried overnight in a vacuum oven at 60 °C and 10 – 14 mg of samples mass were measured at 20 °C.min^{-1} under nitrogen for both cooling and heating thermograms. The temperature profile used for the measurement composed of temperature range starting from -80 to maximum 250 °C, the samples were held for 15 min. at 250 °C to obtain homogenous melt and erase sample history. The melting (T_m) and the crystallization (T_c) temperatures were respectively extracted from the second heating and first cooling runs. The degree of crystallinity was calculated from the experimental melting enthalpy corresponding to the value for neat T4T. Note that the thermograms (2nd heating step), were have been reshaped by means of baseline correction to obtain a flat baseline.

3.3.4 Fourier-Transform Infrared Spectroscopy (FTIR)

Infrared transmission spectra were recorded using a spotlight 200i FT-IR spectrometer with a resolution of 4 cm^{-1}. Microtome sample with 10 μ thickness was pressed in between dry KBr pellet and used for the measurements. Temperature-dependent FT-IR spectra were recorded at a temperature range between 30 °C and 200 °C, with controlled heating and cooling rate of 10 °C.min^{-1}.

3.4 Results and Discussion

3.4.1 Synthesis of the monodisperse T4T-dioctyl HSs

Monodisperse T4T-dioctyl HSs was prepared to use as a starting material for the synthesis of segmented copolymers. Figure 3.2 shows the synthesis scheme for T4T-dioctyl from DOT and DAB. An excess of DOT was used to promote the formation of pure T4T-dioctyl (4.3 mol DOT/mol DAB). Sodium ethyl hexoxide solution was used as a catalyst. T4T-dioctyl precipitates out at room temperature from the reaction mixture in 24 h as a white precipitate. Apart from T4T-dioctyl, the precipitate may also contain impurities like T4, T4T4T, DOT and 2-ethyl hexanol similarly to T4T-dimethylester as explained in section 3.2. The excess of T4, DOT and 2-ethyl hexanol were removed using precipitation of the crude reaction mixture in acetone. T4T4T tetra-amide impurities were removed during the T4T-dioctyl recrystallization by filtration of the hot acetonitrile, as the tetra-amide is insoluble in the hot acetonitrile. The obtained pure T4T-dioctyl compound precipitated upon cooling down of the acetonitrile and was collected by filtration. The pure T4T dioctyl was dried overnight at 65 °C in a vacuum oven to remove the solvent. Finally, the structural and thermal characterization of the T4T-dioctyl HS was done using NMR and DSC technique.

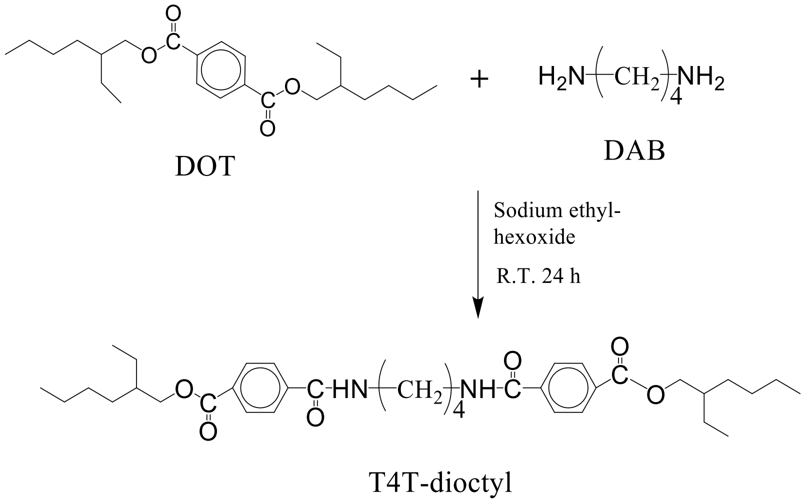

Figure 3.2: Synthesis of T4T-dioctyl from DOT and DAB.

3.4.2 1H-NMR – T4T-dioctyl

The ^{1}H-NMR spectrum corresponding to the T4T-dioctyl was measured in deuterated chloroform ($CDCl_3$) with a drop of TFA. ^{1}H-NMR is presented in Figure 3.3 (a), protons are assigned in 3.3 (b) and chemical shifts are mentioned in Table 2. All peaks can be correlated to the T4T structure, which suggests that indeed the T4T bisamide structure is obtained. In this respect, the absence of a peak at $\delta = 2.6$, corresponding to the methylene protons next to the NH_2 group of starting compound DAB and T4 impurity indicates the absence of these impurities in the final product. Moreover, DOT aromatic protons expected at $\delta = 8.10$ as singlet shows splitting of DOT aromatic protons at $\delta = 8.09$ and 7.88 with nearly equal integration ratio respectively. This confirms the absence of unreacted DOT and monosubstitution product of DOT (T4). On taking the integration ratio for 12 protons of CH_3 group associated with DOT to the amide CH_2 protons i.e. peak g:e, the ratio of 1:3 indicates the formation of T4T di-amide. In the case of formation of tetra-amide (T4T4T) structure, the integration ratio of g:e, should have been in the ratio of 1:1.5, which is not the case. Similarly, the integration ratio between the aromatic protons of DOT i.e. peak a:b, the 1:1 ratio signifies the formation of T4T di-amide. For the tetra-amide structure, the ratio should have been 1:2. Thus, in order to confirm the absence of T4T4T tetra-amide impurities, low-resolution mass spectra was recorded using FINNIGAN MAT-TSQ70 spectrometer with atmospheric pressure chemical ionization (APCI) and Electrospray Ionization (ESI). The mass spectra confirm the synthesis of pure T4T-dioctyl HSs, Figure 3.3 (c). HRMS (+ESI): T4T-dioctyl ($C_{36}H_{53}O_6N_2$): $[M+H]^+$ 609.3904 (calculated) 609.3898 (measured); $[2M+H]^+$ 1217.7650 (calculated) 1217.6635 (measured). However, the tetra-amide impurity T4T4T-dioctyl ($C_{48}H_{67}O_8N_4$): $[M+H]^+$ 828.0760 (calculated) peak was found absent, confirming that the pure and monodisperse T4T-dioctyl HSs were synthesized.

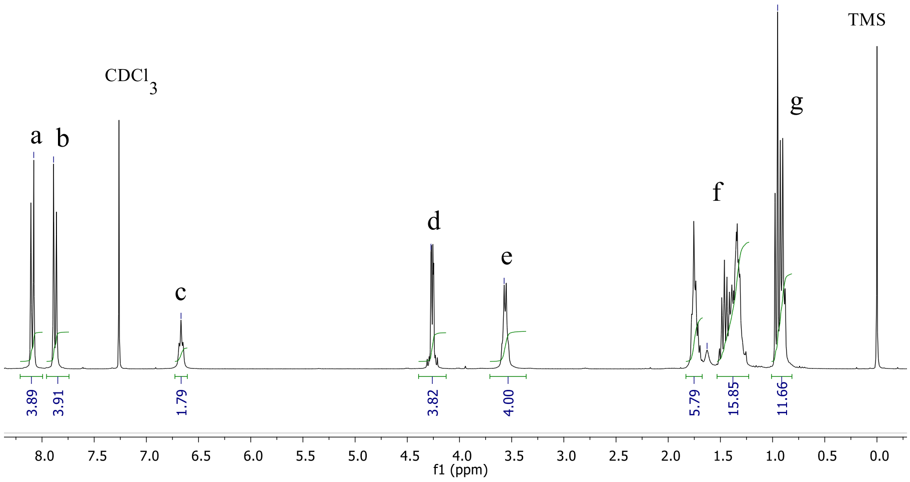

Figure 3.3 (a): ^{1}H-NMR spectra of the T4T-dioctyl compound.

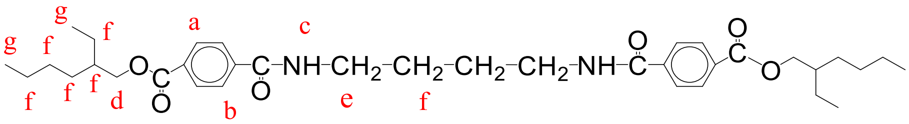

Figure 3.3 (b): Protons assigned for observed peaks of T4T-dioctyl compound.

Table 2: Chemical shift with no. of protons and type of signal for T4T-dioctyl HS.

Assigned protons	Chemical Shift (δ) (ppm)	No. of protons	Type
a	8.09	4	Doublet
b	7.88	4	Doublet
c	6.67	2	Triplet
d	4.43	4	Doublet
e	3.56	4	Quartet
f	2.00 – 1.20	22	Multiplet

g	0.95	12	Multiplet

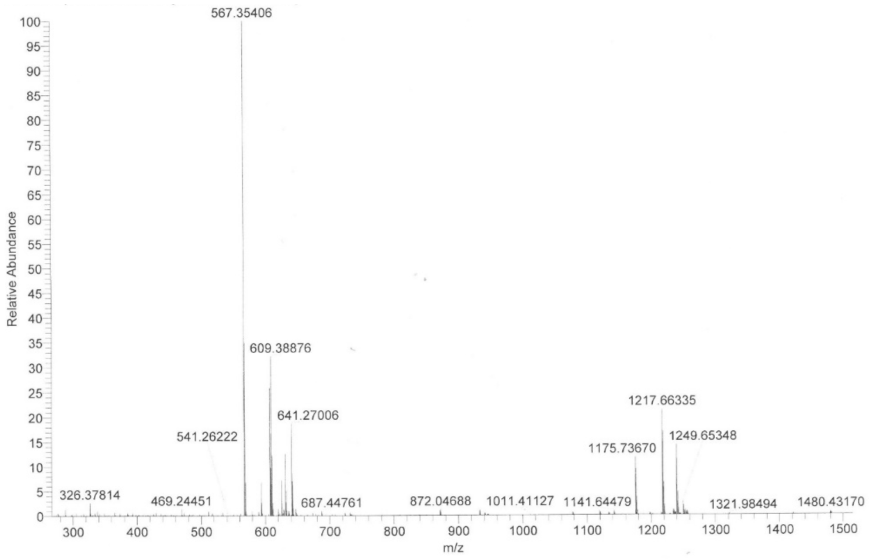

Figure 3.3 (c) : ESI-MS spectra of T4T HS

3.4.3 DSC – T4T-dioctyl

The 2nd heating thermogram corresponding to the T4T-dioctyl HS recrystallized from acetonitrile at 20 °C.min^{-1} is presented in Figure 3.4. It shows a melting transition T_m at 128 °C and a crystallization temperature T_c at 95 °C, with melting and crystallization enthalpy of 77.89 J.g^{-1} and 69.58 J.g^{-1} respectively. The melting temperature for T4T-dioctyl is lower as compared to T4T-dimethyl (~260 ºC),[13] due to the presence of di-octyl bulky groups. This shows that the approach of using Ethylhexyl esters to reduce the melting point of the HS is very effective. The sharp crystallization and melting transition is due to the high purity of T4T-dioctyl HSs.

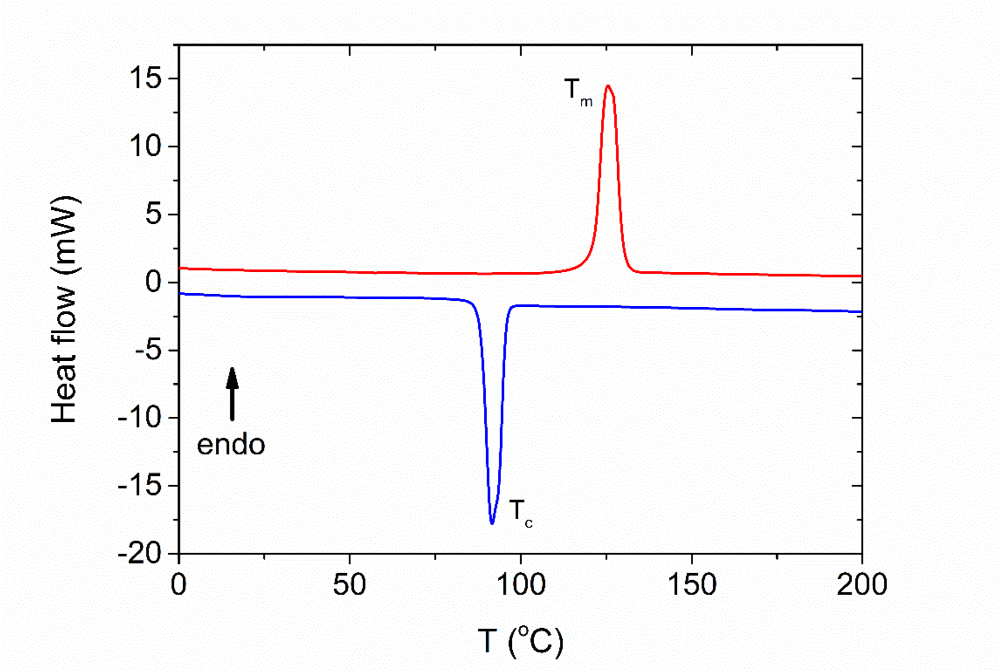

Figure 3.4: Thermogram of the T4T-dioctyl compound performed at 20 °C.min^{-1}.

3.4.4 Melt polycondensation of T4T-(PTMO$_{650}$/DOT/PTMO$_{250}$) copolymers

The T4T-dioctyl precursor was polymerized with hydroxyl functionalized PTMO of molecular weight 250 and 650 g.mol^{-1}. In addition to the nature of the functional end groups, the molecular weight of the polyether has a significant influence on the reactivity. This was discussed by Deleens, who showed that at a molecular weight higher than 2500 g.mol^{-1}, the incompatibility with the amide segment becomes hard to overcome.[23] Therefore, dioctyl terephthalate was used as a chain extender to link the two low molecular weight polyethers and obtain long SS length. The polymerization route is shown in Figure 3.5. The polymerization took place by transesterification followed by a polycondensation reaction at 240 °C. The esterification step requires the reaction of one mole of hydroxyl end-groups with one mole of ester groups. The excess or shortage of one of the end-group would result in a limitation of the molecular weight of the obtained copolymer. In order to avoid it, 10 mol% of PTMO 250 was added in excess to the polymerization process. The low molecular weight PTMO allows for the removal of any excess of OH groups during polycondensation and allows for a good stoichiometry and thus a high molecular weight polymer. Irganox 1330 (0.25%) was added as a stabilizer, to prevent the degradation of PTMO during polymerization and subsequent melt processing. During the transesterification, 2-ethyl hexyl ester end group of T4T HSs were transesterified with the hydroxyl end group of PTMO, to form the alcohol by-product (2-ethylhexanol), which was distilled off. After removal of 2-ethylhexanol the pressure was further reduced to carry out the polycondensation. As the reaction progressed, an increase in molecular weight was revealed by increased viscosity of the melt. Finally, the pressure was further reduced to remove the traces of 2-ethylhexanol, an excess of PTMO (unreacted) to shift the reaction equilibrium to the right and to obtain a high molecular weight polymer. All polymerizations were proceeded to a constant torque of approximately 25 Ncm at 12 RPM to attain a similar and high molecular weight polymer. The obtained copolymers were transparent in nature and a homogenous melt at 240 °C, was obtained for all compositions i.e. 5, 10, 15 and 20% T4T-PTMO$_{650}$/DOT/PTMO$_{250}$ copolymers.

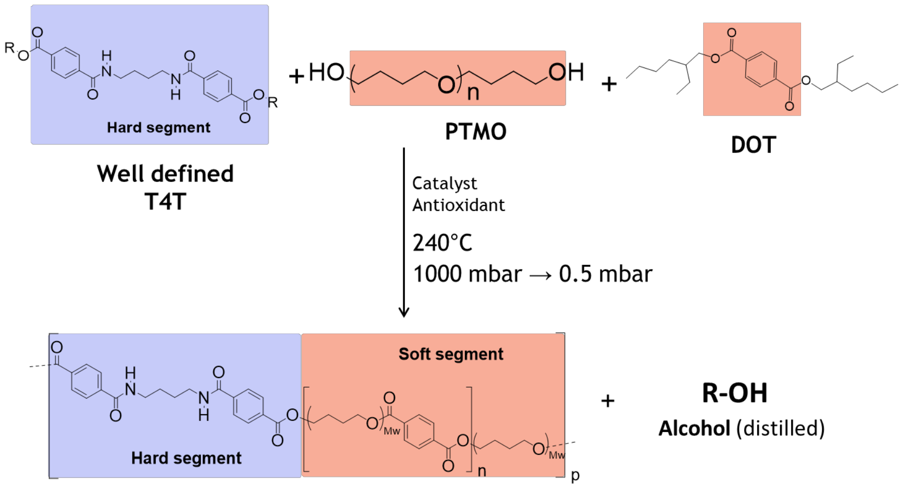

Figure 3.5: Schematic of the PTMO-T4T segmented copolymers. R stands for Octyl group.

3.4.5 1H-NMR – PEA copolymers

The ^{1}H-NMR spectra corresponding to the T4T-PTMO$_{650}$/DOT/PTMO$_{250}$ copolymers were measured in deuterated chloroform ($CDCl_3$) with a drop of TFA. ^{1}H-NMR for 20%HS is presented in Figure 3.6 (a), protons are assigned in 3.6 (b) and respective chemical shifts for all samples are mentioned in Table 3.

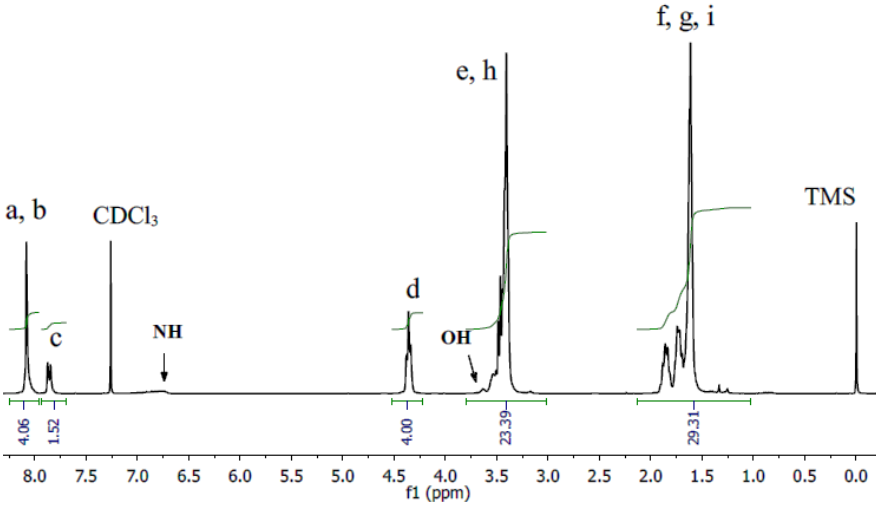

Figure 3.6 (a): ^{1}H-NMR spectra of 20% T4T-PTMO$_{650}$/DOT/PTMO$_{250}$ copolymer.

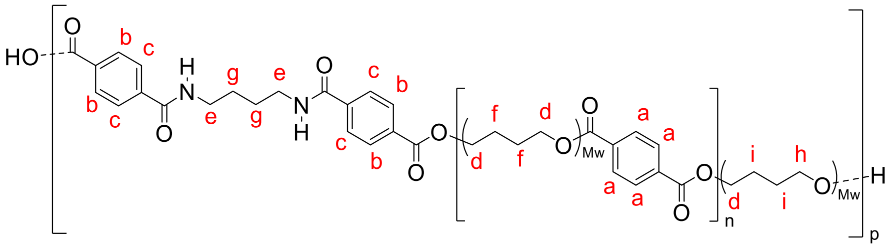

Figure 3.6 (b): Protons assigned for observed peaks of T4T-PTMO$_{650}$/DOT/PTMO$_{250}$ copolymer.

Table 3: Chemical shifts with peak integrals and type of signal for T4T -PTMO$_{650}$/DOT/PTMO$_{250}$ copolymers.

Assigned protons	Chemical Shift δ (ppm)	20% HS integral	15% HS integral	10% HS integral	5% HS integral	Type
a, b	8.08	4.06	4.05	4.03	4.01	Multiplet
c	7.89 – 7.85	1.52	1.10	0.71	0.35	Doublet
d	4.36	4.00	4.00	4.00	4.00	Multiplet
e, h	3.41	23.39	22.75	22.19	21.84	Multiplet
f, g, i	2.00 - 1.00	29.31	29.13	28.19	27.42	Multiplet

^{1}H-NMR spectra show the absence of methyl (CH_3) protons at δ = 0.9 indicated the absence of octyl end group corresponding to 2-ethylhexanol by-product and starting compounds like T4T HS and DOT. This also indicates the efficiency of reaction in the formation of segmented T4T-PTMO copolymers. Among other peaks, well-separated peaks and their integration ratio at δ = 4.36, due to methylene protons next to ester group; at δ = 7.89-7.85, due to aromatic protons of HS terephthalate group and at δ = 8.08, due to aromatic protons of DOT linker can be correlated to the T4T-PTMO copolymer structure. This also signifies that the HSs are intact. However, the possibility of other side reaction taking place cannot be ignored, such side reactions result in polymers of very low molecular weight. For nylon-4, T system Ballistreri et al.[27] reported that the amide bonds undergo β-elimination reaction, which results in primary amide end groups and unsaturated terephthalamide end groups. Further, dehydration of the primary amide undergoes formation of nitrile and water or transamidation respectively. Pilati et al.[28] also reported that for alternating poly(ester amide)s undergo thermal degradation occurred by random cleavage (β-elimination) of ester bonds. The peaks for side reaction products mentioned above are expected to overlap with that of peaks of T4T-PTMO copolymers, but the integration ratio of HS protons to the SS protons indicates the absence of any kind of side reactions taking place. The small peak observed at $\delta = 3.65$ corresponding to OH protons, indicating the polymer chains were hydroxyl end group functionalized.

3.4.6 DSC and GPC analysis – segmented PEA copolymers

Thermal properties of all four segmented PEAs containing 5, 10, 15 and 20%HS were measured using the DSC technique.The Figure 3.7, represents the 2nd heating thermograms at 20 ^{o}Cmin^{-1}, corresponding to all four copolymer samples. The lowest temperature part of the thermograms remains essentially identical for all samples, showing the glass transition T_g of the PTMO around -60 ^{o}C. Then, a small fraction of a SS melting is observed at -15 ^{o}C. It should be noted that the SS melting peak, slightly increases with decreasing %HS, due to larger PTMO strands between the adjacent HSs.[14] On the other hand, at high temperature, the melting point T_m increases from 91.8 to 122.3, 148.6 and 157.8 ^{o}C for 5,10,15 and 20% HS, respectively (see Table 4). Moreover, the thermograms contain “secondary” melting peaks at T ~ T_m-30 ^{o}C, which are clearly visible for 10, 15 and 20% HSs, and which suggest a polymorphism of the T4T crystallites. The degree of undercooling $\Delta T = T_m - T_c$ is below 30 ^{o}C, which is low as compared to fast crystallizing PBT which has undercooling of 36 ^{o}C and indicates fast crystallization upon cooling from the melt.[15] The degree of crystallinity for these materials were extracted by considering the melt enthalpy of 150 J.g^{-1} for pure T4T HS. The value of 150 J.g^{-1} is actually the melting enthalpy of the T4T-dimethyl precursor.[14] This value was found to be nearly equal to the value obtained according to the group treatment by Van Krevelen,[16] who found a value of 57 KJ per mole of crystalline T4T units, corresponding to 150 J.g^{-1}. This melting enthalpy value was also used in the past by Gaymans et al.[14] to calculate the % crystallinity of T4T based PEA copolymers. Here, we apply the same method. Since the synthesized PEAs are also based on T4T HSs, 150 J.g^{-1} melting enthalpy is used to calculate the % crystallinity (X_c) (see Table 4). Interestingly, one can also observe that increasing the HS density causes the shift of the "secondary" broad melting peak toward higher temperature, in a similar way as the main melting peak is shifted. This suggests that both melting processes are interdependent. Table 4 also shows that the synthesized PEA samples are polydisperse (PDI = 2) and possess a high average molecular weight. Since the molecular weight characteristics are similar for all samples, we can consider that the polymer properties are independent of molecular weight and polydispersity and will only differ due to a difference in HS content. As further discussed in Chapter 5, the variation in HS concentration plays an important role in defining the thermal transitions. Increase in HS concentration shows an increase in % crystallinity of the sample. HS % from ^{1}H-NMR was calculated by considering the integration ratio of HS with that of SS, as HSs were added 20 wt% with respect to SS unit comprising of DOT and PTMO. The PTMO CH_2 peak (d) and DOT aromatic protons (a) corresponds to 4 protons each. Thus, by taking the integration ratio of HS peak (b+c) to the SS peak (a+d) gives the value of %HS present in the polymer other than the added %HSs. Since the peak "a" and "b" is overlapping, the integration value of peak b can be obtained by subtraction, as we know the integration value from peak "a" corresponding to four DOT aromatic protons.

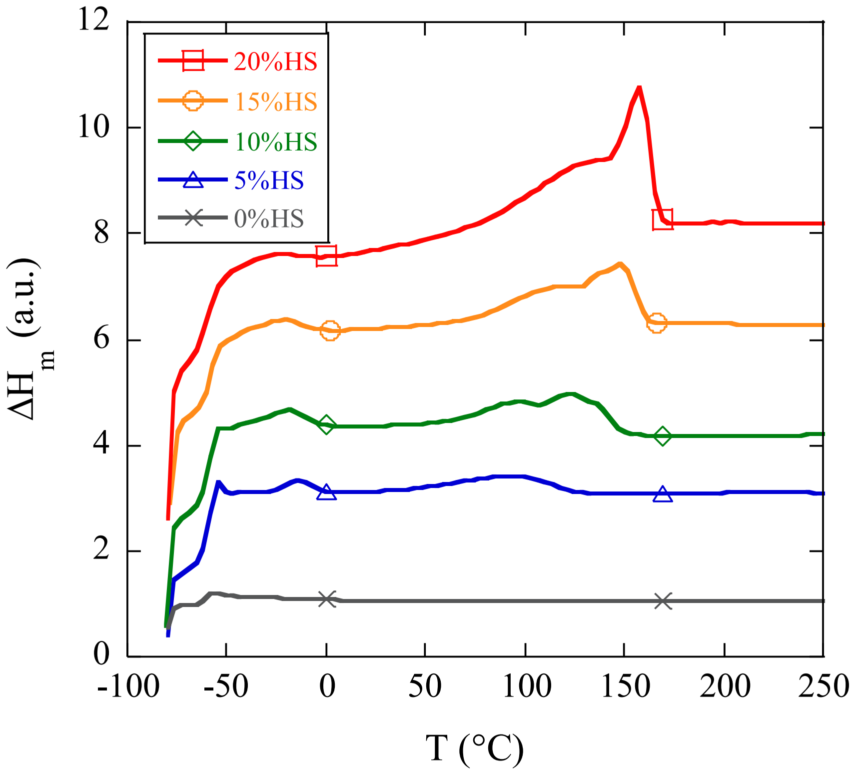

Figure 3.7: Thermograms of the neat PTMO and four corresponding segmented copolymers containing 5,10,15 and 20%HS at 20 ^{o}C.min^{-1}. Data have been vertically shifted for clarity.

Table 4: Physico-chemical information of neat PTMO, 5,10,15 and 20%HS PEAs at 20 ^{o}C.min^{-1}.

HS (%)	**HS % from ^{1}H-NMR****	**M_n g.mol^{-1}**	**M_w g.mol^{-1}**	**M_w/M_n**	**T_g (°C)**	**T_m (°C)**	**T_c (°C)**	**X_c* (%)**
0	-	19000	38900	2.1	-61.5	-	-	-
5	4.5	25200	48900	2	-59.1	91.8	64.5	2.6
10	9.2	22800	44300	2	-58.8	122.3	100.1	6.3
15	14.3	22500	43300	2	-57.9	148.6	119.8	9.3

20	19.7	19300	37600	2	-57.9	157.8	136.4	15.8

* $X_c = (\Delta H_{DSC}/\Delta H_{T4T}) * 100$ where ΔH_{T4T}=150 J.g^{-1} from.[14]

**HS % from ^{1}H-NMR $= \frac{integration\ value\ of\ HS\ peak\ from\ NMR\ (b+c)}{integration\ value\ of\ SS\ peak\ from\ NMR\ (a+d)} * 100$

3.4.7 FTIR – PEA copolymers

Temperature-dependent infrared spectroscopy for 5,10,15 and 20%HS samples were recorded to understand the temperature dependence of various temperature sensitive band throughout the IR spectrum. FTIR spectra for 10 and 20% are shown in Figure 3.8, the relevant bands in the region of 1540 cm^{-1} (C-N or N-H), 1630 cm^{-1} (C=O amide hydrogen bonded), 1670 cm^{-1} (C=O amide non-hydrogen bonded) and 3320 cm^{-1} (N-H hydrogen bonded) respectively.[29] Spectra also show the increase of the intensities of crystalline peaks for 10 and 20%HS samples, as a function of increasing HS concentration at 30 °C.

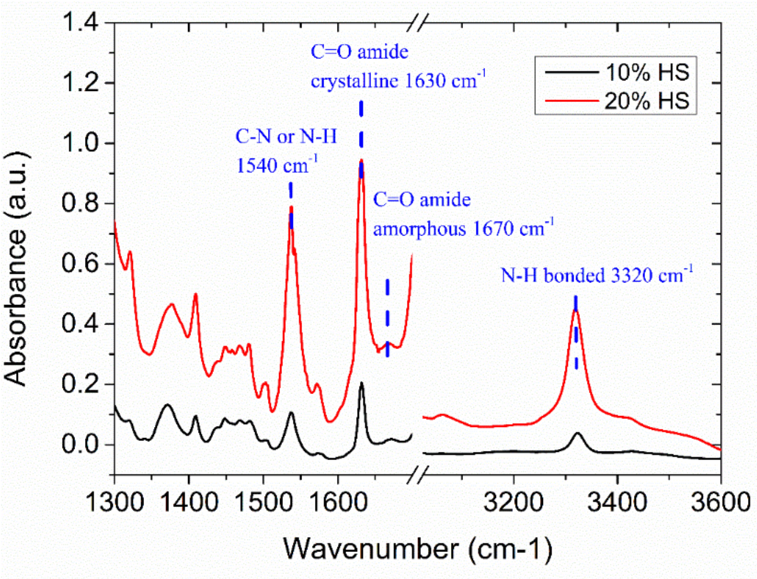

Figure 3.8: FTIR spectra of 10 and 20%HS PEA sample at 30 °C

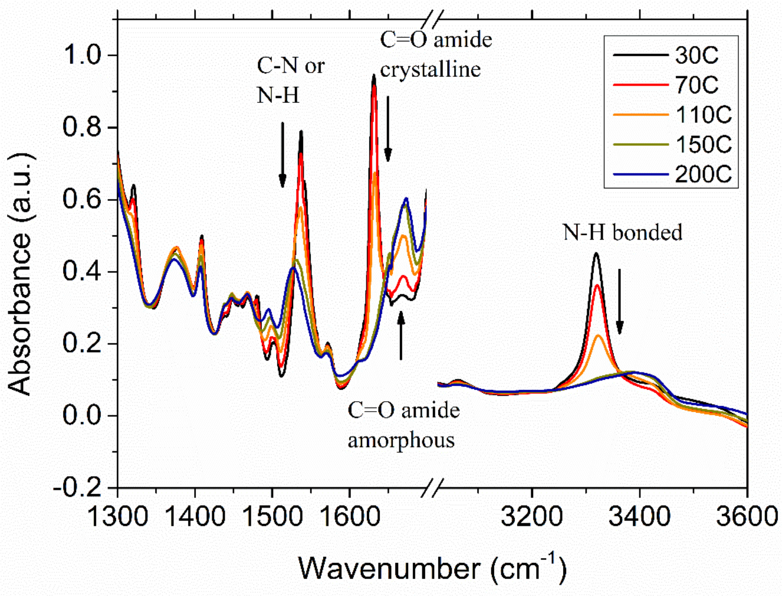

Figure 3.9: FTIR spectra of 20%HS PEA sample during heating from 30 °C to 200 °C.

Polyamides or polymers containing polyamide show the crystal structure transformation on heating and cooling.[17,18] Polyamide 66 was first reported to undergo a change from a triclinic to a pseudo-hexagonal crystal during the heating, known as Brill transition.[19] The temperature at which this transition takes place was defined as Brill temperature. Polyamide 66 IR spectra show a change in Brill bands i.e. C-C skeletal stretching around 950 to 1100 cm^{-1}. In addition, other bands include amide bands at 3300 to 3450 cm^{-1} (ordering and disordering of N-H stretching) and methylene bands at 2800 to 2950 cm^{-1} (CH_2 α, β to N-H or C-O).[20]

In order to explore the possibility of change in crystal structure as a function of temperature, a systematic study was done on 20%HS sample from 30 to 200 °C. Figure 3.9 shows the change in the intensities of temperature sensitive peaks. At 30 °C, the hydrogen bonded amide peak observed at 1540 cm^{-1} was clearly due to C-N or N-H stretching, while the one at 1630 cm^{-1} was due to C=O aliphatic hydrogen bonded amide[21] and the one at 3320 cm^{-1} was due to ordered hydrogen bonded

N-H stretching. All these peaks were important due to the strong absorbance observed. As the temperature was increased, the intensity of crystalline/hydrogen bonded peaks at 1540, 1630 and 3320 cm^{-1} decreases, whereas the intensity of the amorphous/non-hydrogen bonded C=O amide peak at 1670 cm^{-1} showed an increase. Still, it was observed that the N-H band at 3200 cm^{-1} does not disappear completely. In fact, it shifts from 3320 cm-1 to 3420 cm-1, indicating the transformation of ordered (crystalline) hydrogen bonded N-H stretching to free (non-hydrogen bonded) N-H stretching in the melt. However, other bands which could be attributed to the change in HS crystal structure around 950 to 1100 cm^{-1} and 2800 to 2950 cm^{-1} were not observed. Thus, in Chapter 4, other techniques like SAXS and WAXS were used to study the structural organization of HS as a function of temperature in these materials.

3.5 Synthesis of dumbbell PEAs

3.5.1 Materials

1,4-Diaminobutane (DAB), methyl benzoate, acetone, diethyl ether (Et_2O), methanol (MeOH), acetonitrile (MeCN) and triethylamine (Et_3N) were purchased from VWR international. Dioctyl terephthalate (DOT) was purchased from Eastman Chemicals, poly(tetramethylene oxide) (PTMO) with an M_n of 650 and 250 $g.mol^{-1}$ were purchased from BASF chemicals, Irganox© 1330 was purchased from Ciba. Sodium ethoxide (21 wt% in ethanol) with Acroseal© was purchased from Acros, Belgium. All chemicals were used as received. Sodium ethoxide 21% in ethanol was used to prepare sodium 2-ethylhexoxide 1 molar solution by replacing the ethanol by 2-ethyl hexanol using a distillation setup.

3.5.2 Synthesis of monofunctional-T4T HS

3.5.2.1 Step 1: Synthesis of N-(4-aminobutyl)benzamide

A round-bottomed flask was charged with 1,4 diaminobutane (DAB) (107.75 g, 1.22 mol), methyl benzoate (16.5 g, 0.12 mol) along with 21 wt% NaOEt ethanol catalyst (0.85 g, 0.012 mol ~10 mol% of benzoate ester) and a magnetic stirring bar connected to a nitrogen atmosphere through a condenser. The reaction mixture was heated to reflux at 65 °C with stirring for 24h in bulk. The excess of diamine was used to promote the formation of mono-acylation product (10 mol DAB/mol methyl benzoate). The reaction mixture was quenched using water (2 mL). After the reaction, the crude reaction mixture containing an excess of DAB, mono-acylated product, di-acylated product and methanol was mixed with water (200 mL) to keep excess of diamine soluble in water. Then chloroform (200 mL) was used as the organic phase to extract the mono-acylated product via solvent extraction method from the aqueous phase. After extraction, chloroform was efficiently and gently removed using a rotary evaporator to obtain extracted crude reaction mixture. A small portion of the extracted crude reaction mixture was dissolved in methanol for TLC (silica gel) analysis. The TLC separation analysis showed the presence of mono, di-acylated product and DAB components. Based on this, the eluent system was prepared by mixing the polar and non-polar components like Et_2O/MeOH/MeCN/Et_3N (5:2:2:1) in an appropriate volume ratio so that the R_f value of the mono-acylated product fell between 0.2 and 0.4. The unreacted diamine remained at the origin and the di-acylated product (if any) had a R_f above 0.5.[22] This developing solvent was then used as the mobile phase for flash column chromatography to obtain the mono-acylated product. The extracted crude reaction mixture was dissolved in the solvent mixture established by TLC (the volume of the solvent mixture was roughly 3 times of the reaction mixture) and loaded on a silica gel column, which was packed with the same eluent system. Eluting with the same solvent system gave pure mono-acylated product after evaporation of the eluant in vacuo. The practical yield of the obtained mono-acylated product was 56.5%.

3.5.2.2 Step 2: Synthesis of monodisperse T4T-mono-octyl HS

A round-bottomed flask was charged with the mono-acylated product (10.98 g, 0.05711 mol) and DOT (89.20 g, 0.2284). Sodium ethyl hexoxide 1 M solution (0.011 mol) was added as a catalyst and the reaction was carried out for 24 h at room temperature under a nitrogen atmosphere. The reaction mixture was subsequently quenched using 10 mL of water. The T4T-mono-octyl was precipitated using 500 mL of acetone followed by washing with 150 mL and filtered. The crude T4T-mono-octyl ~26 g, was recrystallized from 300 mL hot acetonitrile and washed thrice with 25 mL of acetonitrile. The purified T4T-mono-octyl was finally dried overnight in a vacuum oven at 65 °C. The obtained practical yield of the T4T-mono-octyl product was 64%.

3.5.3 Melt polycondensation of 20% T4T - (PTMO650/DOT/PTMO250) dumbbell PEA

The reaction was carried out in a glass vessel reactor with a nitrogen inlet, distillation setup and mechanical stirrer. The reactor was loaded with T4T-mono-octyl (13.3 g, 0.0293 mol), $PTMO_{650}$ (24.85 g, 0.0382 mol), $PTMO_{250}$ (9.56 g, 0.0382 mol), DOT (18.39 g, 0.0471 mol), Irganox 1330 antioxidant (0.125 g, 0.00015 mol) and Titanium catalyst (0.0288 g, 0.0037 mol) and heated to 240 °C under a reduced pressure of 500 mbar. Subsequently, the pressure was decreased to 10 mbar over a period of 2.5 hours. With increasing the viscosity of the melt, the stirring rate was gradually reduced from 400 RPM to 100 RPM. The pressure was further reduced to 10 mbar in the next 3 hours, and the stirring rate was gradually reduced to 12 RPM. The system was then put under full vacuum (1 mbar) pressure for 1 hour. The polymerization was stopped at a constant torque of approximately 25 Ncm at 12 RPM, similar to the segmented PEAs. The polymer was then removed from the reactor, quenched in water and finally dried overnight in a vacuum oven at 65 °C. Similarly, the procedure was followed for 3 and 5 wt% T4T HS copolymer synthesis by adjusting the amounts of the ingredients.

Table 5: List of reactants with the amount in grams and moles used for the synthesis of 3 and 5%HS dumbbell samples.

Reactants	**3%HS**		**5%HS**	
	(g)	**(mol)**	**(g)**	**(mol)**
T4T-mono-octyl	3.47	0.0293	7.54	0.0166
$PTMO_{650}$	41.17	0.0382	56.63	0.0871
$PTMO_{250}$	15.83	0.0382	21.78	0.0871
DOT	47.97	0.0470	64.8	0.1659

3.6 Results and Discussion

3.6.1 Synthesis of T4T-mono-octyl HSs

T4T-mono-octyl HSs were synthesized by a two-step reaction. First, the mono-acylated product of diamine was synthesized, which in the second step was converted to T4T-mono-octyl HS. In the first step, a high molar ratio of diamine to methyl benzoate was selected (1:10) to avoid the formation of di-acylated product and improve the yield of the mono-acylated product. Figure 3.10 represents the schematic of mono-acylation of symmetric diamine.

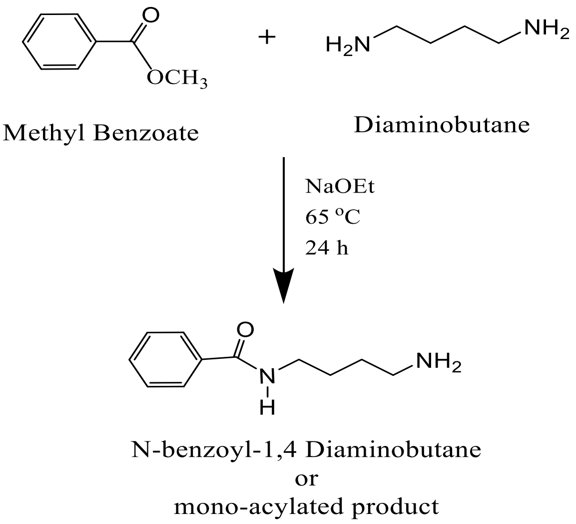

Figure 3.10: Mono-acylation of symmetric diamine (step-1).

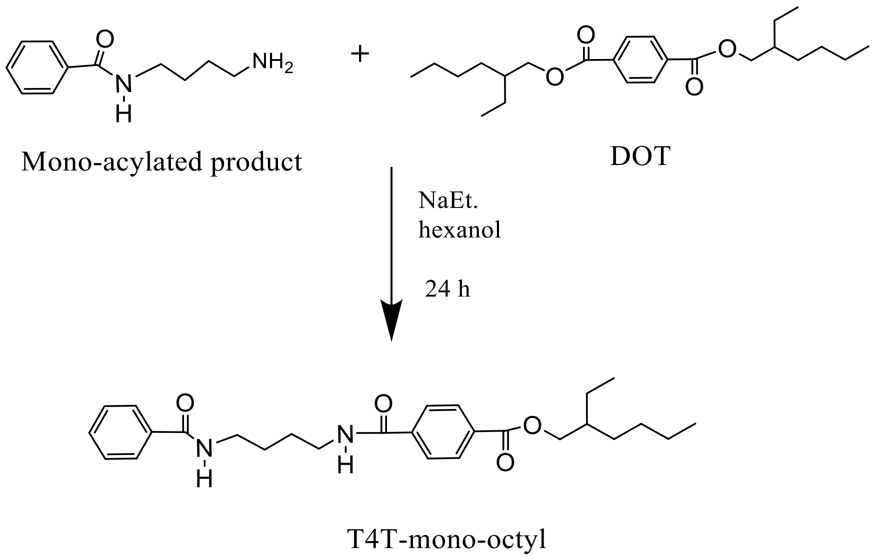

Figure 3.11: Reaction route used to synthesize T4T-mono-octyl HS (step-2).

In the second step, the mono-acylated diamine was reacted with DOT in 1:4 molar ratio to avoid the formation of tetra-amide HSs. Figure 3.11 shows the reaction route of converting mono-acylated diamine to T4T-mono-octyl. However, it must be noted that the possible formation of tetra-amide HS cannot be completely ruled out.

3.6.2 ^{1}H-NMR – mono-acylated diamine and T4T-mono-octyl HSs

The ^{1}H-NMR spectrum corresponding to mono-acylated diamine was measured in deuterated methanol (CD_3OD).[15] ^{1}H-NMR for mono-acylated diamine is presented in Figure 3.12 (a), protons are assigned in Figure 3.12 (b). The disappearance of the peak corresponding to the CH_3 protons next to ester group of methyl benzoate at $\delta = 3.89$ and the presence of a peak corresponding to CH_2 (d in Figure 3.12 b) proton next to the amide group at $\delta = 3.39$ confirm the formation of amide bond between the ester group of methyl benzoate and amine group of diamine. The presence of CH_2 protons peak at $\delta = 2.6$ next to the amine group (e in Figure 3.12 b) also confirms the formation of mono-acylated product and the efficiency of the reaction. The integral ratios of the different signals confirm that the mono-acetylated diamine is obtained. In case of formation of the di-acylated product, the peak at $\delta = 2.6$ should have been absent. The chemical shifts and no. of protons and their multiplicity are mentioned in Table 6.

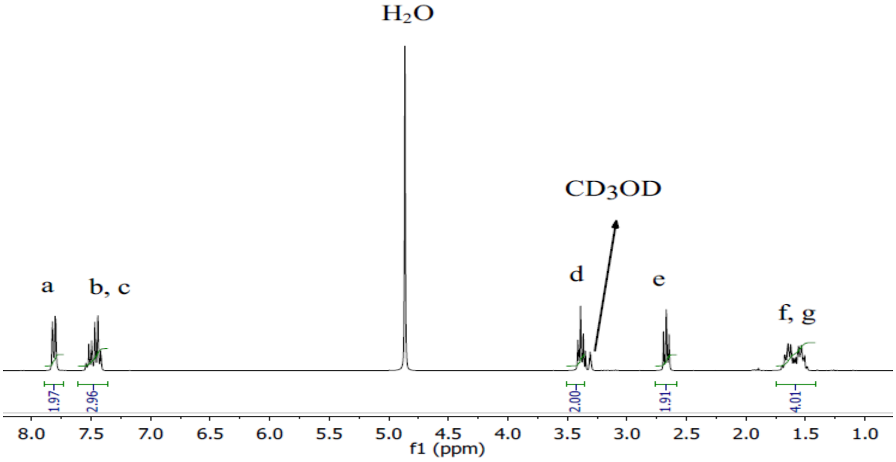

Figure 3.12 (a): ^{1}H-NMR spectra of N-benzoyl-1,4 Diaminobutane (mono-acylated diamine) in CD_3OD.

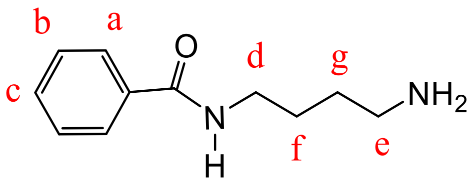

Figure 3.12 (b): Protons assigned for mono-acylated diamine.

Table 6: Chemical shift with no. of protons and type of signals observed for mono-acylated diamine.

Assigned protons	Chemical Shift δ (ppm)	No. of protons	Type
a	7.8	2	Doublet
b, c	7.5	3	Multiplet
d	3.4	2	Triplet
e	2.69	2	Triplet
f	1.56	2	Multiplet
g	1.52	2	Multiplet

^{1}H-NMR for T4T-mono-octyl HS is presented in Figure 3.13 (a), protons are assigned in Figure 3.13 (b) and chemical shift are mentioned in Table 7 respectively. The absence of a peak corresponding to NH_2 protons at $\delta = 2.69$ proves the efficiency of the reaction between the ester group of DOT and mono-acylated product. In addition, the CH_3 protons peaks associated with the octyl side group corresponding to six protons, indicate the mono-substitution of octyl group to the T4T structure. The integration ratio of peak 'h' and 'i' also confirms the presence of one octyl group linked terephthalate moiety. The splitting of two NH protons at $\delta = 6.8$ and 6.5 (f and g) with equal integration ratio, due to the different surrounding chemical environment also confirms T4T-mono-octyl HS structure as shown in Figure 3.13 (b).

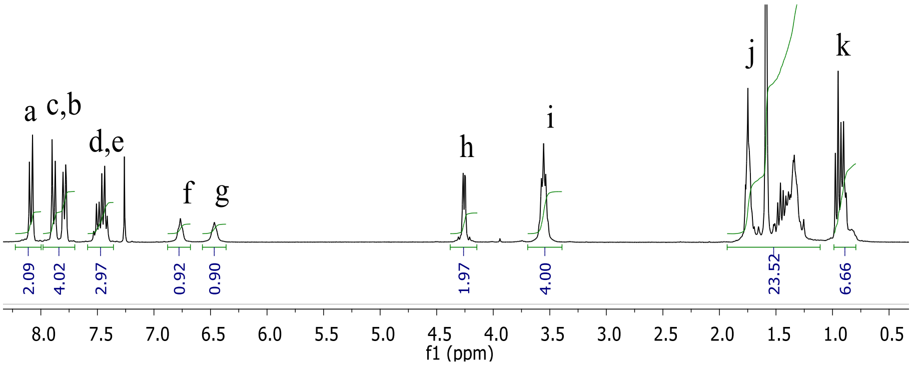

Figure 3.13 (a): ^{1}H-NMR spectra of T4T-mono-octyl HS in $CDCl_3$.

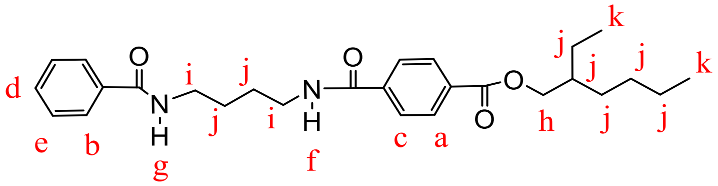

Figure 3.13 (b): Peak assignment of protons for T4T-mono-octyl HS.

Table 7: Chemical shift and assigned proton for T4T-mono-octyl HS.

Assigned protons	Chemical Shift δ (ppm)	No. of protons	Type
a	8.1	2	Doublet
b	7.7	2	Doublet
c	7.9	2	Doublet
d,e	7.5	3	Multiplet
f	6.8	1	Triplet
g	6.5	1	Triplet
h	4.3	2	Doublet
i	3.5	4	Triplet
j	2.0 to 1.2	13	Multiplet
k	0.9	6	Multiplet

3.6.3 DSC – T4T-mono-octyl HS

The 2^{nd} heating thermogram corresponding to the T4T-mono-octyl HS at 20 °C.min^{-1} is presented in figure 3.14. T4T-mono-octyl HS shows melting transition T_m at 141 °C with melt enthalpy of 83.38 J.g^{-1} and crystallization temperature T_c at 136 °C. An increase in melting and crystallization temperature and enthalpy was observed, compared to T4T-dioctyl (T_m= 128 °C with ΔH_m = 77.89 J.g^{-1} and T_c= 95 °C). This is due to the presence of one bulky octyl group resulting in less steric hindrance as compared to of the T4T-dioctyl with two bulky octyl group. Moreover, the degree of undercooling ($\Delta T_m = T_m - T_c$) for T4T-mono-octyl HS is also low, indicating the fast crystallization as compared to T4T-dioctyl HS.

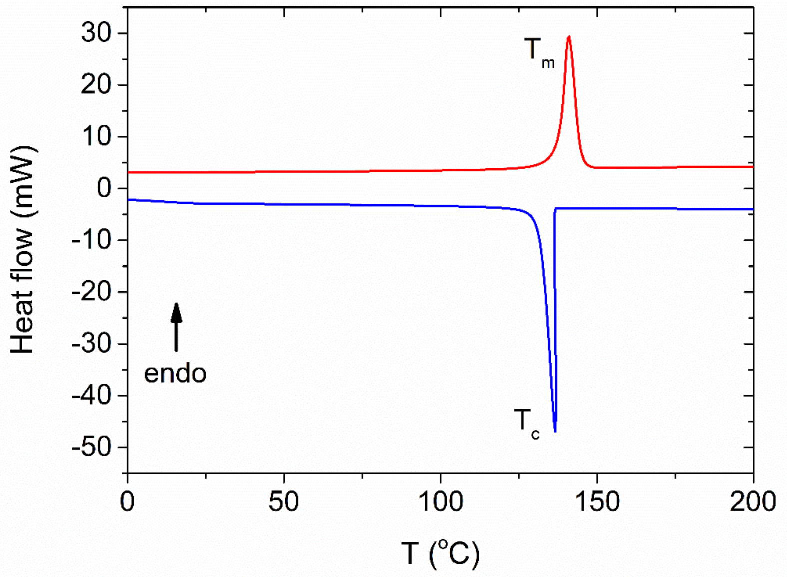

Figure 3.14: Thermogram of the T4T-mono-octyl compound performed at 20 °C.min^{-1}.

3.6.4 Melt polycondensation of T4T-mono-octyl-($PTMO_{650}$/DOT/$PTMO_{250}$) Dumbbell PEA

The T4T-mono-octyl precursor was polymerized with hydroxyl functionalised PTMO of molecular weight 250 and 650 $g.mol^{-1}$. DOT was used as a chain extender to link the two low molecular weight polyethers and obtain long SS length. The condensation polymerization route is shown in Figure 3.15. The polymerization takes place by transesterification followed by a polycondensation at 240 °C. The esterification step requires 1:1 molar ratio of hydroxyl end-groups to that of ester end-groups. Since T4T HSs were mono-functionalized with ester group, which can react with hydroxyl end group to have the terminal position of the polymer chain. Irganox 1330 (0.25%) was added as a stabilizer, to prevent the degradation of PTMO during polymerization and subsequent melt processing. During the transesterification, 2-ethyl hexyl ester end group of mono-functional T4T HSs were transesterified with the hydroxyl end group of PTMO to obtain the alcohol by-product (2-ethylhexanol), which was distilled off. After removal of 2-ethylhexanol the pressure was further reduced to carry out the polycondensation. Finally, the pressure was further reduced to remove the traces of 2-ethylhexanol, an excess of PTMO (unreacted) to shift the reaction equilibrium to the right. The reaction was stopped when the expected amount of distillate (alcohol) was collected, indicating the completion of the polymerization of dumbbell PEAs. Thus, dumbbell PEA with 5 and 20wt% were synthesized just like segmented PEAs, so that the thermal and viscoelastic properties of dumbbell PEAs can be compared with the segmented PEAs to understand the influence of polymer chain architecture. As mono-functional HSs were used, which reacts to ensure terminal position, establishing the dumbbell architecture of the polymer. Also, due to mono-functionality of HSs stoichiometrically equal amount of PTMO hydroxyl end groups are required. Whereby reducing the molecular weight of the dumbbell PEAs with increasing the amount of HSs. Due to decrease in molecular weight of the polymer ultimately SS entanglement is also reduced thus providing an opportunity to study the effect of SS entanglements on the viscoelastic properties. Therefore, dumbbell PEA with 3%HS was also synthesized, having the maximum number of SS entanglement in addition to 5 and 20%HS polymers.

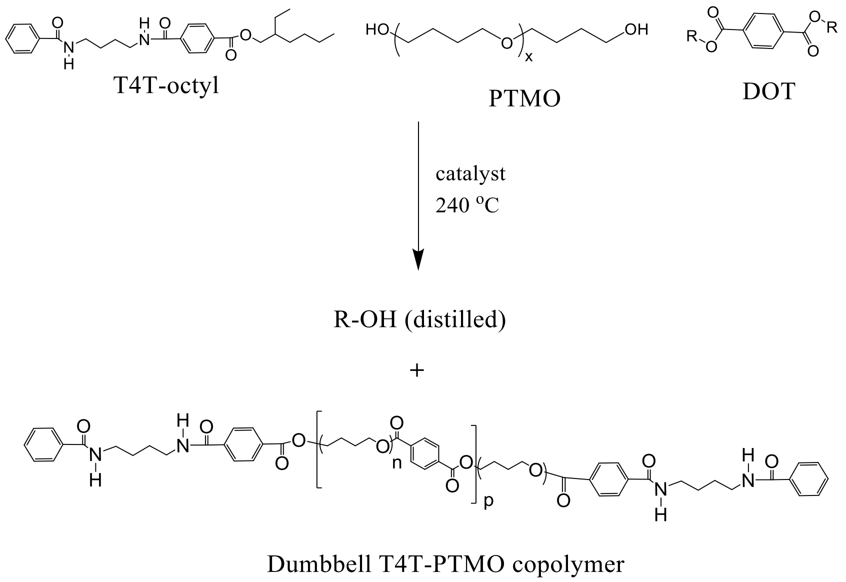

Figure 3.15: Schematic of the T4T-PTMO dumbbell copolymers. R stands for the 2-ethylhexyl group.

3.6.5 ^{1}H-NMR – Dumbbell PEA copolymers

The ^{1}H-NMR spectrum corresponding to the T4T-PTMO$_{650}$/DOT/PTMO$_{250}$ dumbbell samples were measured in deuterated chloroform (CDCl$_3$). ^{1}H-NMR for 20%HS dumbbell copolymer is presented in Figure 3.16 (a), protons are assigned in Figure 3.16 (b) and chemical shift are mentioned in Table 8 respectively.

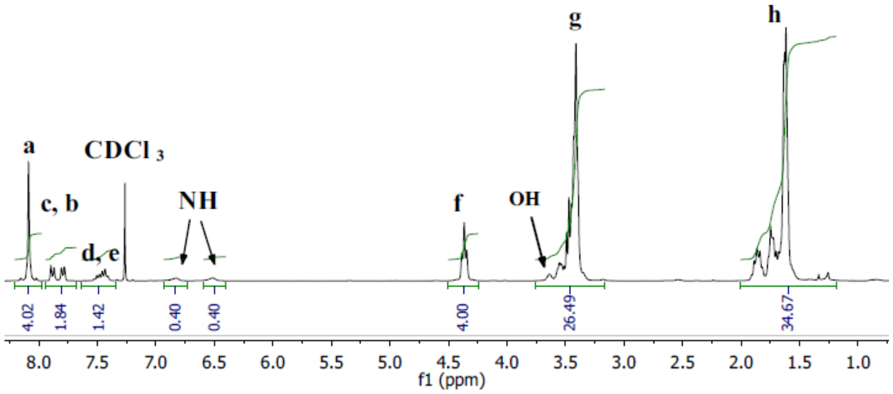

Figure 3.16 (a): ^{1}H-NMR spectra of 20% T4T-PTMO$_{650}$/DOT/PTMO$_{250}$ dumbbell in CDCl$_3$.

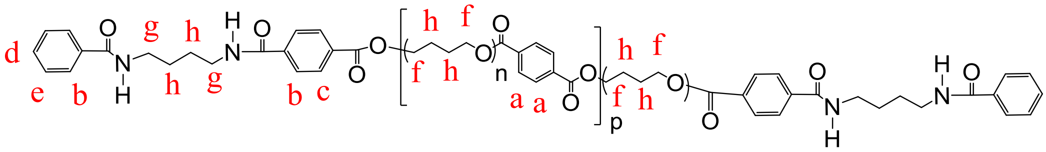

Figure 3.16 (b): Protons assigned for T4T- PTMO$_{650}$/DOT/PTMO$_{250}$ dumbbell PEAs.

Table 8: Chemical shift, with peak integral and type of signal observed for T4T- PTMO$_{650}$/DOT/PTMO$_{250}$ dumbbells PEAs.

Assigned protons	Chemical Shift (δ) (ppm)	20%HS integral	5%HS integral	3%HS integral	Type
a	8.1	4.00	4.06	3.94	Singlet
b, c	7.8-7.7	1.84	0.37	0.23	Doublet
d, e	7.5-7.4	1.44	0.29	0.14	Triplet

f	4.3	4.00	4.00	4.00	Triplet
g	3.4-3.2	26.48	20.21	19.59	Multiplet
h	2.0-1.3	33.67	30.84	26.02	Multiplet

It can be observed from ^{1}NMR spectra that no change in the peak positions standing for mono-functional HS is taking place, except at $\delta = 0.9$. The absence of methyl CH_3 peak at $\delta = 0.9$ due to octyl group of mono-functional HS and the appearance of a peak at $\delta = 8.1$ due to protons of DOT indicates the high efficiency of the reaction. The aromatic protons of DOT (peak a) and methylene (CH_2) protons next to the ester group (peak f), show equal integration ratio, indicating the PTMO covalently bonded to HS and DOT moiety. All the other peaks related to the mono-functional T4T HSs didn't show any change, which indicates that the HSs were intact. However, the OH proton peak at $\delta = 3.65$ indicates the presence of hydroxyl end group chain ends. Therefore, it becomes necessary to know the chain composition of dumbbell samples, using GPC and ^{1}NMR data. As ^{1}NMR spectra were recorded on 300 MHz, the quantification of data is not optimal but tentative polymer chain composition can be estimated.

The number average mol. wt. can be calculated using eqn. 1

$$Mn = (M_{SS} * \#\text{unit}) + p_{HS} * 324 \qquad \text{….. equation 1}$$

where M_{SS} is the mol. wt. of SS repeating unit and #unit is no. of these SS repeating units. Since each repeating unit contains one DOT (of mass 150 g.mol^{-1}) and one PTMO segment (of the average mass of 450 g.mol^{-1}), M_{SS} is estimated to be equal to 600 g.mol^{-1}.

The probability p_{HS} represents the probability for a chain end to be terminated by an HS, of the molar mass of 324 g.mol^{-1}.

From the NMR data of this dumbbells sample containing around 20wt% of HS, it is found that the number of HS present in the sample is 1.5 times smaller than the number of SS repeating units (#unit):

$$\#\mathrm{HS} = \frac{\#\mathrm{unit}}{1.5} = 0.66\ \#\mathrm{units}$$

Therefore, combining this information with the results from the GPC data, according to which the average molar mass of the chains is equal to 2300 g.mol^{-1}, we find that:

$$2300\ g/mol = (600\ \mathrm{g/mol} * \#\mathrm{unit}) + (324\,\frac{\mathrm{g}}{\mathrm{mol}} * 0.66 * \#\mathrm{unit})\ .$$

Thus:

$$\#\mathrm{unit} = \frac{2300\,\frac{\mathrm{g}}{\mathrm{mol}}}{813.84\,\frac{\mathrm{g}}{\mathrm{mol}}} = 2.82.$$

From this last result, the average number of HS per chain can be estimated:

$$\#\mathrm{HS} = 0.66 * 2.82 = 1.861.$$

This allows us to determine the probability to find an HS at the extremity of a chain:

$$P_{HS} = \frac{1.861}{2} * 100 = 93\%\ .$$

From this probability, we can easily determine the proportion of chains ended by an HS at each of its extremities, which is equal to $(0.9305)^2 =$ 86.5%. On the other hand, the proportion of chains with no HS at its extremities is equal to $(1 - 0.9305)^2 = 0.48\%$ of the sample, while the remaining chains, which represent 13.02% of the sample, contain only one HS.

Similarly, for 3% dumbbell sample, we find that the sample contains 9.1% of polymer chains with two HS at their extremities, 48.7% of polymer chains with zero HS and 42.18% of the polymer chain with only one HS at an extremity.

For 5% dumbbell sample, the sample contains 17.4% of polymer chains with two HS, 33.9% of the polymer chain with zero HS and 48.7% of the polymer chain with only one HS.
We can, therefore, conclude that the probability of end-capping the chains with an HS decreases when the length of the chains increases.

3.6.6 DSC and GPC analysis – Dumbbell PEAs copolymers

Figure 3.17, represents the thermograms, corresponding to 3, 5 and 20%HS dumbbell PEAs. All three samples show a value of T_g around -60 °C irrespective of change of polymer chain architecture and amount of HS like segment PEAs. However, only 20%HS sample shows the melting of PTMO SS around 0 °C, probably due to induced crystallization by, the shorter chain length of SS compared to the other samples. In the high-temperature region, an increase of the melting point T_m from 74.2 to 136.5 °C is observed for the dumbbell samples as HS concentration is increased from 3 to 20%. Furthermore, the 20%HS sample shows a broad and multiple melting transitions, probably due to the formation of the different crystal structure. The broad melting nature of 20%HS sample is further discussed in chapter 7. However, in comparison to the segmented PEAs, the 20%HS dumbbell sample shows a significant decrease in T_m, from 156 °C to 136 °C. The reason for this decrease is not clear. Moreover, it was difficult to determine the melting temperature (T_m) for 3%HS sample as melting transition appears broad, probably due to the formation of small crystallites or too weak association of the HSs.

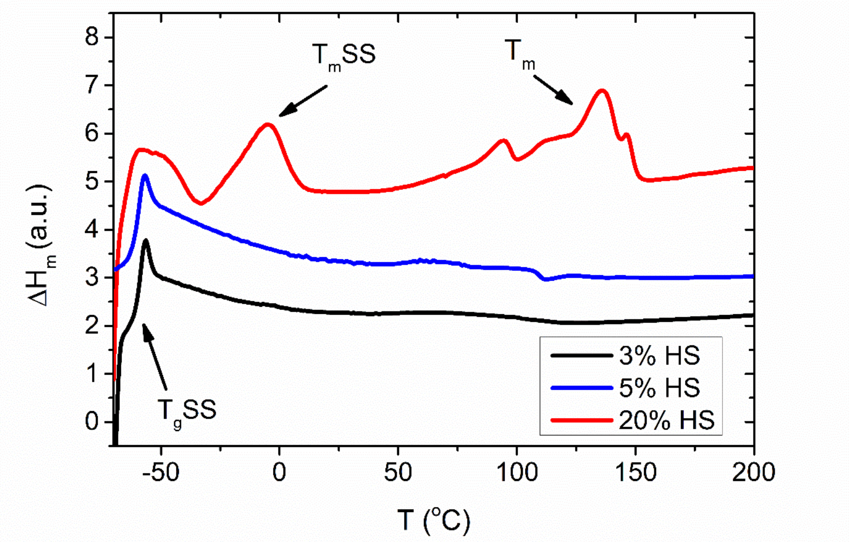

Figure 3.17: Thermograms of the dumbbell copolymers containing 3, 5, 20%HS at 20 °C.min^{-1}. Data have been vertically shifted for clarity.

In Table 9, the physico-chemical information corresponding to the 3, 5 and 20% dumbbell PEAs are presented. All three samples have a polydispersity of around 2, as expected for polycondensates. As mono-functional HSs forms the chain end group, therefore more the %HS, short will be the chain length. Thus, all three samples show different molar mass as shown in the table. The origin of the slightly lower value found for the 20%HS dumbbells is not clear. One can note that the undercooling $\Delta T = T_m - T_c$ for these samples were around 10 °C for 20%HS, whereas it is 17 °C for 3%HS, however, these values are very low as compared to the segmented PEAs sample, highlighting the faster crystallizing nature of dumbbell PEAs as compared to the segmented PEAs.

Table 9: Physico-chemical information of 3, 5 and 20%HS dumbbell PEAs at 20 °C.min^{-1}.

HS (%)	HS % from ^{1}H-NMR**	M$_n$ (g.mol^{-1})	M$_w$ (g.mol^{-1})	M$_w$/ M$_n$	T_g (°C)	T_m (°C)	T_c (°C)	ΔT (°C)
3	2.8	6150	12300	2.0	-59.8	74.2	57.1	17.1
5	4.6	5190	10400	2.0	-58.9	65-95*	85.0	-
20	23	2300	3450	1.5	-58.0	135.6	124.8	10.8

*Broad melting peak, difficult to recognise the melting temperature.

$$\text{**HS \% from } {}^1\text{H-NMR} = \frac{integration\ value\ of\ HS\ peak\ from\ NMR\ (b+c)}{integration\ value\ of\ SS\ peak\ from\ NMR\ (a+f)} * 100$$

3.7 Summary

Segmented PEA copolymers based on monodisperse di-amide T4T HSs and PTMO SSs were synthesized using melt polycondensation reaction. Melt polycondensation of T4T-PTMO copolymer was possible due to a low melting temperature of T4T-dioctyl HSs, compared to T4T-dimethyl HSs. The characterization techniques like ^{1}H-NMR, DSC and mass spectroscopy, confirmed the synthesis of T4T-dioctyl HSs with high purity and were monodisperse in nature. The concentration of these T4T HSs were systematically varied from 5 to 20wt% in order to synthesize a series of four segmented T4T-PTMO PEA copolymers. Figure 3.18 shows the cartoon representation of four segmented PEA samples. The structural and physio-chemical characterization of segmented PEA copolymers were determined using ^{1}H-NMR, GPC, FTIR and DSC techniques. Apart from structure ^{1}H-NMR confirmed that the amount of HS present in the copolymers were equal (± 1%) to the amount of HSs added to the reaction. The melting and crystallization transition of copolymers were found to be dependent on the concentration of the HSs present. The melting transitions were found to be broad and complex for all the four copolymers. GPC confirmed that the obtained copolymers were of equal and high molar mass to achieve good elastic and mechanical properties, thereby making the polymer properties only dependent on the amount of HS content. The undercooling ΔT $(T_m - T_c)$ value in the range of 20 to 30 °C, indicates the fast crystallizing nature of the segmented copolymers as compared to other to fast crystallizing polymers.

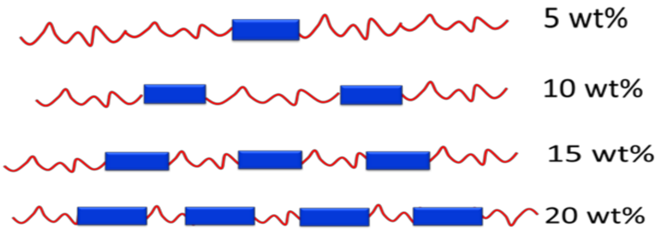

Figure 3.18: Cartoon representation of synthesized segmented PEAs containing 5, 10, 15 and 20%HS.

Similar to the segmented PEAs, dumbbell PEA copolymers were synthesized in order to understand the influence of polymer chain architecture and SS entanglements on viscoelastic and thermal properties of copolymers. The dumbbell copolymers based on di-amide mono-functional T4T HSs and PTMO SSs were also synthesized using melt polycondensation reaction. The T4T-mono-octyl HS was characterized by ^{1}NMR and DSC, the synthesized T4T-mono-octyl HS was found to be pure and monodisperse in nature. Three sets of dumbbell copolymers containing 3, 5 and 20wt%HS were synthesized, and structure of dumbbell copolymers were characterized using ^{1}H-NMR, GPC and DSC techniques. Figure 3.19 show the cartoon representation of three dumbbell PEA samples.

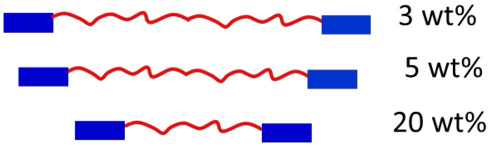

Figure 3.19: Cartoon representation of synthesized dumbbell PEAs containing 3, 5 and 20%HS.

From ^{1}H-NMR the amount of HSs incorporated in copolymers were calculated and the concentration of the HSs in copolymers were found to be close (± 1%) to the amount of HSs added to the reaction, except for 20%HS dumbbell copolymer, where the %HS amount was found to be little higher (23%HS), which indicates the presence of some unreacted (free) HSs. GPC data showed the molar mass for dumbbell copolymers were decreasing with increase in the %HS content. ^{1}H-NMR and GPC data were used together to estimate the polymer chain composition i.e. chains with two HS at the extremities, chains with one HS and chains with no HS. DSC data reveals the increase in the melting and crystallization temperature as the amount of HS concentration is increased. The undercooling $\Delta T = T_m - T_c$ for these samples were in the range of 10 to 20 °C, which are low as compared to the segmented PEAs sample.

3.8 References

1) Holden, G., Legge, N.R., Quirk, R.,.Schroeder, H.E., 'Thermoplastic elastomers', Hanser Publisher, Second Ed. Munich (1996).

2) Dreyfuss, P. et al., 'Encyclopedia of Polymer Science and Engineering', New York (1989).

3) Bouma, Krista, Geertje A. Wester, and Reinoud J. Gaymans. "Polyether-amide segmented copolymers based on ethylene terephthalamide units of uniform length." Journal of applied polymer science 80.8 (2001): 1173-1180.

4) Niesten, M. C. E. J., Jan Feijen, and R. J. Gaymans. "Synthesis and properties of segmented copolymers having aramid units of uniform length." Polymer 41.24 (2000): 8487-8500.

5) Van Hutten, P. F., R. M. Mangnus, and R. J. Gaymans. "Segmented copolymers with polyesteramide units of uniform length: structure analysis." Polymer 34.20 (1993): 4193-4202.

6) Buckwalter, Daniel J., Joseph M. Dennis, and Timothy E. Long. "Amide-containing segmented copolymers." Progress in Polymer Science 45 (2015): 1-22.

7) Williams, J. L. R., T. M. Laakso, and L. E. Contois. "Preparation of regularly alternating polyesteramides." Journal of Polymer Science 61.172 (1962): 353-359.

8) Williams, J. L. R., et al. "Bisesteramides of terephthalic acid." The Journal of Organic Chemistry 25.5 (1960): 817-820.

9) Goodman, I., and D. A. Starmer. "Copolyesteramides—VII. Segmented and random polymers containing bis-terephthalamate units." European polymer journal 27.6 (1991): 515-522.

10) Ciceri L, Di Gregorio F, Platone E. GB Patent 1,365,952, SNAM Progetti S.p.A., Italy, 1971.

11) Gaymans, R. J., and J. L. De Haan. "Segmented copolymers with poly (ester amide) units of uniform length: synthesis." Polymer 34.20 (1993): 4360-4364.

12) Van Bennekom, A. C. M., and R. J. Gaymans. "Amide-modified poly (butylene terephthalate): polycondensation." Polymer 37.24 (1996): 5439-5446.

13) Serrano, P. J. M., A. C. M. Van Bennekom, and R. J. Gaymans. "Alternating polyesteramides based on 1, 4-butylene terephthalamide: 1. Synthesis of the bisesterdiamide." Polymer 39.23 (1998): 5773-5780.

14) P.F. Vanhutten, R.M. Mangnus, R.J. Gaymans, Segmented copolymers with polyesteramide units of uniform length - structure-analysis, Polymer 34 (20) (1993) 4193-4202.

15) Van Bennekom, A.; Gaymans, R., Amide modified polybutylene terephthalate: structure and properties. Polymer 1997, 38 (3), 657-665.

16) Van Krevelen, D. W. 'Properties of Polymers', Elsevier, Amsterdam, 1989, Ch. 5B, p.118

17) Ramesh, C. "New crystalline transitions in nylons 4, 6, 6, 10, and 6, 12 using high temperature X-ray diffraction studies." Macromolecules 32.11 (1999): 3721-3726.

18) Biangardi, H-J. "Brill transition of polyamide 6.12." Journal of Macromolecular Science, Part B: Physics 29.2-3 (1990): 139-153.

19) Brill, R. "Behavior of polyamides on heating." J. prakt. Chem 161 (1942): 49-63.

20) Luo, Jiang, et al. "Mechanism in Brill transition of polyamide 66 studied by two-dimensional correlation infrared spectroscopy." European Polymer Journal 47.2 (2011): 230-237.

21) Dechant, J., 'Ultrarot-spektroskopische Untersuchungen an Polymeren', Maxim Gorki, Berlin (1972).

22) Tang, Wei, and Shiyue Fang. "Mono-acylation of symmetric diamines in the presence of water." Tetrahedron Letters 49.41 (2008): 6003-6006.

23) Deleens, G., P. Foy, and E. Marechal. "Synthese et caracterisation de copolycondensats sequences poly (amide-seq-ether)—I. Synthese et etude de divers oligomeres ω, ω'difonctionnels du poly (amide-11)." European Polymer Journal 13.5 (1977): 337-342.

24) Gaymans, R. J., J. L. De Haan, and O. Van Nieuwenhuize. "Copolymers of PBT and Nylon 4T." Journal of Polymer Science Part A: Polymer Chemistry 31.2 (1993): 575-580.

25) Fakirov, Stoyko, ed. Handbook of condensation thermoplastic elastomers. John Wiley & Sons, 2006.

26) Castaldo, L., G. Maglio, and R. Palumbo. "Synthesis of polyamide-polyether block copolymers." Journal of Polymer Science: Polymer Letters Edition 16.12 (1978): 643-645.

27) Ballistreri, Alberto, et al. "Mechanism of thermal decomposition of nylon 66." Macromolecules 20.12 (1987): 2991-2997.

28) Pilati, F., Masoni, S. and Fortunato, B. Polym. Commun. 1984, 25, 190.

29) Husken, Debby, Jan Feijen, and Reinoud J. Gaymans. "Hydrophilic segmented block copolymers based on poly (ethylene oxide) and monodisperse amide segments." Journal of Polymer Science Part A: Polymer Chemistry 45.19 (2007): 4522-4535.

The content of this chapter has been published in Polymer 107 (2016): 89-101. The contribution of author is limited to synthesis and thermal analysis of all five TPEs sample. This chapter provides understanding of structure organisation in segmented TPEs used, thus useful to understand the results of next chapters.

Chapter 4: **Multiscale Organization of Thermoplastic Elastomers with varying content of Hard Segments**

Abstract

Thermoplastic elastomers (TPEs) based on segmented block-copolymers containing poly (tetramethylene oxide) (PTMO) and terephthalate-based diamide groups (T4T) were synthesized via polycondensation. While PTMO is known to be flexible and amorphous at rest, the more rigid T4T crystallized in different ways depending on both chain composition and sample preparation conditions. Increasing the content of hard segments (HS) from 5 to 20% in weight leads to a substantial increase of the melting point T_m *by more than 60 °C. We have systematically investigated the multiscale (1 Å - 50 nm) organization of the HSs (of fractions from 5% to 20%) by means of DSC, WAXS and (ultra) small angle X-ray scattering (U)SAXS. By increasing HS content, hence the rigidity of the chain, scattering experiments unambiguously show the formation of bigger and better-defined ribbon-like crystallites, as well as the densification of the network they form. We propose a scenario for rationalizing the local T4T-HSs packing and the crystallites anisotropy at the mesoscale (1 – 10 nm) for HS fraction above 5%. Moreover, following in-situ the crystallization of TPEs with large HS fraction (20%), we highlight the presence of "persistent aggregates" present at* $T>T_m$ *and study the*

ribbon-like crystallites growth mechanism during cooling from the melt state.

4.1 Introduction

The name “thermoplastic elastomer” (TPE) refers to polymeric materials exhibiting a dual rubber/melt rheological behavior as opposed to classic vulcanized rubbers.[1,2] Their high elasticity and flexibility at operating temperature (-50 to 50°C) reflects thermo-reversible phase separation,[1] which gives rise to rubber-like properties without involving chemical crosslinks. This reversibility makes the TPEs good candidates for a more sustainable rubber production (recycling of vulcanized rubber is difficult and marginal)[2], in particular in terms of reshaping and recycling many daily consumer goods. Since the 1960’s, a wide variety of industrial relevant TPEs have been synthesized.[3] One of the most popular examples is the PS-PB-PS tri-block copolymer[4] where the segregation of the PS blocks forming rigid subdomains confers rubber-like mechanical properties to the material. While the general phase separation mechanism of these systems is understood, it stays crucial for the industry to be able to control and tailor their properties in order to use them in many different applications. This requires being able to control the transition from their melt to their gel state (and vice versa) in terms of both temperature and mechanical properties. In this direction, rather than letting the (in)compatibility of the two blocks controlling phase separation kinetics and final morphology,[5] researchers have developed new generations of TPEs based on supramolecular interactions, which involve new parameters to tailor the properties of such samples. One of the most popular approaches is the synthesis of segmented (or multi-block) copolymers with flexible units made of poly (tetramethylene oxide) (PTMO) linear motifs (soft-segments “SS”) and rigid units (hard-segments “HS”) based on urea,[6] urethanes[7] or amide groups, as thoroughly studied by Gaymans.[8] The latter segmented copolymers are of particular interest due to their ability to generate multiple hydrogen bonds through the amide (i.e. N-H vs.

C=O) groups, enhancing the aggregation and/or crystallization of the rigid segments in a similar way as in the well-known polyamides PA6 and PA66 *Nylons*.[9] In this context, several studies have shown the importance of monodisperse HSs which crystallize[8, 10] by forming a regular ribbon-like structure (elongated soft objects), providing to the material tunable rheological properties as well as enhanced thermal and chemical stability. Monodisperse HSs also ensure a very fast crystallization upon cooling and a high melting temperature. Furthermore, using short and monodisperse HSs allows reducing liquid-liquid demixing of the hard and SSs when reducing temperature, while keeping a high rate of crystallization.[11]

So far, a lot of effort has been put on the description of the thermomechanical properties,[12] the identification of the crystalline phases[13] as well as the synthesis of new SS/HS motifs[14] with the key result being the systematic raise of both melting point and plateau modulus with increasing the HS content. However, many questions remain about the structure at the mesoscale level (5-100 nm) of the crystalline hard phase, which is a difficult task for semi-crystalline polymers. Nevertheless, this is of central importance for understanding their mechanical and viscoelastic behavior. The most frequently used techniques for determining the structure of such TPEs at the mesoscale level are atomic force microscopy (AFM)[15] and transmission electronic microscopy (TEM)[16] applied on solvent casted films. However, while they reveal interesting structures,[6b, 16-17] one needs to account for the fact that the observed organization strongly depends on the protocol used to prepare the sample. Indeed, structure in solvent casted films significantly differs from the one of the samples processed by extrusion from the melt state (without solvent), i.e. the ones of interest for studying viscoelastic and mechanical properties as well as for developing possible applications (3D printing, fibers production…). The latter, in fact, seem to be characterized by a more complex organization, in which the crystallites are likely more polydisperse and less aligned, hardly accessible with those techniques.[6a]

Small Angle X-ray (or Neutron) Scattering (SAX(N)S) is widely employed[18] but often limited to the observation of the inter-crystallite distance[17] except for the extensive and inspiring work by Sijbrandi et al.[13] which provides a quantitative analysis of the crystal lattice as well as the mesoscale (hexagonal) structure of polyamide based ribbon crystallites. Moreover, the scattering cross section per unit sample volume, or "scattering intensity" $I(q)$, is almost exclusively expressed in arbitrary units (rather than absolute units) limiting *de facto* the structural analysis to the extraction of typical distances in the materials (along the q axis), i.e. ignoring the mass of the scattering objects required to establish a coherent model. Then, because of the very short (yet monodisperse) length of HSs, one cannot use the available molecular theory for similar block-copolymers[19] where phase segregation appears at high values of the Flory-Huggins parameter $(N\chi) \approx (N\chi)_c$ (where $(N\chi)_c$ is the critical value for spinodal decomposition with N the degree of polymerization). Indeed, it does not seem suitable for quick crystallization processes generating phase separation on a micrometer scale.

Going further in the employment of SAXS, one could model ribbon-like objects by using the form factor of semi-flexible chains with self-avoidance calculated by Pedersen et al.[20] This method, which has been successfully used by Hamley et al.[21] for wormlike micelles having a fractal dimension of $D_f \approx 1.7$, allowed the authors to determine directly the contour length, the persistence length and the cross-sectional radius of such elongated structure. However, this model lies on the fact that such objects do not interact with each other, i.e. that their volume fraction must be kept smaller than 1 vol%, far from the type of samples investigated in this work (ca. 5 to 20%v).

Thus, despite the above developments, many questions still need to be addressed in order to understand and control the structure of these TPEs, processed in the melt state. They concern, in particular, (i) the local packing of the T4T units leading to polymorphic crystals, (ii) the crystallites shape and their orientation at the mesoscale being of great interest for the rheology comprehension and (iii) the growth mechanism from the initial state (melt or in solvent). In this context, the key goal is to develop criteria for designing TPE materials with desired performances easily processable at the industrial scale.

The objective of this work is to combine DSC, WAXS and (U)SAXS techniques in order to investigate the multiscale structure of segmented copolymers with a monodisperse hard-segment made of T4T diamide consisting mainly in two terephthalate "T" groups separated by four "4" carbon atoms.[22] (Other "T-amides" groups are reported in the literature).[23] In particular, we would like to study the influence of the HS density on the crystallization and melting of such TPEs. The HS is characterized by a high melting (or crystallization) temperature, e.g., close to T_m = 158°C (or T_c = 136°C)[24] for 20%HS in the chains. On the other side, the SS is made of a sequence of 3 and 8.6 PTMO motifs (respectively called $PTMO_{250}$ and $PTMO_{650}$) between which a terephthalate group is intercalated to limit their crystallization (see chapter 3). Based on these two elementary building blocks, we prepared four different copolymers (following a Flory-type statistic) by adjusting the HS nominal mass fraction to 5, 10, 15 and 20%. The average molar mass of the SSs is varied from 6840 g/mol (5%HS) to 3299 g/mol, (10%HS), 2078 g/mol (15%HS) and 1470 g/mol (20%HS) so that the total molecular weight of the four TPEs remain comparable (see Table 1).

The outline of the chapter is as follows. After the materials and methods description in section 4.2, the results are presented and discussed in section 4.2.3. DSC thermograms of the four TPEs and the neat PTMO are provided in section 3.1. The analysis of the crystal lattice using WAXS is presented in section 3.2, where new arguments to rationalize the T4T diffractograms are provided. Finally, section 3.3 is devoted to the (U)SAXS experiments in which we propose a method to determine the "micro-" (<10 nm) and "meso-" (10-50 nm) scale structure of the ribbons-like crystallites. In this last part, we also propose a growth mechanism based on time resolved SAXS measurements performed between T_m and T_c.

4.2 Material and methods

4.2.1 Materials

All the five segmented TPEs samples containing 0, 5, 10, 15 and 20%HSs were used for this work. The synthesis of these TPEs sample and corresponding characterization information is mentioned in chapter 3.

4.2.2 Samples preparation

The samples measured in DSC, WAXS and (U)SAXS were prepared either by hot pressing or solvent casting. In the former case, ca. 0.5 g of TPE was molten in a vacuum hot press at T_m+10°C applying 0.5 tons weight for 30 minutes and subsequently quenched in ice. In the latter case, the TPE was dissolved for 12 hours in Tetrahydrofuran (THF) or Hexafluoroisopropanol (HFIP) and subsequently dried by evaporating the solvent at room temperature for 48 hours before to be dried one week under vacuum at room temperature.

4.2.3 Differential Scanning Calorimetry (DSC)

DSC measurements were performed using method explained in chapter 3, section 3.3.3. The thermograms are presented in Figure 4.1, note that the data have been corrected in order to have a flat baseline. The physico-chemical data is once again represented in Table 1.

Table 1: Physico-chemical characterization related with the TPEs studied.

%HS (%)	**M_n(PTMO)* (g/mol)**	**<N>****	**T_g^{SS} (°C)**	**T_m (°C)**	**T_c (°C)**	**X_c^{***} (%)**
5	6840	4	-59.1	91.8	64.5	2.6

10	3299	7	-58.8	122.3	100.1	6.3
15	2078	11	-57.9	148.6	119.8	9.3
20	1470	11	-57.9	157.8	136.4	15.8

* Average molar mass of the PTMO segments between two successive HS as calculated based on the synthesis.

** Average number of HS per chain calculated from %HS and M_n.

*** Crystal weight fraction from DSC calculated via $X_c = (\Delta H_{DSC}/\Delta H_{T4T}) * 100$ where ΔH_{T4T}=150 J.g^{-1} from ref.[25]

4.2.4 WAXS

Wide Angle X-ray Scattering experiments were performed on a Rigaku DMAX 12kW setup with λ=1.54 Å. The beam size was 1 cm x 1 mm. We limited the angle range from 2θ = 1.5° to 35° (corresponding to q = 1 nm^{-1} to 25 nm^{-1}) where the signature of all the crystalline phases and the amorphous broad peak were observable.

4.2.5 USAXS and SAXS

We performed USAXS and SAXS measurements on the beam line ID02 at the ESRF in Grenoble, France. The four samples made of segmented block copolymers containing 5, 10, 15 and 20%HS have been measured. Their respective thicknesses were 0.44, 0.81, 0.66 and 1.03 mm. We used two sample-detector distances, 1 m (SAXS) and 30 m (USAXS) with λ=1.1 Å allowing to obtain information over 4 decades in scattering vector $\vec{q}$ (10^{-3} to 10 nm^{-1}) corresponding roughly in the real space to 1 µm to 1 Å. The beam was rectangular with an approximate size of 0.1 x 0.2 mm^2. The well-defined configuration of this experiment associated with the measurement of the empty beam gave us the possibility to access the true sample scattering in absolute units.

In order to complement this data, we also performed SAXS measurements with temperature control on the beam line DUBBLE at the ESRF by using a Haake rheometer equipped with Vespel® parallel plates (no solicitation was applied). The incident horizontal X-ray beam was 90° deviated in order to pass vertically through the rheometer cell (two Vespel plates + sample) and the emerging scattering intensity was measured from the top of the setup, as in ref.[26] For the detection of anisotropic scattering patterns, the novel LAMBDA detector, a 2D photon counting detector, developed at DESY, Hamburg, Pennicard et al.[27] was used. The LAMBDA has a high spatial resolution with a pixel size of 55 x 55 μm^2, a high quantum efficiency close to 100%, and a high speed acquisition of up to 2000 frames/sec[27] at 1.6 m from the sample and using a wavelength of 1.53 Å. Note that the data measured from DUBBLE were then rescaled to the ID02 ones in order to access the absolute units (see the procedure in Figure S4 of supplementary information).

4.3 Results and Discussion

4.3.1 Calorimetry

In Figure 4.1 we present the thermograms corresponding to the four hot-pressed TPEs containing 5, 10, 15 and 20%HS for which the baseline has been forced to be horizontal (see. section 2). On one hand, the lowest temperature part of the thermograms remains essentially identical showing the glass transition of the PTMO at -60 °C (T_g^{SS}) and the melting of a small fraction of it close to -15 °C (T_m^{SS}). One can note, here, the slight increase of this peak with decreasing %HS likely due to larger PTMO domains.[25] On the other hand, the highest temperature part reveals a clear increase of the HS crystallites “terminal” melting point T_m from 91.8 to 122.3, 148.6 and 157.8 °C for 5, 10, 15 and 20%HS, respectively (see Table 1).

Moreover, the thermograms contain “secondary” melting peaks at $T \approx T_m$-30 °C, which are clearly visible for 10, 15 and 20%HS, suggesting a polymorphism of the T4T crystallites in agreement with the complex diffractograms presented in Figure 4.2a below. From the broadening of this secondary peak at lower temperature with increasing

%HS, one could also speculate on the presence of the glass transition temperature of a small fraction of residual amorphous T4T domains[28] (particularly for 20%HS around 20 °C), satisfying the well-known ratio $T_g/T_m \approx 2/3$[29]. This would thus suggest that the HS crystallization is not fully complete for these samples, in agreement with the enthalpy of melting (~ area under the curve) from which the degree of crystallinity can be extracted (see X_c Table 1).

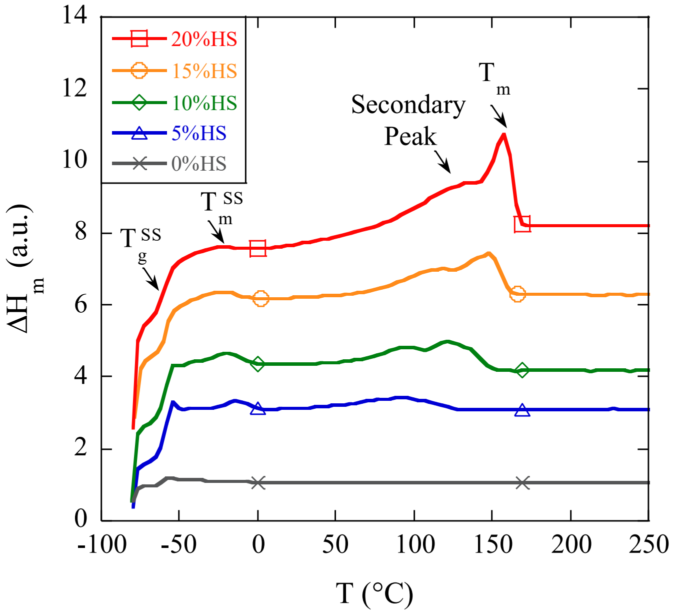

Figure 4.1: Differential Scanning Calorimetry thermograms of the neat PTMO (0%HS) and the four corresponding segmented block copolymers containing 5, 10, 15 and 20%HS. The different $T_g^{SS,}$ T_c (not shown here) and T_m are reported in Table 1. Data have been vertically shifted for clarity.

Interestingly, one can also observe in Figure 4.1 that increasing the HS density causes the shift of the "secondary" broad melting peak toward higher temperature in a similar way than the sharper one suggesting therefore that both melting processes are inter-dependent.

4.3.2 Crystal Structure – WAXS

4.3.2.1 Analysis of scattering intensity and the role of HSs

As it has been already observed in literature, the WAXS pattern related with the T4T crystal is rather complex and has not been elucidated so far.[25] In order to gain further insight, we compare it here to different samples, such as the pure HS sample or a solvent casted version, and follow the relative intensities of the different peaks. In Figure 4.2a, we present the diffractograms measured from the materials synthesized in this work (see section 2) from q = 1 to 25 nm^{-1} (i.e. 2θ = 1.6 to 35°). The main peaks observed through the whole data set are numbered from 1 to 8 from lower to higher q and reported in the Table 2.

While these peaks are nearly absent in the sample containing 5%HS, their respective intensities increase with the fraction of HSs, indicating unambiguously that they are coming from the crystallization of the HSs. Furthermore, a good agreement is found between the positions of most of the peaks in the TPEs chains and the ones coming from the dioctyl-T4T precursor, suggesting that the HS crystal lattice is qualitatively similar in all these materials when hot-pressing at T_m+10°C is used. The broad peak (#4), present in all TPEs (including 0%HS) at 14 nm^{-1} is attributed to the amorphous part of the polymers and tell us about the typical distance between the PTMO segments ($\approx$ 0.45 nm). Overall, the WAXS patterns look similar to the one obtained by van Hutten et al. on similar materials.[25]

Also, we observe in Figure 4.2b, that the WAXS pattern of the 20%HS sample is very sensitive to the sample preparation. Indeed, the comparison between the normalized WAXS signals of sample prepared in the melt state or by solvent casting reveals that 20%HS sample exhibits a different crystal structure when prepared through THF-casting. In particular, it shows that while peak 1 and 5 are enhanced, peaks 3 and 7 are considerably weakened (see Figure S6a-b in supplementary information). Similar results were found for 15%HS, (see Figure S6c-d). DSC confirms qualitatively this result by showing the fall of the broad melting peak originally present around T_m-30 °C, evidencing the polymorphic nature of the T4T crystallites. Additional evidence of polymorphism was also found in Fast Scanning Calorimetry (FSC) experiments and it is reported in chapter 5.[30]

a)

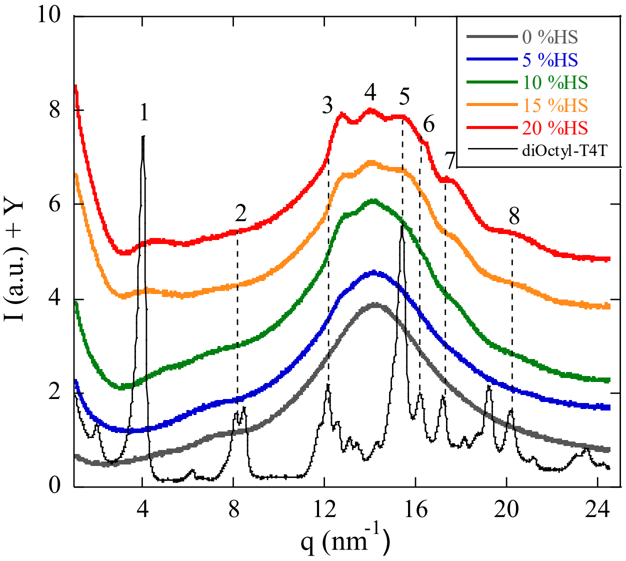

b)

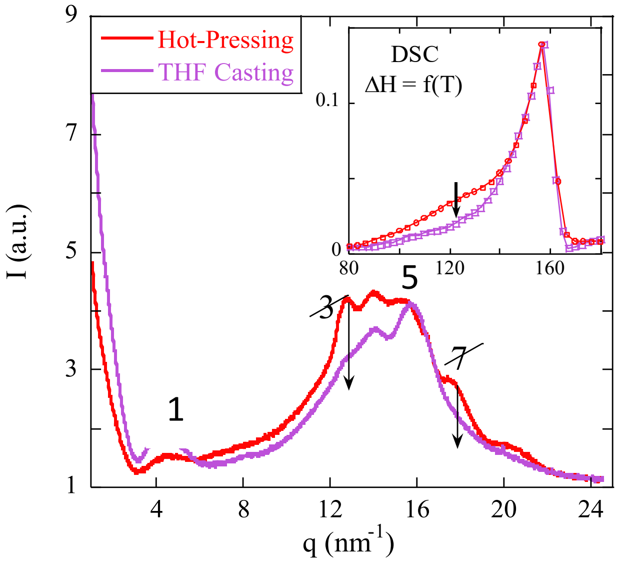

Figure 4.2: a) Scattering intensity measured in WAXS as a function of the transfer momentum q for pure PTMO chains and dioctyl-T4T powder as well as for the four segmented block copolymers prepared by hot-pressing containing 5, 10, 15 and 20%HS. b) Diffractogram from the 20%HS sample prepared by solvent casting vs. the hot-pressed one reproduced from a). The data are normalized in such a way that the intensity of the peak 5 match. Inset: corresponding DSC thermograms in the T_m region confirming the weakening of the secondary melting peak when THF-casting is used.

4.3.2.2 Emerging scenario: formation of ribbons

A way to interpret such WAXS patterns is to go back to the T4T structure (see chapter 3). It suggests that the crystallization can occur via the N-H and C=O groups in a similar fashion as in the Nylon-4,T[31] or in the popular aliphatic Nylon-6 and -66 in which the most stable phase is known as α and corresponds to the anti-parallel stack of the polymer chains.[9] Interestingly, both aromatic and aliphatic Nylons seem to provide similar WAXS patterns most likely due to their common H-bonds driven structure.[31a]

Besides, the succession of the functional groups likely leading to H-bonding in T4T is the following: [C=O - N-H -(C_x)- N-H - C=O] by analogy with the Nylon- 66[32] and in opposition with Nylon-6 in which the motif is [N-H - C=O -(C_x)- N-H - C=O][33] (see also Figure S5 in the supplementary information). This excludes therefore the presence of the γ phase corresponding to the parallel configuration stack of the chains as described in the Nylon-6[34]. Interestingly, Bunn and Garner[32] also reported that a so-called β-phase, similar to the α one in terms of WAXS pattern, could rise from the intermolecular H-bonds bending. Hence, starting from the diffraction pattern of the (aromatic and aliphatic) Nylon's α-phase, one can already identify several peaks obtained from our T4T crystallites (see Table 2). It is notably the case for the peaks 1, 2, 4, 5 and 6 for which positions are found to be in good agreement with the literature.[31, 35] The peak 1, also visible in the high-q range of the SAXS experiment in Figure 4.3a, refers to the inter-T groups distance belonging to a same Nylon 4-T chain,[36] i.e. the distance between the two aromatic rings within the T4T unit (noted α_{001}). The peak 2 has the same origin. Since the peak 4 is not present in the HS precursor but it appears in the pure SS, we assign it to the inter-chain distance, i.e. to the usual amorphous halo present in polymers. We then believe that the peak 5 stands for the HS stacking in the H-bond direction (noted α_{100}) and grows significantly when THF casting is used (longer crystallites, see discussion in section 3.4). Finally, the peak 6, greatly hidden by the previous one, must correspond to the HS stacking in the perpendicular direction (noted α_{010}) and peak 8 is assigned to the N-O distance within one H-bond.

Determining the origin of peaks 3 and 7 is more delicate. The fact that they are strongly weakened in the THF-casted sample and that this goes along with a large reduction of the first broad melting peak in DSC (see the inset of Figure 4.2b) suggests that they correspond to a weaker structure, which is apparently not favored when the chains have a larger mobility, e.g. during the solvent casting procedure. Looking further at the T4T unit, it is interesting to investigate, apart from the amide groups, the possible role of the two aromatic rings. These groups make the HSs intrinsically very rigid and can easily lead to associations via π-π stacking, as it has been observed in a wide variety of systems in the literature (see below). They can therefore increase the HSs coordination number (e.g. allowing the crystal to grow in 2D) i.e. with the H-bonds aligned along one given direction and the π-π interactions perpendicular to it. In fact, the strong H-bonds ($\approx$ 10 kJ/mol each) could even promote this π-π stacking by bringing the HSs close to each other obliging them to pack in a way that suits the excluded volume of aromatic rings (see Figure 4.3). The resulting probability to form π-π stacking should consequently be larger in these particular TPEs than in other H-bonds free ones like polybutylene terephthalate.[37] To summarize, we believe that this second degree of freedom is most likely at the origin of the complex HS lattice because it induces a two-unidirectional crystallization from two distinct molecular interactions.

In order to validate this scenario, one needs to look at the possible configurations for neighboring aromatic rings and see if they are consistent with the peaks 3 and 7 observed in the WAXS pattern. Two possible configurations are reported in the literature known as “Tr” (transverse) and “P” (parallel) with respective distances between the rings’ centers of mass being approximately 5 and 3.5 Å and bonding energy close to 0.72 and 0.48 kJ/mol.[38] Interestingly, these particular distances have been reported from WAXS experiments in both biological and synthetic polymers[39] containing aromatic groups while they do not appear in “rings-free” polyamide.[35] The latter observations seem therefore to confirm the nature of the peak 7. The nature of the peak 3 remains more uncertain since apart from the P rings configuration, it could also very well fit with the α_{110} diffraction for which a decrease of the ribbon thickness would also lead to a weaker intensity.

Table 2: Position of the diffraction peak as found in Figure 4.2 and comparison with the literature about Nylon’s α-phase and π-π stacking. The slight discrepancies are likely due to the fundamental differences between the Nylon-4,T, Nylon-66 and the T4T respective architectures as well as the presence of the SSs.

Peak	**2θ (◦)**	**Position in T4T crystallites (nm^{-1})***	**Position in the literature (nm^{-1})**	**Characteristic distance (nm)****	**Identification**
1	6.48	4.6	4.75[36] - 4.76[35]	1.36	Inter T - α_{001}
2	10.8	7.7	7.1[35]	0.81	α_{002}

3	17.9	12.7	12.8[36-37]	0.49	Tr π- π
4	19.8	14	-	0.45	Amorphous halo
5	21.9	15.5	14.3[35]	0.41	α_{100}
6	23.4	16.5	16.2[31a]-17[35]	0.38	α_{010}
7	25.3	17.8	17.2[35] *17.9*[36-37]	0.35	α_{110} *P π- π?*
8	29.5	21.0	0.28-0.3[31b]	0.30	N---O also seen in[25]

(*) The peak positions come from the tentative of deconvolution of the 20%HS diffractograms presented in supplementary information Figure S6a-d.
(**) The characteristic distances correspond to 2π / "position in T4T crystallites". In the last column, the Miller indices refer to the crystallite axis in the following order: LWH (see Figure 4.3).

We provide in Figure 4.3 a tentative cartoon summarizing our ideas on the T4T crystal lattice. Within this picture, we finally conclude that the length of the ribbons is governed by the "fast" and strong H-bonds while their thickness is influenced by the "slower" and weaker π-π stacking between the "1D-sheets" of associated HSs. Beyond the structure, this last result allows to rationalize the broad melting peak observed in DSC in terms of progressive "unstacking" of the HS sheets before their final melting (H-bonds rupture).

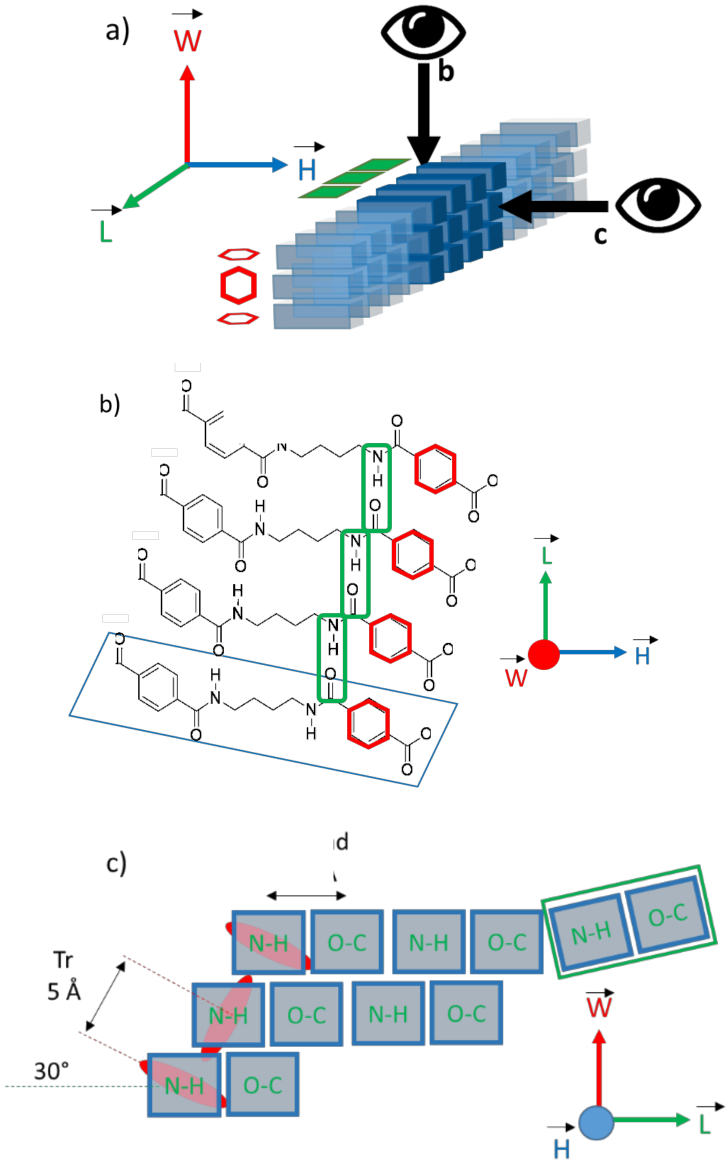

Figure 4.3: Cartoon representing the structure of a crystallite piece. The green polygons represent the H-bonds while the red ones stand for the aromatic rings. a) 3D view, the black arrows indicate the view direction in b) and c), b) top view, c) side view.

In order to investigate the shape of these ribbons at higher lengthscale (>2 nm), SAXS measurements are then needed, as discussed in the section 4.3.3.

4.3.3 Multiscale Structure – SAXS

4.3.3.1 Definition of the elementary HS building-block

The length of one elementary HS can easily be estimated by considering the distances between the atoms and the angles between the bonds as well as the aromatic rings size (see structure in chapter 3), and by accounting for the fact that the conformation induced by the two H-bonds and possible π-π stacking in each segment is stretched. This leads to a HS length of H = 2.1 nm.

On the other hand, determining the exact cross-section of the HS is not obvious. Indeed, the four carbon atoms between the two amide groups are in principle able to slightly bend or rotate inducing a degree of freedom in the crystallite leading to its ribbon-like shape. Consequently, it is *a priori* difficult to know, whether two consecutive aromatic rings belong to the same plane or not. Therefore, for simplicity, we regard the HS as a square based parallelepipedic object having square cross section with R = 0.5 nm being the side (equivalent to the diameter of the aromatic ring accounting with the H atoms). As shown in Figure 4.3, the angle between the H-bond plane (amide group) and the aromatic ring has been reported being around 30° in Nylon-4,T,[31b] it does not however impact our analysis here.

From the previous assumptions, we extract the volume of the HS building-block $\mathrm{V_{HS}} = \mathrm{HR^2} = 0.53\ \mathrm{nm^3}$, the corresponding scattering intensity for $q \rightarrow 0$, $I_{HS}(0) = \mathrm{I_{HS}}^{0} = \Delta\rho^{2\prime}\mathrm{V_{HS}} = 0.49\ \mathrm{cm^{-1}}$ and the radius of gyration $\mathrm{R_{g-HS}} = \sqrt{\frac{1}{3}\left[\left(\frac{\mathrm{H}}{2}\right)^2 + 2\left(\frac{\mathrm{R}}{2}\right)^2\right]} = 0.64\ \mathrm{nm}$.

By further combining these expressions within the Guinier approximation,[40] we can determine the single HS scattering intensity on a wider q-range, $P_{HS}(q)$ being the form factor of a single HS such as:

$$\begin{aligned} \mathrm{I_{HS}(q)} &= \mathrm{I_{HS}}^0\, \mathrm{P}_{HS}(\mathrm{q}) \\ &\approx \mathrm{I_{HS}}^0 \exp\left(\frac{\mathrm{R_{g-HS}}^2 \mathrm{q}^2}{3}\right) \end{aligned} \qquad (1)$$

The result of the previous calculation is plotted in Figure 4.4a (black solid line). As expected, at high q, i.e. for $q \rightarrow q^{\#}$, $\mathrm{I_{HS}(q)}$ becomes comparable with the experimental reduced intensity.

This good agreement supports the approximations made on the T4T structure and on the normalization procedure (see section 1 in supplementary information).

4.3.3.2 Mesoscale organization (crystallites)

Once the single HS dimensions are well defined, we can analyze the TPEs structure at a larger, mesoscopic length scale, i.e. investigating the crystallites morphology. Note that the latter can be formed through the aggregation of HS units in the plane orthogonal to the local chain axis with their thickness being defined by the previously determined HS length *H*. The two other dimensions (width and contour length) are called in the following *W* and *L,* respectively. As explained in section 4.3.2, we believe that the H-bonds are parallel to the long axis of the crystallite $(\vec{L})$[31b] while the weaker π-π stacking (Tr or P) is responsible for their width (W). The total number of HS per crystallites N_{agg} is defined from the aggregation numbers (N_H, N_w, N_L) along each axis $(\vec{H}, \vec{W}, \vec{L})$, respectively, such as $N_{agg} = N_H N_w N_L = N_w N_L$ since N_H is fixed to 1 from the chemical structure (see Figures 1 and 4).

The normalized scattering intensity measured by SAXS as a function of the transfer momentum q are presented in Figure 4.4a for all the hot-pressed TPEs. The general trend of the spectra can be analyzed, looking at the different q-ranges. (see also sections. 1.1 and 1.2 in supplementary information for further details on the data treatment, notably Φ_{eff}):

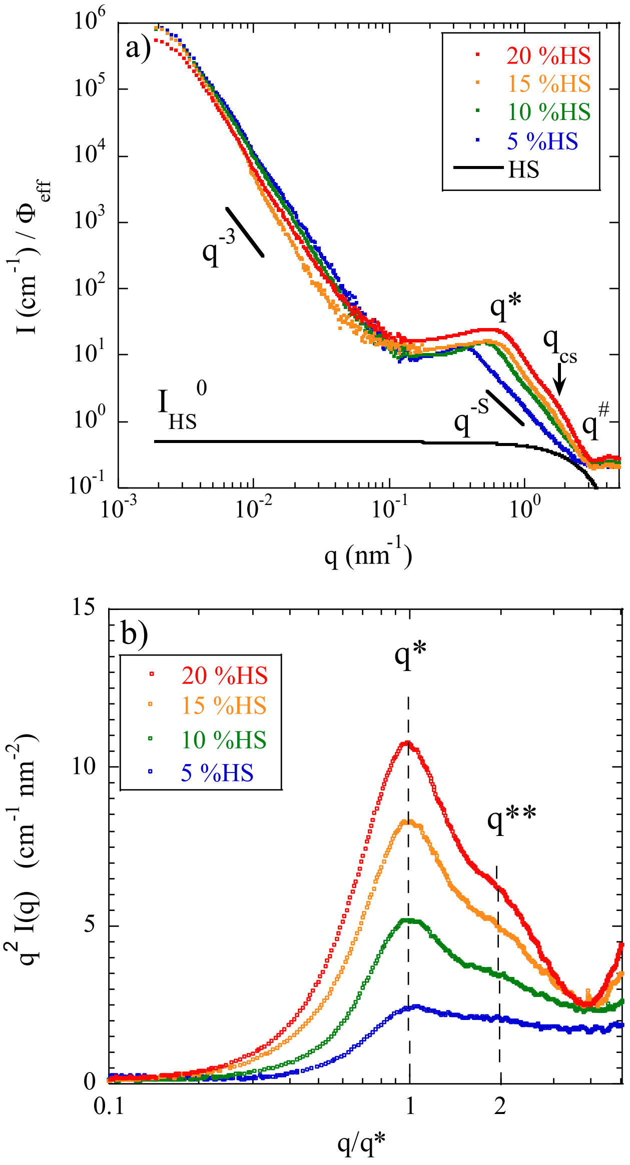

Figure 4.4: a) Normalized scattering intensity measured in SAXS as a function of the transfer momentum q for the four segmented block copolymers containing 5, 10, 15 and 20%HS. The solid black line stands for the reconstruction of $P_{HS}(q)$ calculated in equation 1. b) Kratky representation ($I(q)q^2 = f(q/q^*)$) of the same data set. The

characteristic distance between the crystallite is seen through q^* while the presence of $q^{**} = 2q^*$ suggests a lamellar phase. Note that q_{cs} in a) and q^{**} in b) have a similar value but different meanings (see text).

For q>q#, the X-rays see the matter as a discrete phase, we refer the reader to the WAXS experiments (see section 4.3.2) – a small peak around 4 nm^{-1} (1.57 nm) is nevertheless visible for the 20%HS and corresponds to the distance between the T units in the same chain.[36] Here, one can note that $q^{\#} \approx 3 \text{ nm}^{-1}$, corresponding to $d^{\#} = 2\pi/q^{\#} = 2.1 \text{ nm}$, which is in good agreement with the smallest dimension of a single HS defined above.

For q_{cs}<q<q#, the intensity is described by a power law ~q^{-S} giving information on the local structure of the crystallites. This regime is known as the Porod regime. A value of *S* equal to 2 stands for a flexible object such as a polymer coil in θ-solvent,[41] while a value of S equal to 4 is understood as a sharp interface (equivalent to a surface fractal dimension of 2, i.e. smooth objects like hard colloids[42]). The S values found for the four samples are given in Table 3. One can clearly see that these slopes evolve monotonically with the HS content passing from ≈2.0 (for 5%HS) to 3.7 (for 20%HS), i.e. from a flexible object to an object with a sharp interface.

At q=q*, we observe a maximum, which can be attributed to the most probable distance between the center of mass of the crystallites $d^*=2\pi/q^*$, i.e. with the inter-crystallites structure factor $S_c(q)$. This distance between crystallites, d^*, is reported in Table 3. As expected, it decreases with increasing the HS volume fraction (or number density), which reflects the network densification.

(For q<q* we refer the reader to the sub-section entitled **Considerations on the structural features above d^*** presented later in the chapter).

We can then plot this SAXS data using the Kratky representation[40] (see Figure 4b). Interestingly, normalizing the scattering vector by q^* reveals a second structural feature in the 10, 15 and 20%HS TPEs positioned at q/q^* =2. This is typical of a lamellar organization,[43] and suggests the presence of crystallites stacks, i.e. anisotropic structure from the d^* length scale, which becomes more pronounced when increasing the volume fraction of HS.

By combining this result to the Porod exponent S, we propose the following picture: The Porod exponent having a value close to 2.0 in the 5%HS sample suggests that the crystallites can be seen as thick polymers in θ-solvent, i.e. as objects having non-zero thickness H and width W following a random walk that, by definition, leads to an isotropic morphology. On the contrary, within the same q-range, the Porod exponent for the 20%HS is 3.7 and the intensity shows a shoulder at $q=q^{**}=2q^*$ suggesting the formation of a lamellar structure in which the crystallites have thus the same orientation (at the mesoscale), leading to an anisotropic morphology. These two extreme cases are represented in Figure 4.5 by the morphology A and the morphology B. Between these two samples, the intensity scattered by the 15%HS TPE is close to the 20%HS one (see. Figure 4.5a) suggesting therefore that the morphology B should stand. The situation is more ambiguous for the 10%HS because it shows a distinct scattering pattern from both 5%HS and 15%HS with S=2.6 implying an intermediate structure.

4.3.3.3 Determination of the width of the crystallites (W) and 3D arrangement

Because of these drastic changes in the TPEs structure with the reduction of the PTMO soft-segments in the copolymer chains, we propose to use these two simple albeit plausible geometrical models in order to describe the average situation in a volume element of the TPEs and to determine the corresponding width of the crystallites, W_A and W_B:

A) The crystallites form a network based on a soft cubic cell for which each edge is made of a free crystallite segments with their length being in average d^*. The decrease of d^* with increasing Φ is understood as the shrinkage of this 3D "isotropic" soft cage (no preferential direction as seen in Figure 4.5a) when the number of crystallites increases in the sample.

B) The crystallites are all aligned along the same axis $\vec{L}$ and separated by a distance d^* corresponding to the cell parameter of a square lattice similarly to the hexagonal packing used by Sijbrandi et al..[13] In this case, the decrease of d^* with increasing Φ is understood as the shrinkage of a 2D "locally" (≈10 nm) anisotropic square lattice belonging to the plane $(\vec{H},\vec{W})$ and therefore orthogonal to the crystallite long axis. In this suggested model, the volume fraction Φ is equivalent to a surface fraction Φ_S in the plane $(\vec{H},\vec{W})$.

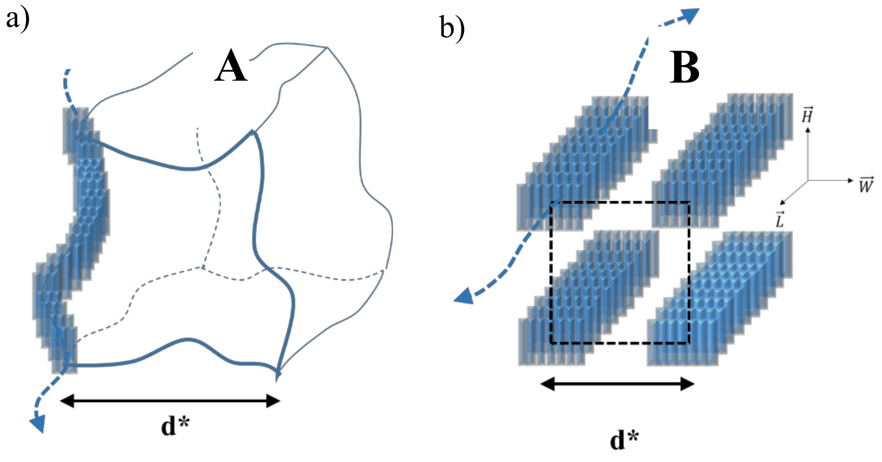

Figure 4.5: a) 3D isotropic model (denoted as A) and b) 2D locally anisotropic model (denoted as B) describing two possible arrangements of the crystallites leading to different evolutions of the inter-crystallites

distance when %HS is changed. In both cases, dashed arrows stand for the (curvi)linear long axis of the crystallites.

Considering that the HS volume fraction (or surface fraction in model B) in one cell is equivalent to the HS volume fraction Φ in the whole sample, one can easily express the HS volume fraction in one cell for A and B morphologies as: $\Phi = N_n HW/d^{*2}$ with N_n being the number of full objects to be considered per lattice giving $N_A=12\times1/4=3$ and $N_B=4\times1/4=1$. Besides, assuming H=2.1 nm as estimated in the precedent section, one can then simply extract the width of the crystallites (reported in Table 3) from each model, only differing by construction by a factor 3 such as: $W_A = W_B/3 = \Phi d^{*2}/3H$.

While for the 15%HS and 20%HS samples, the morphology B is used, we consider the morphology A for the 5%HS sample, and an average of the two for the 10%HS sample, which lies between these two extremes. It must be noted that the values of W are found to be in good agreement with the one reported by van Hutten et al. from the analysis of the breadth's peaks from WAXS experiments.[25]

Table 3: Morphology of the crystallites at the mesoscale extracted from SAXS data for 5, 10, 15 and 20%HS. Their thickness is kept constant H=2.1 nm.

%HS	Φ (%) (1)	q*(nm^{-1})	d* (nm)	S	W (nm) (2)	N_w=W/R
5	3.5	0.43	14.6	2.1	1.18	2
10	7.2	0.62	10.1	2.6	2.28	4
15	10.9	0.72	8.72	3.1	3.94	8
20	14.8	0.77	8.16	3.7	4.69	>9

(1) The values of Φ are calculated from the equation S2 (supplementary information). (2) The calculation of W is made from model A for 5%HS and from model B for 15%HS and 20%HS. The corresponding value

for 10%HS is calculated by averaging the results from model A and B (intermediate case).

From these values and from the estimated size of an elementary HS building block, one can determine the corresponding number of HS in the width direction $\overrightarrow{W}$, N_w, as reported in Table 3. While the lateral packing of the HS is rather limited at low volume fraction of HS, it becomes quite important at larger density. This can be understood by considering the reduced mobility and enhanced proximity of the crystallites at high volume fraction of HS, which are forced to organize into a lamellar structure.

4.3.3.4 Evolution of ribbon-ribbon distance (d) with the HS volume fraction:*

The morphology of the crystallites is strongly influenced by the HS volume fraction. It is therefore interesting to investigate how d^* evolves with Φ, and see if its evolution is well described by the picture proposed above, according to which the morphology of the ribbons evolves from the geometrical model A at low HS volume fraction, to the model B at larger fraction. The evolution of d^* with the HS volume fraction Φ is shown in Figure 4.6. From basic geometrical arguments, we know that this function can be written as the following: $\mathrm{d}^* = \mathrm{P}\Phi^{-1/\mathrm{h}}$ where P is related to the object size (see below), and h is the spatial dimension of the "problem" satisfying $[h] = m^h$. For instance, it is well known that for a homogeneous colloidal suspension the distance between the particles centers of mass evolves with $\Phi^{-1/3}$, i.e. $h = 3$.[44]

In our case, as shown in Figure 4.6, it appears that $h \approx 2$ between 5 and 15%HS. This suggests that the distance between the objects evolves in a similar way as in a 2D space, which is in good agreement with the proposed geometrical model B, and which confirms the anisotropic nature of the crystallites network at high HS content. Below 5%HS, we believe that the softness of the crystallites (S=2) and the absence of peak at q/q^{*} = 2 in Figure 4.4b should lead to a soft isotropic network (i.e. h = 3). In Figure 4.6, we also observe that the value of h between 15 and 20%HS is greater than 3 (close to 4) indicating that most of the additional HS units (from 15 to 20%HS) do not lead to the formation of new crystallites (which would make the inter-crystallites average distance d^{*} weaker) but rather contribute to the growth of the already existing ones. This result is further supported by the very similar patterns measured for the 15 and 20%HS in Figure 4.4a where the slightly higher value of S (Table 3) stands for an even sharper object with a probable enhanced lamellar order.

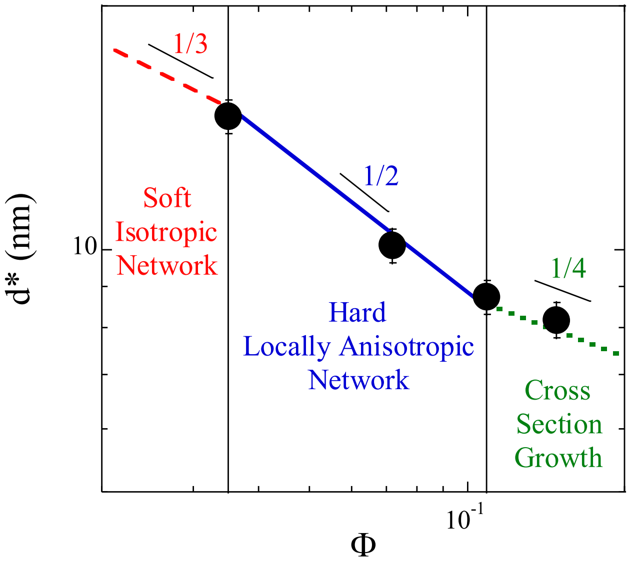

Figure 4.6: Log-log representation of the most probable distance between the crystallites d^{*} as a function of the volume fraction in HS (Φ). The blue solid line is a power law fitted to the data with the exponent being fixed to 1/2. Red and green dashed lines are power law with respective exponent 1/3 and 1/4 and serve as guide for the eyes, they are related with the interpretation in the text.

In addition to the value of h, the above-mentioned expression of d^{*}, provides us with the prefactor of the 1/2 power law in Figure 4.6, estimated to be $P = 2.8$ nm. In a 2D problem, and considering a square lattice as in the model B, one can relate its value to the geometry of the crystallites $\mathrm{P} = \sqrt{\mathrm{HW}_B}$ allowing then to highlight the good agreement with the value of W for 15%HS (see Table 2): $\mathrm{W_B} = \mathrm{P}^2/\mathrm{H} = 3.73$ nm. Note that in order to compare the values of W from the two calculations (from P and d^{*}), the model B needs to be valid (anisotropy) and the thickening of the crystallites due to a high HS loading must not be significant (i.e., among our samples, this comparison can only be done for 15%HS).

4.3.3.5 Cross Section radius of the crystallites

Furthermore, one can also refer to the change in slope observed for the 20%HS sample in Figure 4.4a at $q = q_{cs}$. This singularity (with matches in this case with $2q^{*}$), particularly visible for rigid objects, denotes the transition from the Porod regime to the fractal regime, giving information on the cross section radius of the crystallites $R_{cs} = \pi/q_{cs}$.

In order to validate the morphology picture given by the geometric model B, it is then possible to compare the experimental q_{cs} value of the 20%HS sample with the one derived from the model by approximating the equivalent cross section radius $R_{cs}^{(B)}$ from H and W_B (true rectangular cross-section) such as: $\mathrm{S_{CS}} = \mathrm{HW}_B \approx \pi {\mathrm{R}_{\mathrm{cs}}^{(\mathrm{B})}}^2$ where S_{CS} is the average cross section of the crystallites in the 20%HS TPE. We then directly get the corresponding value for $q_{cs}^{(B)}$ that is reported with a black arrow in Figure 4.4a: $\mathrm{q}_{\mathrm{cs}}^{(\mathrm{B})} = \frac{\pi}{\mathrm{R}_{\mathrm{cs}}^{(\mathrm{B})}} = \frac{\pi\sqrt{\pi}}{\sqrt{\mathrm{HW}_B}} = 1.77\ \mathrm{nm}^{-1}$. Again, a good agreement in found, further reinforcing our data interpretation at the mesoscale.

All the previous analysis suggests thus strongly that, above 10%HS, the crystallites are locally oriented along a given $\vec{L}$ axis forming a structure close to a 2D anisotropic lamellar phase (model B). This meso-scale anisotropy, which undoubtedly has to do with the rigidity of the crystallites, has been pointed in numerous papers in which AFM clearly revealed the orientation of the objects for distances between ≈10 and 100 nm.[6a, 17, 45] It must be noted however that at a higher length scales (i.e. for $d \gg d^{*}$), this anisotropy is lost due to the flexibility of the ribbons, reminding the behavior of soft polycrystalline materials.[46] In the next section, we give arguments to speculate about a methodology to extract structural features at distances greater than d^{*} e.g. the "volume" fractal dimension of the crystallite D_f and its growth mechanism.

4.3.3.6 Considerations on the structural features above d^{*}

For q<q*, as shown in Figure 4.3, the scattering intensity seems to saturate (plateau). At first sight, one could interpret this by the presence of objects with a well-defined mass. However, this plateau should be rather seen as the product of the crystallite average form factor $\langle P_c(q) \rangle$ and the "correlation hole" usually seen in structure factors for q<q*[47] such as:

$$\mathrm{I}(\mathrm{q} < \mathrm{q}^{*}) = \mathrm{I}_0 \langle \mathrm{P_c}(\mathrm{q} < \mathrm{q}^{*}) \rangle \mathrm{S_c}(\mathrm{q} < \mathrm{q}^{*}) \qquad (2)$$

with $\mathrm{I}_0 = \Phi\Delta\rho^{2\prime}$and $\langle \mathrm{P_c}(\mathrm{q} < \mathrm{q}^{*}) \rangle = \mathrm{V_c}\mathrm{q}^{-\mathrm{D_f}}$ where V_c is the average volume of a crystallite and D_f the fractal dimension of the crystallites which must satisfy $1<D_f<2$ for semi-rigid rod-like objects.

Finally, for q<<q*, the scattering intensity follows a power law $\mathrm{I(q)} \sim \mathrm{q}^{-3}$ which can hardly be interpreted in terms of structure (e.g., infinitely dense agglomerates of crystallites). While the origin of such a low-q upturn is not well understood, we believe that it could come from multiple-scattering, possibly limited by using thinner samples.

As previously mentioned, the scattering intensity results in structural features related to the shape and size of the scattering objects (form factor) as well as their respective position from each other (structure factor). While the presence of characteristic distances were expected at molecular (crystal lattice visible in WAXS) and mesoscopic (inter-ribbons distance visible in SAXS) length scales, the lack of organization at larger distances (like in smectic phases[48]) inhibits the direct extraction of structural features through the observation of the emerging structure factor (i.e. scattering peaks). Even "worse", the contribution of the unknown large-scale structure factor within the total scattering intensity $I(q)$, makes impossible the identification of the crystallite morphology via their average form factor $\langle P_c(q) \rangle$. In the literature, the latter is often measured independently. For example, in nanocomposites or suspensions based on well-defined objects such as hard-spheres, it is directly obtained by measuring samples in which Φ is kept low (typically below 1 vol%, where the structure factor is negligible[49]). For more complex industrial nanofillers, a way to proceed, as recently suggested by Baeza et al.,[50] is to dilute a posteriori solid samples through an in-situ polymerization process passing from $\Phi = 20$ vol% to roughly 2 vol% with keeping the same filler morphology. However, since the shape and the size of the crystallites present in our TPEs are intimately related with the HS content, none of these methods can be applied here.

A reliable way to study the large-scale structure resides in studying the TPEs starting from high temperature ($T > T_m$) to low temperature, i.e. starting at temperature at which the crystallite fraction is low enough so that it is possible to extract information about their average form factor. To do so, we performed time-resolved SAXS experiments with temperature control on the 20%HS sample on the beamline DUBBLE at ESRF. The result, similar to the one by Versteegen et al.[51] is presented in Figure 4.7 and allows to highlight several important points:

(i) **$T \geq T_m \approx 170°C$**. Even though the sample is in the melt state, a significant X-ray scattering is measured. This indicates that the HSs are not fully dispersed, i.e. that a fraction of H-bonds, still active, leads to clusters formation. One can here use the Guinier approximation (equation 1) to fit the shoulder observed at 0.7 nm^{-1} allowing to quantify these objects with a typical radius $R_G(T_m) = 1.8$ nm and an aggregation number $N_{agg}(T_m) = I_G(T_m)/I_{HS}{}^0 \approx 18$. Interestingly, the fact that $\pi/R_g(T_m) \approx q_{cs}$ means that, those persistent aggregates have a radius of gyration similar to the cross-section one of the crystallites formed at low temperature. This feature thus strongly suggests that the latter are made of a train-like stacks of the former. Besides, their presence explains the "non-Maxwellian" rheological behavior observed at $T = T_m$+10 °C in (see Figure S8 in supplementary information) where $G'(\omega)$ in particular, exhibits a power law behavior with an exponent significantly lower than 2, indicating the presence of association points ("stickers") between the chains.

(ii) **T_m > T >167°C (t=25 s of cooling – see Figure 4.7b)**. As soon as the temperature starts to decrease, the scattering intensity evolves at low angle (q < 1 nm^{-1}) due to the formation of larger objects through the supramolecular bonds which become statistically more likely to exist. In this regime, we believe that the interactions between the growing scattering objects are still negligible. Indeed, no structural peak, i.e. shoulder or maximum, is observed, suggesting that the total scattering intensity must be proportional to the average form factor of the crystallites $I(q) \sim \langle P_c(q) \rangle$. Nevertheless, as expected, decreasing the temperature leads to bigger and bigger structures characterized by a growing fractal dimension D_f from ≈0 (finite persistent aggregates) at T_m to ≈1.2 at 167 °C (after 25 s of cooling). Interestingly, the latter value, reflects the rod-like shape of the crystallites before they start to stack, in good agreement with the previously proposed model B (see. the black dashed line Figure 4.7b).

(iii) **T <167 °C**. A clear maximum standing for the inter-crystallites distance starts to appear at q^* (see Figure 4.7b). The fall of the scattering intensity at $q < q^*$ when the temperature is decreasing, i.e. when the crystallites are growing ($P_c(q)$ increases), is thus unambiguously related with the appearance of the structure factor "correlation hole". From this point, $I(q) \sim \langle P_c(q) \rangle S_c(q)$. Further decreasing of the temperature (i.e. t>25 s) leads to the deepening of the correlation hole together with the shift of the "q^*-peak" towards higher q. The latter confirms therefore the densification of the crystallites network until T reaches ≈136 °C (t=255 s) at which $I(q)$ saturates, in good agreement with the crystallization temperature T_c determined from DSC. Finally, at $< T_c$, the dynamics are "frozen" for $d > d^*$.

a)

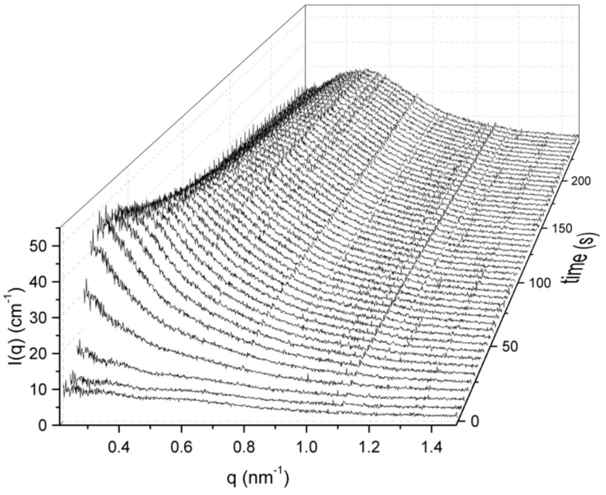

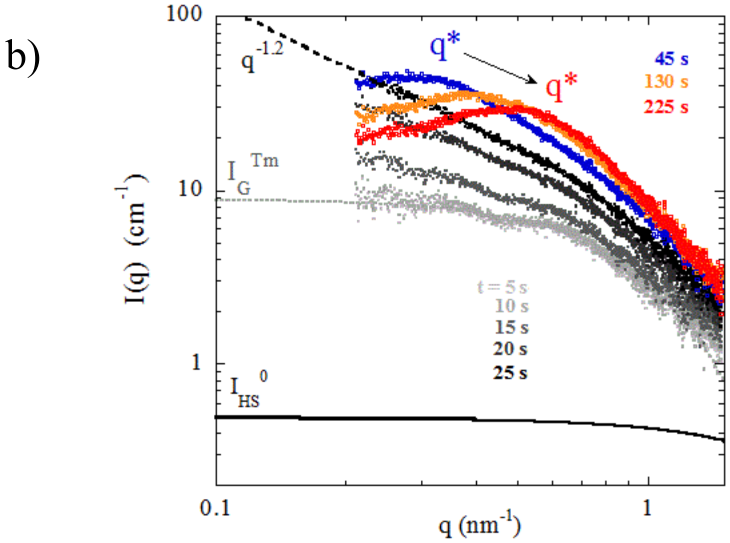

Figure 4.7: a) Reduced scattering intensity as a function of the momentum transfer q for the 20%HS sample with varying the temperature from 170 °C to 40 °C at ≈ 8 °C.min^{-1}. b) Selection of intensity profiles at given cooling times. The grey data are measured during the first 30 seconds of the test ($I(q)\sim\langle P_c(q)\rangle$) while the colorful ones are obtained from 1 to 5 minutes ($I(q)\sim\langle P_c(q)\rangle S_c(q)$). This data set has been rescaled to the corresponding intensity shown in Figure 4.4a in order to access the absolute units (procedure described in supplementary information section 1.3). The dashed line is fitted to the data with the Guinier approximation in order to extract the radius of gyration and the aggregation number of the scattering objects present at T=170°C. The black solid line stands for $I_{HS}(q)$.

4.3.4 Tentative mechanism of HS crystallite growth

Based on the structural results from the previous section and on the tests realized on solvent casted samples, we propose here a tentative growth mechanism for the HS crystallites, as illustrated in Figure 4.8 below.

First, we recall that the crystallization of the HS in TPEs is predominantly driven by the strong attraction due to the H-bonds created through the amide groups of these short units (2.1 nm – see section 3.3.1), which in turn dictates their spatial organization. This is akin to microphase separation in block copolymers, where the domains of the hard block form a crystalline order such as in rod-coil copolymers.[52] In the absence of H-bonds, given the small size and relatively low amount of HS within a chain, a homogeneous amorphous melt should result at $T>ODT$ (order disorder temperature). This H-bond driven process (and the well calibrated HS size) likely explains the high crystallization rate and the corresponding high crystal fraction (≈70% of the HS, see Table 1).

Starting from the melt state (T>T_m≈170°C), it appears that the probability to form H-bonds (crystal) or, to phase separate (amorphous), is non-zero (Figure 4.7b), leading to the formation of the above mentioned persistent aggregates (Figure 4.8a). At this temperature, these small clusters are in equilibrium with isolated building blocks, in an analogous fashion to systems like living polymers.[53] Those aggregates, typically made of 18 HSs (with ${R_g}^{T_m}$=1.8 nm) are nevertheless too few to interact with each other (no structure peak in Figure 4.7b). By following the viscoelastic properties of these TPEs through time at this high temperature, we also observed that the number density of these aggregates slowly increases with time, but are not forming crystallites yet.[30] Decreasing the temperature below T_m enhances the strength of attraction (e.g. H-bonds shortening[54]), hence, the probability to form bigger clusters via H-bonding and other interactions such as π-π stacking (Figure 4.4 and 4.8b). While the former leads to a growth of the clusters (crystallites) along $\vec{L}$, the latter will cause their thickening along $\vec{W}$ (see Figure 4.5). The net result is the formation of elongated ribbons as evidenced in Figure 4.7b through the evolution of their fractal dimension $(\mathrm{dI(q)/dq}\ )$ from 0 to 1.2 (table 3). Interestingly, Figure 4.7b also reveals that the position of the form factor shoulder (at $q \approx 0.7\, nm^{-1}$) remains constant with the time suggesting that the cross section of these growing objects does not evolve significantly during the cooling phase. This implies that the early stage of crystallization is characterized by the presence of small isotropic objects which will associate along $\vec{L}$ such as train's wagons with decreasing the temperature (Figure 4.8c)

Upon further decrease of temperature, the growing anisotropic objects start to interact with each other, giving rise to a broad structure factor peak positioned at $q^*,$ typical of soft potentials. In this situation, $d^* = 2\pi/q^*$ is the most probable inter-object distance. While at low-HS content this soft interaction is akin to that of wormlike chains, at high-HS content we expect orientational order. Indeed, as indicated in Tables 1 and 3, the average number of HS per chain is three times higher for 20%HS TPEs compared to 5%HS and the inter-object distance is about half, suggesting an enhanced tendency for alignment since in this way long ribbons will minimize their free energy (see Figures 4.8c and 4.5b) in a similar fashion as what is found in anisotropic assemblies of peptides.[55]

Finally, the structure virtually freezes when the temperature approaches T_c. In this case, the crystallites are essentially trapped in a region of space around d^* consisting of two potential walls generated by the SSs which can fluctuate between W and $+M$, where M is the length corresponding to a fully stretched SS.

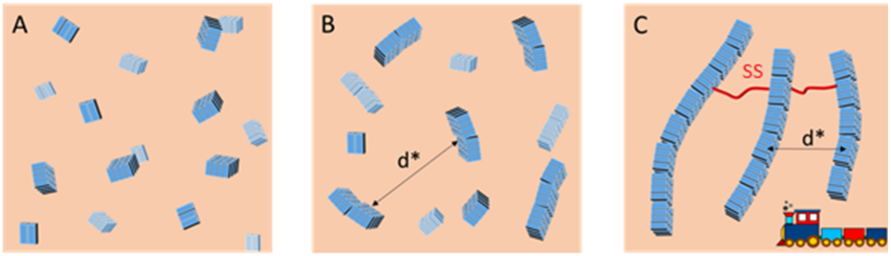

Figure 4.8: Growth mechanism of the HS crystallites with decreasing temperature. The blue objects stand for the HS and the red background for the SS. a) Melt state at T>T_m. b) Agglomeration of the persistent aggregates at T≤T_m. c) "Train" growth and orientation of the crystallites resulting in a "frozen" structure at the mesoscale when T_c is reached.

In the above tentative picture, it is expected that the growth of crystallites and their final state depend on the initial conditions, i.e., on the initial relative positions of the HSs (since the interactions are directional) and on the possible presence of persistent aggregates.

On the other hand, as already mentioned, the crystal formation in the solvent-casted TPEs seems rather different than in the bulk, showing a strong decrease of the π-π interactions signature in DSC (secondary peak in Figure 4.1) and WAXS (peaks 3 and 7 in Figure 4.2). While in the hot-pressed samples, the previously proposed mechanism could be described as a "train growth" process due to the cluster stacking along $\vec{L}$ resulting in a constant cross section radius during the crystallization, one could imagine a fundamentally different but plausible scenario for solvent-casted samples, named "1D-sheet growth", to explain the multi-scale formation in these (room temperature) solvent-casted TPEs. This process would consist in the following. A low volume fraction of TPEs chains is well dispersed in a (polar) H-bond competitor solvent such as THF which is expected to provide a (quasi)single HS dispersion at the beginning of the experiment. During the evaporation of the solvent, because of the lower viscosity with respect to the hot-pressed case, the short-range diffusion of the HS is enhanced allowing their systematic aggregation in the most preferential energetic way, i.e. via H-bonding (rather than π-π stacking). The crystallites can thus quickly grow along $\vec{L}$ until reaching a maximal viscosity (due to solvent evaporation and ribbon growth working together) at which long 1D-sheets are fully formed and "freeze" the system. They will then hardly stack on each other because of big entropic penalty resulting notably in a strong decrease of the π-π interactions signature in DSC or WAXS together with a higher order in the long axis direction (see peak 5 in Figure 4.2b).

4.4 Summary

In this chapter we have undertaken a thermal and structural study of segmented TPEs synthesized by polycondensation of T4T (HS) and PTMO (soft segment) units by means of DSC, WAXS and (U)SAXS. The effect of the hard-segments content has been investigated on four different hot-pressed samples containing 5, 10, 15 and 20%HS. DSC revealed a strong increase of the terminal melting point from 90 to 160 °C jointly with the apparition of a secondary melting peak situated at $\approx T_m$-30 °C when the HS content was increased from 5 to 20%. The latter was however eliminated when the sample was prepared through THF-casting, emphasizing the importance of the sample preparation. Molecular scale (1 Å - 1 nm) WAXS experiments have confirmed the polymorphism in hot-pressed TPEs and unambiguously revealed the presence of π-π stacking interactions in addition to the well-known H-bonds in polyamide-based systems. At larger length-scales (1-30 nm), have simultaneously shown a decrease of the inter-crystallites distance with a raise of their local rigidity, leading partly to a lamellar order, when the hard-segment mass fraction was increased above 10%. These results have been interpreted through two geometrical models, representing the average local situation throughout the whole sample. This allowed us to estimate the width of the ribbon-like objects passing from 2 to 9 elementary T4T units, conforming to the above-mentioned enhanced rigidity. Besides, time resolved SAXS measurements as a function of the temperature have highlighted the presence of persistent HS aggregates at $T>T_m$, which is believed to be at the origin of the slow relaxation that we observed in the terminal regime of the rheological response. Moreover, at larger length-scales (>30 nm), it allowed us to extract the “volume” fractal dimension of the T4T-crystallites (being close to 1.2), evidencing the quite rigid nature of the elongated objects present in the TPEs when the HS content is 20%. Based on this structural evolution we finally gave arguments on the growth mechanism highlighting once again the importance of the initial conditions, i.e. the shaping process.

All in all, the final properties of these thermoplastic elastomers depend strongly on their microstructure, which is largely influenced by different inter-related processes such as phase separation, hydrogen bonding, crystallization or π-π stacking, as well as by the density of HS, which influences the mescoscale organization of the crystallites. This provides an unprecedented tunability at molecular level, hence a better control on their final properties such as their toughness or melting properties. The latter will be investigated in a future work.

4.5 References

1) Legge, N. R., Thermoplastic Elastomers. Rubber Chemistry and Technology 1987, 60 (3), 83-117.

2) Adhikari, B.; De, D.; Maiti, S., Reclamation and recycling of waste rubber. Progress in Polymer Science 2000, 25 (7), 909-948.

3) Cloitre, M.; Vlassopoulos, D., Block copolymers in external fields: Rheology, Flow-induced phenomena, and applications. Applied Polymer Rheology: Polymeric Fluids with Industrial Applications. J. Wiley & Sons: 2011, pp 209-239.

4) Holden, G.; Kricheldorf, H. R.; Quirk, R. P., Thermoplastic elastomers. Hanser Munich: 1996.

5) Leibler, L., Theory of Microphase Separation in Block Co-Polymers. Macromolecules 1980, 13 (6), 1602-1617.

6) (a) Appel, W. P. J.; Portale, G.; Wisse, E.; Dankers, P. Y. W.; Meijer, E. W., Aggregation of Ureido-Pyrimidinone Supramolecular Thermoplastic Elastomers into Nanofibers: A Kinetic Analysis. Macromolecules 2011, 44 (17), 6776-6784; (b) Versteegen, R. M.; Kleppinger, R.; Sijbesma, R. P.; Meijer, E. W., Properties and morphology of segmented copoly(ether urea)s with uniform hard segments. Macromolecules 2006, 39 (2), 772-783.

7) (a) Miller, J. A.; Lin, S. B.; Hwang, K. K. S.; Wu, K. S.; Gibson, P. E.; Cooper, S. L., Properties of Polyether Polyurethane Block

Copolymers - Effects of Hard Segment Length Distribution. Macromolecules 1985, 18 (1), 32-44; (b) Eisenbach, C.; Baumgartner, M.; Günter, C., Polyurethane Elastomers with Monodisperse Segments and their Model Precursors: Synthesis and Properties. In Advances in Elastomers and Rubber Elasticity, Lal, J.; Mark, J., Eds. Springer US: 1986; pp 51-87.

8) Gaymans, R. J., Segmented copolymers with monodisperse crystallizable hard segments: Novel semi-crystalline materials. Progress in Polymer Science 2011, 36 (6), 713-748.

9) Dasgupta, S.; Hammond, W. B.; Goddard, W. A., Crystal Structures and Properties of Nylon Polymers from Theory. J. Am. Chem. Soc. 1996, 118 (49), 12291-12301.

10) vanBennekom, A. C. M.; Gaymans, R. J., Amide-modified poly(butylene terephthalate): Polycondensation. Polymer 1996, 37 (24), 5439-5446.

11) Van Der Schuur, M.; van der Heide, E.; Feijen, J.; Gaymans, R. J., Structure–property relations of segmented block copolymers with liquid–liquid demixed morphologies. Polymer 2005, 46 (11), 3616-3627.

12) Arun, A.; Dullaert, K.; Gaymans, R. J., The Melt Rheological Behavior of AB, ABA, BAB, and (AB)(n) Block Copolymers With Monodisperse Aramide Segments. Polym. Eng. Sci. 2010, 50 (4), 756-761.

13) Sijbrandi, N. J.; Kimenai, A. J.; Mes, E. P. C.; Broos, R.; Bar, G.; Rosenthal, M.; Odarchenko, Y.; Ivanov, D. A.; Dijkstra, P. J.; Feijen, J., Synthesis, Morphology, and Properties of Segmented Poly(ether amide)s with Uniform Oxalamide-Based Hard Segments. Macromolecules 2012, 45 (9), 3948-3961.

14) Husken, D.; Feijen, J.; Gaymans, R. J., Hydrophilic segmented block copolymers based on poly(ethylene oxide) and monodisperse amide segments. J. Polym. Sci. Pol. Chem. 2007, 45 (19), 4522-4535.

15) Sauer, B. B.; McLean, R. S.; Gaymans, R. J.; Niesten, M. C. J. E., Crystalline morphologies in segmented copolymers with hard segments of uniform length. J. Polym. Sci. Pol. Phys. 2004, 42 (9), 1783-1792.
16) Van der Schuur, M.; Gaymans, R. J., Segmented block copolymers based on poly(propylene oxide) and monodisperse polyamide-6,T segments. J. Polym. Sci. Pol. Chem. 2006, 44 (16), 4769-4781.
17) Biemond, G. J. E.; Feijen, J.; Gaymans, R. J., Poly(ether amide) segmented block copolymers with adipic acid based tetraamide segments. J. App. Polym. Sci. 2007, 105 (2), 951-963.
18) Hamley, I. W.; Castelletto, V., Small-angle scattering of block copolymers in the melt, solution and crystal states. Progress in Polymer Science 2004, 29 (9), 909-948.
19) Benoit, H.; Hadziioannou, G., Scattering-Theory and Properties of Block Copolymers with Various Architectures in the Homogeneous Bulk State. Macromolecules 1988, 21 (5), 1449-1464.
20) Pedersen, J. S.; Schurtenberger, P., Scattering functions of semiflexible polymers with and without excluded volume effects. Macromolecules 1996, 29 (23), 7602-7612.
21) Hamley, I. W.; Pedersen, J. S.; Booth, C.; Nace, V. M., A small-angle neutron scattering study of spherical and wormlike micelles formed by poly(oxyethylene)-based diblock copolymers. Langmuir 2001, 17 (20), 6386-6388.
22) Gaymans, R. J.; Dehaan, J. L., Segmented Copolymers with Poly(Ester Amide) Units of Uniform Length - Synthesis. Polymer 1993, 34 (20), 4360-4364.
23) Krijgsman, J.; Husken, D.; Gaymans, R., Synthesis and properties of thermoplastic elastomers based on PTMO and tetra-amide. Polymer 2003, 44 (25), 7573-7588.
24) Gaymans, R. J.; Harkema, S., Melting Behavior of Aliphatic and Aromatic Diamides. J. Polym. Sci. Pol. Phys. 1977, 15 (3), 587-590.
25) Vanhutten, P. F.; Mangnus, R. M.; Gaymans, R. J., Segmented Copolymers with Polyesteramide Units of Uniform Length - Structure-Analysis. Polymer 1993, 34 (20), 4193-4202.

26) Struth, B.; Hyun, K.; Kats, E.; Meins, T.; Walther, M.; Wilhelm, M.; Grübel, G., Observation of New States of Liquid Crystal 8CB under Nonlinear Shear Conditions as Observed via a Novel and Unique Rheology/Small-Angle X-ray Scattering Combination. Langmuir 2011, 27 (6), 2880-2887.

27) Pennicard, D.; Smoljanin, S.; Struth, B.; Hirsemann, H.; Fauler, A.; Fiederle, M.; Tolbanov, O.; Zarubin, A.; Tyazhev, A.; Shelkov, G.; Graafsma, H., The LAMBDA photon-counting pixel detector and high-Z sensor development. Journal of Instrumentation 2014, 9 (12), C12026.

28) Guang, L.; Gaymans, R. J., Polyesteramides with mixtures of poly(tetramethylene oxide) and 1,5-pentanediol. Polymer 1997, 38 (19), 4891-4896.

29) Lee, W. A.; Knight, G. J., Ratio of the glass transition temperature to the melting point in polymers. Brit. Polym. J 1970, 2 (1), 73-80.

30) Sharma, A.; G. P. Baeza, L. Imperiali, W. P.J. Appel, C. Fitie, G. Vanden Poel, E. van Ruymbeke, Fast scanning calorimetry clarifies the understanding of the complex melting and crystallization behavior of polyesteramide multi-block copolymers, accepted in Polymer Int, DOI 10.1002/pi.5713.

31) (a) Gaymans, R. J., The synthesis and some properties of nylon 4,T. Journal of Polymer Science: Polymer Chemistry Edition 1985, 23 (5), 1599-1605; (b) Brisson, J.; Gagné, J.; Brisse, F., Model compounds of aromatic nylons. 3. The conformation of the 4T Nylon, poly(tetramethylene terephthalamide), using X-ray diffraction, solid-state 13C nmr spectroscopy and ir spectroscopy. Canadian Journal of Chemistry 1989, 67 (5), 840-849.

32) Bunn, C. W.; Garner, E. V., The Crystal Structures of Two Polyamides ('Nylons'). Proceedings of the Royal Society of London A: Mathematical, Physical and Engineering Sciences 1947, 189 (1016), 39-68.

33) Stepaniak, R. F.; Garton, A.; Carlsson, D. J.; Wiles, D. M., Examination of the Crystal-Structures Present in Nylon-6 Fibers. J. Polym. Sci. Pol. Phys. 1979, 17 (6), 987-999.

34) Liu, Y.; Cui, L.; Guan, F.; Gao, Y.; Hedin, N. E.; Zhu, L.; Fong, H., Crystalline Morphology and Polymorphic Phase Transitions in Electrospun Nylon-6 Nanofibers. Macromolecules 2007, 40 (17), 6283-6290.

35) Beyer, F. L.; Ziegler, C. Wide-Angle X-Ray Scattering Characterization of the Morphology of Nylon 6 6 Obturator Materials; DTIC Document: 2004.

36) Brisson, J.; Brisse, F., Model Compounds of Aromatic Nylons .2. Study of N,N'-Trimethylenebis(Para-Methoxybenzamide),N,N'-Pentamethylenebis(Para-Methylbenzamide), and N,N'-Heptamethylenebis(Para-Methylbenzamide) by X-Ray-Diffraction, Ir Spectroscopy, and C-13 Cp/Mas Nmr-Spectroscopy. Macromolecules 1989, 22 (4), 1974-1981.

37) Stein, R. S.; Misra, A., Morphological studies on polybutylene terephthalate. Journal of Polymer Science: Polymer Physics Edition 1980, 18 (2), 327-342.

38) (a) McGaughey, G. B.; Gagné, M.; Rappé, A. K., π-Stacking Interactions: ALIVE AND WELL IN PROTEINS. J Biol Chem 1998, 273 (25), 15458-15463; (b) Martinez, C. R.; Iverson, B. L., Rethinking the term "pi-stacking". Chem Sci 2012, 3 (7), 2191-2201; (c) Hunter, C. A.; Sanders, J. K. M., The nature of .pi.-.pi. interactions. J. Am. Chem. Soc. 1990, 112 (14), 5525-5534.

39) (a) Xu, H.; Das, A. K.; Horie, M.; Shaik, M. S.; Smith, A. M.; Luo, Y.; Lu, X.; Collins, R.; Liem, S. Y.; Song, A.; Popelier, P. L. A.; Turner, M. L.; Xiao, P.; Kinloch, I. A.; Ulijn, R. V., An investigation of the conductivity of peptide nanotube networks prepared by enzyme-triggered self-assembly. Nanoscale 2010, 2 (6), 960-966; (b) Joshi, S.; Grigorian, S.; Pietsch, U.; Pingel, P.; Zen, A.; Neher, D.; Scherf, U., Thickness Dependence of the Crystalline Structure and Hole Mobility

in Thin Films of Low Molecular Weight Poly(3-hexylthiophene). Macromolecules 2008, 41 (18), 6800-6808.

40) Pusey, P. N. In Neutrons, X-ray, and Light: Scattering Methods Applied to Soft Condensed Matter; Zemb, T.; Lindner, P.; North-Holland, 2002.

41) Flory, P. J., Statistical Mechanics of Chain Molecules. J. Wiley & Sons: 1969.

42) Chevigny, C.; Dalmas, F.; Di Cola, E.; Gigmes, D.; Bertin, D.; Boue, F.; Jestin, J., Polymer-Grafted-Nanoparticles Nanocomposites: Dispersion, Grafted Chain Conformation, and Rheological Behavior. Macromolecules 2011, 44 (1), 122-133.

43) Hamley, I. W.; Castelletto, V., Small-angle scattering of block copolymers: in the melt, solution and crystal states. Progress in polymer science 2004, 29 (9), 909-948.

44) Harton, S. E.; Kumar, S. K.; Yang, H. C.; Koga, T.; Hicks, K.; Lee, E.; Mijovic, J.; Liu, M.; Vallery, R. S.; Gidley, D. W., Immobilized Polymer Layers on Spherical Nanoparticles. Macromolecules 2010, 43 (7), 3415-3421.

45) Van Der Schuur, M.; Gaymans, R. J., Segmented block copolymers based on poly (propylene oxide) and monodisperse polyamide-6, T segments. Journal of Polymer Science Part A: Polymer Chemistry 2006, 44 (16), 4769-4781.

46) Louhichi, A.; Tamborini, E.; Ghofraniha, N.; Caton, F.; Roux, D.; Oberdisse, J.; Cipelletti, L.; Ramos, L., Nucleation and growth of micellar polycrystals under time-dependent volume fraction conditions. Phys. Rev. E 2013, 87 (3), 032306.

47) Baeza, G. P.; Genix, A. C.; Degrandcourt, C.; Petitjean, L.; Gummel, J.; Couty, M.; Oberdisse, J., Multiscale Filler Structure in Simplified Industrial Nanocomposite Silica/SBR Systems Studied by SAXS and TEM. Macromolecules 2013, 46 (1), 317-329.

48) Vroege, G. J.; Thies-Weesie, D. M.; Petukhov, A. V.; Lemaire, B. J.; Davidson, P., Smectic Liquid-Crystalline Order in Suspensions of

Highly Polydisperse Goethite Nanorods. Adv. Mater. 2006, 18 (19), 2565-2568.

49) Banc, A.; Genix, A.-C.; Dupas, C.; Sztucki, M.; Schweins, R.; Appavou, M.-S.; Oberdisse, J., Origin of Small-Angle Scattering from Contrast-Matched Nanoparticles: A Study of Chain and Filler Structure in Polymer Nanocomposites. Macromolecules 2015, 48 (18), 6596-6605.

50) Baeza, G.; Genix, A.-C.; Paupy-Peyronnet, N.; Degrandcourt, C.; Couty, M.; Oberdisse, j., Revealing nanocomposites filler structure by swelling and small-angle X-ray scattering. Faraday Discuss. 2015.

51) Versteegen, R. M.; Kleppinger, R.; Sijbesma, R. P.; Meijer, E., Properties and morphology of segmented copoly (ether urea) s with uniform hard segments. Macromolecules 2006, 39 (2), 772-783.

52) Olsen, B. D.; Segalman, R. A., Self-assembly of rod–coil block copolymers. Materials Science and Engineering: R: Reports 2008, 62 (2), 37-66.

53) Wang, X.; Guerin, G.; Wang, H.; Wang, Y.; Manners, I.; Winnik, M. A., Cylindrical block copolymer micelles and co-micelles of controlled length and architecture. Science 2007, 317 (5838), 644-647.

54) Dougherty, R. C., Temperature and pressure dependence of hydrogen bond strength: A perturbation molecular orbital approach. The Journal of chemical physics 1998, 109 (17), 7372-7378.

55) Gauthier, D.; Baillargeon, P.; Drouin, M.; Dory, Y. L., Self-assembly of cyclic peptides into nanotubes and then into highly anisotropic crystalline materials. Angewandte Chemie International Edition 2001, 40 (24), 4635-4638.

4.6 Appendix (Supplementary information, chapter 4)

4.6.1 SAXS data treatment

4.6.1.1 General considerations – measurements performed on ID02

In order to get rid of the sample geometry and the "empty beam" (EB) contribution, we normalize the raw intensity I_{raw} by the thickness e and the transmission t as in the following expression: $I(q) = \frac{I_{raw}(q)}{e.t} - EB$. The empty beam signal measured on ID02 is provided in Figure S1):

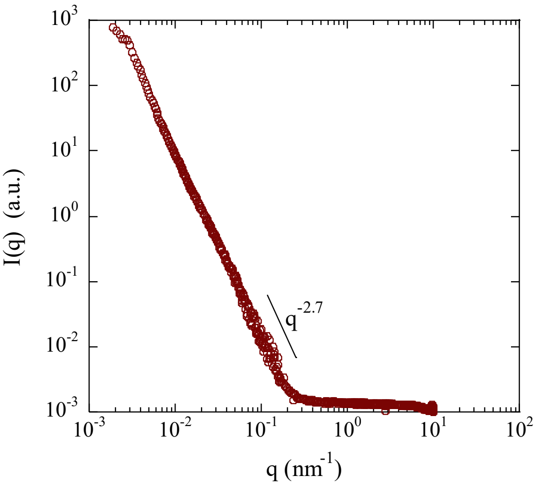

Figure S1: Empty beam contribution coming from the beam line ID02 at ESRF, Grenoble.

The theoretical X-ray contrast ($\Delta\rho^2$) between the two phases (soft and HSs), highly relevant in this work, is calculated from their chemical structure and their densities (respectively $d_{SS} = 0.98$ g/cm^3 and $d_{HS} = 1.41$ g/cm^3) such as: $\Delta\rho^2 = (\rho_1 - \rho_2)^2$ with $\rho_i = \frac{b_e}{v}\sum Z_j N_j$. Here, $v = M/\rho N_a$ and b_e is the scattering length of an electron ($2.85.10^{-13}$ cm). Z_j and N_j are respectively the atomic number and the number of corresponding atoms in the considered molecule i. Following this calculation, we obtain: ρ_{soft}=9.36 10^{10} cm^{-2}, ρ_{hard}=1.25 10^{11} cm^{-2} and finally $\Delta\rho^2$=9.89 10^{20} cm^{-4}.

This calculation allows us to approximate the true X-rays contrast needed to calculate properly the "mass" of the scattering objects ($[I(q)]$=cm^{-1}). However, in our analysis, we prefer to consider the "experimental" contrast $\Delta\rho^{2'}$ calculated from the invariant Q theorem[1] (equation. S1) considering both volume fractions in HS (Φ) and SS ($1-\Phi$).

$$Q = \int_0^\infty I(q)q^2dq = 2\pi^2\Phi(1-\Phi)\Delta\rho^{2'} \qquad \text{(S1)}$$

Giving $\Delta\rho^{2'}$= 9.19 10^{20} cm^{-4}. One can note that while the two values $\Delta\rho^2$ and $\Delta\rho^{2'}$are in reasonable good agreement, Supplementary Figure S2b reveals a clear discrepancy at 5%HS. We believe that this is caused by the uncomplete T4T crystallization, i.e. the presence of amorphous domains of hard-segments (see Table 1) and by the polymorphism of the crystal leading to different scattering length densities as discussed in the following (see also Table 1: X_c).

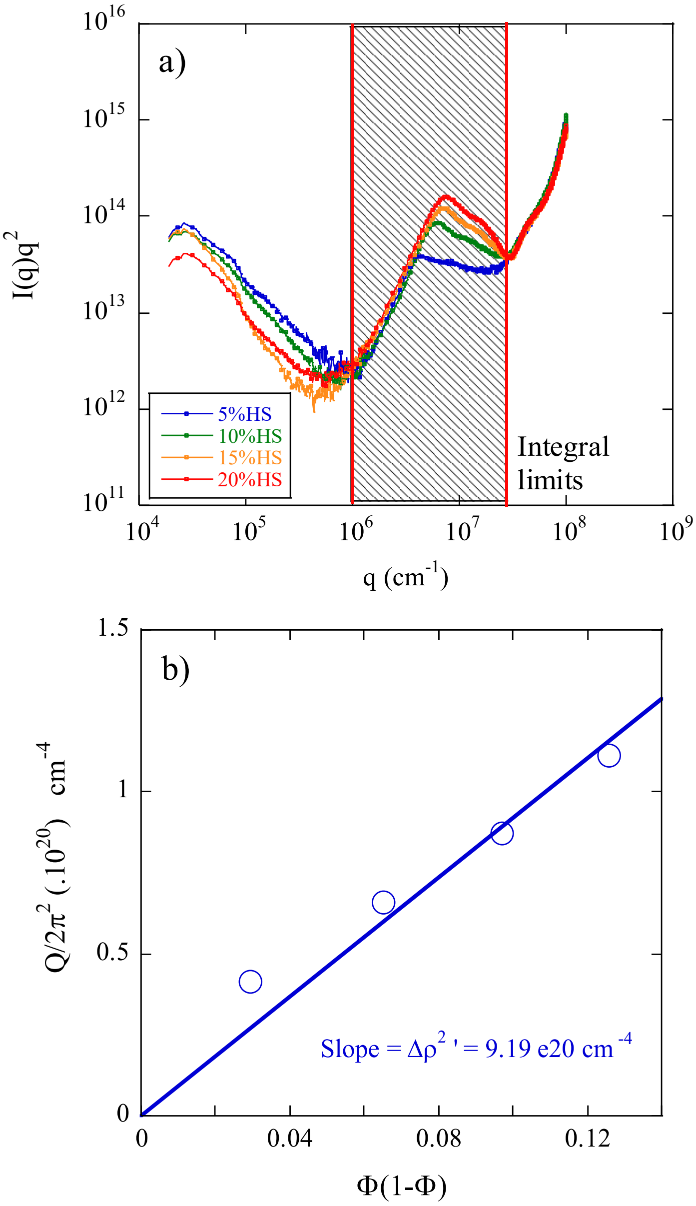

Figure S2: a) Reduced scattered intensity $I(q)q^2$ as a function of the scattering vector q. The low-q limit is defined by the beginning of the upturn while the upper limit is chosen as $q^{\#}$(see Figure5 in the chapter). b) Reduced invariant as a function of the product Φ(1-Φ). The solid line is a fit to the data with an affine function giving the experimental contrast.

4.6.1.2 Normalization of scattering data by Φ

In Figure 5 (chapter), we present the reduced scattered intensity for the TPEs containing 5, 10, 15 and 20 %HS. In order to access the real size of the scattering objects, i.e. not considering the impact of the number density between the different samples, one should normalize the scattering intensity $I(q)$ by the volume fraction in crystallites *Φ*. Assuming a biphasic material, this quantity can be calculated in a straightforward way from the mass fraction in HS (x_{HS}) and the densities of each phase d_{SS} and d_{HS} such as:

$$\Phi = \left(1 + \left(\frac{\mathrm{d_{HS}}}{\mathrm{x_{HS} d_{SS}}}\right) - \left(\frac{\mathrm{d_{HS}}}{\mathrm{d_{SS}}}\right)\right)^{-1} \qquad \text{(S2)}$$

However, this normalization leads to the results presented in Figure S3 in which a clear mismatch of the different signal can be seen at high-q. Indeed, for a biphasic material, one should expect the data to collapse at large angle once normalized by the volume fraction[2] since the scattered intensity in this q-range satisfies $\mathrm{I}(\mathrm{q} \to \mathrm{q}^{\#}) = \Delta\rho^{2\prime} \frac{\mathrm{NV_{HS}}}{\mathrm{V_{tot}}} \mathrm{P_{HS}(q)} = \Delta\rho^{2\prime} \Phi\, \mathrm{P_{HS}}(q)$, with N being the number of HS unit in the irradiated volume V_{tot}. We believe that this issue comes mainly from the incomplete crystallization, i.e. that the crystallites volume fraction is different from *Φ*. It could also be due to the polymorphism of the T4T crystals (see section 3.1 and 3.2) leading to a multiphasic mixture in which different contrasts (or differences in densities) could be considered. This discrepancy is also revealed by the invariant analysis (Figure S2) showing, in particular for 5%HS, an unexpectedly high value.

Consequently, in order to treat the data in a coherent way, we choose the 20%HS data as a reference (because a good agreement is found between theoretical and experimental contrast, see Figure S2b). We normalize the corresponding data by *Φ* (= 0.148), and we subsequently used the ratio $\Phi_{eff} = X_c(\%HS)/X_c(20\%HS)$ to shift the data from the 5%HS (×0.16), 10%HS (×0.40) and 15%HS (×0.59) samples. One can finally observe in Figure 5a (in the chapter), the expected good match between all the signals at $q=q^{\#}$. From this data, it becomes then possible to describe the evolution of the T4T crystals morphology at the mesoscale when the chain rigidity is varied.

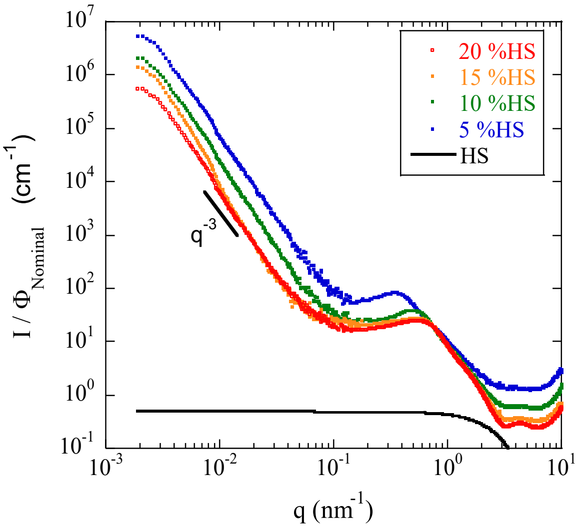

Figure S3: Reduced scattered intensity for the TPEs containing 5, 10, 15 and 20%HS considering nominal values of Φ (Table 3 in the chapter). The solid black line stands for the HS unit scattering intensity.

4.6.1.3 Correction of the data set from DUBBLE

The data presented in the chapter Figure 8 has been collected on the beamline DUBBLE at the ESRF using a vertical beam passing through a sample (20 %HS) placed inside a purpose modified rheometer (see. section 2) with the detector placed on the top of it (at 1.6 m). Hence, in order to consider the additional scattering (“empty beam”) and to be coherent with the data properly measured on ID02, we correct the full DUBBLE data set in the following way:

(i) We subtract on the whole q-range the same constant value to the whole data set standing for the empty beam contribution at large angles. This operation is made in such a way that the slope of the high-q regime (q>1 nm^{-1}) matches with the one measured on ID02 (Figure S4a).

(ii) We then subtract a power law $I_p = U\,q^{-2.6}$ in order to remove the low-q part of the empty beam with the same philosophy as in (i). Remarkably, one can note that the subtraction steps described in (i) and (ii) match very well with the ID02 empty beam depicted in Figuew S3. In particular the position of the low-q upturn from 0.38 nm^{-1} (instead of 0.3 nm^{-1}) and the power law exponent 2.6 (instead of 2.7) are in very good agreement.

(iii) The data set is then vertically shifted so that the room temperature measurement from DUBBLE matches with the renormalized spectrum from ID02 (measured at room temperature too). The final result is shown in Figure S4b.

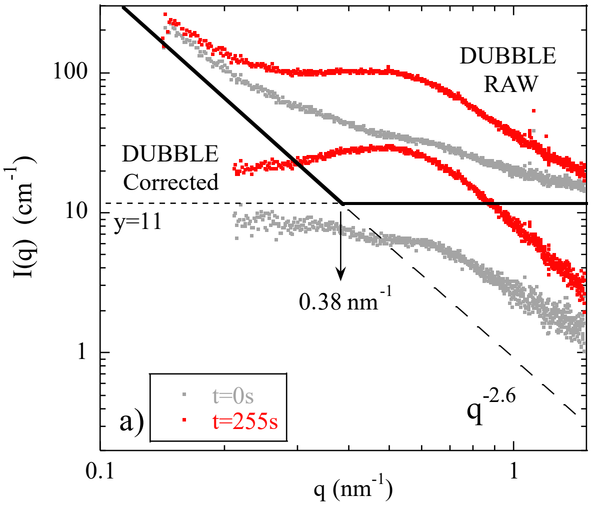

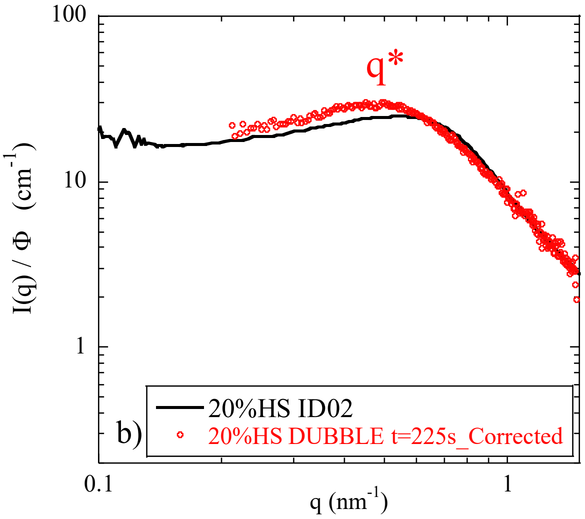

Figure S4: a) Subtraction of the "empty" beam contribution. Symbols on the top stand for the raw data (at 0 and 255 s cooling) while the ones at the bottom stand for the corrected ones. Dotted and dashed lines represent respectively the operations (i) and (ii) depicted in the text (they cross each other at q=0.38 nm^{-1}). b) Final result after corrections showing a good agreement between the data from DUBBLE and the ID02's one at room temperature.

4.6.2 WAXS additional data

4.6.2.1 Structure of PA66 and PA6

As one can see in the following picture, the chain structures of PA66 and PA6 lead to different crystal lattices. The T4T unit, in its atomic sequence (C,N), is similar to the PA66.

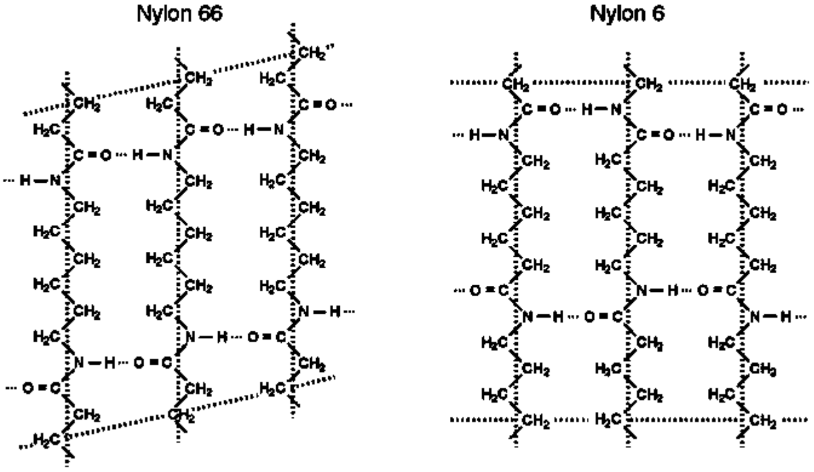

Figure S5: Crystal structure of the α-phase (antiparallel configuration) for PA66 and PA6.

4.6.2.2 Tentative of deconvolution

In Figures S6a-d below, we show an arbitrary Gaussian-based deconvolution of the WAXS diffractograms presented in the chapter (Figure 3) for 20 and 15%HS in both hot-pressed and solvent casted samples. The weight of the peak 5 is systematically enhanced when THF-casting is used (peaks 3 and 7 are relatively weakened).

A total of nine peaks plus an amorphous contribution (broad peak) are utilized to fit the data. Their positions are reported in Figure 3a (in the chapter) with a number from 1 to 8. The weak peak (yellow) situated at 11 nm^{-1} is however dismissed.

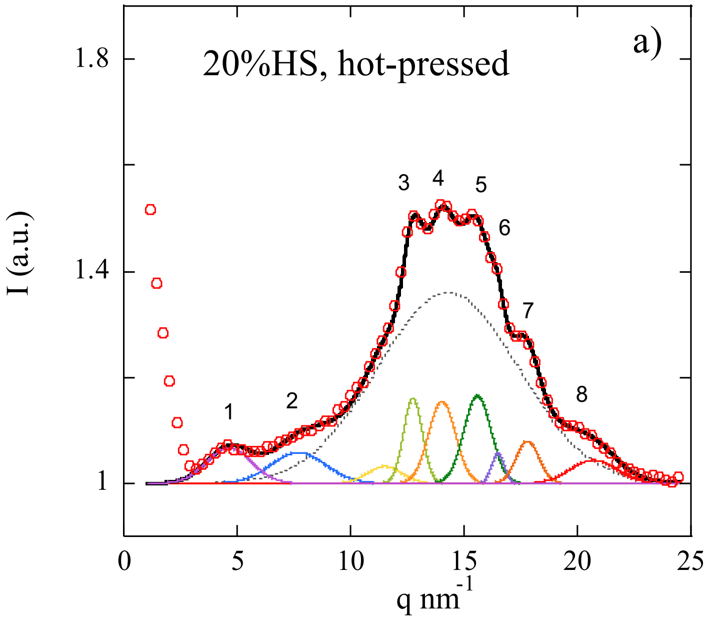
a)
20%HS, hot-pressed
1
2
3
4
5
6
7
8
I (a.u.)
1.8
1.4
1
0
5
10
15
20
25
q nm^{-1}

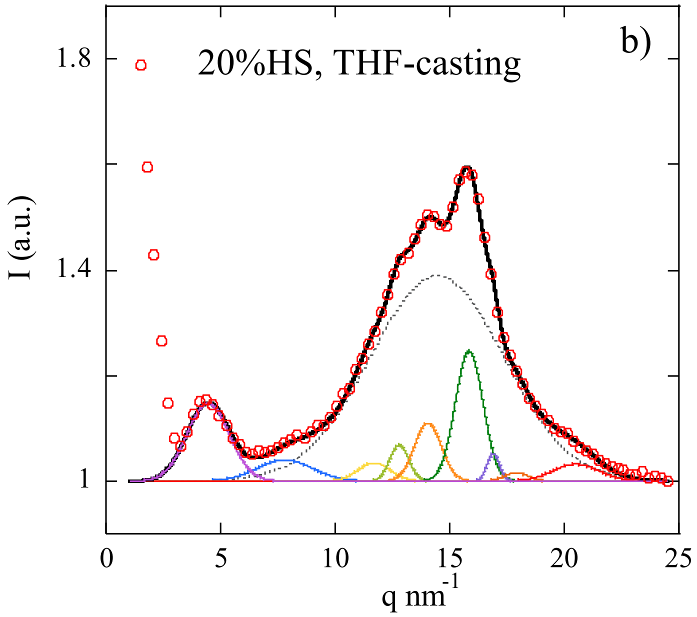
b)
20%HS, THF-casting
I (a.u.)
1.8
1.4
1
0
5
10
15
20
25
q nm^{-1}

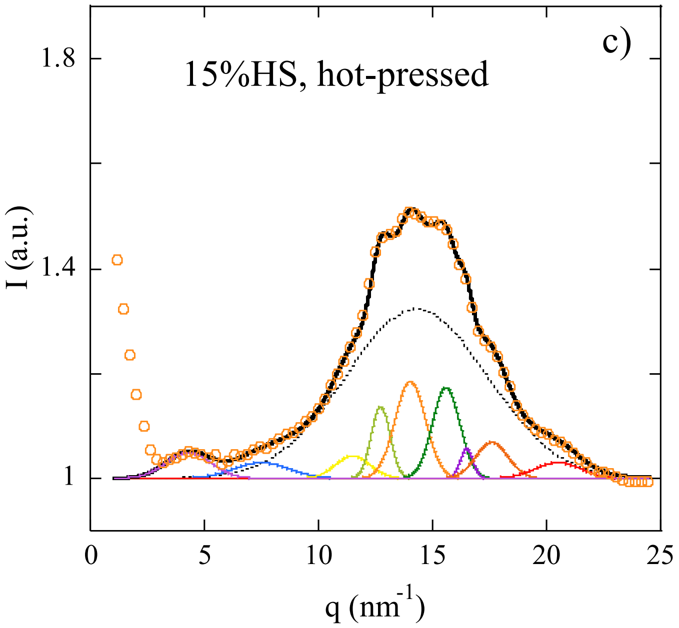

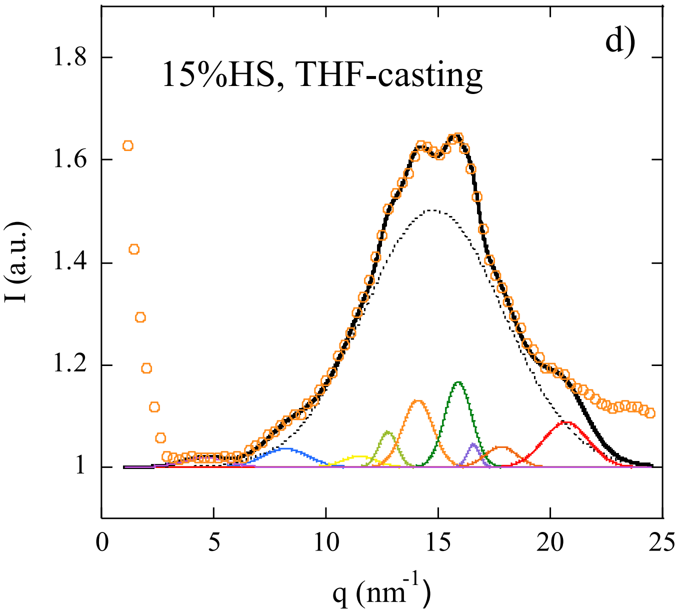

Figure S6: Arbitrary deconvolution of the diffractograms for samples containing 20%HS (a-b) and 15%HS (c-d) made by hot-pressing (a-c) and THF-casting (b-d).

4.6.2.3 Comparison of THF and HFIP casting

As detailed in the chapter and above, the THF-casting leads to a different crystal structure from the one we get by using hot-pressing. It is however interesting to note that a similar procedure with Hexa-Fluoro-Iso-Propanol (HFIP), a strong H-bond competitor, does not have any significant effect on the WAXS pattern (Figure S7a). In addition, polarized light reveals that only THF-casted films are birefringent (Figure S7b). These observations support the scenario of a quick growth of the crystallites in a preferred direction (see discussion in section 3.4) making the mesoscale structure anisotropic (birefringent) in casted samples by opposition to the hot-pressed ones in which the ribbons remain disordered and thus isotropic at length scales bigger than 100 nm.

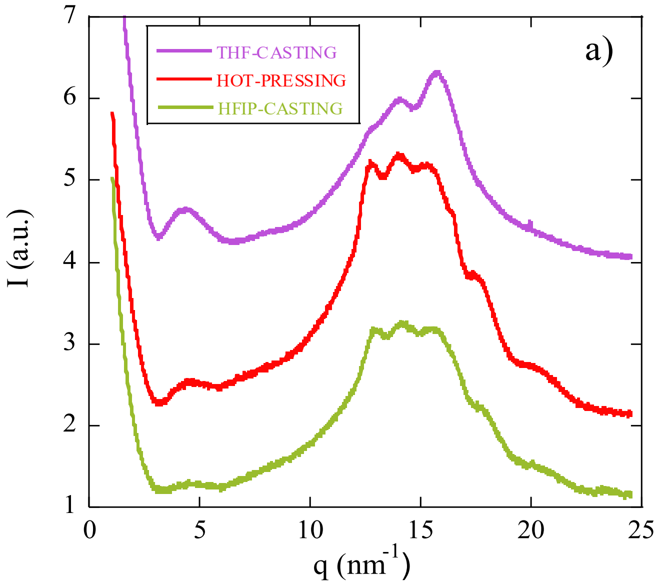

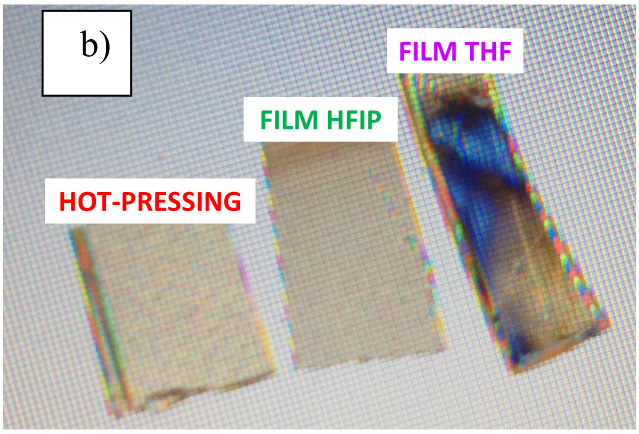

Figure S7: Impact of the processing on the local structure of the crystallites. a) WAXS diffractograms of THF and HFIP solvent casted samples (20%HS) vs. the corresponding hot-pressed one. b) Photograph taken with polarized light showing the birefringent nature of the THF-casted sample.

4.6.2.4 Rheology at T>T_m

For ideal polymer melts,[3] the rheological properties in the terminal regime $\omega < 1/\tau_d$ (τ_d is the disentanglement time) are usually described by $G'{\sim}\omega^2$ and $G''{\sim}\omega^1$ (with G' and G'' being respectively the storage and loss shear moduli). In the TPEs (Figure S8), at T>T_m, the corresponding slopes in the log-log representation are close to 1 for G'' but significantly lower than 2 for G' regardless of the %HS. This observation suggests that some of the H-bonds between the T4T units are still active, i.e. delay the material flow by storing energy, in good agreement with the presence of persistent aggregates expected from Figure 8 in the chapter.

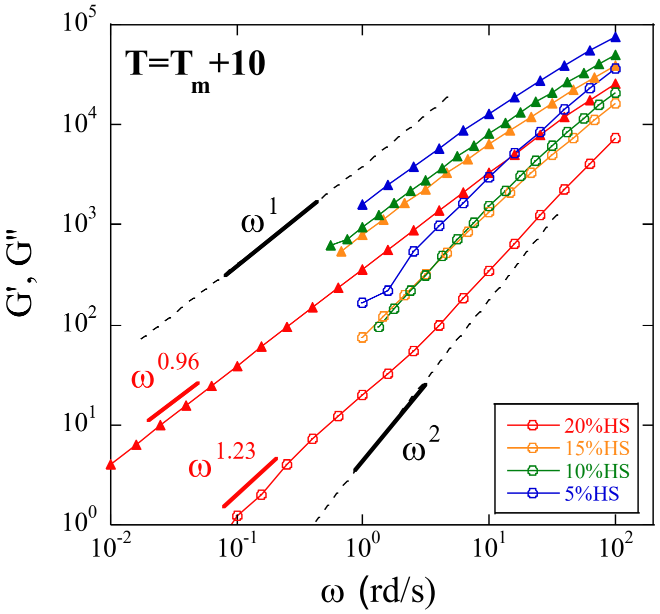

Figure S8: Storage (G') and loss (G'') moduli for the TPEs in the terminal regime revealing their non-Maxwellian behavior.

4.6.3 Supplementary References

1) Zemb, T.; Lindner, P., Neutrons, X-ray, and Light: Scattering Methods Applied to Soft Condensed Matter. 2002.

2) Baeza, G. P.; Genix, A. C.; Degrandcourt, C.; Petitjean, L.; Gummel, J.; Couty, M.; Oberdisse, J., Multiscale Filler Structure in Simplified Industrial Nanocomposite Silica/SBR Systems Studied by SAXS and TEM. Macromolecules 2013, 46 (1), 317-329.

3) Rubinstein, M.; Colby, R., Polymers physics. Oxford Oxford, UK: 2003; Vol. 767.

The content of this chapter has been published in Polymer International, 68(2), 283-293.

Chapter 5: **Fast Scanning Calorimetry clarifies the understanding of the complex melting and crystallization behavior of polyesteramide multi-block copolymers**

Abstract

In order to understand the Phase transitions in thermoplastic elastomers (TPE) based on well-defined multi-block copolymers made of "soft" poly(tetramethylene oxide) (PTMO) and "hard" terephthalate ester diamides (T4T), Fast scanning calorimetry (FSC) has been applied. The intrinsically complex chemical structure of TPEs leads to complex phase transitions. By changing their thermal history in a wide range of temperatures (from -100 °C to 200 °C) and cooling rates (from 10 to 4000 °C.s-1), we clarify the origins of the various phases present in these materials. We study the different possibilities for the hard-segments to associate depending on their mobility during the quenching phase, forming either strong and stable structures, or weaker and metastable ones. Besides, we demonstrate that a minimal cooling rate of 800 °C.s-1 is necessary to keep these TPEs (made of short and monodisperse hard-segments) amorphous leading to a subsequent cold-crystallization when heating back, at around 30 °C. Finally, we validate our interpretations by varying the copolymer composition (from 10 to 20%w in hard-segment), revealing the thermal invariance of poorly organized domains. Based on these data, we also discuss the importance of chain diffusion in the crystallization process.

Applying the FSC allows us to link fundamental understanding towards industrial application.

5.1 Introduction

Thermoplastic elastomers (TPEs) form an industrially relevant class of materials due to their tunable engineering properties and find numerous applications in automotive, consumer electronics as well as household appliance sectors.[1] The philosophy behind these elastomers resides in the phase separation of block-copolymer into hard and soft-domains providing good mechanical properties and elasticity combined with ease of processing.[2,3] The hard domains are either amorphous, high-T_g [4,5] or crystalline,[6, 7] made of aggregated "hard"-segments (HS) playing the role of physical crosslinks while the soft domains encompass low-T_g "soft"-segments (SS) such as polybutadiene,[4] polypropylene oxide[8] or poly(tetramethylene oxide)[9] (PTMO). In industrial applications, the SS molecular weight is most often a few kilograms per mole, likely limiting their crystallization.[10] On the other hand, the crystallization behavior of the HSs is governed by their distribution along the chain, as well as by the molecular weight of the SSs and of the whole chains.

The strong asset of TPEs consists in behaving as rubbers at room temperature while being melt-processable above their order-disorder transition temperature. This dual behavior makes them important candidates to replace vulcanized elastomers in a wide variety of consumer goods, notably from a recycling or reshaping point of view.[11] Another important advantage lies on the high-tunability of their properties by modifying both the composition and the chemical architecture[12] of the copolymers, particularly by using HS interacting through supramolecular bonds enhancing their phase separation. Lately, the utilization of e.g. urea,[13] urethanes,[5,14] or amide groups[9,15] as HS have been reported, leading in the latter case, to ribbon-like crystallites observable through microscopy,[14,16] and/or scattering techniques,[17,44] providing materials with strong mechanical properties.[20]

Among the various class of TPEs such as styrene based (TPS) or olefin based (TPO), polyesteramides present assets from both polyester and polyamides such as high melting temperature, fast crystallization and good mechanical properties. Moreover, they consist of one T_g and one main T_m with values in between the T_g and T_m of polyesters and polyamides, showing T_g/T_m ratio of 0.65, as HS separates by crystallization.[15] Such multi-block polyesteramides are usually prepared through a two-step synthesis. First, well-defined HS units (bisesterdiamide, T4T) are synthesized from 1,4-butane diamine and dimethyl terephthalate, further purified by recrystallization.[24] Then, HS units are connected with SS via condensation polymerization in order to form multi-block-copolymers.[2,15,19] Of a great importance, Gaymans and co-workers reported a strong dependence of both thermal and mechanical properties with the length and polydispersity of the HS they contain. Based on experimental techniques like DSC, FTIR, DMTA and tensile set measurements, they demonstrated that small and monodisperse hard units were providing faster crystallization, higher elasticity (with minor temperature dependence) and higher fracture strain.[19,20]

Recently, we have studied the multi-scale structure of one of these TPEs consisting in a sequence of PTMO and terephthalate based diamide "T4T" segments with varying the HS content from 5 to 20 wt%.[17] At the local length-scale, we reported the different ways for the HS to stack, i.e. either by directive H-bonding or Van der Waals interactions with possible π-π stacking. It is stated that while the former is responsible for the fast growth along a preferential direction, and thus, for the elongated (ribbon-like) nature of the aggregates, the latter allows the crystallites to widen perpendicularly (the thickness being fixed by the HS dimension ≈ 2.1 nm).[17] Also, by showing quite broad endothermic peaks, conventional DSC suggested that these hot-pressed materials were made of a wide molecular weight distribution of hard-domains similarly as in other TPE based on PBT or PA6,6.[21,22] On the contrary, their solvent casted counterparts were characterized by sharp transitions at high temperature, i.e. an enhanced order, likely due to the higher chain mobility during the drying phase.

Besides, we observed a low degree of undercooling ($\Delta T_m = T_m - T_c \approx 20$ °C ± 4 °C) for these samples (containing 5, 10, 15 and 20 wt% HS) due to enhanced HS order, in comparison to PBT based TPEs ($\Delta T_m \approx 36$ °C).[15,23] Beyond the faster kinetics of aggregation provided by the H-bonds, these low ΔT values suggest a pre-existing order in the melt state likely coming from persistent interactions at high temperatures. In fact, while no phase separation nor order were detected with classic polarized light microscopy,[25] small angle X-ray scattering resolved in time and temperature revealed unambiguously the presence of HS persistent aggregates at $T > T_m$.[17]

To sum it up, it appears that most of the final properties of semi-crystalline TPEs strongly depend on a large variety of parameters starting from the chemical nature of the chain-segments, their phase separation kinetics, and their underlying microstructure. While the chemical composition is crucial, it does not completely set the final behavior of a product: the processing conditions must be taken in consideration. For instance, industrial techniques/manufacturing processes like e.g. *plastic molding, blow molding*, *fiber spinning or 3D-printing* in which crystallization must occur quickly to reduce cycle times and therefore enhance production rate, are likely to lead to unique micro-structures due to the very particular temperature gradient and high mechanical stress applied to the materials.[29] The objective of the present work is to apply FSC in order to investigate the crystallization behavior of polyesteramides up to extreme conditions, i.e., varying the cooling rate from 10 to 4000 °C.s^{-1}. Our results evidence the latter's effect on the TPE mesoscopic structure, providing new insights for the control of the mechanical properties.

In addition, we will discuss the role of isothermal time, temperature and chain mobility on the formation of the crystallites (either stable T4T ribbon or metastable ‘baby-ribbon’) and study their consequences on the sample properties. As a more general objective, we would like to show the importance of understanding the crystallization behavior to improve industrial application.

The chapter is organized as follows: the sample preparation for FSC and the related methods used for the different experiments are presented in Section 5.2. In Section 5.3, we present and discuss the thermograms obtained during the heating phase (so-called “the measurement”) by varying: (i) the cooling rate from the melt state prior the measurement, (ii) the cooling path, i.e., comparing single ramp with two-step quenching, (iii) the isothermal crystallization temperature (T_{iso}) at which the sample is set prior the measurement, and (iv) the corresponding time t_{iso} spent at a given T_{iso}. The last part (v) is dedicated to the impact of the chain composition by varying the HS content from 10 to 20%. We then use these different results to discuss and interpret the bimodal distribution found for the crystallization rates as function of the isothermal crystallization temperature at high density of HS. Conclusions are drawn in Section 5.4.

5.2 Instrumentation and sample preparation

5.2.1 Conventional DSC

DSC thermograms were recorded on a Mettler Toledo DSC821e equipped with the STARe software. The method for the measurement is reported in chapter 3, section 3.3.3. Instead of cooling and heating rate of 20 ^{o}C.min^{-1}, rate of 10 ^{o}C.min^{-1} was used for these measurements.

5.2.2 Fast Scanning Calorimetry (FSC)

Fast-scan measurements were performed by using a commercially available Fast Scanning Calorimetry from Mettler-

Toledo, Switzerland, with a Huber TC100 intercooler and nitrogen purge gas of 50 mL.min^{-1}. The detailed description about instrumentation, operating procedure and calibration is already stated in the literature.[30-34] The performance of Fast Scanning Calorimetry depicts the actual high cooling and heating rates as a function of the purge gas and flow rate studied by G. Vanden Poel et al.[32] showing the possible window to quench rate of the instrument. The calorimetric chip-sensor was conditioned three times followed by temperature-correction/adjustment considering the specific thermal environment. This procedure was performed according to the instrument specification prior to use. The bulk sample was reduced to a small piece (of about 100 nanograms) and then transferred to the sensor centre having diameter of 0.5mm.[26] The sample mass of the PTMO-T4T samples was determined based on the method explained in the recent book on fast scanning calorimetry by C. Schick and V. Mathot,[35] using $m = \frac{\Delta H_{FSC}}{\Delta h}$, where ΔH_{FSC} is the enthalpy of melting measured by using fast scanning calorimetry at typical heating rate (10, 100 or 500 ^{o}C.s^{-1}) and Δh is the specific enthalpy of melting using conventional DSC at 20 ^{o}C.min^{-1}. Here, the tiny amount of samples aims to reduce drastically the thermal inertia ("lag") within the materials, allowing high scanning rate measurements.[32,34] Samples were well preserved from degradation due to the nitrogen atmosphere allowing the same piece of TPE to be measured through successive temperature loops.[27] Additional information can be found in SI section 1.

Effect of cooling rate – Starting from the melt state (200 ^{o}C) 10 s, the sample was cooled down to -80 ^{o}C at a rate varying from 10 ^{o}C.s^{-1} to 4000 ^{o}C.s^{-1}. After having held the sample for 10 s at -80 ^{o}C it was subsequently heated back to 200 ^{o}C at a constant heating rate of 1000 ^{o}C.s^{-1}. Heating rate of 1000 ^{o}C.s^{-1} was selected based on the previous studies by G. Vanden Poel et al.[32], showing that the thermal lag corrections remain relatively low up to this heating rate (a maximum lag of -1.4 °C was observed for a 1 μg sample).[32] The corresponding temperature program is presented in Figure 5.1a.

Isothermal crystallization $(T_m - T_g)$ – Isothermal crystallization measurements were performed on samples covering the entire temperature range from T_m (Table 1) to T_g (ca -60 °C), to calculate the crystallization rate. Starting from the melt state (200 °C), the sample was quenched to T_{iso} at a cooling rate of 4000 °C.s^{-1} to avoid any crystallization to occur and held at this temperature for a time $t_{iso} = 2$s, where after the material is further quenched to -80 °C at the same cooling rate. To understand the crystallization behavior of the PTMO-T4T material small steps of 5 °C at T_{iso} were performed, from T_m to T_g. After holding for 10 s at -80 °C, it was finally heated back to 200 °C at 1000 °C.s^{-1} (see Figure 5.1b). In the following sections, this protocol is referred as a two-step quenching. A similar set of measurements have also been performed with increasing t_{iso} to 60s (see Figure 5.1c).

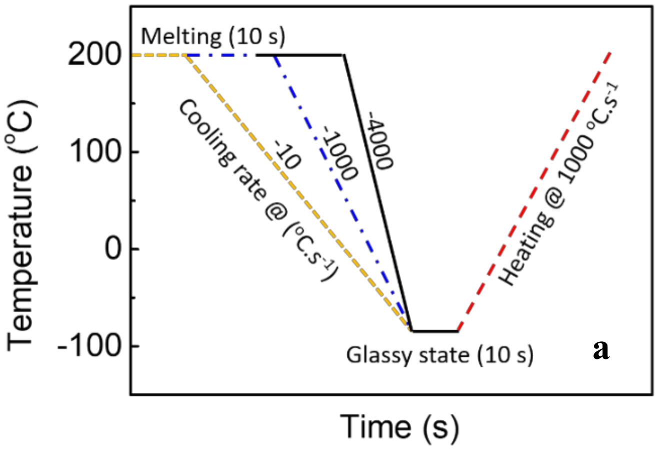

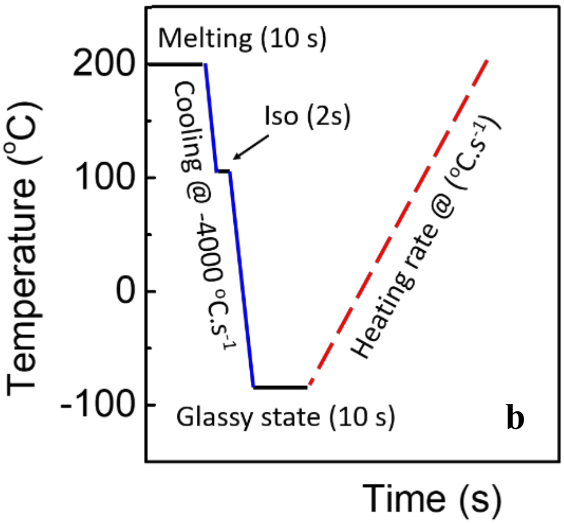

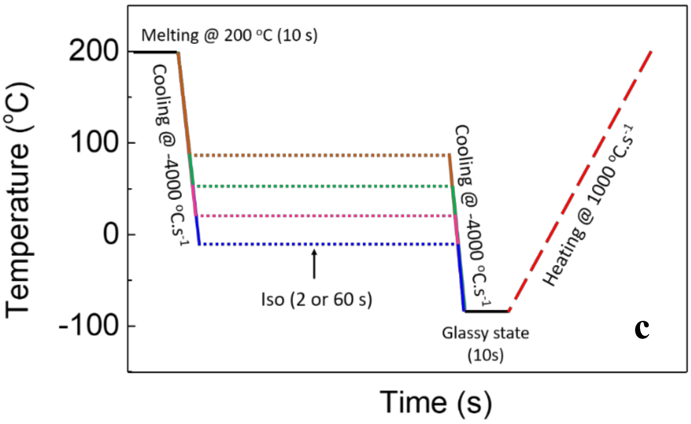

Figure 5.1: Different thermal treatments used in Fast Scanning Calorimetry all along this chapter a) varying the cooling rate, b) under isothermal crystallization at $T_{iso} = 100$ °C, based on a two-step quenching protocol, c) varying the temperature T_{iso} at which the sample is kept 2s before the measurement as well as the waiting time at T_{iso}.

5.2.3 Atomic Force Microscopy (AFM)

The morphology of the 20%HS sample was studied with a Bruker Icon Dimension AFM in tapping mode using an AR5T-NCHR high aspect ratio tip (k = 42 N.m^{-1}, f = 330 kHz, tip radius = 15 nm) commercially obtained from Nanosensors. Silicon wafers with 20 nm of electron-beam deposited silver were used as substrates. The 20%HS sample was first dissolved in THF at a concentration of 1% by weight and subsequently drop casted (500 µl) on the substrate before to be dried overnight in a vacuum oven at 65 °C. The resulting film of ca. 500 nm in thickness was then heated to 200 °C under inert atmosphere and finally either quenched in liquid nitrogen or slowly cooled down (6 °C.min^{-1}) to room temperature (see Figure 5.5), to mimic the slow and fast cooling experiments. The uniform surface of the film was scanned for morphology study of these samples (see SI section 7).

5.2.4 Rheology measurements (time sweeps)

Dynamic time sweeps were performed in the linear regime with a stress-controlled rheometer (MCR 301 from Anton Paar, Austria) equipped with stainless steel parallel plates of diameter 8 mm (1% strain, 10 rad.s^{-1}). All measurements were carried out in nitrogen gas atmosphere and temperature control was achieved by means of a convection oven (better than ±0.3 °C). Samples were first heated above T_m and then cooled down to $T_c + 10$ °C where the storage and loss moduli were measured as function of time.

5.3 Results and Discussion

The thermal properties of the four TPE samples, containing 5, 10, 15 and 20%HS have been first studied using conventional DSC, with a heating rate of 10 °C.min^{-1} (see Figure 5.2). The thermograms exhibit the glass transition of the PTMO SSs (T_g) at around -60 °C followed by the melting point of the SS close to -10 °C. The latter is known to occur for SS having a molecular weight above 2 kg.mol^{-1}.[10,17] As expected, the fraction of such SS crystallites decreases with increasing the HS content. On the other hand, the melting peak (T_m) of the T4T crystallites well follows the HS content, increasing from 92 °C to 158 °C when the HS density is varied from 5 to 20%HS. FTIR spectra reported in chapter 3, also shows an increase in absorbance at 1630 cm^{-1}, 1670 cm^{-1} and 3320 cm^{-1} corresponding respectively to the crystalline amide, the amorphous amide and the hydrogen bonded N-H when the HS content is increased. For the whole sample set, we report in Table 1 the above-mentioned parameters as well as the crystallization temperature T_c measured during the cooling step performed at 10°C.min^{-1}.

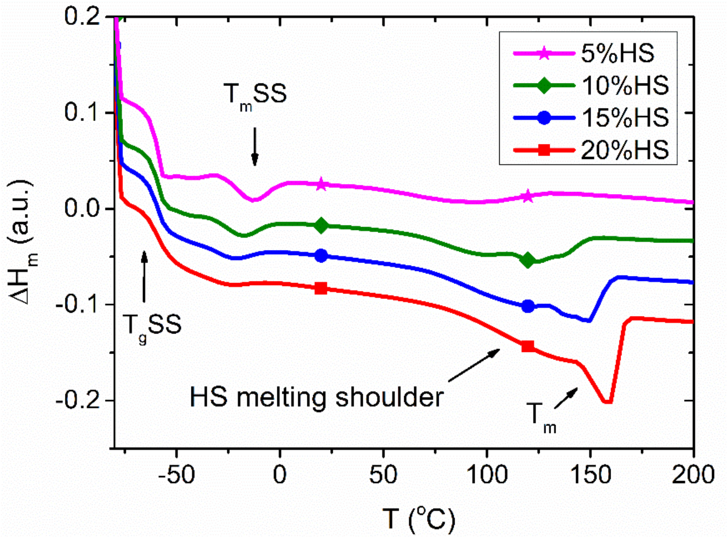

Figure 5.2: Differential Scanning Calorimetry thermograms of TPEs containing 5, 10, 15 and 20%HS performed at a heating rate of 10 °C.min^{-1}. Data have been vertically shifted for clarity. Respective values of T_g, T_c and T_m are reported in Table 1.

Table 1: Physico-chemical characterization for all four TPE samples based on SEC and DSC.

HS (wt %)	M_n **(g.mol^{-1})**	M_w **(g.mol^{-1})**	ΔT† **(°C)**	T_g **(°C)**	T_c **(°C)**	T_m **(°C)**	X_c ‡ **(wt %)**
5	25,200	48,900	19.2	-60.0	72.8	92.0	2.6
10	22,800	44,300	18.8	-59.1	103.8	122.6	6.3
15	22,500	43,300	20.9	-59.2	125.5	146.4	9.3
20	19,300	37,600	19.2	-59.5	139.2	158.4	15.8

† $\Delta T = T_m - T_c$

‡Mass fraction of T4T crystallites: X_c (%)= ($\Delta H_{DSC}/\Delta H_{T4T}^*$) 100 where ΔH_{T4T}^* = 150 J.g^{-1} from ref 17.

We present in Figure 5.3 the variation of both T_m and T_c with the HS content showing that the difference between these two characteristic temperatures ($\Delta T = T_m - T_c$) is rather small (~20 °C) in comparison with other TPEs such as PBT/PTMO (~36 °C).[39] This observation suggests a fast crystallization process, most likely due to the presence of strong hydrogen bonds acting over a longer range, further enhanced by the monomeric (i.e., short and monodisperse) nature of the HS.[17] Beyond the usual increase of thermal stability (higher T_m) with larger crystallites, conventional DSC also reveals that the melting behavior is rather broad showing multiple melting areas for samples containing more than 5%HS. Indeed, it seems that well-defined ribbons (melting at the highest T_m) are systematically accompanied with smaller imperfect domains for which the characteristic melting temperature is significantly lower, leading towards broad transition melting. As mentioned in our previous study,[17] we believe that this second population, which corresponds to 'weaker' crystallites, is formed by HS belonging to chain segments trapped between the most perfect crystallites, i.e. having a limited mobility, preventing the formation of more stable structures. In good agreement with the latter statement, this effect greatly disappears when one uses solvent casting to prepare TPE films, leading towards a sharp single melting behaviour[17] confirming that the sample processing plays a major role on the final sample structure and eventually properties. Conventional thermal analysis does not allow to deep dive into the effect of processing the final thermal properties and morphology. The aim of the following FSC experiments is therefore to clarify both kinetic and thermodynamic aspects of such association/dissociation mechanisms and their consequences on the melting properties, through a systematic and progressive variation of the thermal history.

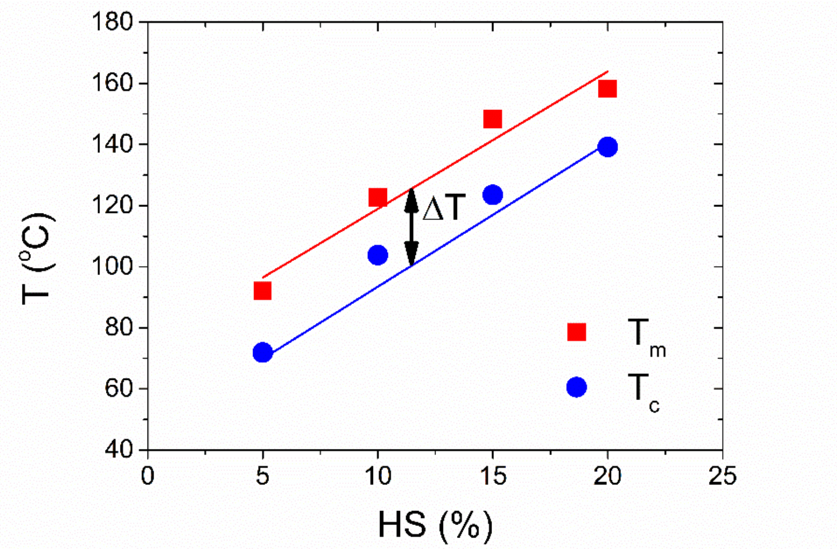

Figure 5.3: Melting (T_m) and crystallization (T_c) temperatures extracted from conventional DSC performed at 10 °C.min^{-1} as a function of HS content.

5.3.1 Impact of the cooling rate on the crystallization and melting

The TPE containing 20%HS was investigated by using the method summarized in Figure 5.1a, with the aim to understand the effect of high and low cooling rate on the structural evolution of the T4T hard-domains. The results are presented in Figure 5.4a as heating curves recorded at 1000 °C.s^{-1} after a cooling step performed at rates from 10 to 4000 °C.s^{-1} down to -80 °C. At low temperatures, the thermograms show the glass transition of the PTMO SSs (T_g) around -50 ºC, in reasonable good agreement with conventional DSC (see Figure 5.2). No clear melting of the soft segment can be observed, which suggests the fast cooling prevents SS to crystallize. No further attention towards melting of SS is considered in this chapter. Upon increasing the cooling rates above 800 °C.s^{-1}, a cold crystallization peak appears around 50 °C, pointing at so-called critical or quenching rate.[33] Apparently the T4T HS is completely staying amorphous at cooling rates of 1000 °C.s^{-1} or more (see also AFM in Figure 5.5a).[19] For T>120 °C, an endothermal event is seen, undoubtedly standing for the melting of T4T crystallites. In all cases the melting temperature of HS (shown in Figure 5.4a) increases in a monotonic way (from 130 to 147 °C) with decreasing the cooling rate. The slower the cooling rate, the better the T4T crystals can organize into well-organized ribbon structures. (See also SI section 2).

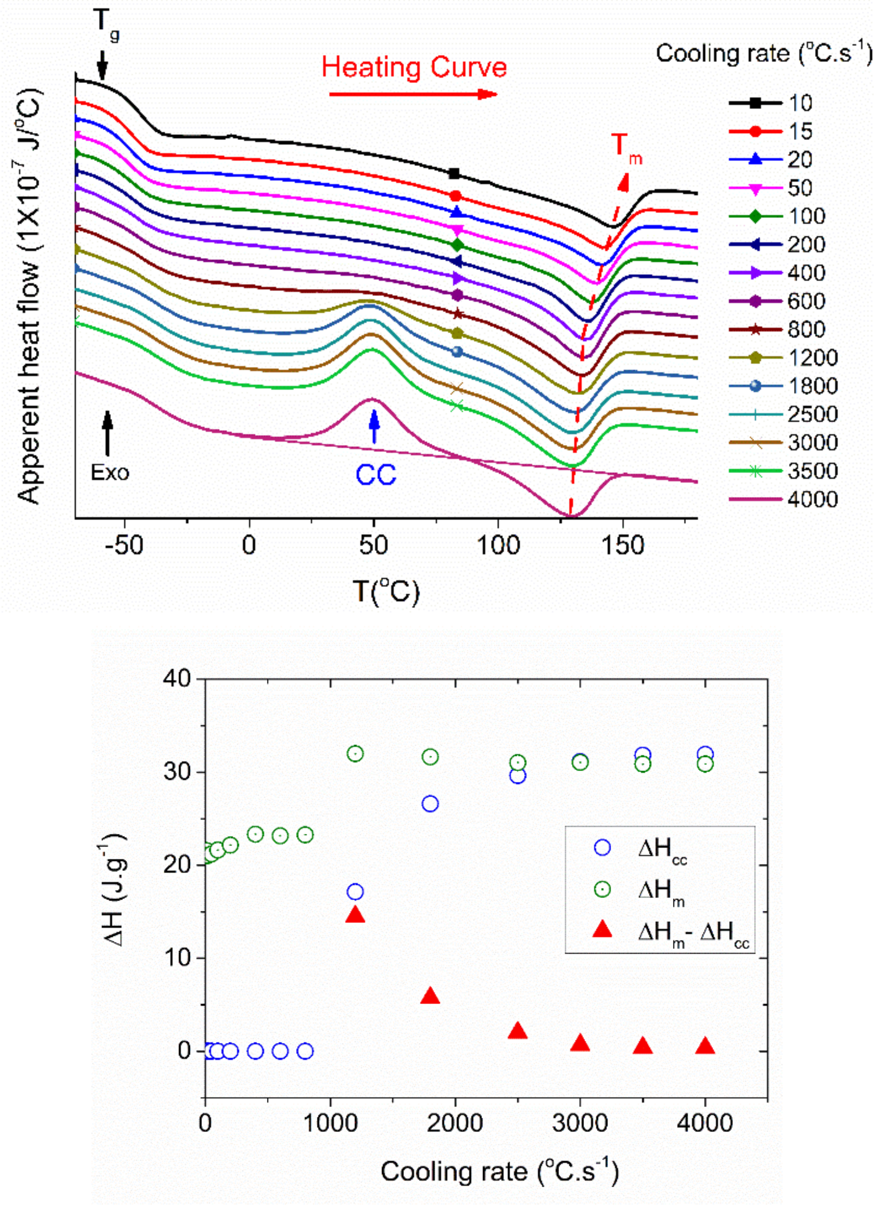

Figure 5.4: a) Thermograms measured on a 20%HS sample during a heating step performed at 1000 °C.s^{-1}. Prior to the measurements, the sample was cooled down from 200 to -80 °C at different cooling rates going from 10 °C.s^{-1} to 4000 °C.s^{-1}. Data is shifted vertically for clarity and the last thermogram shows the flat base line selected for peak integration. b) Variation of enthalpy in 20%HS for Cold Crystallization

(ΔH_{cc}), terminal melting (ΔH_m) and the difference (ΔH_m - ΔH_{cc}) emphasizing the maximum cooling rate (800 °C.s^{-1}) at which no crystallization takes place during the cooling phase.

To evaluate the cold crystallization and melting behavior of the HS, the specific enthalpy variations (± 2 J.g^{-1}) ΔH_m and ΔH_{cc} were quantified, which are shown in Figure 5.4b). No CC is observed at low cooling rate i.e. from 10 °C.s^{-1} to 800 °C.s^{-1}, providing an almost unchanged ΔH_m≈22 J.g^{-1} (X_c≈ 15 wt%). However, the CC start to occur and ΔH_{cc} significantly increases at rates above 800 °C.s^{-1} until it reaches its maximum value of 32 J.g^{-1}, at quenching rate of 3000 °C.s-1 and above. On the other hand, the enthalpy of melting at cooling rates below 800 °C.s^{-1} is explained by trapping of the T4T HSs due to the ribbons formed during cooling. At fast cooling the formation of these ribbons is more prohibited, which leads, after cold crystallization, to an intrinsically higher crystallinity (~20%). Nevertheless the $T_m$is slightly lower because cold crystallization takes place at 50 ºC, which is too low to allow the formation of perfect ribbon as observed upon slower cooling. This suggests that a higher fraction of HS can crystallize during the heating step (by CC) when crystallization was prevented during the cooling step. This result can be understood from the fact that upon heating, the free HS will tend to crystallize driven by a very strong attractive potential (due to the low temperature). However, because of a lack of mobility, the so-formed crystallites (appearing at T_{cc}) are expected to be smaller than the ones formed below T_c during the cooling phase (see Figure 5.5b). In good agreement with the latter interpretation, it is found that T_m significantly decreases when CC occurs (see Figure 5.4a) corroborating the idea that CC leads to a higher fraction of crystallites but limits their size.

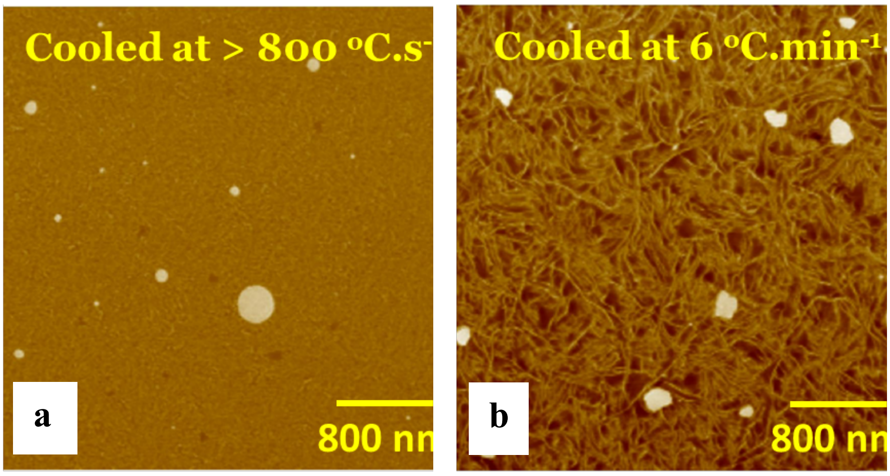

Figure 5.5: AFM phase image of a 20%HS sample. a) cooled in liquid nitrogen, showing amorphous morphology and b) cooled down at 6 °C.min^{-1} from the melt state (200 °C), showing ribbon structure.

5.3.2 Continuous cooling vs. two-step quenching

In this part, we wish to understand the impact of the cooling history on the thermal behavior of TPEs structure from a qualitative variation of the procedure. To do so, we propose to compare the results from the section 5.3.1 ("continuous cooling") with the so-called "two-step quenched" materials for which the thermal history is summarized in Figure 5.1b. In the latter case, critical quenching rate of 4000 °C.s^{-1} was used to avoid any crystallization occurring during the successive cooling phases. In between the two quenching steps, and by opposition with the continuous cooling, the sample was crystallized isothermally at T_{iso}=100 °C. This temperature was chosen to optimize the crystallization rate (see section 5.3.5) while the corresponding time was varied from t_{iso}=2 to 60s.

For continuous cooling, it is expected that the nucleation takes place below T_m, at a certain undercooling grade, and is followed by a progressive growth of the T4T crystallites, most likely leading to large and stable crystals accompanied with a wide variety of smaller ones. This scenario is corroborated by AFM in Figure 5.5b, where long ribbon-like crystals are clearly observable. As a result, the corresponding melting peak in Figure 5.6a is rather broad, confirming the large polydispersity in crystals size. On the other hand, when the two-step quenching is applied, the TPE quickly crystallizes due to the high (thermodynamic) association rate at T_{iso} = 100 °C, limiting therefore strongly the "progressive" character of the ribbons growth. As a matter of fact, this procedure results in a lower melting temperature and in a sharper melting peak made of two distinct contributions denoted T_m and T_{sh} (see Figure 5.6a). This bimodal distribution is due to a primary crystallization at early stages, i.e., when the copolymers still have a high mobility, followed by a secondary crystallization (related to T_{sh}) due to the association of chain segments having their extremities trapped into the primary network.[17] Because of their reduced mobility, these HS take time to crystallize and the corresponding growing crystals cannot reach their equilibrium size if t_{iso} is too short. This picture is further validated in Figure 5.6b, where it is seen that the second melting peak (T_{sh}) is more visible when t_{iso} is shorter, i.e. when that waiting time does not allow the crystallites to fully grow. In contrast, if a longer t_{iso} is used (60s instead of 2s), this secondary peak is shifted towards higher melting temperatures and eventually merges with the main melting peak (T_m). In addition, Figure 5.6b shows that decreasing T_{iso} from 100 to 60 °C results in a lower temperature for T_m and T_{sh} respectively. Considering the slower crystallization rate at 60 °C (see section 3.5), synonymous of a lower chains mobility, we believe here that the secondary crystals formed at 60 °C are far from their equilibrium state, in comparison with the ones created at 100 °C, explaining the large difference in T_{sh}. We also observe that the fraction of equilibrated ribbons is smaller, with a more pronounced size dispersion than at T_{iso}=100 °C. The impact of both T_{iso} and t_{iso} are investigated systematically in the two next sections.

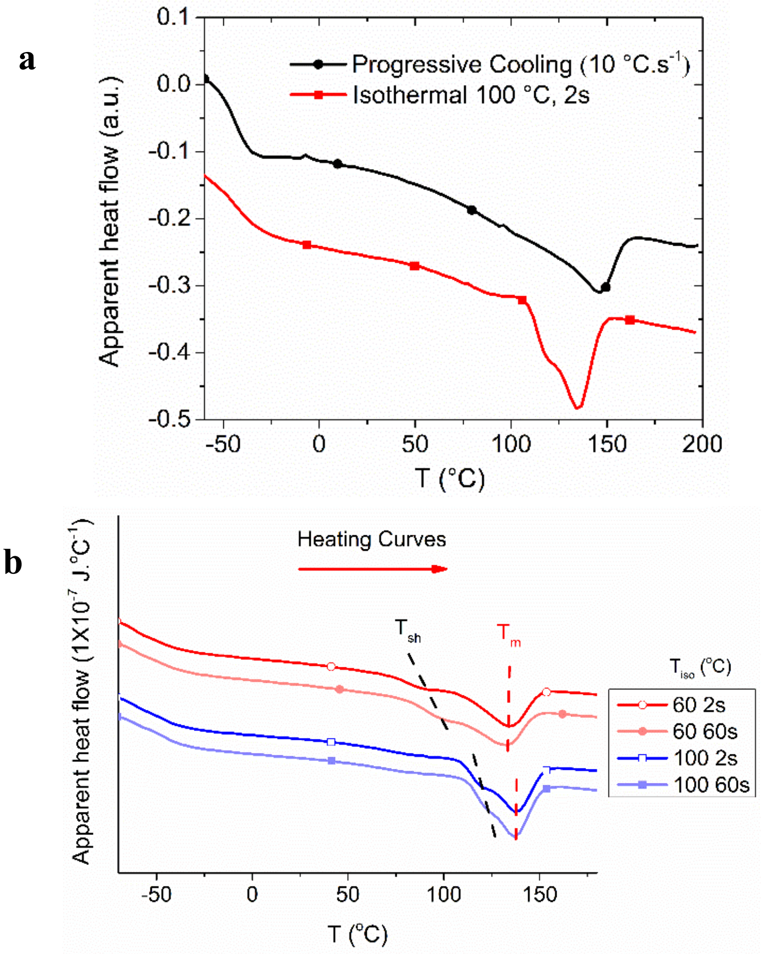

Figure 5.6: a) Effect of the cooling procedure, thermograms recorded during heating phase at 1000 °C.s^{-1} on samples progressively cooled down at 10 °C.s^{-1} from melt and two-steps quenched (4000 °C.s^{-1}) maintained 2s at 100 °C. Data is shifted vertically for clarity. b) Thermograms recorded from the 20%HS sample during the heating phase at 1000 °C.s^{-1}, after a two-step quenching with T_{iso} = 60 °C and 100 °C. For each sequence, the sample was isothermally held for 2s and 60s at T_{iso}. Data are shifted vertically for clarity.

5.3.3 Impact of T_{iso} on the TPEs crystallization

In order to further understand the thermal behavior of these copolymers, we propose in this section to vary T_{iso}, from T_m to T_g, and to investigate its influence on the crystallites formation following the procedure depicted Figure 5.1b. Representative thermograms are presented in Figure 5.7, showing a rich variety of melting behaviors, that we analyse below by separating the isothermal temperatures into several regions:, (The whole data set, without vertical shift factor can be found in SI section 5)

For T_{iso} ≥=140°C, the thermograms are like the ones extracted from direct rapid quenching (Figure 5.4). This is in good agreement with the fact that the material stays amorphous after 2 seconds spent at these high values of T_{iso}. It is subsequently quenched below its T_g, letting no chance for the crystallization to occur during the cooling phase. Therefore, once the material is heated back, one expects CC (seen at around 35 °C) followed by the melting of the so-formed crystallites (seen at around 135 °C). A difference with the continuous cooling procedure can however be noticed on the temperature at which the CC occurs. In fact, it is found to be ca. 15 °C below the one reported in Figure 5.4. This difference is attributed to the formation of pre-nuclei formed during the 2s isothermal break (since $T_{iso} < T_m$) due to intra and inter molecular hydrogen bond association in melt, implying a deepening of phase separation which is likely to enable the cold crystallization to occur earlier during the subsequent heating.[37]

At T_{iso} = 135 °C, an additional peak appears at high temperature (≈155 °C) suggesting the creation of very stable crystallites whereas it is not observed anymore for lower T_{iso}. We assign this melting peak to the fact that at such high T_{iso}, the chains have a large mobility, which let them the time to disentangle and diffuse (similarly to solvent casting) before starting to crystallize, favouring thus the creation of well-organized crystals within the isothermal time frame. The melting peak at high temperatures belongs to annealing at 135 °C which is within the melting area of the T4T crystals shown in Figure 5.7. On the other hand, it is observed that not all T4T crystals crystallize into such strong crystals, the remaining HS cold crystallizing during the heating process. The latter is attributed to the low driving force for crystallization at high T_{iso}. In conclusion, crystallization just below T_c seems of interest since it allows the crystallites formation from chains having an optimal mobility.

By decreasing further T_{iso}, from **135 °C to 105 °C**, this equilibrium between chain mobility and crystallization driving force is modified toward higher crystallization rate (see section 5.3.5) and lower chain mobility. It is observed that the lower T_{iso}, the lower T_m, but the higher the melting enthalpy. This can be attributed to the fact that higher crystallization rate leads to the formation of a larger number of smaller crystallites, which cannot grow further due to the lower mobility of the (associated) chains. Also, while part of the HSs are seen to crystallize during the cooling phase, a significant fraction of them is observed to cold crystallize during the subsequent heating (SI section 5 Figure S5a). The corresponding CC temperature is found to be higher than the one reported for higher T_{iso}, strongly suggesting that the HS associations made along the cooling step hinder the chains motion. This is also supported by a lower melting point of the smaller crystals originating during cold crystallization.

For 0 °C < T_{iso} < 105 °C, CC is no longer observed since the sample has a high crystallization rate and fully crystallizes during the isothermal 2 seconds-break. Completing precedent results, Figure 5.7 further reveals that the melting temperature of the largest ribbons, T_m, formed in this range of temperatures is nearly independent of T_{iso}. More precisely, as observed in Figures S5b and S5c of SI, decreasing T_{iso} from 105 °C to 50 °C leads to the formation of few crystallites melting at lower temperatures, while decreasing T_{iso} from 50 °C to 0 °C does not influence the melting behavior of the crystallites anymore. In both cases, T_m is much lower than the high melting temperature observed at T_{iso} = 135 °C. It must be noted here that this high melting peak cannot be attributed to a melting recrystallization process as observed in several semi crystalline polymers. Indeed, one can disprove this possibility since the melting temperature of this high melting peak is not affected by varying the heating rate. This suggests that in this range of temperatures, the formation of crystals is spontaneous below the equilibrium melting point due to high undercooling temperature, leading to the fast formation of ribbons taking place before any significant chain's diffusion allowing the eventual creation of strong crystallites (high T_m).

On the contrary, the melting temperature of the secondary peak, T_{sh} is decreasing in a monotonic way with decreasing T_{iso} until disappearing when the latter reaches 0 °C. As already suggested, this secondary melting peak stands for the melting of short metastable crystallites (called here as "baby-ribbons"). Based on these results as well as Figures S5b and S5c in SI, one can postulate that their melting temperature T_{sh} is related to their size, i.e. decreasing T_{iso} would make them smaller and smaller. This scenario is further supported by the fact that at a temperature at which shoulder peak disappears (T_{iso}=0 °C), part of the HS has a too low mobility to even be able to create short crystals during the 2s break at T_{iso} and cold crystallization appears again (T_{iso}=-15 °C). The decreasing size of these "baby-ribbons" with decreasing T_{iso} is a direct consequence of the very low mobility of the chain segments, as further discussed in section 5.3.5.

Finally, for T_{iso}<0 °C, the experiments in Figure 5.7 are like the one from Figure 5.4 since the sample is quenched from 200 °C to a temperature close to T_g at which no significant crystals have time to develop due to the quasi-arrested chain dynamics. Around T_g the growth of the T4T crystals is highly restricted due to very low chain mobility. This is also shown by a decreasing crystallization rate, observed when reaching 0 ºC (see section 5.3.5). As already mentioned, at T_{iso}=-15 °C, CC reappears at the same temperature than previously observed (≈35 °C).

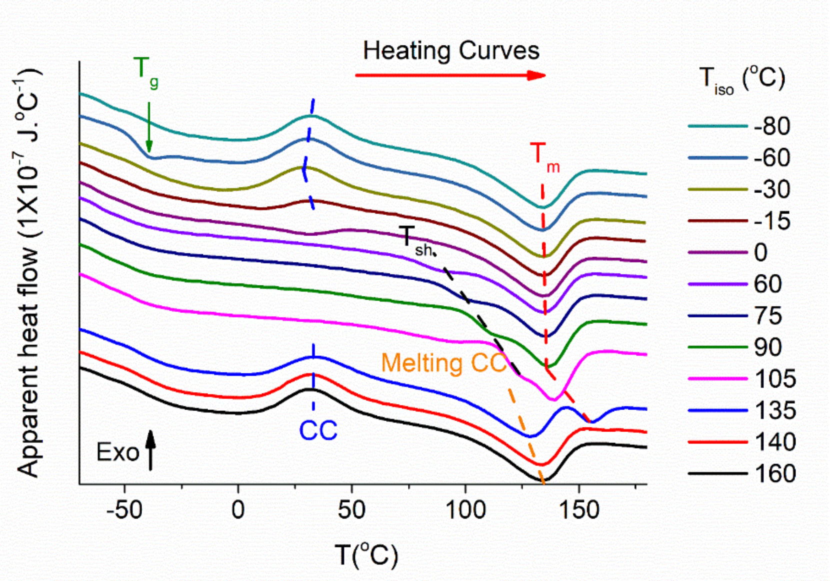

Figure 5.7: Thermograms recorded from the 20%HS sample during the heating phase at 1000 °C.s^{-1}, after a two-step quenching with varying T_{iso} from T_m to T_g. For each sequence, the sample was isothermally held for 2s at T_{iso}. Data is shifted vertically for clarity.

5.3.4 Influence of holding time t_{iso}

<u>*General trend*</u>

In Figure 5.7, the 2 seconds waiting time at T_{iso} is not long enough to reach a thermodynamic equilibrium (e.g. CC detected for high and low T_{iso} values). Therefore, the waiting time is increased to t_{iso} = 60 seconds (see Figure 5.8), to understand the development of the ribbon like structure. First, it is seen that at T_{iso}=135 °C and 140 °C, a longer waiting time allows enhancing the fraction of much more perfect crystallites, characterized by a very high melting temperature. This phenomenon which is called annealing, can be quantified by looking at the enthalpy variation of the end melting which grows significantly in both cases (see Table 2). One hypothesis can be that there is a lamellar doubling of the ribbon-like crystals. This may explain the discontinuity observed in the melting, and the high-end melting temperatures. This result is in line with the discussion proposed in section 5.3.3: a high value of T_{iso} (around T_c) leads to much more perfectly organized crystals, taking however a long time to grow due to their low crystallization driving force. Furthermore, it unambiguously appears that a longer t_{iso} pushes up the temperature of CC. This observation can be simply rationalized through similar arguments as previously mentioned, i.e. increasing t_{iso} (or decreasing T_{iso}) favors the chains association, which limits the segments mobility when heating, and therefore delays the CC.

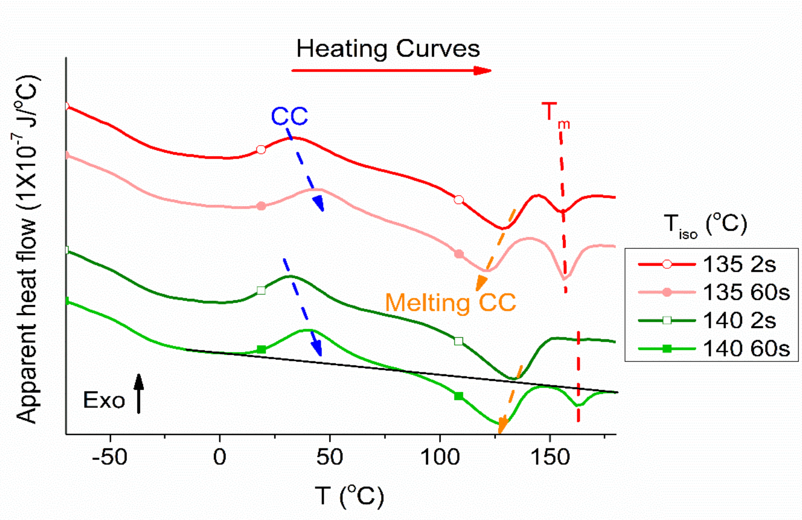

Figure 5.8: Thermograms recorded during the heating phase (1000 °C.s^{-1}) of the 20%HS sample after a two-step quenching (4000 °C.s^{-1}) with T_{iso} being either 2 or 60s and T_{iso}= 135 or 140 °C. Data is shifted vertically for clarity and selected base line for integrating the peaks is shown.

A full quantitative analysis of various enthalpies observed such as cold crystals (ΔH_{cc}), melting of cold-crystals (ΔH_{mcc}) and end melting (ΔH_m) were extracted using the suitable baseline shown in Figure 5.8 supporting our qualitative conclusions (see Table 2). The increase of T_m with t_{iso} is due to the annealing effect, as longer waiting time allows a better stacking of hydrogen-bonded HS. One can also remark that the enthalpies of CC (ΔH_{cc}) and their associated melting (ΔH_{mcc}) are very close to each other, avoiding any doubt about the nature of such phase transitions. Furthermore, around T_c, increasing the isothermal temperature provides the chance to form more perfect crystal structure (higher T_m) despite their longer time needed to develop (lower ΔH_m). The latter point suggests once again that a higher mobility of the chains leads to the formation of larger objects (as it is the case in solvent casted TPEs), characterized by higher melting temperatures. There is thus always a balance between the ribbon crystals and the 'baby-ribbon' crystallite structures.

Table 2: Variation of enthalpies in 20%HS, for cold crystallization (ΔH_{cc}), melting of cold crystals (ΔH_{mcc}) and terminal melting point (ΔH_m)

T_{iso} (°C)	Isothermal time (s)	T_{mcc} (°C)	ΔH_{mcc} (J. g^{-1})	T_m (°C)	ΔH_m (J. g^{-1})	Xc (%)
140	2	134	34.4	-	-	-
	60	128	30.9	163	4.4	2.9
135	2	129	31.5	156	7.0	4.6
	60	121	26.1	156	10.6	7.0

The previous explanation and observations are further apprehended by rheology measurement presented in Figure 5.9 below. It shows the evolution of the storage modulus for multi-block copolymers containing 10 and 20%HS as a function of time, measured under small oscillatory shear measurement performed at a frequency of 10 rad.s^{-1}. The temperature of the experiment T_{exp} was reached at 6 °C.min^{-1} from 200 °C. It was chosen such as $T_{exp} = T_c$ +10 °C i.e. 113 °C for 10% and 150 °C for 20%HS.

Despite the temperature being above T_c, the storage modulus continuously increases with time, which suggests that the HS associate more and more to form new or larger crystals. Crystallization is thus possible at such high temperature but has a very low crystallization rate. As seen in Figure 5.9, the corresponding modulus continuously increases during a very long time, and only starts to saturate after around 10^4s, indicating that the systems are slowly approaching their equilibrium state. Thus, based on these results, one can conclude that in the temperature range at which the crystallization rate is slow, longer waiting time, t_{iso}, at isothermal temperature favors the creation of a larger fraction of crystallites. As a last comment on Figure 5.9, it must be noted that the fact that the initial modulus of the 10%HS sample is larger than the one measured for the 20%HS sample is due to the difference in temperature of measurement (113 °C vs 150 °C).

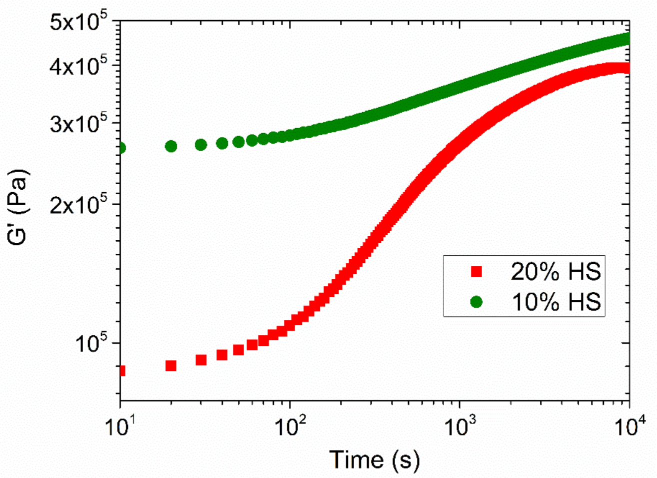

Figure 5.9: Storage modulus (G') at 10 rad.s^{-1} as a function of holding time (s) for isothermal temperature T_{exp}=T_c+10 °C.

To extend these observations to the full range of T_{iso}, we summarize in Figure 5.10 the evolution of the end melting point (T_m) and the corresponding melting temperature of the secondary peak (T_{sh})

as a function of T_{iso} for 2s and 60s. We remind the reader that these experiments still refer to the two-step quenching procedure (4000 °C.s^{-1}) on a TPE containing 20%HS. This representation allows highlighting several important features. i) The end melting point of the T4T crystallites is nearly constant (≈ 135 °C) for 0 °C < T_{iso} < 100 °C whereas, beyond this point, it continuously increases up to 160 °C at T_{iso} =140 °C (≈T_c in conventional DSC). ii) The melting temperature of the secondary peak evolves in a quasi-linear way with T_{iso} and iii) while the waiting time at T_{iso} has no effect on T_m (whatever the value of T_{iso}), it significantly enhances T_{sh} by ca. 15 °C for (T_{iso}< 80 °C).

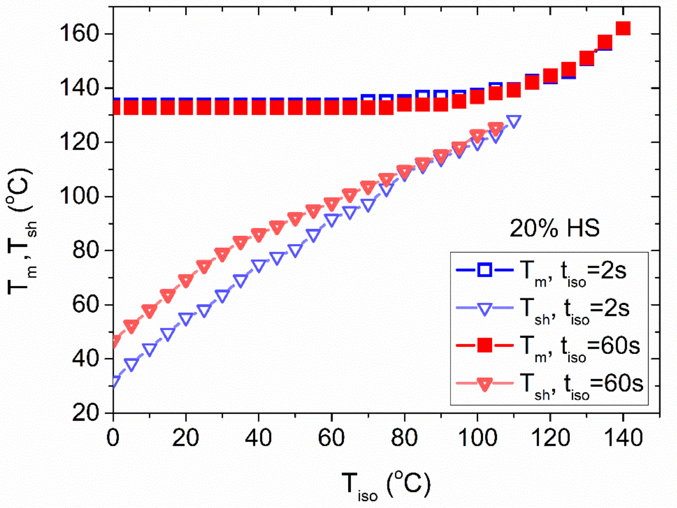

Figure 5.10: Terminal melting temperature of the crystallites (T_m) and melting temperature of the secondary peak (T_{sh}) as a function of isothermal temperature (T_{iso}) for waiting time $T_{iso}$of 2s and 60s.

These results are consistent with our hypothesis that the secondary melting point, T_{sh}, is associated to the melting of shorter crystal structures, defined as ‘baby-ribbons’, which did not have time to grow up to their final, equilibrium state.

Furthermore, the observations (i) and (iii) are understood as from T_{iso} = 0 to 100 °C, the crystallites had time to grow and to reach their thermodynamic equilibrium, which leads to similar crystals in all this range of T_{iso}. Indeed, in this range of temperatures, longer waiting time between the two temperatures ramps does not affect this final melting point T_{m}. Moreover, as discussed with Figure 5.7, the crystallization rate of the HS is too fast compared to the necessary time for the whole chains to diffuse and better organize, so that the formation of much more perfect crystal (with T_m above 140 °C) is prevented. Therefore, the equilibrium state of such a crystal corresponds to the best crystallites which can be built, knowing that the driving force for crystallization is high and that the HS can only diffuse locally. This leads to crystallites with moderately high melting point.

Above this temperature, the large mobility of the chains (T= T_g+160 °C) allows them to disentangle and diffuse in larger length scale, and the crystallites are characterized by a higher melting point (i.e. the one visible in conventional DSC, Figure 5.2, due to low cooling rate), but they are only present a small proportion (see section 5.3.3). It is also observed that waiting longer time at T_{iso} does not influence their melting point, while the proportion of crystals increases (see Figure 5.8).

The second observation (ii), already commented in section 5.3.2, highlights an important point. While it is clear that 2s are enough for stable crystallites to form in a broad range of T_{iso}, the reduction of the mobility caused by the latter and by the low temperature limits the subsequent formation of metastable baby-ribbons, explaining the drop of T_{sh}.

The third observation (iii) confirms that the ‘baby-ribbons’ associated to the secondary melting peak are non-equilibrated structures. Indeed, the higher melting point measured for a longer time at T_{iso} confirms their growing nature possibly leading subsequently to a merging with a larger crystallite.

5.3.5 Impact of the HS fraction in the chain

In this last part, we propose to investigate a parameter playing a crucial role on the crystallites structure: the HS content, i.e. the number of T4T groups along the TPE chains. As already shown from SAXS and rheology measurements,[17,45] this parameter is responsible for a drastic change on the crystallite size, which should strongly impact the thermo-mechanical properties (e.g. modulus and melting point) of the samples.

In Figure 5.11, we investigate the influence of HS content on the evolution of the melting temperatures T_m and T_{sh}. Figure 5.11a reveals that while the melting point (T_m) is lower for 10%HS sample than for the 20%HS sample due to the formation of smaller stable crystallites,[38] the melting temperature associated to the 'baby-ribbons', T_{sh} remains unchanged. This observation suggests that similar metastable crystals are created in both samples, their growth being limited by the same mechanisms, related to the local dynamics of the molecular segments (trapped between two associated HS) and their ability of the free HS to explore their surroundings. In both samples, it is observed that longer waiting times leads to higher values of T_{sh}, as already discussed.

When t_{iso} is increased from 2s to 60s (see Figure 5.11b), a significant increase of the melting point (T_m) from 113 till 139 °C is observed for 10%HS sample, while it stays constant for the 20%HS sample. This means that the crystallization rate of the 10%HS sample is too slow to allow the T4T crystallites to reach their critical size (or thermodynamic equilibrium) after 2s. Thus, the formation of larger and stronger ribbons requires longer waiting time t_{iso}. On the contrary, for the 20%HS sample, the crystallites formed during the isothermal break have time to reach their critical size after 2s and will not grow further by waiting 60s (see Figure 5.11 and related discussion).

As already observed with the 20%HS sample, high melting temperatures T_m can be obtained if the sample is brought to isothermal temperatures just below T_c (=104 °C for 10%HS via. conventional DSC see table 1), temperature at which the chains have time to diffuse before starting to crystallize. However, since the crystallization rate of the

10%HS sample is significantly lower than the one of 20%HS sample, such crystals do not have time to be formed if the break at T_{iso} is too short (see Figure 5.11a, with a 2s break), and only CC crystals are observed. Therefore, longer waiting time must be considered (such as 60s, see Figure 5.11b) to allow these very stable crystals to grow.

Therefore, the melting temperatures corresponding to T_{iso} between 40 °C and 60 °C are not reported on Figure 5.11b. Indeed, in this range of temperature, both the melting peak and the secondary melting peak are merging, and one cannot easily then determine their respective temperatures (see SI section S6).

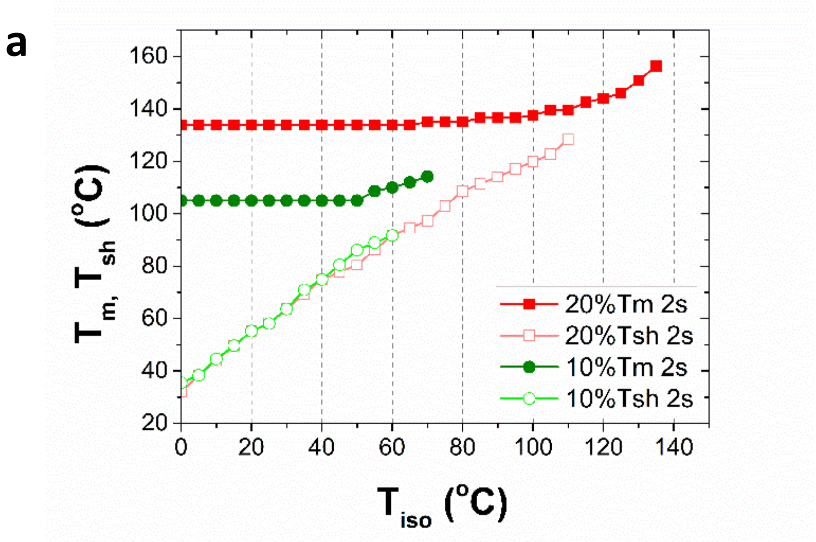

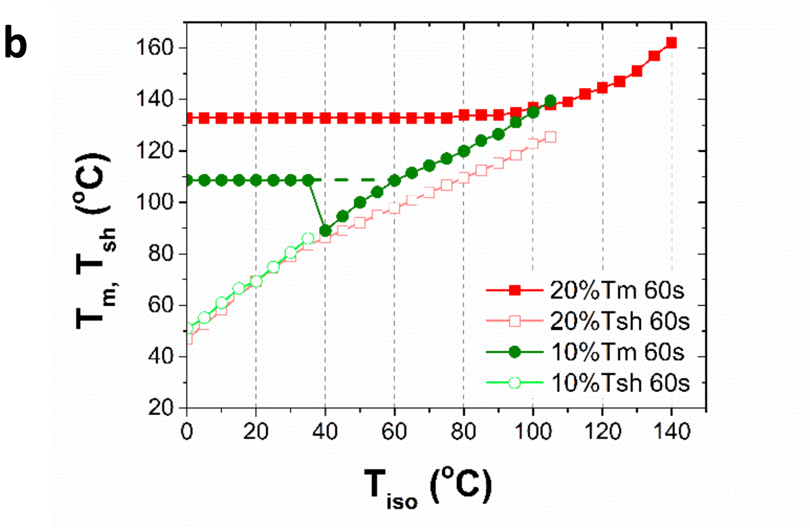

Figure 5.11: Melting temperature (T_m) and secondary peak melting temperature (T_{sh}) for 10 and 20%HS TPE as a function of isothermal temperature for a waiting time of 2s (a) and 60s (b).

To summarize the above observations, we compare in Figure 5.12 the crystallization rates of the 10%HS and 20%HS samples, in function of their isothermal temperature. The crystallization rates have been extracted according to the method developed by Vander Poel[33] (also see SI section 3 and 4). For the 20%HS sample, a bimodal distribution of crystallization rate is observed, with two maxima located at 86 °C and 36 °C, while the 10%HS only show one maximum, located at around 25 °C. These maxima are unambiguously related to the crystallization of the T4T units, arising from the balance between the thermodynamically-driven crystallization forces and the chains mobility. In case of the 20%HS sample, the maximum located at high T can easily be explained, based on the discussion in sections 5.3.3 and 5.3.4. Starting from high T_{iso}, as expected from Turnbull-Fisher description,[23] the crystallization rate increases as the thermodynamic driving force for nucleation increases due to supercooling of sample.[36] Consequently, as long as thermodynamic forces dominate, the crystallites are growing faster and faster with decreasing T_{iso}. However, decreasing T_{iso} further, thermodynamic effect is counterbalanced by the reduced intrinsic chain mobility, which slows down the crystals formation.[42] Therefore, because of these two mechanisms, there is an optimum temperature, 86 °C, at which the crystallization rate is maximum.

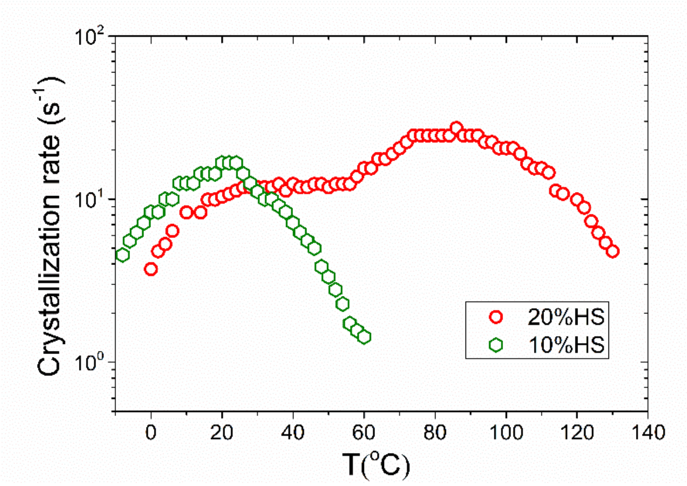

Figure 5.12: Crystallization rate as a function of temperature T_{iso}, for 10 and 20% HS samples.

Below this maximum temperature, weaker crystals are formed, all characterized by a similar melting temperature (see Figure 5.11a) and a significant reduction of the crystallites formation rate is observed.

Then, at around 55°C, the crystallization rate of the 20%HS sample stops to decrease and reaches a quasi-plateau before falling again at 20°C, generating the second maximum. While its origin is not fully clear, such bimodal distribution was already observed for PBT and other polymers in literature.[33] In ref. 43, it was attributed to the possible formation of an amorphous-rigid fraction or due to change of the crystal structure and dimensions.[28,40,41,42] In the present case, we propose the following picture to explain this behavior: At around T_{iso} = 55°C, the large-scale diffusion of the chains is becoming so slow that it does not take place anymore. However, locally, the molecular segments (for example, trapped between two consecutive entanglements or two associated HS) still have a large mobility and can easily explore their (close) surrounding and crystallize into less perfect crystal structure i.e. baby-ribbon. Therefore, combined with a high driving force for crystallization, the corresponding rate is constant as long as local mobility is not affected by temperature, and the ribbons obtained are all characterized by exactly the same melting peak and melting temperature, T_m (see Figure S5c of SI). Moreover, the decrease of the crystallization rate is then observed below 20°C, when local mobility of the entangled segments starts to be affected, and it disappears at T_{iso} <0°C, reaching its T_g value. Basically, one can depict the bimodal clock-curve as a sum of two separate clock-curves: one for the ribbon like crystals, the other imperfect crystals due to decreased chain mobility. If we refer to the work of Androsch et al.[45], these different types of crystal could be attributed to a change in the nucleation mechanism, this last one depending on the chain mobility.

On the other hand, in case of the 10%HS sample, only one maximum is observed in the crystallization rate curve. This is attributed to its much lower melting temperature: above 60 °C, the chain mobility competes with the attractive forces for crystallization, which is too low in comparison to chain mobility. The crystallization rate only increases at lower temperature, when the chains diffusion is becoming slow enough. So, in the case of 10%HS only one type of ribbon like crystal can be formed. To proof this concept, real time FSC combined with X-ray should be performed.[46,47]

To conclude this part, according to the proposed picture, bimodal distribution of the crystallization rates can be observed if both temperature at which crystallization starts and temperature at which the global diffusion of the chains is suppressed (due to chain entanglements or chain segments trapped between associated HS) are much higher than the temperature at which the segmental dynamics is slowed down. Since the mobility of the chains strongly depends on their length and on the average number of HS they contain, we expect that the position of the high temperature peak could be varied with the sample composition, which will be tested in a future work.

5.4 Summary

To summarize, by using FSC, we have shown in this work the great variety of phases likely to exist in well-defined TPEs. By exploring different thermal manipulations, we have demonstrated that different structures, i.e. different properties, were reachable, being potentially of a great interest for the industry. We have shown on one side that a progressive cooling step was allowing the crystallites to grow in a rather homogeneous way from nucleation points, whereas on the other side, a sudden quenching between T_m and T_g was leading to amorphous HS or a high fraction of smaller and metastable baby-ribbons depending on the isothermal temperature. While in the former case stronger mechanical properties are expected, the latter one is more likely to provide the material higher electrical permittivity confirming the great polyvalence of such polymers in terms of applications (fibres, electrolytes…). From a more fundamental point of view, we have been able to accurately quantify the minimal cooling rate allowing to keep the TPE 20%HS amorphous when quenched from the melt state being -800 C.s^{-1}. This extreme value appears as a strong asset for this chemistry since it allows the hard network formation and thus the material elasticity emerging in a quasi-instantaneous way. We also showed, how playing with the temperature for these TPEs allow controlling the influence of chain mobility, both at the level of the whole chains and at a more local level, in the formation of stable ribbons.

5.5 References

1) Holden, G.; Legge, N. R.; Quirk, R. P.; Schroeder, H. E., Thermoplastic Elastomers. Hanser Publisher: Munich, 1996.

2) Serrano, P. J. M.; van de Werff, B. A.; Gaymans, R. J., Alternating polyesteramides based on 1,4-butylene terephthalamide: 3. Alternating polyesteramides based on mixtures of linear diols (4NTm,p). Polymer 1998, 39 (1), 83-92.

3) Leibler, L., Theory of microphase separation in block copolymers. Macromolecules 1980, 13 (6), 1602-1617.

4) Vinogradov, G.; Dreval, V.; Malkin, A. Y.; Yanovsky, Y. G.; Barancheeva, V.; Borisenkova, E.; Zabugina, M.; Plotnikova, E.; Sabsai, O. Y., Viscoelastic Properties of Butadiene-Styrene Block Copolymers. Rheologica Acta 1978, 17 (3), 258-263.

5) Eisenbach, C. D.; Baumgartner, M.; Günter, C., Polyurethane Elastomers with Monodisperse Segments and their Model Precursors: Synthesis and Properties. In Advances in Elastomers and Rubber Elasticity, Lal, J.; Mark, J. E., Eds. Springer US: Boston, MA, 1986; pp 51-87.

6) Stribeck, N.; Fakirov, S.; Apostolov, A. A.; Denchev, Z.; Gehrke, R., Deformation Behavior of PET, PBT and PBT-Based Thermoplastic Elastomers as Revealed by SAXS from Synchrotron. Macromol Chem Physic 2003, 204 (7), 1000-1013.

7) Gabriëlse, W.; Soliman, M.; Dijkstra, K., Microstructure and Phase Behavior of Block Copoly(ether ester) Thermoplastic Elastomers. Macromolecules 2001, 34 (6), 1685-1693.

8) Van der Schuur, M.; Gaymans, R. J., Segmented Block Copolymers Based on Poly(Propylene Oxide) and Monodisperse Polyamide-6,T Segments. Journal of Polymer Science Part A: Polymer Chemistry 2006, 44 (16), 4769-4781.

9) Niesten, M. C. E. J.; Feijen, J.; Gaymans, R. J., Synthesis and properties of segmented copolymers having aramid units of uniform length. Polymer 2000, 41 (24), 8487-8500.

10) Van Hutten, P.; Mangnus, R.; Gaymans, R., Segmented copolymers with polyesteramide units of uniform length: structure analysis. Polymer 1993, 34 (20), 4193-4202.

11) Chapman, A. V.; Porter, M., Sulphur Vulcanization Chemistry. In Natural Rubber Science and Technology, Roberts, A. D., Ed. Oxford University Press: New York, 1988; p 516.

12) Arun, A.; Dullaert, K.; Gaymans, R. J., The melt rheological behavior of AB, ABA, BAB, and (AB)n block copolymers with monodisperse aramide segments. Polymer Engineering & Science 2010, 50 (4), 756-761.

13) Appel, W. P. J.; Portale, G.; Wisse, E.; Dankers, P. Y. W.; Meijer, E. W., Aggregation of Ureido-Pyrimidinone Supramolecular Thermoplastic Elastomers into Nanofibers: A Kinetic Analysis. Macromolecules 2011, 44 (17), 6776-6784.

14) Miller, J. A.; Lin, S. B.; Hwang, K. K. S.; Wu, K. S.; Gibson, P. E.; Cooper, S. L., Properties of Polyether-Polyurethane Block Copolymers: Effects of Hard Segment Length Distribution. Macromolecules 1985, 18 (1), 32-44.

15) Gaymans, R.; De Haan, J., Segmented copolymers with poly (ester amide) units of uniform length: synthesis. Polymer 1993, 34 (20), 4360-4364.

16) Biemond, G. J. E.; Feijen, J.; Gaymans, R. J., Poly(Ether Amide) Segmented Block Copolymers with Adipic Acid based Tetraamide Segments. J Appl Polym Sci 2007, 105 (2), 951-963.

17) Baeza, G. P.; Sharma, A.; Louhichi, A.; Imperiali, L.; Appel, W. P. J.; Fitié, C. F. C.; Lettinga, M. P.; Van Ruymbeke, E.; Vlassopoulos, D., Multiscale Organization of Thermoplastic Elastomers With Varying Content of Hard Segments. Polymer 2016, 107, 89-101.

18) Sijbrandi, N. J.; Kimenai, A. J.; Mes, E. P. C.; Broos, R.; Bar, G.; Rosenthal, M.; Odarchenko, Y.; Ivanov, D. A.; Dijkstra, P. J.; Feijen, J., Synthesis, Morphology, and Properties of Segmented Poly(ether amide)s with Uniform Oxalamide-Based Hard Segments. Macromolecules 2012, 45 (9), 3948-3961.

19) Gaymans, R. J., Segmented Copolymers With Monodisperse Crystallizable Hard Segments: Novel Semi-Crystalline Materials. Prog Polym Sci 2011, 36 (6), 713-748.

20) Biemond, G. J. E.; Feijen, J.; Gaymans, R. J., Influence of Polydispersity of Crystallizable Segments on the Properties of Segmented Block Copolymers. Polym Eng Sci 2008, 48 (7), 1389-1400.

21) Hobbs, S.; Pratt, C., Multiple melting in poly (butylene terephthalate). Polymer 1975, 16 (6), 462-464.

22) Nichols, M. E.; Robertson, R. E., The origin of multiple melting endotherms in the thermal analysis of polymers. Journal of Polymer Science Part B: Polymer Physics 1992, 30 (3), 305-307.

23) Van Bennekom, A.; Gaymans, R., Amide modified polybutylene terephthalate: structure and properties. Polymer 1997, 38 (3), 657-665.

24) Serrano, P. J. M., A. C. M. Van Bennekom, and R. J. Gaymans. "Alternating polyesteramides based on 1, 4-butylene terephthalamide: 1. Synthesis of the bisesterdiamide." Polymer 39.23 (1998): 5773-5780.

25) Aharoni, S. M., Hydrogen-bonded highly regular strictly alternating aliphatic-aromatic liquid-crystalline poly (ester amides). Macromolecules 1988, 21 (7), 1941-1961.

26) Mathot, V.; Pyda, M.; Pijpers, T.; Vanden Poel, G.; van de Kerkhof, E.; van Herwaarden, S.; van Herwaarden, F.; Leenaers, A., The Flash DSC 1, a power compensation twin-type, chip-based fast scanning calorimeter (FSC): First findings on polymers. Thermochimica Acta 2011, 522 (1–2), 36-45.

27) Chen, Y.; Chen, X.; Zhou, D.; Shen, Q.-D.; Hu, W., Low-temperature crystallization of P (VDF-TrFE-CFE) studied by Flash DSC. Polymer 2016, 84, 319-327.

28) Silvestre, C.; Cimmino, S.; Duraccio, D.; Schick, C., Isothermal Crystallization of Isotactic Poly(propylene) Studied by Superfast Calorimetry. Macromolecular Rapid Communications 2007, 28 (7), 875-881.

29) Schick, Christoph, and Vincent Mathot, eds. Fast scanning calorimetry. Vol. 1680. Switzerland: Springer, 2016.
30) Mathot, Vincent, et al. "The Flash DSC 1, a power compensation twin-type, chip-based fast scanning calorimeter (FSC): first findings on polymers." Thermochimica Acta 522.1-2 (2011): 36-45.
31) Zhuravlev, E., and C. Schick. "Fast scanning power compensated differential scanning nano-calorimeter: 1. The device." Thermochimica Acta 505.1-2 (2010): 1-13.
32) Poel, Geert Vanden, et al. "Performance and calibration of the Flash DSC 1, a new, MEMS-based fast scanning calorimeter." Journal of thermal analysis and calorimetry 110.3 (2012): 1533-1546.
33) Schick, Christoph, and Vincent Mathot. Fast Scanning Calorimetry. Springer, 2016., chapter 18 (pp. 611-632).
34) Poel, G. V., et al. "Recommendation for temperature calibration of fast scanning calorimeters (FsCs) for sample mass and scan rate." Beuth Verlag GmbH, Berlin Adam Metal (2014) In vivo and in vitro investigations of a nanostructured coating material—a preclinical study. Int J Nanomedicine 9.1 (2011): 975-984.
35) Schick, Christoph, and Vincent Mathot. Fast Scanning Calorimetry. Springer, 2016., chapter 1 (pp. 3-80).
36) McCrum, Norman Gerard, et al. Principles of polymer engineering. Oxford University Press, USA, 1997.
37) Zhuravlev, Evgeny, et al. "Experimental test of Tammann's nuclei development approach in crystallization of macromolecules." International Polymer Processing 31.5 (2016): 628-637.
38) Flory, Paul J. "Theory of crystallization in copolymers." Transactions of the Faraday Society 51 (1955): 848-857.
39) Niesten, M. C. E. J., and R. J. Gaymans. "Comparison of properties of segmented copolyetheresteramides containing uniform aramid segments with commercial segmented copolymers." Journal of applied polymer science 81.6 (2001): 1372-1381.

40) Mileva, D.; Androsch, R., Effect of co-unit type in random propylene copolymers on the kinetics of mesophase formation and crystallization. Colloid Polym Sci 2012, 290 (5), 465-471.
41) Zhuravlev, E.; Schmelzer, J. W. P.; Wunderlich, B.; Schick, C., Kinetics of nucleation and crystallization in poly(ε-caprolactone) (PCL). Polymer 2011, 52 (9), 1983-1997.
42) Höhne, G. W. H. "Another approach to the Gibbs–Thomson equation and the melting point of polymers and oligomers." Polymer 43.17 (2002): 4689-4698.
43) Pyda, M., et al. "Melting and crystallization of poly (butylene terephthalate) by temperature-modulated and superfast calorimetry." Journal of Polymer Science Part B: Polymer Physics 44.9 (2006): 1364-1377.
44) Odarchenko, Yaroslav I., et al. "Primary Chemical Sequence Ultimately Determines Crystal Thickness in Segmented All-Aliphatic Copolymers." Macromolecules 47.22 (2014): 7890-7899.
45) Baeza, Guilhem P. "The Reinforcement Effect in Well-Defined Segmented Copolymers: Counting the Topological Constraints at the Mesoscopic Scale." Macromolecules 51.5 (2018): 1957-1966.
46) Jariyavidyanont, Katalee, René Androsch, and Christoph Schick. "Crystal reorganization of poly (butylene terephthalate)." Polymer 124 (2017): 274-283.
47) van Drongelen, Martin, et al. "Microfocus wide-angle X-ray scattering of polymers crystallized in a fast scanning chip calorimeter." Thermochimica acta 563 (2013): 33-37.
48) Baeten, Dorien, et al. "Simultaneous synchrotron WAXD and fast scanning (Chip) calorimetry: on the (isothermal) crystallization of HDPE and PA11 at high supercoolings and cooling rates up to 200 C s− 1." Macromolecular rapid communications 36.12 (2015): 1184-1191.

5.6 Appendix (Supporting information, chapter-5)

1) Following measurements shows the stability of sample mass during the FSC measurement of 10%HS sample -

In supporting Figure S1a, we show 10%HS sample at T_{iso} 110 ºC i.e. above T_c for varies isothermal time from 2 sec to 10 min. Again, supporting Figure S1b shows, 10%HS sample isothermally hold at 110 ºC, where by thermogram A and B represents the initial (taken from supporting Figure S1a) and final measurement. The overlap is the sign of reproducibility for two measurement showing stability of sample mass, good inert atmosphere during measurements of the sample.

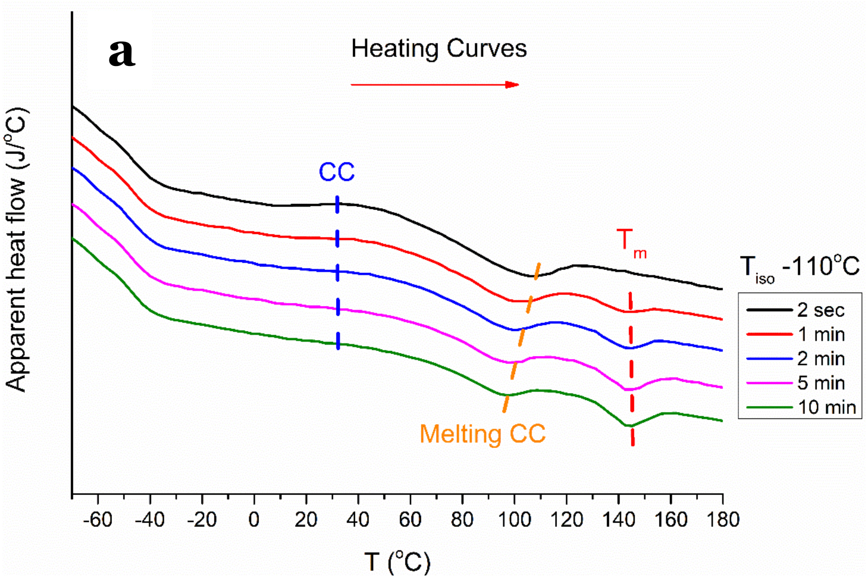

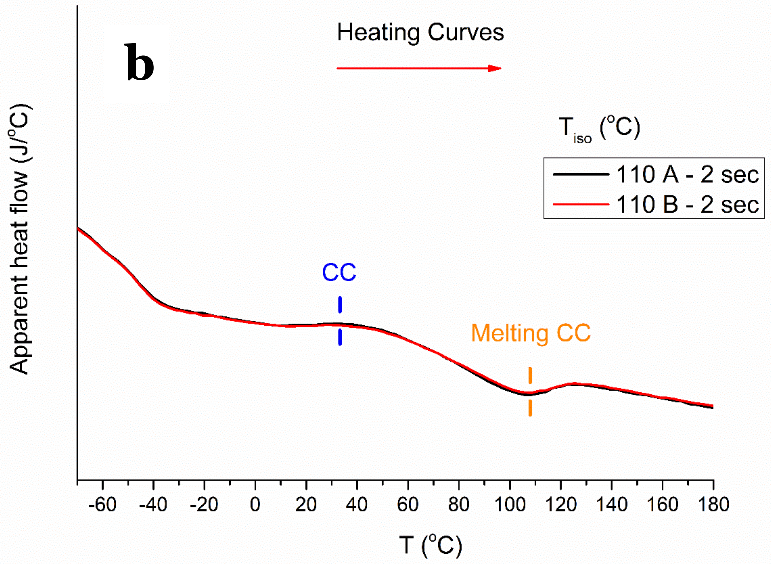

Figure S1: a) Heating curves for 10%HS sample for T_{iso}110 °C at different T_{iso} holding time. b) Heating curves for 10%HS sample for T_{iso} 110 °C, A) done initially B) done after completing the measurements to check the reproducibility.

2) Melting temperature as a function of cooling rate 20%HS -

Following supplementary Figure S2, shows the monotonic increase in melting temperature for 20%HS sample as cooling rate is decreased from 4000 to 10 °C.s^{-1}. Decrease in the melting temperature signifies the kind of morphology or structure formed during the cooling. Highest melting point observed when sample is cooled with the rate of 10 °C.s^{-1} indicating the formation of stable T4T crystals. As cooling rate is increased melting point decreases and forms the amorphous domain at 4000 °C.s^{-1}.

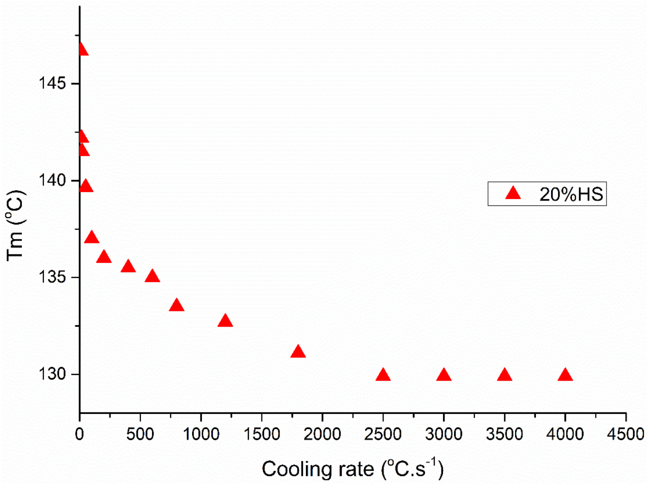

Figure S2: Melting temperature for 20%HS TPE as a function of cooling rate.

3) Crystallization kinetics for 20%HS TPE sample -

Supplementary Figure S3, show the exothermal peaks for 20%HS from 135 °C to -10 °C as a function of time. The maximum of crystallization peak time was used to obtain the crystallization kinetics plot (shown in red line).

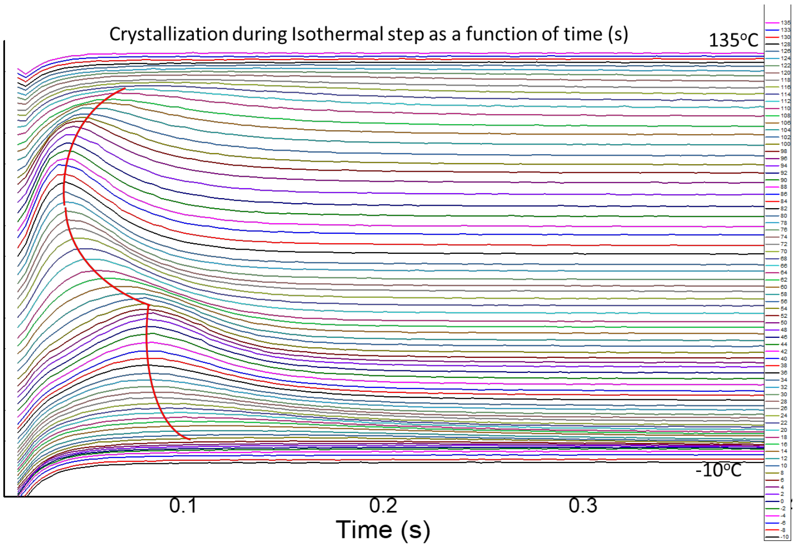

Figure S3: Isothermal curves from 135 to -10 ºC for 20%HS sample as a function of isothermal holding time.

4) Crystallization kinetics for 10%HS TPE sample -

Supplementary Figure S4, show the exothermal peaks for 10%HS from 60 ºC to 0 ºC as a function of time. The maximum of crystallization peak time was used to obtain the crystallization kinetics plot (shown in red line).

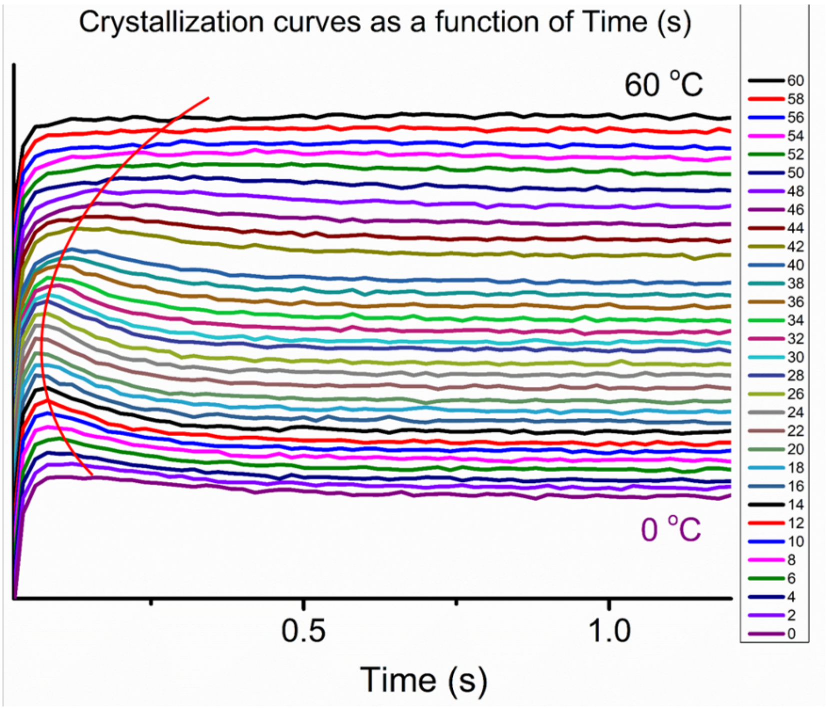

Figure S4: Isothermal curves from 60 to 0 ºC for 10%HS sample as a function of isothermal holding time.

5) Isothermal crystallization (T_g to T_m) of 20%HS TPE -

Following Figure S5 a, b, c, d and e shows the heating curves for the isothermal steps from T_g to T_m during cooling. The data is plotted as measured in FSC instrument, without shifting, to show the various phenomena taking place over entire range of temperature.

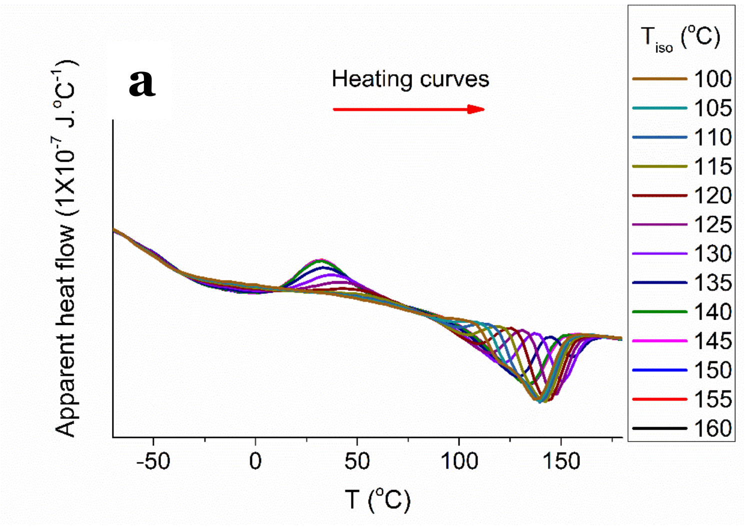
a
Heating curves
Apparent heat flow (1X10^{-7} J.°C^{-1})
T (°C)
-50
0
50
100
150
T$_{iso}$ (°C)
100
105
110
115
120
125
130
135
140
145
150
155
160

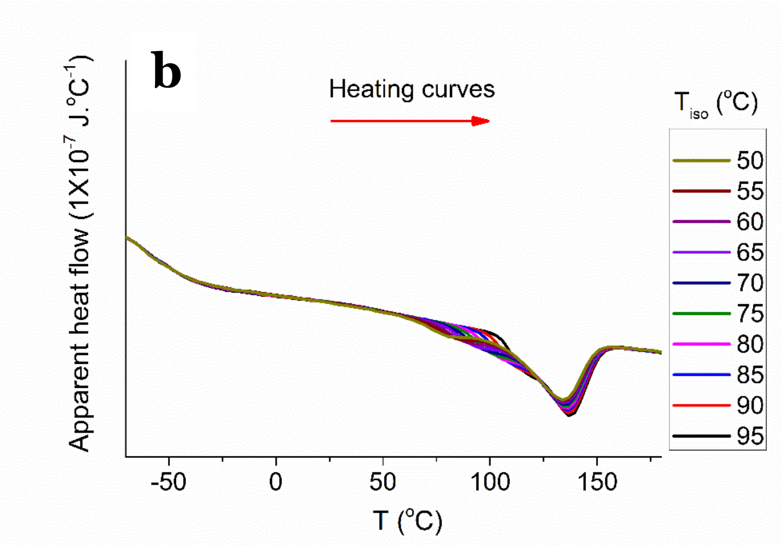
b
Heating curves
Apparent heat flow (1X10^{-7} J.°C^{-1})
T (°C)
-50
0
50
100
150
T$_{iso}$ (°C)
50
55
60
65
70
75
80
85
90
95

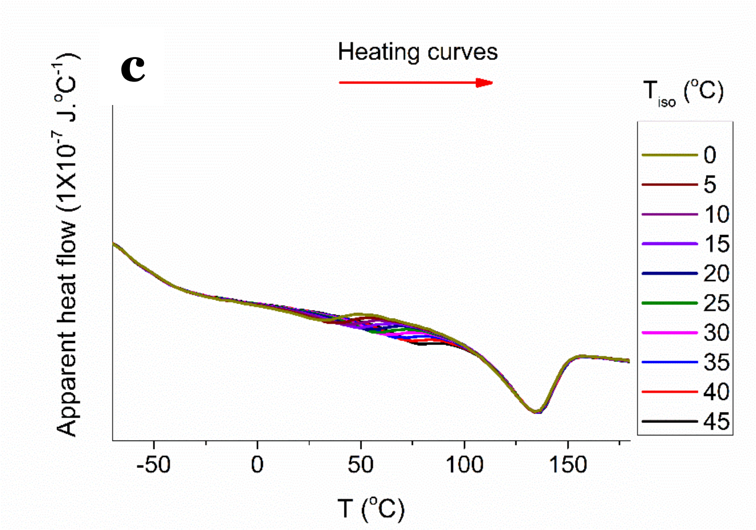
c
Heating curves
T_{iso} (°C)
0
5
10
15
20
25
30
35
40
45
Apparent heat flow (1X10^{-7} J.°C^{-1})
-50
0
50
100
150
T (°C)

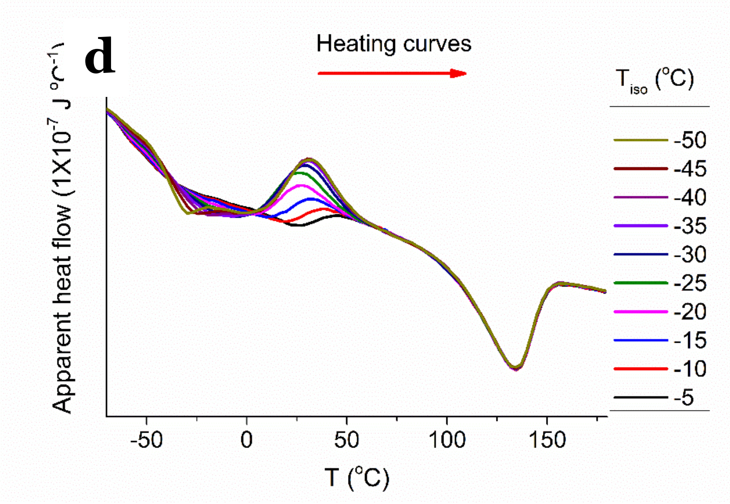
d
Heating curves
T_{iso} (°C)
-50
-45
-40
-35
-30
-25
-20
-15
-10
-5
Apparent heat flow (1X10^{-7} J °C^{-1})
-50
0
50
100
150
T (°C)

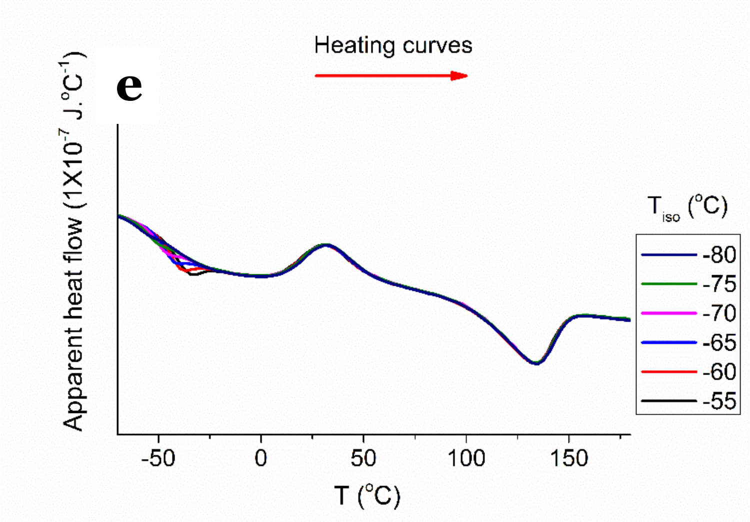

Figure S5: Heating curves for 20%HS sample, isothermally crystallized during cooling from T_g to T_m a) represents isothermal temperature range from 160 to 100 °C. b) isothermal temperature range from 95 to 50 °C. c) isothermal temperature range from 45 to 0 °C. d) isothermal temperature range from 0 to -50 °C. e) isothermal temperature range from -55 to -80 °C.

6) Melting temperature (T_m) and shoulder melting temperature (T_{sh}) for 10%HS TPE at different T_{iso} for 2s and 60s -

In Figure S6, starting from the T_{iso} 50 °C for 10%HS at 2s, T_{sh} and T_m are observed at 85 °C and 105 °C. Whereas at 60s, only T_m is observed, which is well pronounced at 100 °C merging the T_{sh} and T_m as a result of chain mobility. Following the trend at T_{iso} 40 °C again T_m is observed showing same melting point but T_{sh} is found to be shifted to lower temperature in comparison to T_{iso} 50 °C for 2s. But interestingly, at T_{iso} 40 °C for 60s, broad melting peak is observed which is again merged with T_{sh}. It can be further established with the decrease in the melting point as compared to T_{iso} 50 °C for 2 and 60s. Interestingly at T_{iso} 30 °C, again we observe the separation of T_m and

T_{sh} for 2 and 60s. At T_{iso} 30 °C, T_m shows again the high melting point same as observed for T_{iso} 50 °C for 2s and T_{sh} shifting towards the lower temperature. Due to this merging of the peaks for 60s it is difficult to distinguish between T_{sh} and T_m and therefore it is denoted by green dash line.

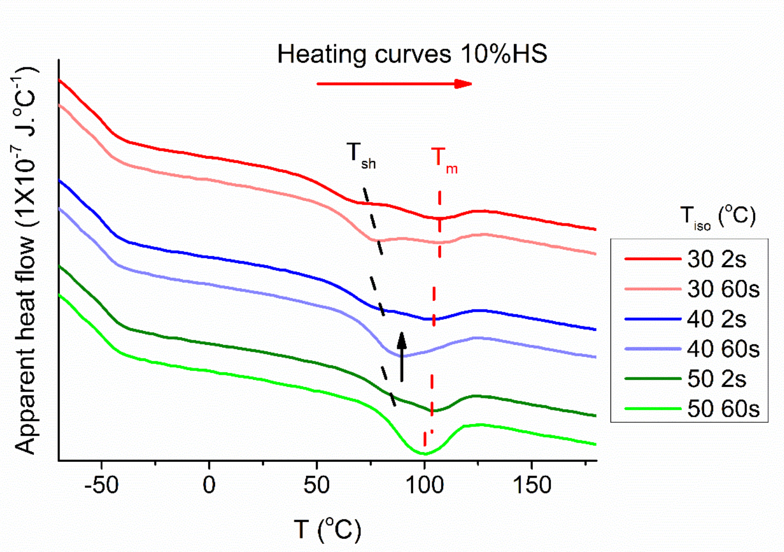

Figure S6: Heating curves for 10%HS sample for T_{iso} 50 to 30 °C at different T_{iso} holding time i.e. 2 and 60s

7) AFM 20%HS TPE –

Figure S7, shows the height sensor AFM images as a supporting information for the Figure 5.5 a and b of the chapter. The surface of the 20%HS film along with the substrate seems to quite uniform especially for quenched sample as the sample remains amorphous. Whereas the progressively cooled surface shows quite rough surface in terms of height, which signifies the crystalline nature of the sample.

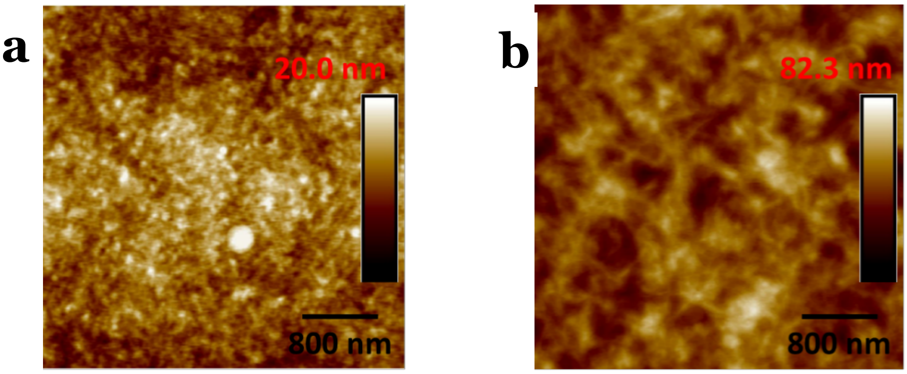

Cooled at > 800 °C.s^{-1}

Cooled at 6 °C.min^{-1}

Figure S7: Height sensor images of 20%HS sample a) Cooled at > 800 °C.s^{-1}, b) Cooled at 6 °C.min.

Chapter 6: Tunable viscoelasticity of well-defined entangled segmented copolymers: effects of temperature, time and shear flow

Abstract

In order to obtain a fundamental link between molecular structure and properties of thermoplastic elastomers (TPEs), we present a systematic investigation of the shear rheological properties of segmented copolymers made of terephthalate-based diamide (T4T) HSs and soft (poly(tetramethylene oxide)) units as functions of time, frequency and strain amplitude over a broad temperature range. Data are interpreted with the help of a newly developed statistical approach, in order to determine the influence of both the entanglements and the associated HSs on the samples modulus. Small amplitude oscillatory shear (SAOS) tests show unambiguously that on increasing the fraction of HSs from 5 wt% to 20 wt% the crystallization rate is accelerated and the hard domains are becoming stronger resulting in reinforcement of the polymer matrix with increased elastic modulus (from 2 to 10 MPa) and melting point (from 90 °C to 160 °C). In addition, at intermediate temperatures, between crystallization and melting temperatures, cyclic large amplitude oscillatory shear (LAOS) measurements show that the fast association tendency of HSs, i.e. the crystallite expansion, competes with the diffusion of the overall chains, resulting in a metastable state with unexpected viscoelastic properties. The investigation of the effect of strain amplitude and temperature on these properties suggests a partial loss of effective entanglements under flow below the melting temperature. Thus, controlling the competition

between HSs association and chain entanglements a key point for tuning the properties of this class of materials at wish.

6.1 Introduction

Thermoplastic elastomers (TPEs) based on segmented block copolymers, are characterized by a two-phase morphology, comprising a soft phase with a low glass transition temperature (T_g), and a hard phase with a high T_g.[1] Between these two transition temperatures, micro-phase separation occurs, giving rise to equilibrium morphologies, which are often characterized by long-range order.[2] The HS, forming either a glassy or a crystalline phase, can then be thought of as physical cross-linkers for the soft blocks, leading to the creation of a physical network. As largely studied in literature[2-12], micro-phase separation is strongly influenced by parameters such as the volume fraction of HSs[7], the Flory-Huggins interaction parameter[8] and the total degree of polymerization.[9] Depending on these parameters, different micro-structures can be obtained, as for example lamellar, cubic or cylindrical phases.[10--17]

In this work, we would like to focus on a special type of TPEs with uniform, monodisperse, crystallizable amide HSs. With such systems, crystallization occurs very fast, through association of the HSs via hydrogen bonding between the amide groups.[18-20] This forces the crystals to rapidly grow in the H bonding direction, which leads to the creation of ribbon-like crystals immersed in a soft-segment matrix.[18-24] The crystallization rate is further increased if monodisperse short HSs are used, favoring the formation of regular crystallite with enhanced association strength. In such a case, crystallites with a very high aspect ratio are formed, characterized by a uniform thickness determined by the HSs length, and a relatively short width which depends on the ability of the chains to bond via van der Waals interactions[19] or pi-pi stacking.[1,19,25] These long uniform ribbons lead to improved mechanical properties, high critical stress at fracture and high melting temperature,

T_m .[18] Furthermore, due to their growth process, they do not form large structures such as spherulitic structures[1], and are usually transparent. Thus, by combining superb mechanical properties, good processability and the ability to be re-used, this class of materials offers a large potential for developing new applications.[18] This explains the large number of studies proposed in the literature, which focus on their elastic moduli and yielding characteristics as functions of composition.[1,18,26-29] For example, it has been shown that under small strains, the reinforcing effect of the HS crystallites can be understood by making an analogy of TPEs to composites made of independent fibers in a polymer matrix[1], i.e. considering that the modulus mainly depends on the concentration and aspect ratio of the fibers. However, at high strains, the yielding and morphological change of the crystallites cannot be explained with such a picture. Indeed, the sample properties will be largely dictated by the ability of the hard phase to resist large strain as well as by the way the broken ribbon-like crystallites will be able to re-organize.[9,19,30,31] Therefore, all parameters which are influencing the strength and deformability of the crystallites, such as the concentration and structure of the crystallites, the nature and density of the HSs, the length of the copolymers, or the temperature, will play a key role[1] and it is important to understand how they can be tuned in order to control the rupture and flow properties of the TPEs. A way to rationalize their effect is to discuss their influence in term of 1) the association strength of the HSs, 2) mobility of the chains and 3) network connectivity, since these three features directly influence the melting properties of the segmented copolymers:

Association strength of the HSs: Obviously, TPEs containing HSs with large association strength will better resist straining. This is the strategy which has been followed by selecting TPEs with well-defined, *monodisperse* and rather short HSs, able to interact via hydrogen bonding.[26, 31-33] Indeed, it has been observed that in addition to lead to very well-defined structures, these TPEs exhibit stronger resistance to strain, compared to segmented copolymers containing HSs of various sizes. Furthermore, their nearly complete phase separation process (characterized by the virtual absence of non-crystallized HSs in the soft phase) ensures the softness, deformability and low T_g of the soft phase, concomitant with a sharper melting transition of the hard phase.[27,29,34] This general strategy of mechanical reinforcement by means of directed bonding interactions has been used in several works with diverse systems ranging from TPEs to nanocomposites.[1,19,26,33,35]

As already mentioned, the HSs association strength also strongly depends on temperature.[18,36] At low T, larger association strength is observed, which enhances the creation of larger crystallites characterized by high melting temperature. This was shown, for example, in ref.[37], where the crystallinity of TPEs based on PTMO (poly(tetramethylene oxide)) SSs and monodisperse T6A6T (biester-tetra-amide) HSs was different upon heating or cooling the sample, exhibiting large hysteresis effects with consequences on the final properties.

Besides the HSs nature and the temperature, another important parameter in order to control the association strength of the HSs is their density. Indeed, it has been observed that increasing the length of the SS, i.e. reducing the HSs density, results in a systematic decrease of the flow temperature and storage modulus of the copolymers.[18, 25, 29] This effect, which is generally observed for segmented copolymers, is explained by the solvent effect proposed by Flory.[38] By decreasing the density of HSs, the average size of the crystal is becoming smaller, and these last ones melt more easily.[29, 39-41] The HS crystallization with long SSs was also found to develop much more slowly[39], compared to their crystallization at higher HS density.

***The mobility of the chains and sample equilibration**:* The complex morphology of the segmented block copolymers is largely influenced by the chain mobility, i.e. by their ability to form equilibrated structures before being trapped into a non-equilibrated ('frozen') state. For example, it was shown in refs.[42-44] that TPEs based on polyurethane HSs formed films of lamellar crystallites when annealed from solution, while they create ribbon-like structures when prepared in the melt state. This suggests that while in both situations crystals grow very fast in the H-bonding direction, the width of their crystallites, which is due to the weaker van der Waals bonding, strongly depends on sample preparation protocol and more specifically, on the ability of the chains to create equilibrated structures before losing their mobility. Besides thermal history, the distribution of the HSs along the chains also seems to play an important role. Interestingly, it was found that a triblock copolymer with soft middle block and di-amide HSs at the chain extremities form ribbon-like structures with a larger aspect ratio, characterized by a more efficient packing of crystallites and a stronger reinforcing effect, compared to a respective multi-block segmented copolymer with similar fraction of HSs.[26] This suggests that if few HSs along the same molecule are associated, the HSs which are localized in between have a reduced mobility and cannot freely explore their surrounding anymore, in order to form stronger crystallites. A similar conclusion was drawn in our previous study based on fast scanning calorimetry data.[45]

Thus, in segmented copolymers, the chain mobility is expected to affect the formation and shape of the crystallites. We expect the latter point to be especially relevant when the copolymers form entanglements, which slow-down chain mobility considerably.[37]

Network connectivity:

As mentioned above, the modulus and linear response of the TPEs vary in function of the ability of the chains to create large and strong crystallites, which mostly depends on the nature, and density of the copolymer segments, on the average number of HSs per chain, on the entanglement state (or length) of the chain and on temperature. However, under large deformation, other parameters must also be taken into account. In particular, besides the association strength of the HSs, network connectivity plays a key role in the resistance to flow since it determines how many HSs in average must dissociate in order to observe the rupture of the sample.[36] At constant HSs density, increasing the length of the chains should, therefore, improve the resistance to flow of the TPEs, since each of them contains a larger number of associated segments as well as a larger number of entanglements, i.e. a larger number of connection points with the other chains.[36, 46] This picture was confirmed by Matsumiya et al. in ref.[47], who studied the elongational behavior of a series of symmetric styrene (S)-isoprene (I) – styrene (S) multi-block copolymers of $(SIS)_p$-type (with p=1,2,3 and 5), in a selective solvent that dissolves the I blocks and precipitates the S blocks. While under small elongation all these systems had similar rheological behavior, a remarkable difference was found under large elongation, where it was observed that the maximum stretch ratio at rupture significantly increases with the repeating number p of the SIS units. The authors attributed this observation to the fact that full percolation of the network was surviving well after the breaking of the first bonds, the material being able to stand the elongation as long as at least two PS blocks, on average, was remaining intact in each $(SIS)_p$ copolymer backbone. Obviously, the probability of having such intact S blocks is larger with a larger number of repeating units *p*. Same conclusions were also drawn in the recent work of Aime et al.[36] on TPEs similar to the ones used in the present work.

Besides the number of HSs per chain, another parameter which influences the connectivity of the network is the ratio between the association of HSs within the same chain and surrounding chains. Indeed, while intra-associations are expected to contribute to the formation of the nano-ribbons and thus, to the reinforcement of the TPEs, they will not directly contribute to the percolation properties of the network. In previous works, it was shown that this last parameter is especially important in order to explain the influence of a flow field on the spatial organization of the HSs domains, which governs the resistance of the sample to flow.[1,2,48,49] Upon specific shear or elongation condition, depending on the chain connectivity, induced parallel or perpendicular orientations of the HS domains have been observed.[3, 50-55] For example, it was shown that parallel orientation of the lamellae are usually found at high frequencies or large strain amplitudes of deformation with bi- or tri-blocks, while perpendicular orientation are generally observed with pentablocks.[3,51,55] This difference in alignment was attributed to the fact that parallel pentablock chains have a significant fraction of bridging segments and entangled looping, which are stretched under large shear, making the parallel orientation unfavorable. Consequently, the perpendicular orientation of the ribbons is favored and accompanied by the breakage of the ribbons into smaller structures.[1, 53]

However, as it was discussed in[3,53,56], under specific high shear conditions, parallel orientation can also be observed with pentablocks or heptablocks. This was attributed to the creation of slip planes via a bridge-to-unentangled loop transformation, thus allowing layer-by-layer sliding and reducing the SSs stretching. This last example shows that shear flow can cause dissociation of certain physical bonds and subsequent reformation into a different configuration. But it also illustrates the fact that LAOS-induced alignment of lamellar block copolymers at a given distance from the order-disorder transition temperature, depends in a rather complicated way on a combination of several parameters, such as temperature, frequency, strain amplitude and time.[57,58] Thus, for such systems, the exact mechanisms behind the formation of the crystallites are not fully understood, although it is established that chain entanglements, chain relaxation time and annealing conditions influence the final properties of the lamellae and are associated with their substantial thixotropic response.[59] Hence, flow can result in a complex interplay of chain alignment and intermolecular associations.[57]

It is evident from the above that, even for model segmented copolymers characterized by identical, short and monodisperse H-bonding HSs, playing with the density of HSs is not sufficient to control the material properties. The thermal history, the length of the segments and the sample preparation protocol can influence the packing and strength of the HS domains, with direct consequences on the modulus and yielding properties. In view of this background, a central question concerning segmented copolymers is how HSs density, shear flow, temperature and time affect their ultimate mechanical properties. The objective of the present work is to address this challenge by exploring the influence of these different parameters on their viscoelastic properties.

To this end, we investigate the rheological behavior of several well-defined model segmented copolymers of similar total molar mass but the different fraction of monodisperse amide-based HSs (5 - 20 wt%) and PTMO (polytetramethylene oxide) SSs. We interpret our results using the knowledge of the equilibrium structure, which has been described in ref.[25], and by developing a statistical model in order to describe the sample composition based on its synthesis. With these samples, the network connectivity is varied by playing with the HSs density, while keeping the same chain length. On the other hand, the association strength of the HSs is varied by playing with temperature and HSs density, and the chain mobility is tuned by playing with the thermal history of the samples. Their behavior under LAOS is also investigated.

The chapter is organized as follows: in Section 6.2, the materials characteristics and experimental details are given. The statistical approach is also described. In Section 6.3, the results are presented and discussed: first, we look at the chain composition and proportion of free dangling ends as functions of HSs density. We then discuss the melting temperature and transitions, the rheological data obtained in the linear regime (Section 6.3.2) and under LAOS (Section 6.3.3). Finally, the conclusions are summarized in Section 6.4.

6.2 Experimental

6.2.1 Materials

Linear segmented block copolymers of similar weight-average molar mass (M_w=42 ± 5 kg.mol^{-1}), made of SSs (PTMO) and different fraction of monodisperse hard terephthalate-based diamide (T4T) segments have been synthesized through polycondensation, as discussed in ref.[26]. Differential scanning calorimetry (DSC) measurements (at a heating/cooling rate of 15 °C.min^{-1}) for samples containing 0, 5, 10, 15 and 20 wt% HS are shown in Figure 6.1.

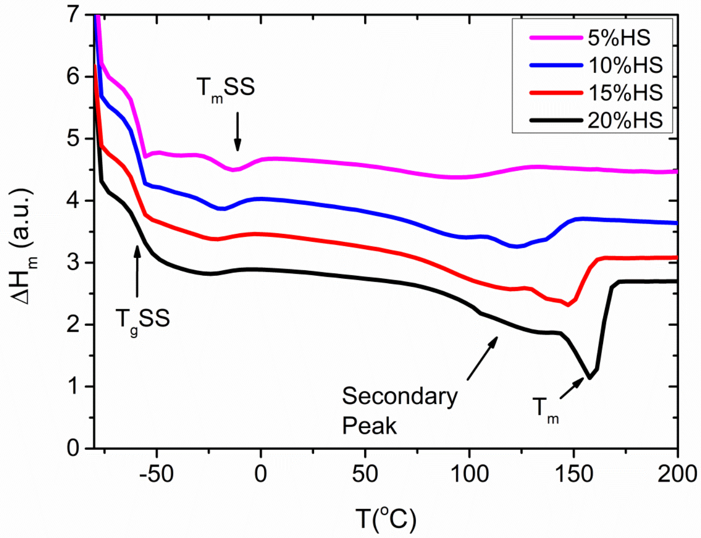

Figure 6.1: Differential scanning calorimetry (DSC) measurements at a heating rate of 15 °C.min^{-1} for samples containing 0, 5, 10, 15 and 20%HS.

Results of their physico-chemical characterization are presented in Table 1. Figure 6.2 below illustrates the basic mesoscopic structure of these TPE chains and the postulated network they form.[1] They are well-entangled since the entanglement molar mass of pure PTMO is M_e≈1.5 kg.mol^{-1}.[59]

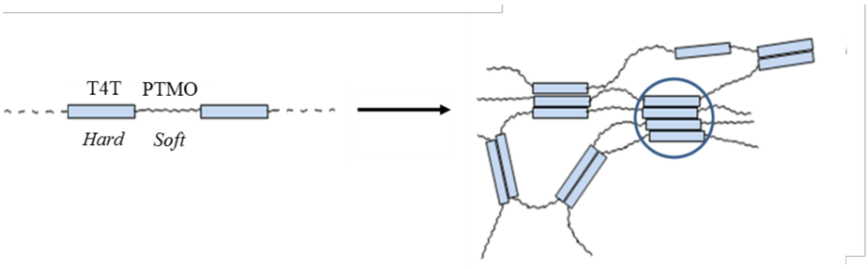

Figure 6.2: Schematic illustration of TPE chains association through crystallization of HSs.

Table 2: Physico-chemical characterization related to the TPEs studied at 15 °C.min^{-1}.

HS density (wt%)	**M_w/ M_n**	M_n(PTMO) (g.mol^{-1}) *	<N>**	T_g^{SS} (°C)	T_m (°C)	T_c (°C)	X_c*** (%)
5	2	6840	4	-59	92	65	2.6
10	2	3300	7	-59	122	100	6.3
15	2	2080	11	-58	149	120	9.3
20	2	1470	11	-58	158	136	15.8

* Average molar mass of the PTMO segments between two successive HS as calculated based on the synthesis.

** Average number of HS per chain calculated from wt% HS and M_n.

*** Crystal weight fraction from DSC (with a heating/cooling rate of 20 °C.min^{-1}) calculated via $X_c = (\Delta H_{DSC}/\Delta H_{T4T}) * 100$ where ΔH_{T4T}=150 J.g^{-1} from ref.[39]

6.2.2 Rheological measurements

The rheological measurements (dynamic frequency, strain and temperature sweeps) were performed with a stress-controlled rheometer (MCR 301 from Anton Paar, Austria) equipped with stainless steel parallel plates of diameter 8 mm. Before measuring, the samples were molten at a temperature T=180 °C (for 5% or 10% HS) or 190 °C (for 15% or 90% HS), and subsequently cooled down at the target temperature. All measurements were carried out in a nitrogen gas atmosphere, whereas temperature control (better than ±0.3 °C) was achieved by means of a convection oven.

6.2.3 Statistical description of the segmented copolymers

In order to determine the sample composition, we have developed a statistical model which builds a large ensemble of segmented copolymers and allows analyzing their length distribution as well as the number and location of their HSs. Despite the polydispersity of the samples, statistical construction of the different TPE chains is relatively simple since their SSs are polyester chains synthesized via polycondensation reactions[25] and the short HSs have been used as chain extenders. This means that the molar mass distributions of both the SSs and the whole chains are well described by a Flory distribution[60], which corresponds to the assumption that each THF monomer added to a growing SS has the same probability, $p_{end,\,SS}$, to be the last monomer added to this SS, i.e. to be located either just before a HS or at the end of the whole chain. An example of such monomers (related to $p_{end,\,SS}$) is shown in Figure 6.3.

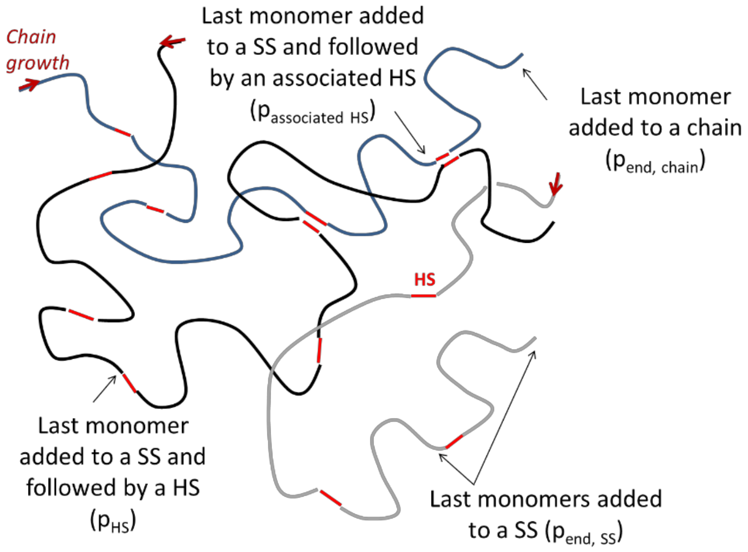

Figure 6.3: Cartoon representing different chains built from the statistical model. The arrows indicate in which direction the algorithm is building the chains, by taking randomly in a ‘statistical box’ either THF monomers, either HS or chain ends. While most monomers are located in the middle of the SSs, some monomers are located at the end of a chain, or just before an HS. The corresponding probabilities to find such monomers are $p_{end,\ chain}$ and p_{HS}, respectively, while the probability that a THF monomer to be located at the end of a SS (i.e. either followed by an HS or at the chain extremity) is named $p_{end,\ SS}$. These three probabilities are related through Eq. 5.

Furthermore, each THF monomer has the same probability $p_{end,\ chain}$, to be located at a chain extremity. Therefore, the chains can be statistically built following a Monte Carlo algorithm, in which the chains are created by randomly taking either a THF monomer, either a HS or a chain end from a ‘statistical box’ and by adding this unit to the growing chain.[61] The corresponding number proportions of these different units in the box are determined based on their occurrence probabilities, $(1 - p_{HS} - p_{end,\ chain})$, p_{HS} and $p_{end,\ chain}$, respectively. Here, it is worth mentioning that each HS is taken as a single unit since we know a priori that they are monodisperse and that they are all composed of exactly one T4T unit. Since the average molar masses of the SSs and of the whole chains, $M_{n,SS}$ and $M_{n,\ chain}$, have been determined from size exclusion chromatography, one can determine the corresponding values of $p_{end,SS}$ and $p_{end,\ chain}$ without further assumptions:

$$p_{end,SS} = \frac{1}{(M_{n,SS}/m_0)}, \qquad (1)$$

$$p_{end,chain} = \frac{1}{(M_{n,chain}/m_0)}, \qquad (2)$$

with m_0 being the molar mass of a PTMO monomer (i.e. tetrahydrofuran, 72.11 g.mol^{-1}).

The corresponding molar mass distribution can then be determined, by calculating the probabilities $p_{SS}(N)$ and $p_{chain}(N)$ of a selected SS or a selected chain to contain N monomers [60]:

$$p_{SS}(N) = \left(1 - p_{end,SS}\right)^{N-1}\ p_{end,SS}, \qquad (3)$$

$$p_{chain}(N) = \left(1 - p_{end,chain}\right)^{N-1}\ p_{end,chain}. \qquad (4)$$

Furthermore, based on Equations 1 and 2 and by considering the fact that each SS is followed either by a chain end or by an HS, one can determine the probability p_{HS} that a monomer randomly selected along a chain is both the last monomer of a SS and followed by an HS (i.e. excluding the chain end position, see Figure 6.3). Indeed, since

$$\begin{aligned} p_{end,SS} &= 1 - p(\mathit{the\ monomer\ is\ not\ at\ the\ extremity\ of\ a\ SS}) \\ &= 1 - p(\mathit{the\ monomer\ is\ neither\ before\ an\ HS\ nor\ a\ chain\ end}) \\ &= 1 - \left((1 - p_{HB})\left(1 - p_{end,chain}\right)\right), \end{aligned} \qquad (5.a)$$

We find that:

$$p_{HS} = 1 - \frac{1-p_{end,SS}}{1-p_{end,chain}}. \tag{5.b}$$

Thus, the probabilities presented in the above equations can all be accurately determined based on the information of Table 1, hence allowing us to keep track of the number and location of the HSs in different chains. Since the HSs will associate and dissociate over time, one also needs to define a new, yet unknown, parameter, p_{ass}, which is the probability for a HS to be associated. This value is considered identical for all HSs along the chain, and is expected to vary with temperature. From this value, the probability for a SS to be followed by an '*associated HS'* can be determined as:

$$p_{associated\ HS} = p_{HS} \cdot p_{ass} \tag{6}$$

In this work, the parameter p_{ass} is the only parameter which cannot be determined from the experimental molar mass distributions of the SSs or the copolymers.

6.3 Results and Discussion

6.3.1 Statistical composition of the segmented copolymers

In order to investigate how the structure and strength of the hard domains depend on the mobility and connectivity of the chains, which in turn depend on the number and localization of the HSs, an accurate description of the HS distribution along the chains is needed. This will also allow us to properly take into account the contribution from the chains entanglements to the sample modulus, which is important at high temperature, at which the samples often contain more entanglements than associated HSs. Indeed, based on ref.[62], the entanglement density is estimated to 1 entanglement per subchain of mass $M_e = 2000$ g.mol^{-1}. This number is comparable to the molar mass of a SS trapped between two associated HSs for the sample containing 15 wt% of HSs if we consider that all its HSs are associated ($M_{n,SS} = 2080$ g.mol^{-1}, see Table 1). It is therefore expected that at a temperature where the HSs association is not too strong (i.e. above T_m), the sample modulus is mainly governed by the entanglements which are trapped between two associated HSs and can only relax after dissociation of the HSs, which act as physical cross-links. Therefore, it is important to quantify the contribution of these topological constraints to the modulus as a function of the association probability of HSs, p_{ass}. This is achieved with the aid of the statistical approach proposed in Section 6.2.3.

The key results are presented in Figures 6.4 and 6.6. Figure 6.4 depicts the weight fraction of chains containing a specific number of HSs, for the four segmented copolymers investigated. The proportions of the main classes of SSs and the probabilities $p_{end\ chain}$ and p_{HS} are given in Table 2. Concerning the former we consider different situations for SSs, which are represented in the cartoon on Figure 6.5: (i) belonging to a molecule without HS, (ii) belonging to a molecule containing only one HS, (iii) being the dangling segment of a copolymer chain containing at least two HSs, (iv) localized between two HSs in a chain containing at least two HSs. We observe that the segmented copolymer with 5 wt% HS fraction contains a large fraction of molecules with zero or one HS, and has only about 50 wt% of SSs localized in-between two HSs. This means that at least half of its soft phase will always be able to relax, either by diffusion (reptation) in case of chains with 0 HS, either by fluctuations in case of chains with one HS and for the dangling SSs of the other chains, even at low temperatures where most of the HSs are associated and may form crystallites. Thus, as long as the temperature is above the T_g of the PTMO soft phase (see Table 1), only half of this sample can be trapped between two associated HSs and relax at long time scales. In the other limiting case, the relevant fraction of localized SSs between HSs for the sample with 20 wt%HS is about 85wt%. In that case, chain relaxation takes place at times beyond the HS dissociation.

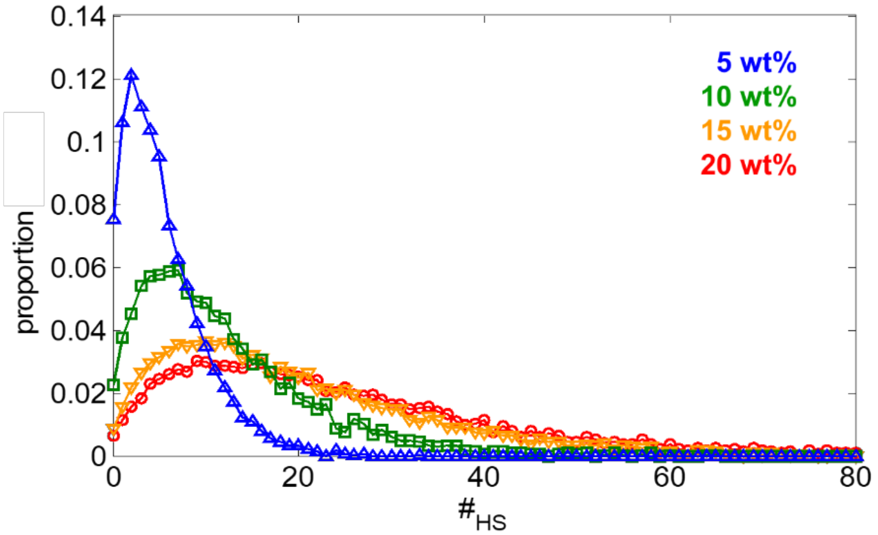

Figure 6.4: Weight proportion of molecules versus the number of HSs they contain, for samples 5 wt%HS (blue, Δ), 10 wt%HS (green, □), 15 wt%HS (orange, ∇) and 20 wt%HS (red, ○).

Table 2: Weight fractions of the main classes of SSs in the TPEs: (i) belonging to a molecule without HS, (ii) belonging to a molecule with only 1 HS, (iii) being a dangling SS of a copolymer chain containing at least 2 HSs, (iv) localized between two HSs in a chain containing at least 2 HSs.

	P_{HS}, $p_{end,chain}$	SSs belonging to chains with 0 HS (wt%)	SSs belonging to chains with one HS (wt%)	Dangling SSs of chains containing at least two HS (wt%)	SSs localized between two HSs (wt%)
5 wt%HS	7.7/1000, 2.86/1000	8	11	29.6	51.4

10 wt%HS	1.88/100 3.16/1000	2.2	3.5	21.7	72.6
15 wt%HS	3.16/100 3.2/1000	1.1	1.6	17	80.3
20 wt%HS	4.5/100 3.7/1000	0.7	1	14	84.3

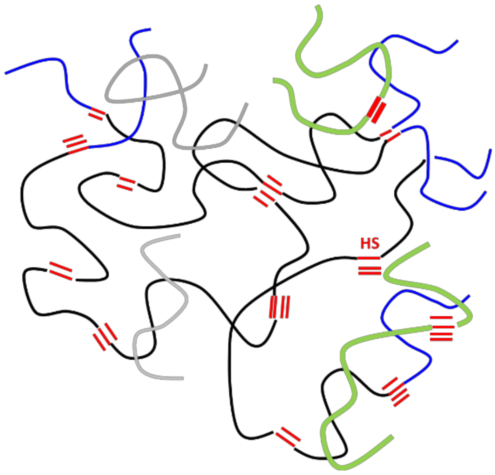

Figure 6.5: Cartoon representing the different kinds of SSs: 1) SSs belonging to chain with 0 HS (see the grey curves), 2) SSs belonging to chain with one HS (see the thick green curves), 3) SSs belong to chains with at least two HSs (see the blue and black curves). This last category of SSs contains dangling SSs (see the blue curves) and SSs localized between two HSs (see the black curves). Note that for clarity, only a part of the chains are represented (all HSs are considered as trapped in HSs domains).

The fractions given in Table 2 correspond to the specific case where all HSs are associated, i.e., $p_{ass}=1$. However, in reality only a part of HSs is associated, depending on temperature and thermal history of the sample (see Section 6.3.2). Consequently, the smaller the association probability p_{ass}, the smaller the proportion of SSs trapped between two associated HSs. In order to determine this influence, we analyze the composition of a population of about 10^4 molecules, which were constructed by randomly taking units (of the same statistical weight) in a 'statistical box' containing a fraction $p_{associated\ HS}$ of associated HSs (see Figure 6.3), a fraction $[(1-p_{ass})p_{HS}]$ of free HSs, a fraction $p_{end,\ chain}$ of chain ends and a fraction $(1-p_{end,chain}-p_{HS})$ of THF monomers located between two other THF monomers along the chain , and by adding these monomers one-by-one until an end chain was randomly taken in the statistical box (see Section 6.2.3).

Results are shown in Figure 6.6a, which represents the weight fraction of molecular SSs trapped between two associated HSs, $p_{trapped}$, as a function of their association probability, for the four different HSs densities. In the estimation of $p_{trapped}$, only the monomers located between two associated HSs are considered. From this ensemble of molecules, we also determine the corresponding fraction of molecules containing unassociated HS (called $p_{0\text{-}ass\text{-}HS}$) or only one associated HS (called $p_{1-ass-HS}$) as a function of p_{ass}, as well as the fraction of dangling SSs belonging to chains with at least two associated HSs, $p_{dangling\text{-}SS}$. These fractions are shown in Figures 6b, 6c and 6d, respectively. It is seen that for a sample with 5 wt% of HS and low association probability ($p_{ass}=0.05$), most of the chains are free. By increasing the fraction of associated HSs, part of these free chains are effectively transferred to the chains containing one associated HS (with a maximum at $p_{ass}=0.15$). At the higher p_{ass}, chains with 0 or one associated HSs are becoming less probable, giving rise to a larger fraction of chains with at least two associated HSs, hence contributing to the fraction of trapped chains and dangling ends (rather than to $p_{0\text{-}ass\text{-}HS}$ or $p_{1\text{-}ass\text{-}HS}$). But as already mentioned above, these samples always contain a significant fraction of chains with no or just one associated segment, even if all HSs are associated (i.e. $p_{ass}=1$). In contrast, with larger densities of HSs, the fraction of chains with 0 or one associated HS decreases rapidly in favor of the dangling SSs belonging to molecules with at least two associated HSs. With increasing the fraction of associated HSs, the fraction of these dangling ends decreases in favor of SSs trapped between two HSs.

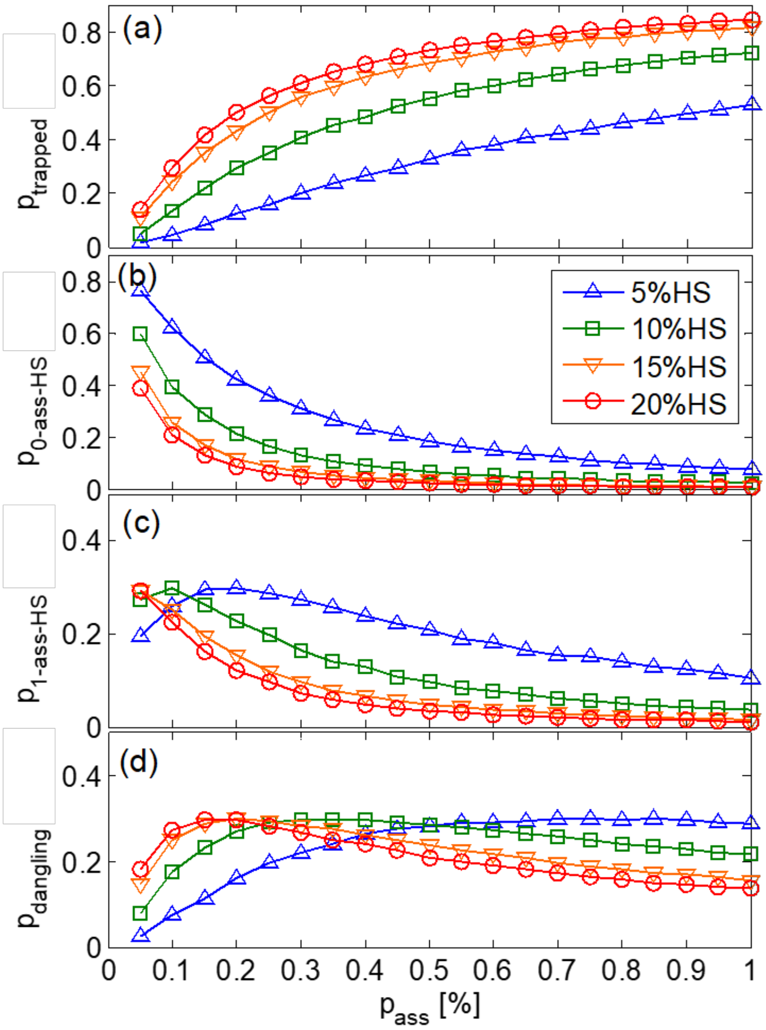

Figure 6.6: Weight proportion of (a) molecular segments trapped between two associated HSs, (b) free chains, (c) chains with only one

associated HS, (d) dangling end in chains containing at least two associated HSs, as a function of the association probability. Results are shown for samples with 5 wt%HS (blue, Δ), 10 wt%HS (green, □), 15 wt%HS (orange, ∇) and 20 wt%HS (red, ○).

One can clearly see in Figure 6.6 that the fraction of trapped segments increases more sharply at high HS density (15 wt% or more). This means that for samples with larger HS density, when the temperature is decreased (i.e., p_{ass} increases), the state at which most of the chain entanglements are trapped between two associated HSs is quickly reached. As discussed in Section 6.3.3, this is expected to strongly affect the overall chain mobility and consequently, its ability to form stable HSs domains.

6.3.2 Influence of HS density, temperature and time on linear viscoelastic properties

As reported in ref.[25] and presented in the DSC data (Figure 6.1), the HSs of the present segmented copolymers can associate into different structures exhibiting distinct melting temperatures (see Figure 6.1). As described in the Introduction, these structures are elongated crystallites (ribbons) due to the presence of relatively strong and directional hydrogen bonds. Concomitantly, their width reflects van der Waals associations (and possibly π-π stacking as well).[1] Thus, the final properties of these segmented copolymers strongly depend on the way the crystallites grow, until they reach a 'frozen' state, at which the HSs are kinetically trapped and cannot dissociate anymore in order to create energetically more favorable new structures.[25, 42-44] In this Section we explore the role of HS density, temperature and time on the macroscopic properties of such well-defined TPEs of varying composition and in particular, on their linear viscoelastic response. We discuss the thermal protocol needed in order to enhance the formation of strong crystallites, defined by a high melting temperature and show the great significance of intermediate temperatures at which chain mobility competes with HSs association.

6.3.2.1 Influence of HS density

The DSC results of our well-defined TPEs are shown in Figure 6.1 in the case of a heating/cooling rate of 15 °C.min^{-1}. As is known from analogous multiblock copolymers.[1, 45], all samples have similar values of glass transition temperature, T_g, with little influence of HS density (Table 1). This observation is consistent with the low fraction of HSs present in the soft phase, as expected from the synthesis of TPEs containing well-defined, monodisperse HSs.[27] Furthermore, the broadness of the corresponding melting peaks corroborates the co-existence of phase-separated HS domains and crystallites of different stability in the four TPEs. The fact that the hard phase does not consist entirely of crystallites with high melting peak suggests that part of the HSs did not form well-organized structures in such melt-processed materials. We attribute this to the very fast association of the HSs at low temperature, together with the low mobility of the entangled chains, which easily leads to trapping some HSs into a metastable state.[26, 45] In addition, the melting peaks are strongly influenced by the fraction of HSs: the "terminal" melting point $T_{m,t}$ (i.e., the temperature at which the sample is totally molten) is shifted from 91.8 to 122.3, 148.6 and 157.8 °C as the HS fraction increases from 5 to 10, 15 and 20 wt%, respectively, in harmony with the literature.[25, 32, 63-65] This can be rationalized by considering the fact that the probability for an HS to associate, hence to create longer and thicker crystallites, is much larger for high compared to low HS density, due to the 'solvent' effect of the amorphous phase, as described by Flory.[29, 39-41] Besides increasing the melting temperature of the samples, the effect of HSs density, at constant copolymer length is to significantly enhance their plateau modulus. This is shown in Figure 6.7, where the value of $G_{N,exp}^{0}$, which has been approximated by the storage modulus of the TPEs at a frequency of 10rad.s^{-1}, is presented in function of the HS density. An obvious explanation of the observed increase in $G_{N,exp}^{0}$ is the effective physical crosslinking role of associated HSs along the polymeric chain, which contribute to the plateau, in addition to the contribution from the entanglement. This effect can be quantified by determining the plateau modulus, including both stickers and entanglement contributions: [66]

$$G_{N,SS}^{0} = \nu kT = \frac{\rho RT}{M_x}, \tag{7}$$

where $$M_x = \left(\frac{1}{M_e} + \frac{1}{M_{strand}}\right)^{-1}, \tag{8}$$

with M_e, the average molar mass between two entanglements for PTMO molecules (≈2 kg.mol^{-1})[62] and M_{strand}, the average molar mass of the molecular segments between two associated HSs. The values of $G_{N,SS}^{0}$ obtained from Eq. 7 are then compared to $G_{N,ent}^{0}$, the entanglement plateau modulus (which takes into account only the contribution of the entanglements of the TPE chains), and the plateau modulus determined experimentally, $G_{N,exp}^{0}$. Whereas the contribution of HS crosslinks to $G_{N,SS}^{0}$ is important, it is clearly not sufficient to explain the very large experimental $G_{N,exp}^{0}$ values. This implies that at low temperatures the modulus is mainly governed by the HS-based crystallites rather than SSs trapped between the entanglements or associated HSs. Even with only 5 wt% of HSs, the long ribbon-like crystallites which are formed at room temperature[25] allow a significant reinforcement of the TPEs.

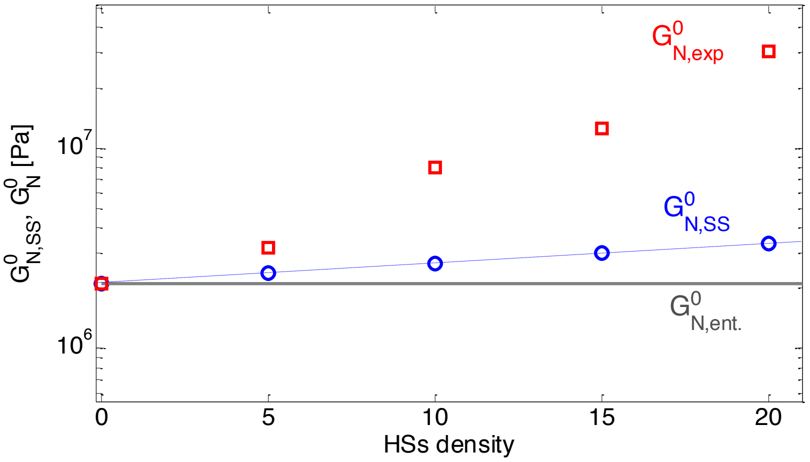

Figure 6.7: Plateau modulus as a function of HSs density at a temperature of 25°C, determined experimentally (red, □), from Eq. 7 (blue, ○), or by considering only the contribution from the SS entanglements (grey, line). The dashed line is drawn to guide the eye.

6.3.2.2 Influence of time

In Figure 6.8, we study the influence of time on the evolution of the viscoelastic properties of the segmented copolymer containing 10 wt% of HSs, at different temperatures. Before each measurement, the sample was heated at 180 °C, i.e. well above its melting temperature (122 °C), in order to melt the possible crystals formed during the time sweep tests, and a frequency sweep test was performed at this high temperature in order to confirm that the sample did not evolved irreversibly during the experiment.

As shown in Figure 6.8, while at low and high temperatures the viscoelastic data of the samples do not really evolve through time, the storage modulus significantly increases, sometimes by almost a decade, in the intermediate temperature range $T_c<T<T_m$.

The emerging picture calls for the formation of short HS-mediated aggregates on cooling, which in turn associate into stronger crystallites. At intermediate temperature, the association strength of

HSs via hydrogen bonding is expected to be weaker and their crystallization kinetics much slower than at low temperature. Therefore, in order to enhance the HSs association and to form stronger crystallites, much longer waiting times are necessary in order to compensate for the lower association probability. On the other hand, at low temperature, the system reaches nearly instantaneously its maximum associated state, leading to a too low mobility of the chains to allow them to further associate, while at high temperature, the driving force for crystallization is too low to observe the formation of crystals.

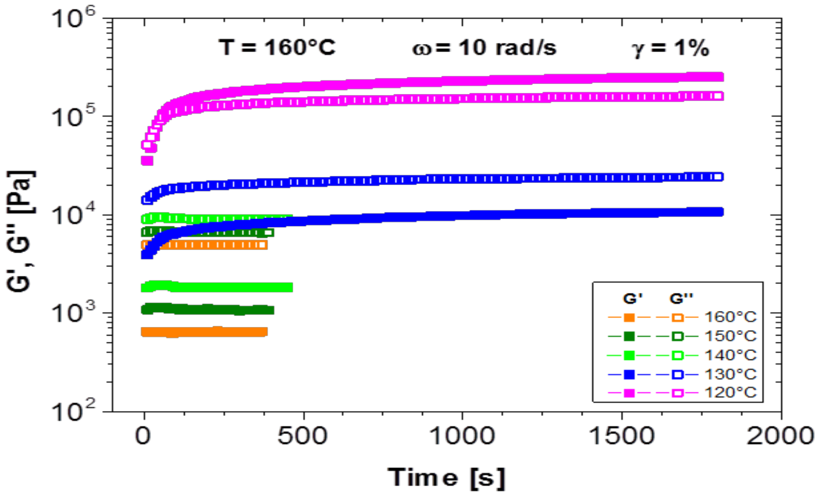

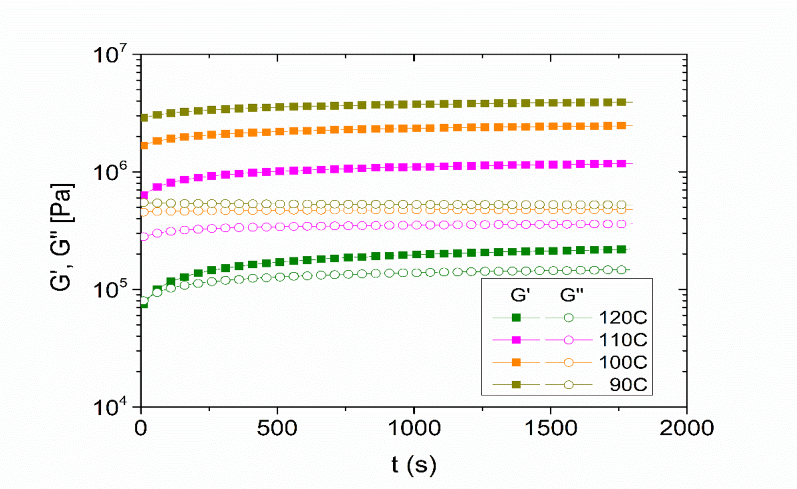

Figure 6.8: Time sweep measurements of the storage and loss moduli of the sample containing 10%HS, at a frequency of 10 rad.s^{-1}, γ=1%, and at various temperatures. Prior to each measurement, the sample was heated at 180°C.

This result demonstrates the importance of controlling the thermal history of the sample, as well as using well-defined protocols in order to ensure the reproducibility of the data.

6.3.2.3 Influence of temperature

The linear viscoelastic spectra of samples 10%HS over a wide range of temperatures are depicted in Figure 6.9, from T=180 °C to T=120 °C. Prior to each measurement, the sample was heated at 180 °C, then cooled down to the measurement temperature. Depending on the temperature, a waiting time of 30 or 60 minutes was then applied in order to ensure relatively stable viscoelastic properties. At intermediate temperatures, data obtained both after 30 min and 60 min are shown. They only show a small difference.

A liquid-to-solid transition is observed with decreasing temperature. The transition temperature is taking place at approximately 130 °C, which is close to T_m. Above this temperature, the attractive interactions between HSs due to hydrogen bonding weaken, hence the sample flow. There is however a small fraction of the TPEs which cannot fully relax within the experimental frequency window, as suggested by the fact that the -2 slope of the storage modulus is not observed below 180 °C, the temperature at which the sample relaxes as an entangled (non-sticky) linear chain. This small fraction of unrelaxing chains is attributed to the formation of a few very stable HS micro-domains[25], which are responsible for the longer lifetime of HS associations, hence slower terminal relaxation.

By gradually decreasing the temperature, the chains are still able to relax but their terminal relaxation becomes broader and slower. At 130 °C, a second plateau, G_2, emerges at low frequencies, suggesting that a significant fraction of the sample is trapped between associated

HSs, while dangling ends relax. This secondary plateau increases sharply with further decrease in the temperature, whereas the high-frequency "primary plateau" is only slightly enhanced. Indeed, the value of $G_{N,exp}^0$ is very close to $G_{N,SS}^0$, determined by assuming that all HSs are associated as discussed above (see Figure 6.7). This suggests indirectly that most of the HSs are associated into small structures (low-coordination number) acting as physical crosslinks, whereas long and thick crystallites[25] able to significantly reinforce the samples (high coordination number) are not yet formed at these relatively high temperatures. In order to observe a large enhancement of the modulus, the temperature must be decreased even more. Thus, at the intermediate temperature, only association of the HSs into small structures seems to take place through time, the driving force for building larger crystallites being too small.

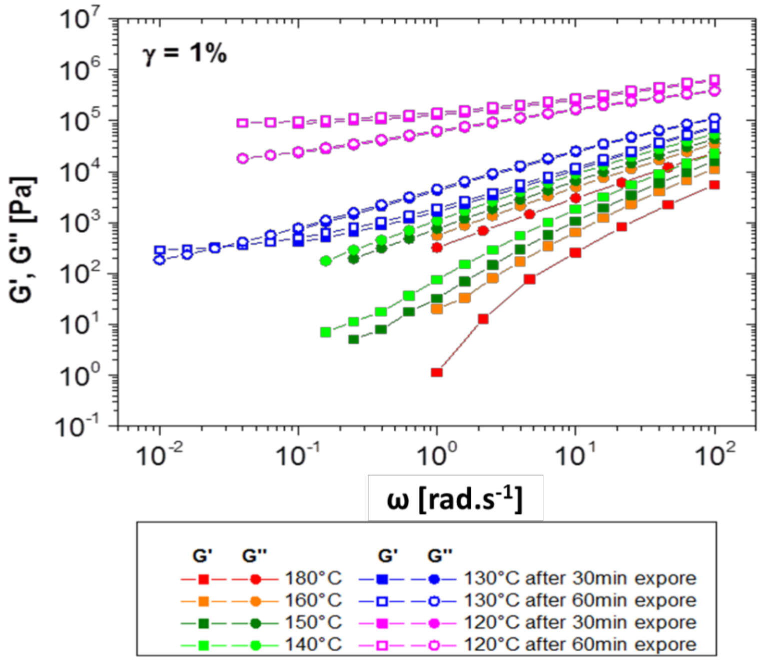

Figure 6.9: Frequency-dependent storage moduli of a sample containing 10%HS, measured from high (T=180 °C) to low temperature

($T=T_m$-70 °C). Prior to each measurement, the sample was heated at 180 °C and a time sweep of 30min or 60min.

As shown in Figure 6.10, similar behavior is found for the other samples, containing 5, 15 or 20 wt% of HSs. The respective transition temperatures between liquid-to-solid behavior are approximately 100, 140 and 155 ºC for 5, 15 and 20%HS, respectively (see Table 1). A sharp increase of the secondary plateau is observed below these temperatures. Furthermore, reinforcement effect ($G_{N,exp}^{0} > G_{N,SS}^{0}$) is seen when the temperature is further decreased (below 80, 110 and 130 °C for 5, 15 and 20 %HS, respectively), allowing the short associated structures to assemble into larger structures.[19,45]

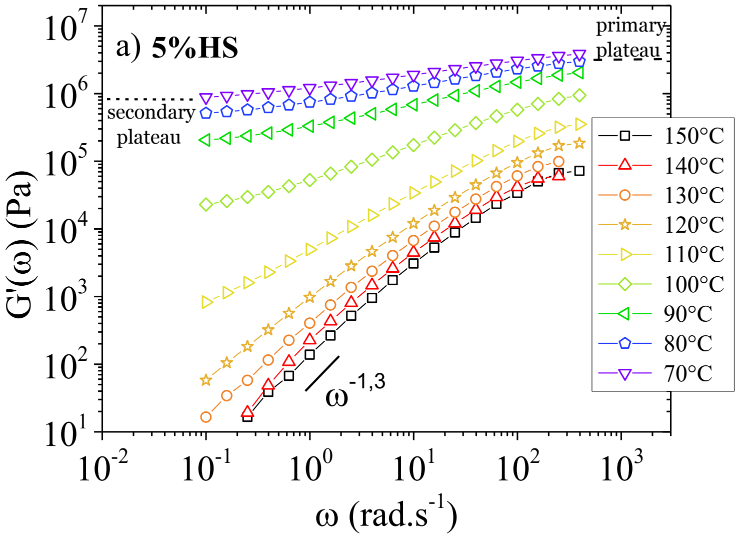

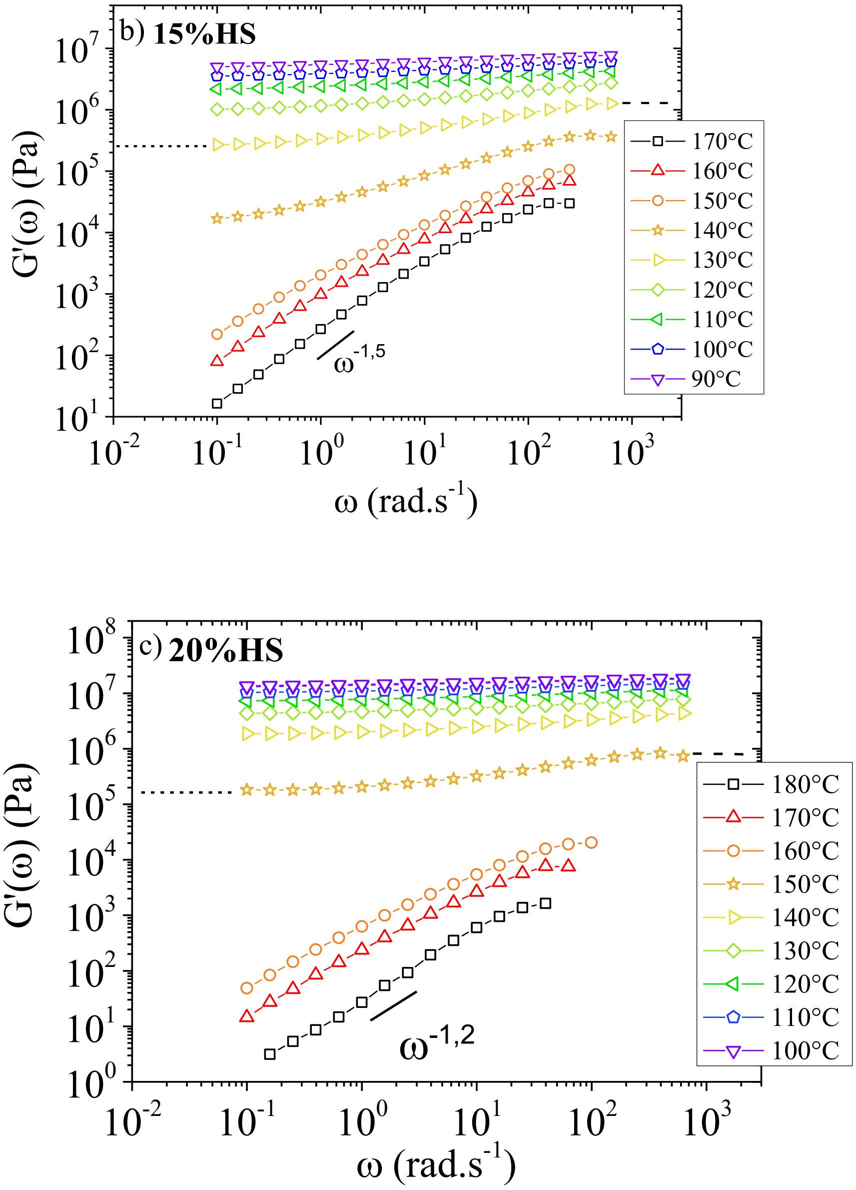

Figure 6.10: Frequency-dependent storage moduli of sample containing (a) 5 wt%HS, (b) 15 wt%HS and (c) 20 wt%HS, measured from high (T_m+10 °C) to low temperature (($T=T_m$-70 °C).

We also remark from Figure 6.10 that the liquid-to-solid transition is sharper at high HS density and that at low temperature the two plateau regimes in *G'* are more distinguishable at lower HS density. To explain these observations we invoke the statistical approach developed in Section 6.3.1: as soon as the HSs start to associate, the fraction of SSs trapped between associated HSs increases fast when the density of HSs is large (Figure 6.6a), which explains the sharp transition in sample 20 wt%HS. In such a case, if all HSs are associated, only 15.7 wt% of the SSs are free to move, hence to relax at high frequency (see Table 2). Therefore, as soon as the chains are able to associate via their HSs, the storage modulus evolves rapidly (Figure 6.10c). On the other hand, for 5 wt%HS, as much as about 50 wt% of the SSs will remain free (not trapped between associated HSs, see Table 2). These dangling ends will, therefore, disentangle at higher frequencies (primary plateau), yielding an elastic response characterized by two plateau regimes and a slower increase of the modulus. The role of the dangling ends is further rationalized in Figure 6.11, which depicts the theoretical evolution of the secondary plateau, $G_2(p_{ass})$, as a function of the association probability of HSs. For comparison, the primary plateau modulus, $G_1(p_{ass})$, is shown as well. Its value has been determined by considering that at short times, all chains entanglements and associated HS act as physical crosslinks. On the other hand, the values of $G_2(p_{ass})$ are determined by considering that only the chains entanglements trapped between two associated stickers are contributing to the plateau (thus, assuming that the entanglements of the dangling ends had time to relax).[66] These theoretical data allow us to highlight the fact that the ratio between the first and the second *G'*-plateau regimes are particularly large at low association probability ($p_{ass}<0.6$) and at low HS density, i.e., at the onset of the network formation. We also observe the large value of $G_2(p_{ass})$ at high HSs density, even if only a part of HSs are associated (such as p_{ass}=50%).

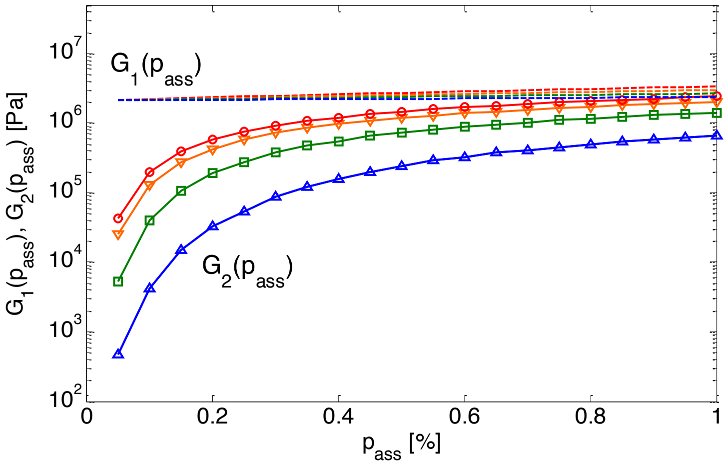

Figure 6.11: Evolution of the primary (high frequency) and secondary (low frequency) plateau moduli *$G_1(p_{ass})$* (dashed curves) and *$G_2(p_{ass})$* (continuous curves), as function of the association probability of the HSs, for sample 5 wt%HS (blue, Δ), 10 wt%HS (green, □), 15 wt%HS (orange, ∇) and 20 wt%HS (red, ○).

Based on Figure 6.11, the proportion of associated stickers for the sample containing 10wt% HSs (see Figure 6.9) can be estimated in function of the temperature. A value of around 25% of associated stickers is found at 120 °C while at 130 °C, this value decreases below 5%.

Since at lower temperatures, small HS aggregates associate in order to create long and thick crystallites[25], temperature ramps in both cooling and heating directions represent an appropriate protocol for monitoring their stability and influence on the viscoelastic properties of the material. The measured temperature-dependent G' at 10 rad.s^{-1} are depicted in Figure 6.12 for the TPE sample containing 10%HS.

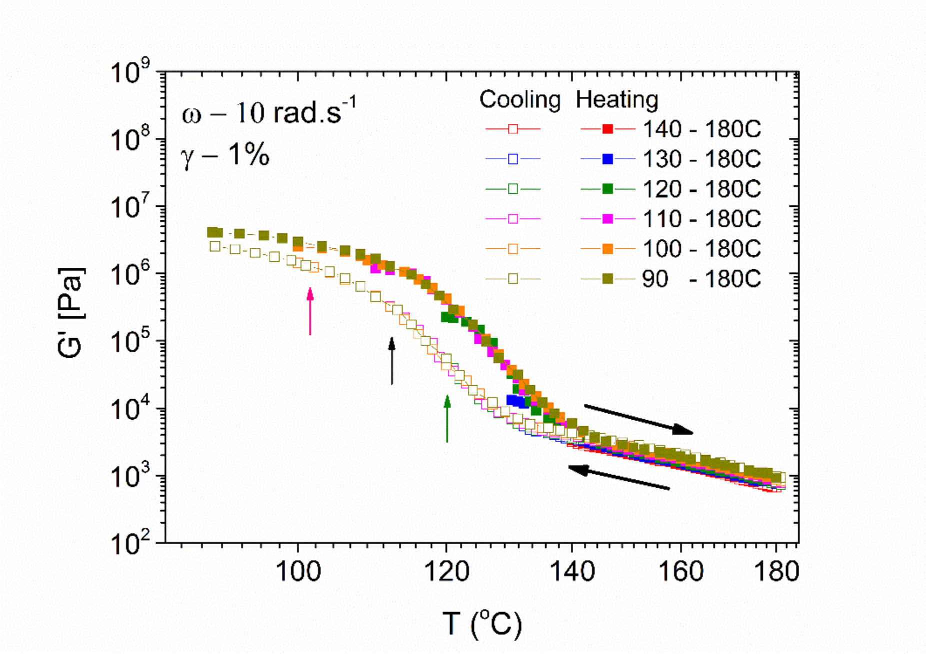

Figure 6.12: Dynamic temperature ramps of storage modulus at 10 rad.s^{-1}, for a sample containing 10% HS. Data are shown from high to low temperatures (open symbols), followed by heating back to initial temperature (filled symbols), at a constant rate of 6 °C.min^{-1}. The cooling ramps were performed from 180 °C down to different low temperatures (see the legend), followed by a time sweep performed until the increase of G' saturates, before performing the heating ramp back to 180 °C.

Coming from high temperatures, the storage modulus is first governed by the contribution of the entanglements and by the contribution of an increasing amount of HSs acting as cross-linkers (with $G_N^0 = G_1(p_{ass})$, see Figure 6.11). Then, on cooling, it reaches much larger values, governed by the formation of (eventually long) crystallites which interact with each other and reinforce the sample (with $G_N^0 = G_{N,exp}^0$, see Figure 6.7). The observed hysteresis confirms that low temperatures enhance the association of the short aggregates into larger crystallites characterized by higher melting temperature.

Figure 6.12 also shows that at intermediate temperatures where hysteresis is significant, the viscoelastic properties strongly depend on thermal history: while coming from low temperature, a large fraction of the HSs stay associated into crystallites, the amount of associated HSs is much lower if the same temperature is reached upon cooling from high temperatures. Indeed, in the latter case, the crystallites take a long time to develop in this intermediate region, as discussed in Section 6.3.2.2. In order to illustrate this effect, we performed temperature ramps from 180 °C down to specific temperatures (see legend), followed by a time sweep test, in order to let the sample reach an equilibrium state, before heating the sample back to 180 °C. It is observed that long waiting time leads to similar properties as the ones obtained by cooling down the sample to low temperature. From this comparison, we can, therefore, conclude that at intermediate temperature, 1) equilibrated structures take time to develop because of the low association driving force of the HSs, 2) the structures obtained after long waiting time are not characterized by a higher melting temperature (compared to the crystal formed at low T). The fact that the larger mobility of the chains does not allow them to equilibrate into stronger structures[45] indicates that the dynamics of the TPEs is mostly governed by the associated HSs (and the corresponding trapped entanglements), rather than by the segmental dynamics of the chains: at each temperature, there is a certain amount of HSs which should be associated. Coming from high temperature, too few HSs are associated so additional HSs will associate with time, while coming from low temperature, a too large fraction of HSs are associated, so part of them will dissociate in order to reach the same equilibrium value.

This process is further confirmed in Figure 6.13, which shows that in this intermediate range of temperatures ($T_c < T < T_m$), obtaining higher storage modulus does not require to bring the sample to low temperature (70 °C) and form large, reinforcing crystallites. Cooling down the sample only slightly below the target temperature is enough to favor the association of a larger proportion of HSs and keep them associated when heating the sample until the superior hysteresis curve of G' is reached.

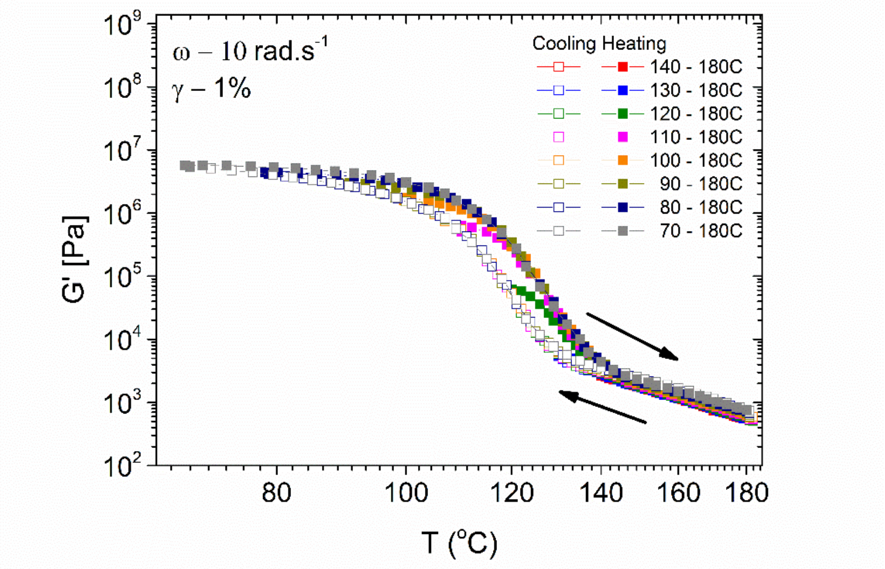

Figure 6.13: Dynamic temperature ramps of storage modulus at 10 rad.s^{-1}, for a sample containing 10% HS. Data are shown from high to low temperatures (open symbols), followed by heating back to initial temperature (filled symbols), at a constant rate of 6 °C.min^{-1}. The temperature ramps were performed from 180 °C down to different lowest temperatures (see the legend).

It must be also noted that the modulus at the low-temperature range does not evolve through time: whatever the thermal history of the sample, the same amount of large crystallites are created,[26] which dictate the (identical) viscoelastic properties.

The influence of HS density on the hysteresis properties is then studied in Figure 6.14.

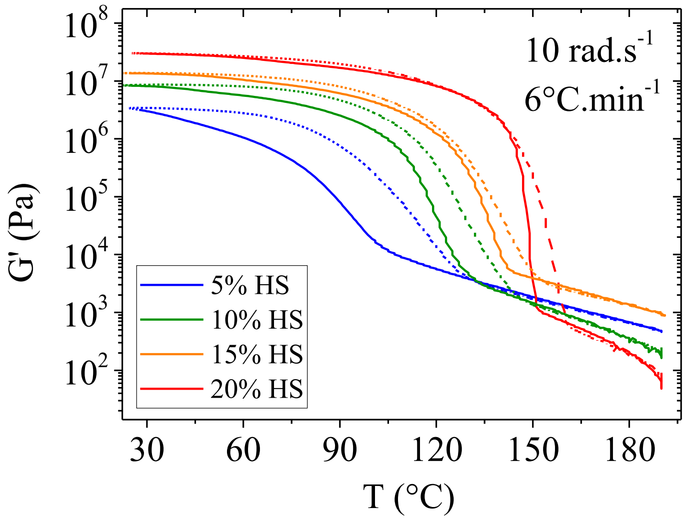

Figure 6.14: Dynamic temperature ramps of storage modulus at 10 rad.s^{-1}. Data are shown for the four different samples and for ramps from high to low temperatures (solid lines), followed by heating back to initial temperature (dashed lines), at a constant rate of 6 °C.min^{-1}.

It is observed that the hysteresis is larger for smaller HS density. Furthermore, the transition between viscoelastic and solid-like behavior is much smoother at low HS density, compared to higher HS density, for which the storage modulus varies by almost four decades when the temperature is varied from 160 °C to 150 °C. This result is in agreement with the above discussion: at intermediate temperatures, the main effect of the HSs domains is to increase the fraction of chains kinetically trapped between two associated HSs, and this fraction increases faster at high HS density (see Figure 6.6). This, together with a faster crystallization dynamics, leads to a very short range of intermediate temperatures at which hysteresis appears. Thus, the effect of thermal history on the linear viscoelastic properties is minimized, compared to samples containing a low density of HSs.

To conclude this section, the interplay of temperature and time offers unique opportunities to interrogate and tailor the viscoelastic properties of the TPEs, especially at intermediate temperatures, where the properties of the samples are dominated by the chain entanglements which can be partially trapped between associated HSs. In this range of temperature, hysteresis is observed, due to the slow crystallization dynamics of the HSs. Therefore, long waiting times are needed in order to ensure reaching a stable state.

It must be noted however that long waiting time at intermediate temperature does not always mean that the sample will reach its equilibrium structure. Indeed, as discussed in the following section, certain damages caused to the associated network can only be fully repaired upon re-melting the sample at high temperature.

6.3.3 Influence of large-amplitude oscillatory shear flow

In this section, we study the influence of flow on HS associations, HS domain stability and chain entanglements. To this end, we focus on large amplitude oscillatory shear (LAOS), expecting that applying a large deformation amplitude will lead to partial disengagement of the physical network. This is also motivated by the known effect of LAOS on ordered block copolymers in promoting the flow alignment.[50-55] The recovery time after flow cessation can be long since it depends on the association/dissociation dynamics of the physical bonds, leading to strong thixotropic behavior.

We first examine the behavior of sample 10 wt%HS at low, intermediate and high temperature. The samples have been measured following the same protocol, which consists of initial equilibration for 10 minutes at 180 ºC, followed by cooling to the test temperature (with a cooling rate of 6 °C.min^{-1}) and performing directly a LAOS cycle amplitude sweep performed at a frequency of 10 rad.s^{-1}.[67] Thus, we do not let the time to the sample to reach its equilibrated state. In addition to these tests, the data measured at 120 °C are then compared to the behavior of an equilibrated sample, which has been first cooled down to 70 °C (in order to promote the formation of HS associations) then heated to 120 °C (see Section 6.3.2.3).

Results are shown in Figure 6.15. At high strain amplitude, we see that the plateau decreases; the sample is forced to flow.

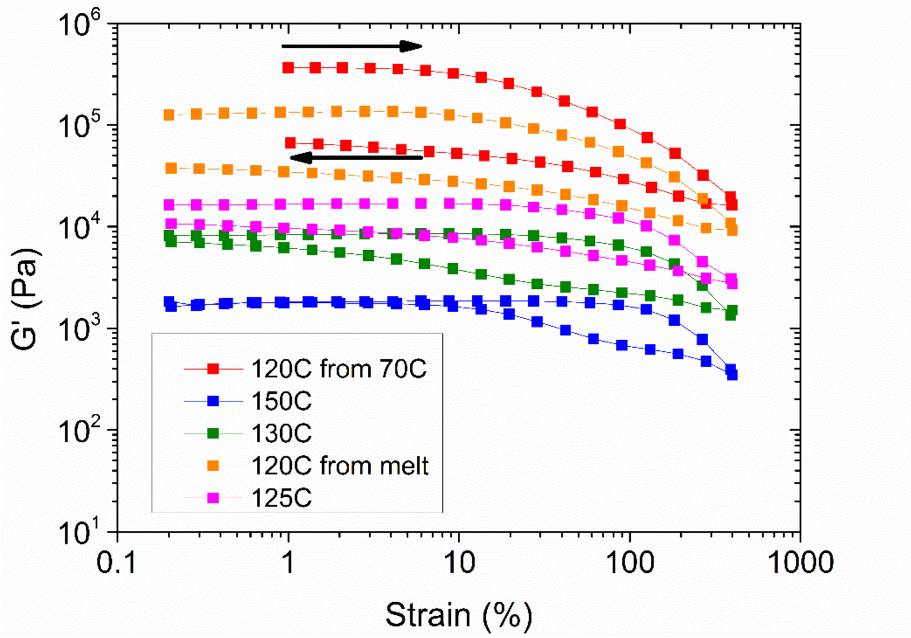

Figure 6.15: Storage modulus of sample 10 wt%HS as a function of strain amplitude during LAOS cycles at different temperature and 10 rad.s^{-1}. Measurements were performed from low to high (the upper curve) and high to low (the lower curve) strain amplitudes, respectively.

At high temperature, a small hysteresis is observed in the cyclic curve. We attribute it to the flow-induced dissociation of the few HS domains which are already present at such temperature. These last ones are formed again when the strain amplitudes are decreased towards small deformation, and the initial modulus of the sample is recovered. At lower temperature, the hysteresis is becoming more important. Below 125 °C, while we observe the progressive recovery of HSs associations, the initial level of the storage modulus is not recovered in the linear regime, unlike the situation at high temperatures. Moreover, the equilibrated sample at 120 °C, which contains a larger proportion of associated HSs, shows an even larger effect of the amplitude sweep.

The large decrease of the linear modulus suggests that this copolymer is trapped into a metastable state, where only parts of the chains contribute to the low-frequency plateau, G_2. Therefore, this possible thixotropic behavior is studied by looking at the evolution of the sample left at rest for a long time after LAOS cessation, in order to see if slow recovery takes place back to the initial *G'* value. Recovery was observed at high temperature, but not at intermediate temperature. In particular, long waiting time after the cyclic deformation of the equilibrated sample at 120 °C led to very poor recovery (see Figure 6.16), with an increase of the modulus of less than 10%. In order to further investigate this non-reversible effect of deformation, cyclic deformation was then applied on the equilibrated sample at 120 °C up to different maximum strain amplitudes, followed by a time sweep. Results are shown in Figure 6.16.

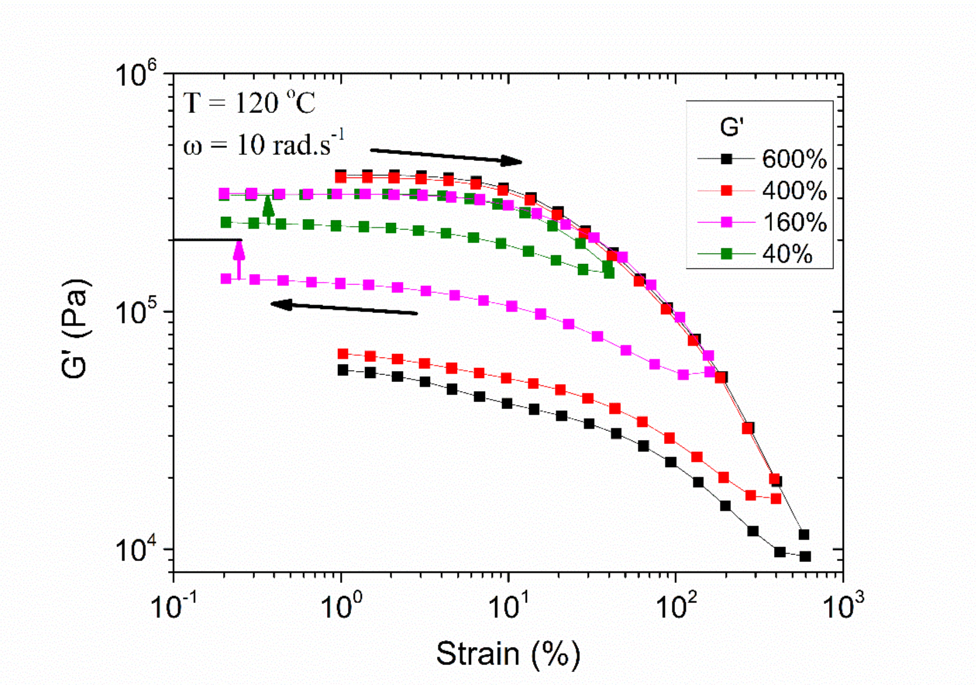

Figure 6.16: Storage modulus of sample 10%HS as a function of strain amplitude during LAOS cycles at different temperature and 10 rad.s^{-1}. Measurements were performed from low to high and high to low strain amplitudes, respectively. Time sweeps for 1 hr. (indicated by arrow) performed just after the LAOS cycles are also shown.

While below 100% of deformation, the sample evolves with time until it reaches its initial properties, applying larger strain amplitudes leads to irreversible changes (under these conditions) in the sample, characterized by a lower modulus: Keeping temperature at 120 °C for very long time does not allow the sample to reorganize and reform its initial structure. We attribute these changes to a change of state induced by the large deformation. Indeed, as shown below, if the sample is heated again above its melting temperature (180 °C), the effect of large strain is erased and the sample recovers its initial properties. The fact that at 120 °C, the sample cannot change its state toward equilibrium shows that at this temperature, the lifetime of the associated HSs is much longer than the experimental lifetime.

As shown in literature,[9, 19, 30, 31] such a decrease of modulus could be due to an orderly transition induced by the breaking of the ribbon-like crystallites under flow, leading to the sample yielding. Therefore, after cessation of flow, the sample properties are evolving, depending on the way the broken crystallites are able to re-organize. In particular, the reinforcement effect of the crystallites can be lost if these last ones are not able to form a network anymore, if they are too small or if they lose their isotropic orientation. However, while the crystallites structure strongly influences the sample modulus at low temperature, at the intermediate temperature, sample elasticity it mostly coming from the chains entanglements (see Section 6.3.2.2). Indeed, as shown in Figure 6.9, in this range of temperature ($T_c<T<T_m$), the rubbery plateau is similar to the entanglement plateau, and the low level of the second (low frequency) plateau highlights the presence of a large proportion of dangling ends. Therefore, we cannot ensure that the decrease of storage modulus observed under high shear flow only to the breaking of the crystallites. It could also be due to either a decrease of the proportion of associated HSs able to trap chain segments or a decrease of the average density of chain entanglements.

In order to investigate the possible reduction of the associated HSs, the temperature is decreased after the strain sweep test, in order to promote the creation of new HS associations. Results are shown in Figure 6.17 (see the T sweep 3, taking place just after the strain sweep test, which was performed between T sweep 2 and T sweep 3). While the modulus increases at low T, its value stays much lower than the one found with the same sample only deformed in the linear regime. Since at this temperature, the sample elasticity is governed by the crystallites, this demonstrates the different rearrangement of the crystallites due to flow. But the surprising point is that if we heat the sample back to 120 °C, a small hysteresis is observed, such as the storage modulus recovers its low value, similar to the one found just as after the strain sweep i.e.

T sweep 3. This hysteresis is probably due to the decrease in the size of the crystallites, followed by the dissociation of a part of the associated HSs in order to reach the equilibrium value of associated HSs at 120 °C. Based on this, together with the fact that the sample modulus does not evolve with time at this intermediate temperature, its low value does not seem to be due to a reduced amount of associated HSs.

As shown in Figure 6.17, if now the sample is progressively heated to a higher temperature through back-and-forth temperature sweeps (4, 5, 6, 7, 8 and 9), initial properties are progressively recovered, after each step. This suggests that the associated HSs must dissociate in order to allow the reformation of the initial structure and allow the sample to reach its equilibrated state (after cooling). Indeed, the probability of an HS to be associated decreases with increasing temperature, so at each heating step, increasing T leads to a larger fraction of unassociated HSs. Once the temperature reaches 150 °C, i.e. the end of the hysteresis region, the sample behaves as if it was never deformed under large oscillatory shear. Since in this range of temperature, the corresponding value of the storage modulus is low, we believe that this change of behaviour is not due to the melting of interacting crystallites, as the small HS domains rather act as cross-linking points and not as large objects.

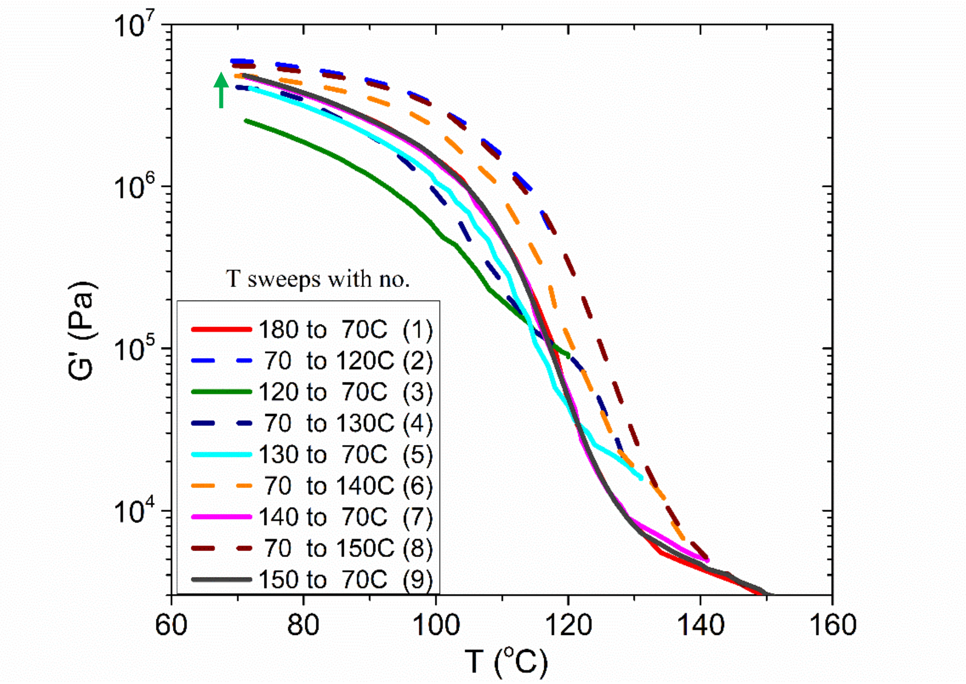

Figure 6.17: Dynamic temperature ramps of storage modulus at 10 rad.s^{-1}. Data are shown for ramps from high to low temperatures (solid lines), followed by heating back to initial temperature (dashed lines), at a constant rate of 6 °C.min^{-1}. The small green arrow shown represents a couple of to and fro temperature ramp from 70 °C to 120 °C, which increased the modulus.

Therefore, a plausible scenario to explain this behavior is that a fraction of the entanglements are lost under high shear, which forces the HSs to dissociate and the chains to disentangle in order to flow. On reducing the strain amplitude, new HS associations are rapidly reformed due to the enhanced association probability at low temperatures. This, however, prevents the trapped SSs from further diffusing and creating new entanglements. Thus, the formation of unentangled (or weakly entangled) junctions of SSs is favored, and the level of the corresponding low-frequency modulus is lowered. Therefore, the entanglement network is not homogeneous anymore and part of the chain connectivity is lost.

In fact, this process can be compared to the results of refs.[3,53,56], where it was observed that slip planes are created via a bridge-to-unentangled loop transformation, in order to allow layer-by-layer sliding and reducing the SSs stretching. Thus, shear flow can cause dissociation of certain physical bonds and subsequent reformation into a different configuration.

In order to further test this picture, we performed successive strain sweep loops on sample 15%HS at a different temperature, and study the evolution of the corresponding modulus. Results are shown in Figure 6.18. The temperature was chosen below, within and above the intermediate temperature range, where hysteresis is observed (120 °C < T < 150 °C). Furthermore, the frequency was fixed to 1 rad.s^{-1} in order to be representative of the value of the second (low frequency) plateau (see Figure 6.9).

At high temperature, T=170 °C, a slight increase of the modulus is observed through time. While it could be due to the formation of very strong, phase separated HS domains, we rather believe that this is due to a chemical evolution of the sample. This evolution only takes place above 170 °C, never stops (until a full gel is obtained) and is irreversible.

At 150 °C, the temperature at which the sample is still flowing (as seen in Figure 6.9, there is no second plateau), the data measured during the different cycles of deformation superimpose. There is a small hysteresis effect, which is attributed to dissociation/association of few HSs, as it was also observed at 150 °C for sample 10%HS (see Figure 6.15).

However, at intermediate temperatures, we see that the first cycle of deformation is very different from the other ones, starting to a much higher modulus. This is in agreement with the results found with sample 10%HS: high deformation forces the associated HSs to dissociate and the chains to disentangle. When decreasing the deformation amplitude, restoration of the entanglement of the SSs requires the molecules to be able to diffuse before the creation of new HSs associations. Therefore, this process is only possible if the HSs associations are weak enough, i.e., if the sample is at high temperature, which is not verified in this range of temperatures. In this T window, since a frequency of 1 rad.s^{-1} has been chosen for the oscillatory shear measurements, the values found correspond to the second plateau G_2, and the influence of entanglements on this value can be quantified, as shown in Figure 6.19. In this Figure, the second plateau determined by accounting for both the entanglements and the HS association is compared to the level that the second plateau should have if the junctions would only come from the HS associations. Looking at the difference between the two curves, it is indeed observed that the entanglements largely contribute to the sample elasticity.

Then, during the second and following cycles of deformation, the evolution of the storage modulus is weak and a limited hysteresis is observed. This is due to the fact that the network could not recover its initial structure between the first and other cycles.

At even lower temperature, T=110 °C, the high value of the initial plateau modulus indicates that the crystallites are reinforcing the sample. Therefore, under large deformation, it is expected that these last ones break and reorganize into smaller structures allowing the sample to flow. In this case, it is observed that the storage modulus in the linear regime is gradually decreasing with the deformation cycles.

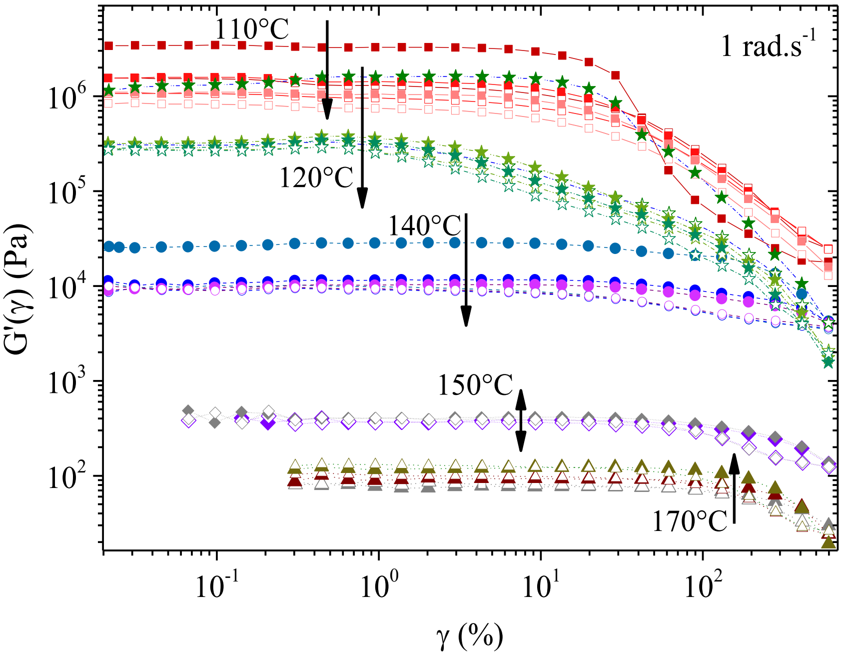

Figure 6.18: Storage modulus of sample 15 wt%HS during consecutive cyclic strain sweep curves at several temperatures ranging from T= 110 °C to T=170 °C. Filled symbols refer to increasing strain and open symbols to decreasing strain.

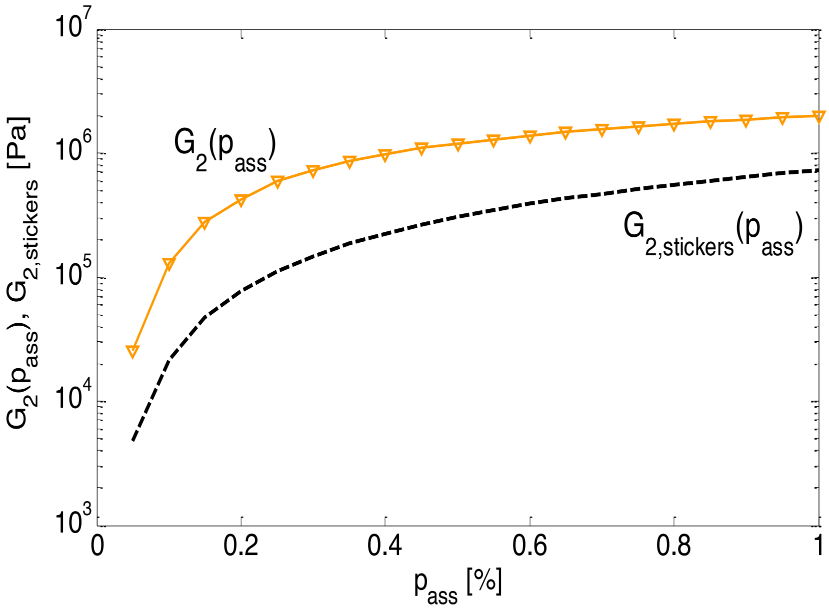

Figure 6.19: Evolution of the second plateau of sample 15 wt%HS, $G_2(p_{ass})$ (solid curves, ∇) and of the second plateau determined by accounting for the HSs associations only, $G_{2,\,HS}\,(p_{ass})$, as a function of the association probability of the HSs.

As the last test, we study the influence of the protocol used in order to reach an equilibrium state for sample 10%HSs. Indeed, as mentioned above, equilibrium state (i.e. the upper curve of hysteresis) can be reached either by cooling down the sample and heating it back to the desired temperature or by waiting a very long time at the desired temperature while coming from high T. In Figure 6.20, we compare the nonlinear viscoelastic response of two samples prepared following to the two protocols. As we can observe, both samples display the same behavior, thus validating the fact that both time and low temperature lead to the same structure of the sample in the hysteresis region (see Section 6.3.2.2).

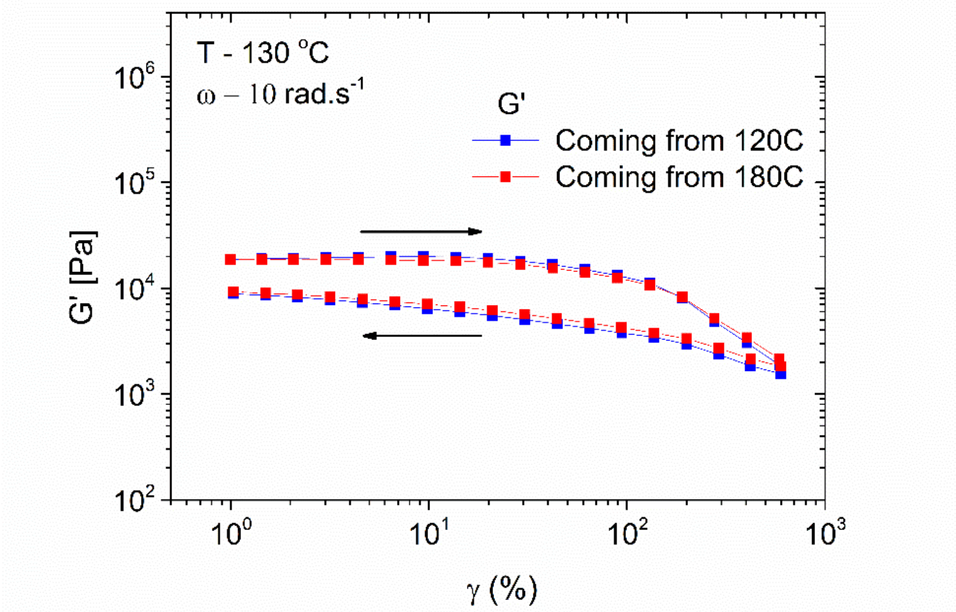

Figure 6.20: Storage modulus of sample 10%HS as a function of strain amplitude during LAOS cycle at 130 °C and 10 rad.s^{-1}. Measurements were performed from low to high and high to low strain amplitudes, respectively. The sample has been equilibrated either by cooling it from 180 °C to 120 °C and then heating it at 130 °C or by cooling it from 180 °C to 130 °C and waiting a long time in order to let the sample the time to equilibrate.

6.4 Summary

In this work, we attempted at decoupling the roles of external (temperature, time, flow) and molecular (composition) parameters on the rheology of segmented copolymers, in order to understand how to control their properties. To this end, we have performed a systematic rheological investigation with model systems made of PTMO SS and monodisperse, H-bonding, T4T HSs.

With the help of a statistical model, we have determined and analyzed the composition of the segmented copolymers. This has allowed us to understand the influence of the HSs density and their association probability on the amount of SSs trapped between associated HSs, and to link this information to the evolution of the high- and low-frequency moduli of the samples.

Entanglements trapped between associated HSs have been found to be responsible for the sharp liquid-to-solid transition of the samples during cooling. At these intermediate temperatures, hysteresis is observed, and we attributed it to the low driving force for the HSs to associate, which require long waiting time before reaching their equilibrium state. Thus, in this T region, the sample properties were found to strongly depend on their thermal history. On the other hand, at low temperatures, the HSs association is very fast and leads to the formation of strong and stable crystallites which reinforce the samples.

We then studied the influence of flow by means of cyclic LAOS strain tests. At high temperatures, we pointed out the influence of a few HS domains detectable through the appearance of a small hysteresis. On the other hand, at intermediate temperatures, we have shown that large flow is affecting the sample modulus in an irreversible way (under this T condition). We attributed this effect to partial disentanglement of the network under shear, due to the fact that when the high shear deformation is suppressed, the chains do not have time to re-entangle before being trapped again between associated HSs. This metastable state is important since it has large implications on the material properties, in term of connectivity of the sample, as reflected by its lower modulus. Then, we have shown that applying large flow at low temperature leads to a change of state of the sample, induced by the reorganization of the crystallites in order to adapt to the flow. As for the partial disentanglement, this order transition has a large effect on the final properties of the sample.

Hence, the large flow has a large effect on the final state of the materials and thus, on their properties. However, this effect can be modulated by playing with temperature.

6.5 References

1) Gaymans, R.J., Segmented copolymers with monodisperse crystallizable hard segments: Novel semi-crystalline materials. Progress in Polymer Science, 2011. 36(6): p. 713-748.

2) Cloitre, M. and D. Vlassopoulos, Block Copolymers in External Fields: Rheology, Flow-Induced Phenomena, and Applications, in Applied Polymer Rheology 2011, John Wiley & Sons, Inc. p. 209-239.

3) Wu, L.; T. P. Lodge, F. S. Bates, Effect of block number on multiblock copolymer lamellae alignment under oscillatory shear, J. Rheol., 49, 1231 (2005).

4) Lodge, T.P., Block copolymers: Past successes and future challenges, Macromol. Chem. Phys. 204, 265-273 (2003).

5) Hu, H.; M. Gopinadhan, C. O. Osuji, Soft Matter, 2014, Directed self-assembly of block copolymers: a tutorial review of strategies for enabling nanotechnology with soft matter, 10, 3867-3889.

6) Li, W.; M. Muller, Direct self-assembly of block copolymers by chemical or topographical guiding patterns: Optimizing molecular architecture, thin-film properties, and kinetics, Progress in Polymer Science 2016, 54-55, 47-75.

7) Gaymans, R. J., and J. L. De Haan. "Segmented copolymers with poly (ester amide) units of uniform length: synthesis." Polymer 34.20 (1993): 4360-4364.

8) Flory, P.J.; "Thermodynamics of high polymer solutions" J. Chem. Phys. 10:51-61 (1942) No. 18, May 6, 1985.

9) Lunardon, G., Y. Sumida, and O. Vogl, Effects of molecular weight and molecular weight distribution of polyester based SSs on the physical properties of linear polyurethane elastomers. Die Angewandte Makromolekulare Chemie, 1980. 87(1): p. 1-33.

10) Khandpur, A.K.; J.S. Farster, F.S. Bates, et al., Macromolecules, 28, 8796 (1995).

11) Ryan, A.J.; S-M Mai, J.P.A. Fairlough, et al., Phys. Chem. Chem. Phys., 3, 2961-2971, (2001).

12) Matsen, M. M., J. Chem. Phys., 113, 5539 (2000).
13) Floudas, G.; D. Vlassopoulos, M. Pitsikalis, et al., J. Chem. Phys., 104, 2083 (1996).
14) G. Floudas, T. Pakula, E.W. Fischer, et al., Acta Polym. 45, 176 (1994).
15) H.H. Winter, D.B. Scott, W. Gronski, et al., Macromolecules, 26, 7236 (1993).
16) J.L. Adams, D.J. Quiram, W.W. Graessley, and R.A. Register, Macromolecules, 29,
2929 (1996).
17) B. Stuhn, A. Vilesov, and H.G. Zachmann, Macromolecules, 27, 3560 (1994).
18) Buckwalter, D.J., J.M. Dennis, and T.E. Long, Amide-containing segmented copolymers. Progress in Polymer Science, 2015. 45: p. 1-22.
19) Biemond, G.J.E., J. Feijen, and R.J. Gaymans, Segmented Block Copolymers with Monodisperse Hard Segments: The Influence of H-Bonding on Various Properties. Macromolecular Materials and Engineering, 2009. 294(8): p. 492-501.
20) Sijbrandi, N. J.; A.J. Kimenai, E. P. C. Mes, R. Broos, G. Bar, M. Rosenthal, Y. Odarchenko, D. A. Ivanov, P. J. Dijstra, J. Feijen, Synthesis, Morphology, and Properties of Segmented Poly(etheramide)s with Uniform Oxalamide-Based Hard Segments, Macromol. 2012, 45, 3948-3961.
21) Holden, G., et al., Thermoplastic Elastomers1996, Munich: Hanser Publisher.
22) Velankar, S. and S.L. Cooper, Microphase Separation and Rheological Properties of Polyurethane Melts. 1. Effect of Block Length. Macromolecules, 1998. 31(26): p. 9181-9192.
23) Castagna, A.M., et al., The Role of Soft Segment Molecular Weight on Microphase Separation and Dynamics of Bulk Polymerized Polyureas. Macromolecules, 2012. 45(20): p. 8438-8444.

24) Ng, H.N., et al., Effect of Segment Size and Polydispersity on Properties of Polyurethane Block Polymers. Polymer, 1973. 14(6): p. 255-261.

25) Baeza, G.P., A. Sharma, A. Louhichi, L. Imperiali, W. P. J. Appel, C. F. C. Fitie, M.P. Lettinga, E. van Ruymbeke, D. Vlassopoulos, Multiscale organization of thermoplastic elastomers with varying content of hard segments. Polymer, 2016. 107: p. 89-101.

26) Arun, A., K. Dullaert, and R.J. Gaymans, Structure and Properties of Mono-, Di-, Tri- and Multiblock Segmented Copolymers with Diamide Hard Segments. Macromolecular Chemistry and Physics, 2009. 210(1): p. 48-59.

27) Eisenbach, C.D., M. Baumgartner, and C. Günter, Polyurethane Elastomers with Monodisperse Segments and their Model Precursors: Synthesis and Properties, in Advances in Elastomers and Rubber Elasticity, J. Lal and J.E. Mark, Editors. 1986, Springer US: Boston, MA. p. 51-87.

28) Arun, A., K. Dullaert, and R.J. Gaymans, The melt rheological behavior of AB, ABA, BAB, and (AB)n block copolymers with monodisperse aramide segments. Polymer Engineering & Science, 2010. 50(4): p. 756-761.

29) Lips, P.A.M.; R. Broos, M.J.M. van Heeringen, P.J. Dijkstra, J. Feijen, Synthesis and characterization of poly(ester amide)s containing crystallizable amide segments, Polymer 46 (2005), 7823-7833.

30) Fredrickson, G.H., S.T. Milner, and L. Leibler, Multicritical phenomena and microphase ordering in random block copolymers melts. Macromolecules, 1992. 25(23): p. 6341-6354.

31) Shirasaka, H., et al., Polyurethane Urea Elastomer Having Monodisperse Poly(oxytetramethylene) as a Soft Segment with a Uniform Hard Segment. Macromolecules, 2000. 33(7): p. 2776-2778.

32) van der Schuur, M. and R.J. Gaymans, Segmented block copolymers based on poly(propylene oxide) and monodisperse polyamide-6,T segments. Journal of Polymer Science Part A: Polymer Chemistry, 2006. 44(16): p. 4769-4781.

33) Biemond, G.J.E., J. Feijen, and R.J. Gaymans, Influence of polydispersity of crystallizable segments on the properties of segmented block copolymers. Polymer Engineering and Science, 2008. 48(7): p. 1389-1400.
34) Eisenbach, C.D. and H. Nefzeger, New insights in the structure and properties of segmented polyurethane elastomers from non-hydrogen bond forming model systems. In: Multiphase macromolecular systems, contemporary topics in polymer science, 1989, Plenium Publ Corp: New-York. p. 339-361.
35) Baeza, G.P., et al., Network dynamics in nanofilled polymers. Nature Communications, 2016. **7**.
36) Aime, S, N. Eisenmenger, T. Engels, A model for failure in thermoplastic elastomers based on Eyring kinetics and network connectivity, J. Rheol 2017, 61.
37) Bates, F.S., et al., Multiblock Polymers: Panacea or Pandora's Box? Science, 2012. 336(6080): p. 434-440.
38) Flory, P. J.; Trans. Faraday Soc. 1955, 51, 848.
39) Vanhutten, P.F., R.M. Mangnus, and R.J. Gaymans, Segmented Copolymers with Polyesteramide Units of Uniform Length - Structure-Analysis. Polymer, 1993. 34(20): p. 4193-4202.
40) Boussias, C. M. R.H. Peters, R.H. Still, J. Appl. Polym. Sci., 1980, 25, 855.
41) Takahashi, T.; F. Nagata, J. Macromol. Sci. Phys., 1991, 30, 25.
42) Schneider, N.S., et al., Structural studies of crystalline MDI-based polyurethanes. Journal of Macromolecular Science, Part B, 1975. 11(4): p. 527-552.
43) Foks, J., I. Naumann, and G.H. Michler, Beitrag zur Aufklärung der Morphologie von segmentierten Polyurethanen. Die Angewandte
44) Foks, J., H. Janik, and R. Russo, Morphology, thermal and mechanical properties of solution-cast polyurethane films. European Polymer Journal, 1990. 26(3): p. 309-314.
45) Sharma, A.; G. P. Baeza, L. Imperiali, W. P.J. Appel, C. Fitie, G. Vanden Poel, E. van Ruymbeke, Fast scanning calorimetry clarifies the

understanding of the complex melting and crystallization behavior of polyesteramide multi-block copolymers, accepted in Polymer Int, DOI 10.1002/pi.5713.

46) VR Tirumala, T Tominaga, S Lee, PD Butler, E Lin, JP. Gong, W. Wu, J. Phys. Chem. B 2008, 8024

47) Y. Matsumita, H. Watanabe, A. Takano, Y. Takahashi, Macromol. 2013, 2681.

48) S.S. Patel, R.G. Larson, K.I. Winey, and H. Watanabe, Macromolecules, 28, 4313
(1995.

49) K. Luo and Y. Yang, Macromolecules, 35, 3722–3730 (2002).

50) E. Di Cola, C. Fleury, P. Panine, and M. Cloitre, Macromolecules, 41, 3627 (2008).

51) M.E. Vigild, C. Chu, M. Sugiyama, et al., Macromolecules, 34, 951 (2001).

52) A. Phatak, C. W. Macosko, F. S. Bates, and S. F. Hahn, J. Rheol. 49, 197 (2005).

53) Wu, L., T. Lodge, F. Bates, Bridge to Loop transition in a shear aligned lamellae forming heptablock copolymer, Macromo., 37, 8184-8187, 2004

54) L. Wu, T.P. Lodge, F.S. Bates, Macromolecules, 39, 294 (2006).

55) Mori, Y.; L. S. Lim, F. S. Bates, Consequences of molecular bridging in lamellae-forming triblock/pentablock copolymer blends, Macromol. 36, 9879-9888, 2003.

56) V. Ganesan and G.H. Fredrickson, Model for the rheology and nonlinear response of layered materials, J. Rheol., 45, 161 (2001).

57) Chen, Z.R. and J.A. Kornfield, Flow-induced alignment of lamellar block copolymer melts. Polymer, 1998. 39(19): p. 4679-4699.

58) Ianniruberto, G. and G. Marrucci, Do Repeated Shear Startup Runs of Polymeric Liquids Reveal Structural Changes? ACS Macro Letters, 2014. 3(6): p. 552-555.

59) L. J. Fetters, D. J. Lohse, D. Richter, T. A. Witten, and A. Zirkel, Connection between Polymer Molecular Weight, Density, Chain

Dimensions, and Melt Viscoelastic Properties, Macromolecules, 1994, 27 (17), 4639–4647.

60) E Van Ruymbeke, JJM Slot, M Kapnistos, PAM Steeman, Structure and rheology of branched polyamide 6 polymers from their reaction recipe, Soft Matter 9 (29), 6921-6935.

61) E. van Ruymbeke, A Kaivez, A Hagenaars, D. Daoust, P. Godard, R. Keunings, C. Bailly, Characterization of sparsely long chain branched polycarbonate by a combination of solution, rheology and simulation methods, 2006, Journal of Rheology, 949.

62) D. Richter, B. Farago, L. J. Fetters, J. S. Huang, B. Ewen, and C. Lartigue, Direct microscopic observation of the entanglement distance in a polymer melt, 1989, Phys. Rev. Lett. 64, 1389.

63) Niesten, M.C.E.J., J. Feijen, and R.J. Gaymans, Synthesis and properties of segmented copolymers having aramid units of uniform length. Polymer, 2000. 41(24): p. 8487-8500.

64) Krijgsman, J., D. Husken, and R.J. Gaymans, Synthesis and properties of thermoplastic elastomers based on PTMO and tetra-amide. Polymer, 2003. 44(25): p. 7573-7588.

65) Husken, D., J. Feijen, and R.J. Gaymans, Hydrophilic segmented block copolymers based on poly(ethylene oxide) and monodisperse amide segments. Journal of Polymer Science Part A: Polymer Chemistry, 2007. 45(19): p. 4522-4535.

66) LGD Hawke, M Ahmadi, H Goldansaz, E Van Ruymbeke, Viscoelastic properties of linear associating poly (n-butyl acrylate) chains, Journal of Rheology 60 (2), 297-310.

Chapter 7: **Thermal and viscoelastic properties of Dumbbell PEAs**

Abstract

In this chapter, we study the properties of the polyesteramides (PEAs) with a dumbbell architecture. As mentioned in chapter 3 (section 3.5), they were synthesized based on poly(tetramethylene oxide) (PTMO) soft and T4T HSs. These samples show unexpectedly broad and complex melting transition irrespective of change of polymer chain architecture. In order to understand these transitions, Fast Scanning Calorimetry (FSC) measurements were performed, following the same protocol as the one used for segmented PEAs over the wide range of temperature i.e. from -100 °C to 200 °C. This allows us to present a systematic comparative study on the association of HSs as a result of polymer chain architecture. Moreover, the crystallization rate and effect of chain mobility on the formation of metastable ribbon-structure is also highlighted.

In order to understand the effect of polymer chain architecture on viscoelastic properties, we present shear rheological results in comparison to segmented PEAs. In particular, the influence of time, frequency and strain amplitude over a broad temperature range on the association of HSs were studied, accounting for the influence of chain entanglements and mobility on their viscoelastic response.

7.1 Introduction

Structure development and its effect on thermal and viscoelastic properties of segmented PEAs containing PTMO SS and well-defined T4T HS have been studied in chapters 4, 5 and 6. The concentration of HSs was varied, and we showed that it had a huge consequence on thermal and viscoelastic properties. It was attributed to the ability of the HSs to associate more or less easily, based on the hydrogen bonding density of these materials.

It was evident from DSC that the melting temperature of these segmented PEAs is strongly dependent on the concentration of HSs in the polymer. However, the melting endotherms were broad and complex.[1] This complex melting was related to the different kinds of T4T structure formed based on the processing condition, as it was confirmed with FSC measurements. The effect of progressive cooling of these materials from melt leads to the formation of crystallites from nucleation points, whereas a sudden quenching between T_m and T_g led to formation of amorphous morphology.[2] In between these two extremes the isothermal measurements, a high fraction of smaller and metastable baby-ribbons can be obtained, depending on the isothermal temperature. Moreover, the crystallization kinetic study for the 20%HS sample revealed that two crystallization processes can take place, involving the global or the local mobility of the chains. At high temperature, the driving force for crystallization is low, however, the chains have time to diffuse and create strong crystals.[2] On the other hand, at low temperature, the crystallization is too fast compared to the chain mobility, which leads to the formation of another kind of crystal, characterized by lower melting temperature. In this second case, we showed that the chains do not have time to diffuse before the association of the HSs. Interestingly, the 10%HS samples showed only one crystallization process, since, at high temperature, crystallization driving forces are too weak to lead to the crystal formation. In consequence, only weaker crystals, associated to the local motion of the chains, could be formed. This again confirmed the important role of chain mobility. Complementary to the FSC measurements, rheological studies of these segmented PEAs revealed a great influence of concentration of HSs and parameters like time and temperature and flow on the viscoelastic properties. Rheological measurements highlighted the importance of chain entanglements at intermediate and high temperatures. Entanglements trapped between associated HSs were found to be responsible for the sharp liquid-to-solid transition of the samples during cooling. Then, the fast HS association at low temperatures leads to the formation of strong and stable crystallites. At intermediate temperatures, hysteresis was observed. We showed that it can be attributed to the long waiting time needed in order to form stable crystallites and reach an equilibrium state. We also studied the effect of large shear flow on the properties of these samples. At low temperatures, it was found that after the flow cessation, the fast HSs association takes place before the chains fully re-entangle, leading to a lower elasticity. This metastable state is rheologically important as entanglements ensure sample cohesion after the breakage of the HSs domains. Hence, temperature variation combined with time and flow allows controlling chain re-entanglement and thus tuning the final properties of the network.

In this chapter, our objective is to design new copolymers, characterized by both a large density of HSs and high chain mobility. To this end, ‘dumbbell' copolymers, with the HSs localized at the chain extremities were synthesized (see chapter 3). Indeed, with such architecture, we should, a priori, avoid the presence of HS trapped between two associated HSs, and therefore not able to associate into a strong crystal structure. Furthermore, since the HSs density can be large, we expect that these samples show a high modulus. It must be noted however that, contrary to the segmented copolymers, the molar mass of the chain strongly varies with the HSs density. This is, therefore, a new parameter to consider.

7.2 Materials

Dumbbell copolymers containing PTMO SS and monofunctional T4T HSs were synthesized via condensation polymerization reaction (see chapter 3). The concentration of HSs was systematically varied corresponding to the samples with 3, 5 and 20wt%. The samples were dried in a vacuum oven at 65 °C before use.

7.3 Instrumentation and Sample preparation

7.3.1 Differential Scanning Calorimetry (DSC)

DSC thermograms were recorded on a Mettler Toledo DSC821e equipped with the STARe software. Calibration of an instrument was performed using Indium and Tin standards, covering the wide temperature range required for measuring the synthesized dumbbell PEA copolymers (-90 to 300 °C). Polymer samples were dried overnight in a vacuum oven at 60 °C and 10 – 14 mg of samples mass were measured at 20 °C.min^{-1} under nitrogen for both cooling and heating thermograms. The temperature profile used for the measurement ranges from -80 to 250 °C, temperature at which the samples were held for 15 min. to obtain homogenous melt and erase sample history. The melting (T_m) and the crystallization (T_c) temperatures were respectively extracted from the second heating and first cooling runs. In addition to this, in order to discuss the influence of waiting time on the sample properties, similar method was used but with different cooling and heating rate. First, a rate of 5 °C.min^{-1} was used during cooling while the heating was performed at 20 °C.min^{-1} during heating, then opposite rates were used (i.e. cooling with 20 °C.min^{-1} and heating with 5 °C.min^{-1}).

7.3.2 Fast Scanning Calorimetry (FSC)

Fast-scan measurements were performed by using a commercially available Fast Scanning Chip Calorimetry (FSC) from

Mettler-Toledo, Switzerland, with a Huber TC100 intercooler and nitrogen purge gas of 50 mL.min^{-1}. The detailed description about instrumentation, operating procedure and calibration has been described in chapter 5 and ref.[3-7] Sample mass of 250 nanograms was calculated for 20%HS samples using the method mentioned in the section 5.2.2 and ref.[5, 7]

Effect of cooling rate – Starting from the melt state (200 °C) 10 s, the sample was cooled down to -80 °C at a rate varying from 10 °C.s^{-1} to 4000 °C.s^{-1}. After having held the sample for 10 s at -80 °C it was subsequently heated back to 200 °C at a constant heating rate of 1000 °C.s^{-1}. The heating rate of 1000 °C.s^{-1} was selected based on the previous studies by G. Vanden Poel et al.[5], showing that the thermal lag corrections remain relatively low up to this heating rate (a maximum lag of -1.4 °C was observed for a 1 µg sample).[5] The corresponding temperature program is presented in Figure 1a.

Isothermal crystallization $(T_m - T_g)$ – Isothermal crystallization measurements were performed on samples covering the entire temperature range from T_m (134 °C to T_g (ca -60°C), in order to calculate the crystallization rate. Starting from the melt state (200 °C), the sample was quenched to T_{iso} at a cooling rate of 4000 °C.s^{-1} to avoid any crystallization to occur and held at this temperature for a time $t_{iso} =$ 2 s, whereafter the material is further quenched to -80 °C at the same cooling rate. In order to understand the crystallization behavior of the PTMO-T4T material small steps of 5 °C at T_{iso} were performed, from T_m to T_g. After holding for 10 s at -80 °C, it was finally heated back to 200 °C at 1000 °C.s^{-1} (see Figure 1b). In the following sections, this protocol is referred to as a two-step quenching. A similar set of measurements have also been performed with increasing t_{iso} to 60 s.

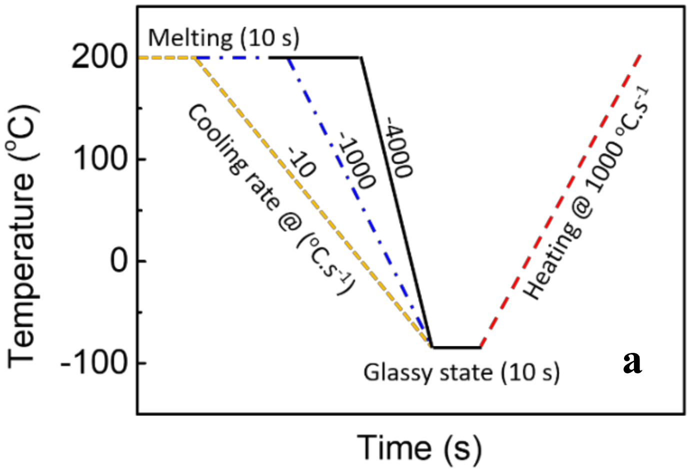

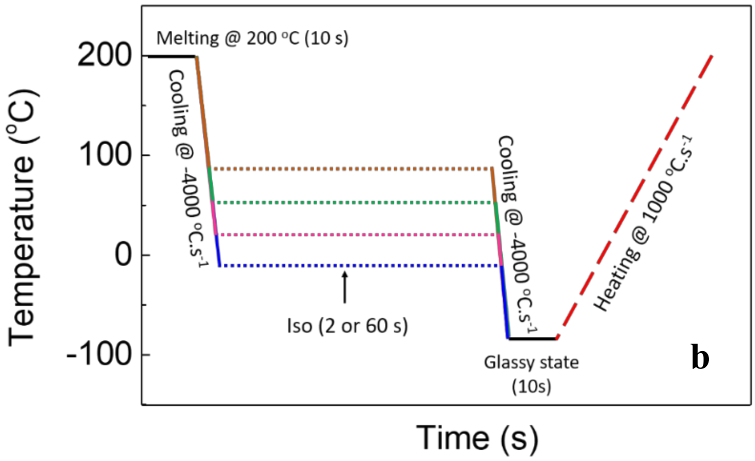

Figure 7.1: Different thermal treatments used in FSC a) varying the cooling rate, b) varying the temperature T_{iso} at which the sample is kept 2 s before the measurement as well as the waiting time at T_{iso}.

7.3.3 Rheological measurements

Rheological measurements (dynamic frequency, strain and temperature sweeps) were performed with a stress-controlled rheometer

(MCR 301 from Anton Paar, Austria) equipped with stainless steel parallel plates of diameter 8 mm. Before measuring, the samples were molten at a temperature $T = T_m + 10$, trimmed, and subsequently cooled down at the target temperature. These measurements were performed at a frequency of 10 rad.s^{-1} and strain amplitude of 1% and 0.1%. All measurements were carried out in a nitrogen gas atmosphere, whereas temperature control (better than ±0.3 °C) was achieved by means of a convection oven.

7.4 Result and Discussion

7.4.1 DSC analysis

The thermal properties of the three dumbbell PEA samples, containing 3, 5 and 20%HS were studied using conventional DSC, in chapter 3 (section 3.6.6) with a heating rate of 20 °C.min^{-1}. The respective thermograms are reproduced from chapter 3 as shown in Figure 7.2. It was observed that all three samples show a value of T_g around -60 °C irrespective of change of polymer chain architecture and amount of HS like segment PEAs. However, only 20%HS sample shows the melting of PTMO SS around 0 °C, unlike segmented copolymers (at -15 °C) probably due to induced crystallization by, the shorter chain length of SS compared to the other dumbbell PEA samples. In the high-temperature region, an increase of the melting point T_m from 74.2 to 136.5 °C is observed as HS concentration is increased from 3 to 20%. Furthermore, the 20%HS sample shows a broad and multiple melting transitions, which was not expected since a priori a better organization of HSs should be observed due to the polymer chain architecture. The 20%HS sample shows the undercooling ($\Delta T = T_m - T_c$) of ~11 °C, which is low as compared to segment PEAs and PBT based polymers.[8, 9] This observation suggests a fast crystallization process, likely due to the architecture of polymer chain or due to the short chain length. The crystallization temperature

(T_c) was determined from the cooling exothermal curve, the cooling curves are however not shown in Figure 7.2.

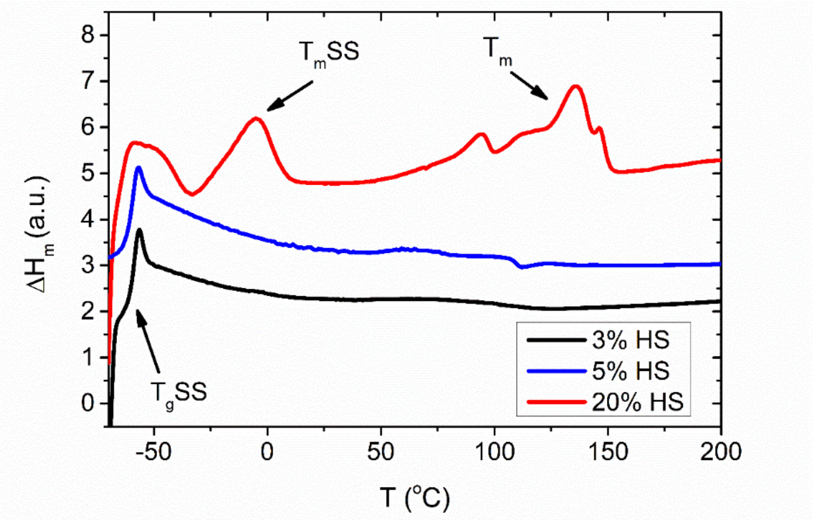

Figure 7.2: Differential Scanning Calorimetry thermograms of PEAs containing 3, 5 and 20%HS performed at a heating rate of 20 °C.min^{-1}. Data have been vertically shifted for clarity.

To understand the broad nature of melting peaks and organisation of T4T HS structures, the 20%HS dumbbell sample was subjected to the different cooling and heating rate as shown in Figure 7.3. When the sample was cooled slowly (5 °C.min^{-1}) and heated fast with the rate of 20 °C.min^{-1} (red curve), only two melting peaks were observed. It seems therefore that the complex melting obtained in Figure 7.2 is due to a too fast cooling of the sample, leading to some cold crystallization process. The slow cooling of the sample leads to two melting peaks endotherms, can be attributed to the different kind of T4T HS associations, one representing the baby-ribbon like structure having melting peak at 80 °C and other having ribbon like structure showing melting at 124 °C. The higher melting temperature i.e. 124 °C is however lower as compared to 135 °C reported for 20%HS dumbbell in chapter 3. This difference is comparable to the difference in crystallization temperatures, equal to 124.8 °C with the segmented copolymer and to 115 °C with the dumbbell chains.

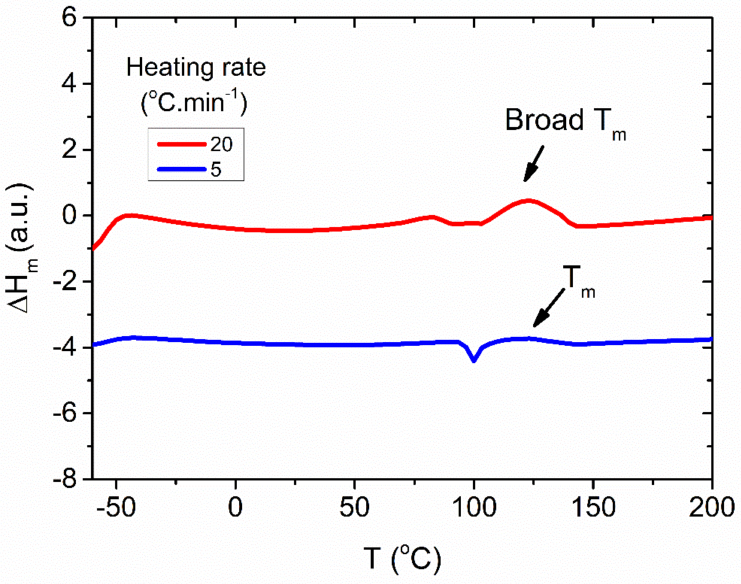

Figure 7.3: DSC heating curves for 20%HS dumbbell sample during heating rate of 5 and 20 °C.min^{-1}, after having cooled down the sample with a rate of 20 and 5 °C.min^{-1}

Figure 7.3 also shows the heating curves obtained when the sample was cooled fast (20 °C.min^{-1}) and heated slow with the rate of 5 °C.min^{-1} (blue curve). In such a case, the melting peak was observed at 124 °C, which was identical to the fast heating method. However, a small exotherm is observed at around 100 °C. It is probably due to the cold crystallization of a part of the T4T hard domains. On contrary to Figure 7.2, no melting of the SS was observed, which is not easy to understand. Due to the limitation on further increasing and decreasing the cooling and heating rate with conventional DSC is not feasible and to get the better understanding on the organisation of T4T HS, further studies were done using FSC measurements.

7.4.2 Effect of cooling rate on the crystallization and melting

The Dumbbell PEA sample containing 20%HS is investigated by using the method summarized in Figure 7.1 (a). The aim is to understand the effect of high and low cooling rate on the structural evolution of the T4T hard-domains when chain architecture of polymer is changed. The results are presented in Figure 7.4, as heating curves are fixed at the rate of 1000 °C.s^{-1} after a cooling step performed at rates from 10 to 4000 °C.s^{-1}, from 200 °C down to -80 °C. At low temperatures, the thermograms show the glass transition of the PTMO SSs (T_g) around -60 ^{o}C, as observed in conventional DSC (see Figure 7.2). No clear melting of the SS can be observed, whereas it was observed in conventional DSC. Upon increasing the cooling rates above 200 °C.s^{-1}, a cold crystallization peak appears around 50 °C, pointing at the so-called critical or quenching rate.[6] It can be noticed here that while the cold crystallization temperature is similar for dumbbell and segmented PEAs, the rate at which the cold crystallization is observed are very different i.e. 800 °C.s^{-1} for the segmented sample and 200 °C.s^{-1} for the dumbbell copolymers, both samples containing 20%HS. For T>108 °C, an endothermal event is seen, standing for the melting of T4T crystallites. However, the melting temperature of HSs (shown in Figure 7.4) only slightly increases in a monotonic way (from 108 to 115 °C) with decreasing the cooling rate. While with segmented PEAs, it was clear that the slower the cooling rate, the better the T4T crystals can organize into well-organized ribbon structures characterized by a higher melting temperature, this is not the case with dumbbell copolymers since the slow cooling leads to the formation of T4T crystals which melts at 115 ^{o}C, whereas the cold crystallized T4T at high cooling rate melts at 108 ^{o}C, which is not a large difference in comparison to segmented PEAs. This low effect of cooling rate suggests that the cold crystallized structures are nearly as good as the ones which are crystallized at a slow cooling rate. Since the chains are short and the HSs are located at the chain extremity, chain mobility is very high and does not seem to affect the way the crystallites are formed, which differs from the segmented copolymers.

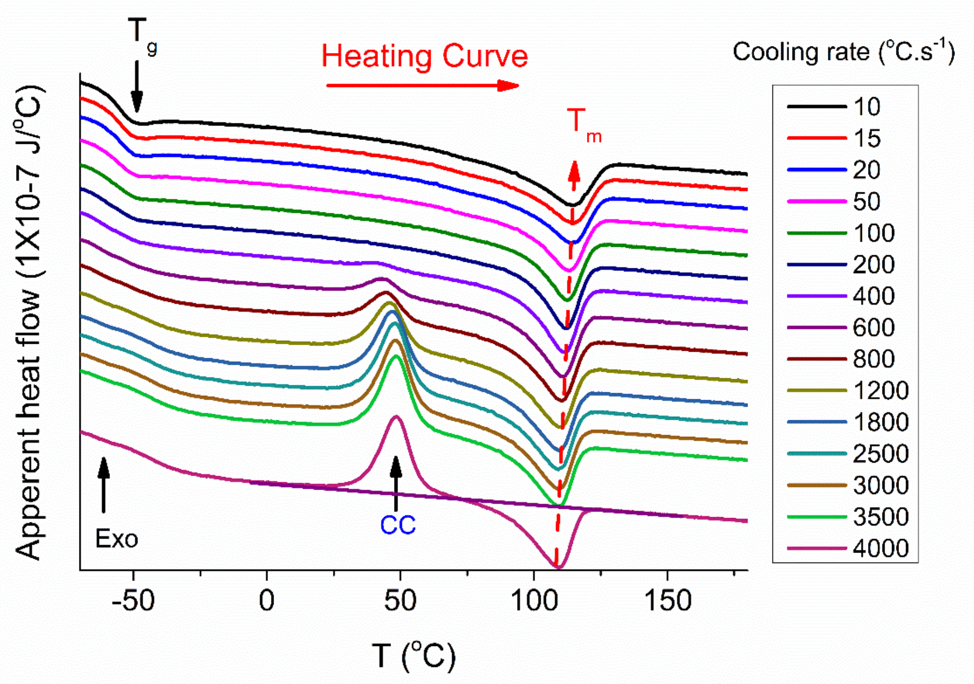

Figure 7.4: Thermograms measured on a 20%HS sample during a heating step performed at 1000 °C.s^{-1}. Prior to the measurements, the sample was cooled down from 200 to -80 °C at different cooling rates going from 10 °C.s^{-1} to 4000 °C.s^{-1}. Data is shifted vertically for clarity and the last thermogram shows the flat baseline selected for peak integration.

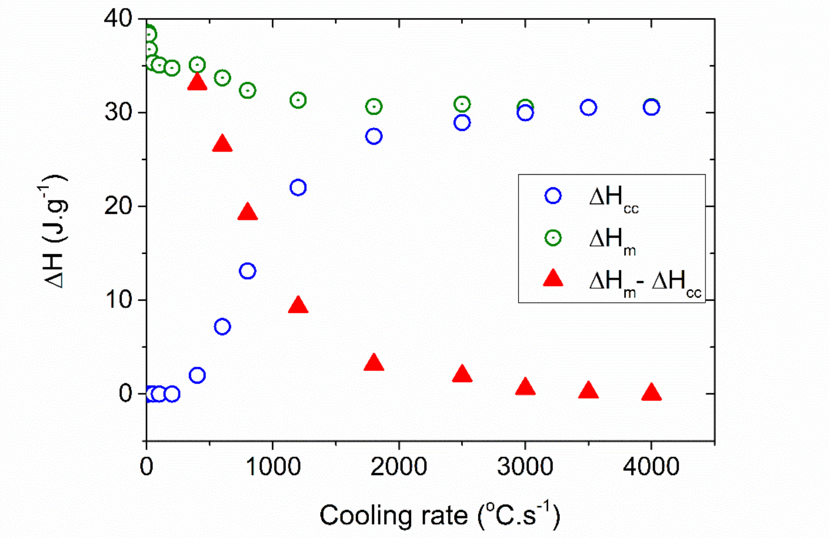

Figure 7.5: Variation of enthalpy in 20%HS dumbbell for Cold Crystallization (ΔH_{cc}), terminal melting (ΔH_m) and the difference (ΔH_m - ΔH_{cc}).

In order to evaluate the cold crystallization and melting behaviour of the HSs, the specific enthalpy variations (± 2 J.g^{-1}) ΔH_m and ΔH_{cc} were quantified, as shown in Figure 7.5. No CC is observed at low cooling rate i.e. from 10 °C.s^{-1} to 200 °C.s^{-1}, but a slight decrease in ΔH_m is observed. However, the CC starts to occur and ΔH_{cc} significantly increases at rates above 200 °C.s^{-1} until it reaches its maximum value of 30 J.g^{-1}, at a quenching rate of 3500 °C.s^{-1} and above. The enthalpy of melting at cooling rates below 200 °C.s^{-1} are high due to the formation of T4T ribbon structures. At fast cooling, the formation of these ribbons is prohibited, which leads, after cold crystallization, to an almost equal amount of melting enthalpy. This can be explained by the fact that when the amorphous dumbbell sample is heated, it can quickly reorganize into an almost perfect structure, as already mentioned based on Figure 7.4, where end melting endotherm does not show much difference as a function of cooling rate.

7.4.3 Impact of T_{iso} on the crystallization of dumbbell PEA

In order to further understand the thermal behavior of these copolymers, the isothermal measurements were performed i.e. T_{iso}, from T_m to T_g, in order to investigate the influence of temperature on the crystallite's formation. The method for this measurement is depicted in Figure 7.1 (b). The obtained thermograms are presented in Figure 7.6, showing a rich variety of melting behaviors. Therefore, these results are analyzed separately, by dividing the isothermal temperatures into several regions:

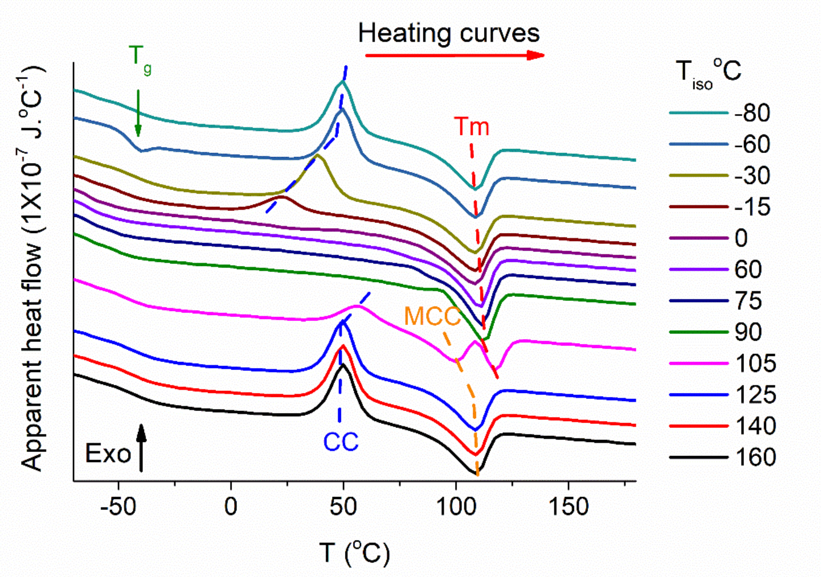

Figure 7.6: Thermograms recorded from the 20%HS sample during the heating at 1000 °C.s^{-1}, after a two-step quenching with varying T_{iso} from T_m to T_g. For each sequence, the sample was isothermally held for 2 s at T_{iso}. Data is shifted vertically for clarity.

For T_{iso} ≥115°C, the thermograms after 2 seconds spent at these high values of T_{iso} and then subsequently quenched below its T_g, do not allow any crystallization to occur during the cooling phase. Therefore, once the material is heated back, as expected, cold crystallization (CC) takes place. CC temperature is around 50 °C, which is 15 °C more as compared to segmented 20%HS samples, indicating more energy required for dumbbell T4T HSs to crystallize. These so-formed cold crystals melt (MCC) at around 109 °C.

At T_{iso} = 105 °C, an additional peak appears at high temperature (≈117 °C) due to the creation of very stable T4T crystallites whereas it is not observed anymore for lower T_{iso}. At such high T_{iso}, chains have large mobility combined with a low driving force for crystallization. Therefore, the chains have the time to disentangle and diffuse before starting to crystallize, which favors the creation of well-organized crystals within the isothermal temperature and time frame. On the other hand, it is observed that not all T4T crystals crystallize into such strong crystals, the remaining HS cold crystallizing during the heating process. The corresponding amplitude of the CC peak decreases, while the CC temperature is increased. In conclusion, crystallization just below T_c i.e. 124 °C (see chapter 3, Table 9) seems of interest since it allows the formation of crystallites characterized by a higher melting temperature.

By decreasing further T_{iso}, from **105 °C to 100 °C**, this equilibrium between chain mobility and crystallization driving force is modified toward a higher crystallization rate (see section 7.4.5) and lower chain mobility. In particular, it is observed that the lower T_{iso}, the lower is the T_m. This can be attributed to the fact that higher crystallization rate leads to the formation of a larger number of smaller crystallites, which cannot grow further due to the lower mobility of the (associated) chains. Also, while part of the HSs is seen to crystallize during the cooling phase, a small fraction of them is observed to cold crystallize during the subsequent heating. The corresponding CC temperature is found to be higher than the one reported for higher T_{iso}, suggesting that the HS associations made along the cooling step hinder the motion of the chains. This is also supported by a lower melting point of the smaller crystals originating during cold crystallization.

For 0 °C < $\boldsymbol{T_{iso}}$ < 100 °C, CC is no longer observed since the sample has a high crystallization rate and fully crystallizes during the isothermal 2 seconds-waiting time. Figure 7.6 further reveals that the melting temperature of the largest ribbons, T_m, formed in this range of temperatures is nearly independent of T_{iso}. More precisely, decreasing T_{iso} from 100 °C to 90 °C leads to the formation of crystallites melting at lower temperatures while decreasing T_{iso} from 90 °C to 0 °C does not influence the melting behavior of the crystallites anymore. In both cases, T_m is a bit lower than the high melting temperature observed at T_{iso} = 105 °C. It must be noted here that this high melting peak cannot be attributed to a melting recrystallization process as observed in several semi-crystalline polymers. Indeed, one can disprove this possibility since the melting temperature of this high melting peak is not affected by varying the heating rate. This suggests that in this range of temperatures, the formation of the crystals is mostly governed by the high thermodynamic driving force, leading to the fast formation of ribbons taking place before any significant chain's diffusion allowing the eventual creation of strong crystallites (high T_m).

Interestingly, the secondary peak, T_{sh} observed for segmented PEAs is not observed for dumbbell, indicating the good and fast association of the HSs without getting trapped due to associating HSs. Based on these results it is clear that the change in polymer chain architecture plays an important role to control the low-temperature structures. It can also be associated with the short chain length of the polymer, avoiding the trapping of the HSs.

Finally for $\boldsymbol{T_{iso}}$<0 $\boldsymbol{°C}$, the experiments are shown in Figure 7.6 show that when the sample is quenched from 200 °C to a temperature close to T_g, no significant crystals have time to develop due to the quasi-arrested chain dynamics. Around T_g, the growth of the T4T crystals is highly restricted due to very low chain mobility. This is also shown by a decreasing crystallization rate, observed when reaching 0 °C (see section 7.4.5). It can also be noted that under these conditions, SS crystallization or melting is not observed, which is evident from conventional DSC.

7.4.4 Influence of holding time t_{iso}

In Figure 7.6, the 2 seconds waiting time at T_{iso} may be enough for the HSs to crystallize in the temperature range of T_{iso} 95 °C to 0 °C, but not enough to reach a thermodynamic equilibrium for high and low T_{iso}, (leading to CC detected at these T_{iso} values). Therefore, in order to investigate the influence of time on the possible formation of crystals, the waiting time was increased to $t_{iso} = 60$ seconds (see Figure 7.7), in order to understand the development of the ribbon-like structure. First, it is observed that at T_{iso} = 125 °C, a longer waiting time allows the formation of a small fraction of much more perfect crystallites, characterized by a very high melting temperature close to 150 °C. This melting temperature is similar to the one found with segmented copolymers (see chapter 5): a high value of T_{iso} (around T_c = 124 °C) leads to the formation of well-organized crystals but needs a long time to grow due to their low crystallization driving force. It was observed for segmented PEAs that, increasing t_{iso}, the larger fraction of associated HSs limits the mobility of the trapped, unassociated, segments, therefore leading to a delay of their corresponding CC. As seen in Figure 7.7. this is not true for the dumbbell sample, as the CC temperature stays the same with 2s or 60s waiting time at iso-temperature. Only the decrease in amplitude of the CC peak is observed. This observation confirms that the HS trapping doesn't take place due to dumbbell architecture.

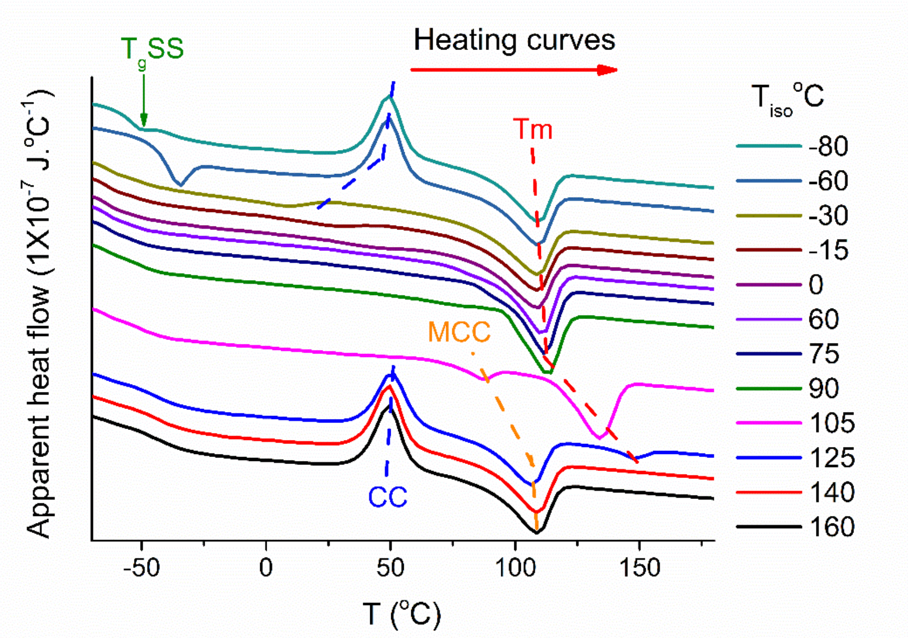

Figure 7.7: Thermograms recorded from the 20%HS sample during the heating phase at 1000 °C.s^{-1}, after a two-step quenching with varying T_{iso} from T_m to T_g. For each sequence, the sample was isothermally held for 2 s at T_{iso}. Data is shifted vertically for clarity.

Same conclusions can be drawn from the low-temperature observations i.e. T_{iso} ranging from 90 to -15 °C. At these temperatures, only the terminal melting peak is observed. Due to the dumbbell architecture of the chains, HSs being on both the end of the chain have more freedom to associate with other segments without getting trapped. All HSs crystallize forming a ribbon-like structure, which melts at around 110 °C.

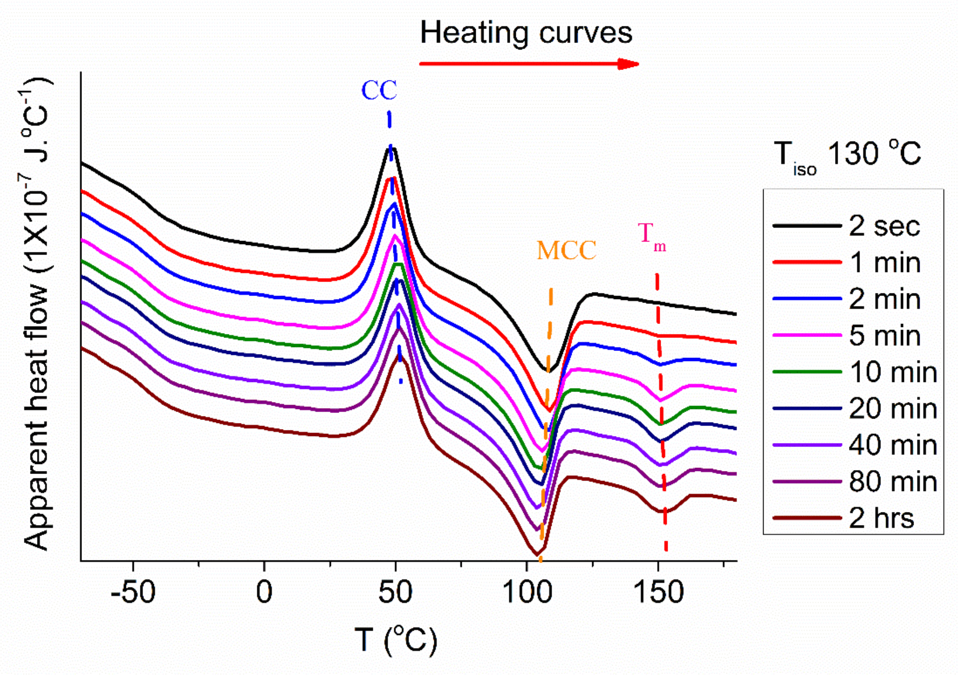

Figure 7.8: Thermograms recorded from the 20%HS sample during the heating phase at 1000 °C.s^{-1}, after an isothermal step at 130 °C. is shifted vertically for clarity.

In order to understand the effect of chain mobility and formation of perfect crystals, isothermal measuring as a function of holding time was performed at T_{iso}=130 °C, just below the melting temperature of the 20% dumbbell copolymer. The obtain thermograms are shown in Figure 7.8. For a waiting time of 2 s, as observed in previous isothermal measurements, crystals are only formed by CC at 50 °C and their corresponding melting takes place at around 105 °C. However, as the holding time is further increased from 1 min to 2 hrs an extra melting peak appears at 150 °C, the amplitude of which increases with holding time. This peak is due to the formation of T4T crystals. Thus, this result shows that at such high temperature (130 °C), the driving force for crystal formation is low but not negligible. Therefore, it must be compensated by a long waiting time.

7.4.5 Crystallization kinetics of 20% dumbbell

In order to understand the above observations, we compare in Figure 7.9 the crystallization rates of the dumbbell copolymers containing 20% of HSs with the corresponding 20%HS segmented samples, as a function of their isothermal temperature. The crystallization rates have been extracted according to the method developed by Vanden Poel.[5] The 20%HS segmented and dumbbell sample, a bimodal distribution of crystallization rate, with two maxima located for each i.e. at 86 and 36 °C for segmented whereas 70 and 30 °C for dumbbell respectively. These maxima are related to the crystallization process of T4T when isothermally hold at respective temperatures. The high-temperature maximum is attributed to the crystallization taking place due to an equilibrium between the thermodynamic driving force and chain mobility.

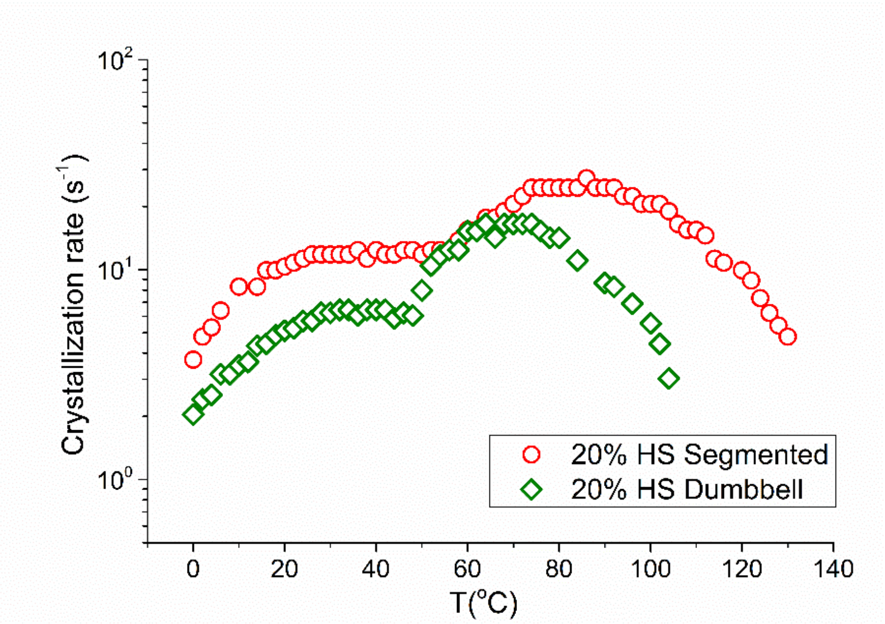

Figure 7.9: Crystallization rate as a function of temperature T_{iso}, for 20%HS dumbbell and segmented samples.

As shown in Figure 7.9, at high temperature the crystallization rate is slow and isothermal time play an important role in the crystallization of T4T HSs. As it is evident from Figure 7.8, crystalline structures can still be formed at 130°C even if their crystallization rate is too small to be measured. Further decreasing T_{iso} shows an increase in crystallization rate, with a maximum at 70 °C. This is consistent with the previous results since the heating curves obtained after a 2 s waiting time at constant temperature in the range of 100 to 70 °C do not show any cold crystallization peak. On further decreasing T_{iso}, the crystallization rate passes through a minimum and around 50 °C, attributed to the reduction of the ability of the chain to diffuse. However, the crystallization rate is still large enough to ensure the crystallization of all T4T HSs and no cold crystallization is observed at T_{iso} ranging from 70 °C to 30 °C, with second maximum observed at 30 °C. Similar second maximum was observed for segmented PEA sample, due to the formation of baby-ribbons as chain mobility is very low at these temperatures. Moreover, the melting of baby-ribbon was observed during the heating step. Interestingly, for dumbbell sample, this low temperature does not affect the melting peak position and does not lead to cold crystallization. From this result, one can conclude that even at low T_{iso} the dumbbell PEAs stay mobile enough to crystallize, with a terminal melting peak equal to the melting peak obtained for T_{iso} = 90 °C. We attribute this behaviour to the short length of the chains and to the low amount of the HSs per chain, which helps in complete crystallization of terminal T4T HSs.

7.5 Viscoelastic measurements and influence of temperature

Frequency sweep tests conducted within the linear viscoelastic regime of deformation are shown in Figure 7.10. for the 5%HSs sample. Data were measured at different temperatures ranging from T = 120 °C (melting temperature) to T = T_m-60 °C. Each of these measurements was performed after a waiting time of at least 30 minutes to makes sure that the sample is well equilibrated, and all the residual stresses are relaxed. An identical protocol was used for all rheological measurements presented in this section.

As we can see from Figure 7.10, with decreasing temperature, apparently a liquid-to-solid transition is observed. This transition occurs approximately at 85 °C. This transition is quite sharp compared to the viscoelastic response of the segmented PEAs containing 5% of HSs (see chapter 6) and is in good agreement with the conventional DSC results.

At low temperatures, HSs associate and the sample behaves like a rubber. The fact that at high temperatures (above 90 °C), a secondary plateau emerges means that only a part of the sample, which corresponds to the dangling ends, is able to relax, while part of the chains are trapped between two associated HSs and cannot disentangle, leading to a secondary plateau. The temperature range at which this behavior is observed is similar for the dumbbell and the segmented PEAs. Above T_m, the attractive interactions between HSs (due to hydrogen bonding) weaken. Consequently, the crystallites soften and eventually melt, leading to the flow of the sample. As shown in Figure 7.10., the level of the plateau seems to saturate at 65 °C, meaning that all HS are associated. At this temperature, the second plateau merges with the first, rubbery, plateau. It must be noted that this situation never happens with the corresponding segmented copolymer containing 5% of HSs. Indeed, as described in chapter 6, even if all HSs are associated, around 50% of the segmented sample behaves as dangling ends. The level of this plateau is, however, slightly below the entanglement rubbery plateau (of 2 10^6Pa), which could be due to the presence of a small fraction of chains only partially functionalized, as discussed in Chapter 3. But this fraction seems limited, which contradicts the proposed interpretation of the NMR results.

At higher temperatures, there is an equilibrium between associated and free HSs, which leads to gradual lowering of the second plateau with increasing T. The fact that at high temperature (95 °C –

105 °C), the typical terminal slope of 2 is not observed for the storage modulus at low frequency suggests that some HSs domains still exist at these temperatures.

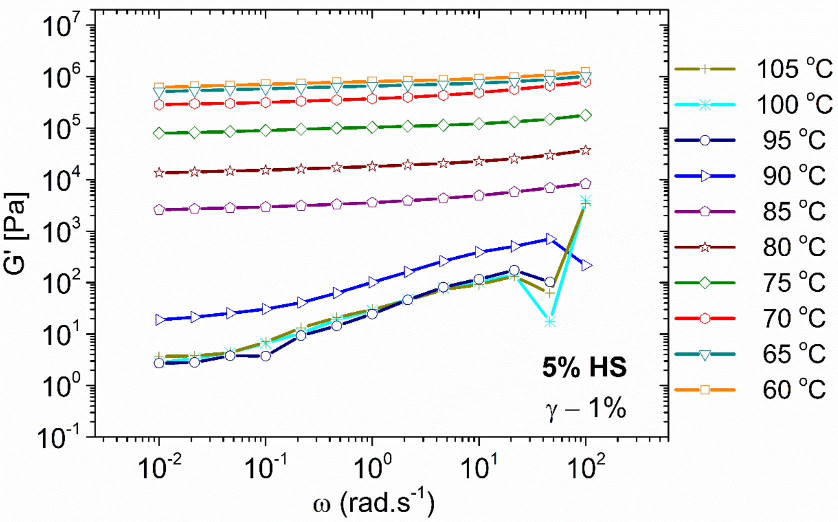

Figure 7.10: Frequency-dependent storage moduli of the sample containing 5%HS, measured at high ($T = \mathrm{Tm}_{+}$ 10°C) to low temperature ($T = \mathrm{Tm}_{-}$ 60°C).

We now investigate the viscoelastic behavior of the dumbbell sample containing 20% of HSs. As the first test, the amplitude sweep test is performed, as shown in Figure 7.11. It is observed that the linear regime for this sample already stops at around 0.2% strain. We also observe that this sample takes time – around one hour - to equilibrate. Then, frequency sweep tests were performed at 0.1% strain in order to preserve the network. The viscoelastic responses are shown in Figure 7.12, showing a fully elastic response.

In order to check the reproducibility of the data, four consecutive frequency tests (at T = 100 °C) were performed. Interestingly, they do not overlap with each other and show a continuous decrease (1st FS, 2nd FS and 3rd FS). This non-reproducible nature of the data reveals the large sensitivity of the formed T4T structures: as soon as the sample is deformed, even under extremely low amplitude of deformation, part of the crystallite's breaks. TheseT4T structures are thus very delicate in nature unlike the one formed in segmented PEAs.

Thus, the dumbbell copolymer containing 20%HS sample fails to form crystal structures able to resist deformation. This 'brittle' behavior of the sample is attributed to the very small mesh size between the associated HSs as well as to the low connectivity between the chains.

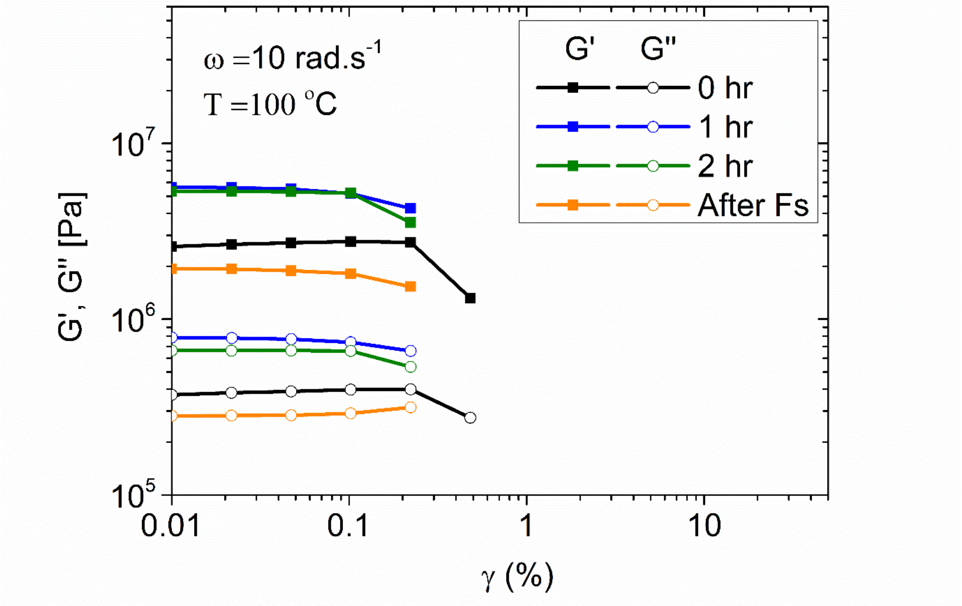

Figure 7.11: Storage and loss moduli of 20%HS sample, as a function of strain amplitude.

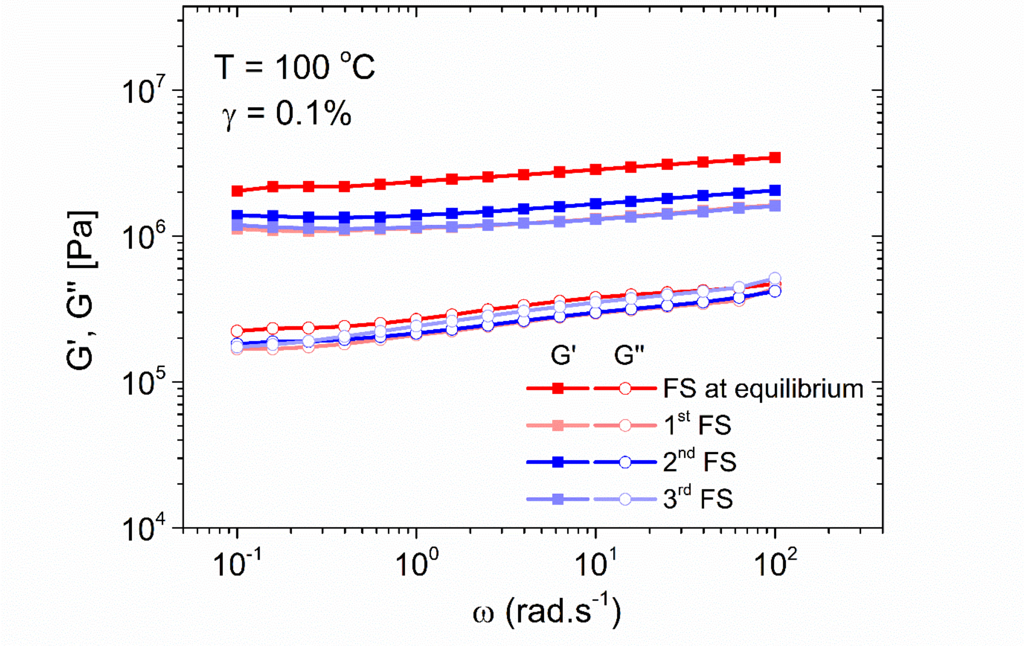

Figure 7.12: Frequency-dependent storage and loss moduli of 20%HS sample.

Then, temperature ramps are performed with samples 5% and 20%HSs, in both cooling and heating directions in order to monitor their stability and influence on the viscoelastic properties of the material. The measured temperature-dependent *G'* at 10 rad.s^{-1} and 1% strain rate are depicted in Figure 7.13 and 7.14 respectively for 5 and 20% HS PEAs.

For the copolymer containing 5%HSs, coming from the melt state, the storage modulus is not observed until 90 °C. Then, the storage modulus suddenly increases, governed by the formation of the crystallites, which prevent the chains to disentangle and relax. At room temperature, the sample reaches the value of 10^6 Pa. This value is almost equal to the one obtained with the segmented 5%HS sample due to the formation of T4T crystallites, and it corresponds to the entanglement plateau of the SSs. We then conclude that with 5% of HSs, the associate HSs behave more as crosslinking points for the entangled chains, rather than as large structures able to reinforce the sample. During heating ramp, a hysteresis effect appears, like the behavior of the segmented copolymer. However, the hysteresis behavior observed in the segmented sample was more pronounced as compared to the dumbbell, probably due to the larger number of HSs along the chains, able to progressively trap the chain segments.

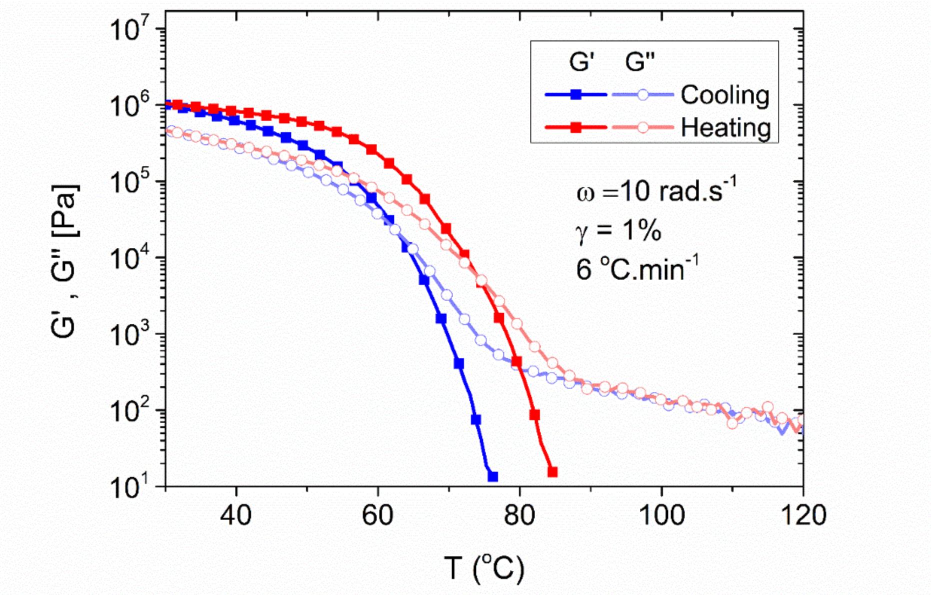

Figure 7.13: Dynamic temperature ramps of storage and loss modulus for 5%HS at 10 rad.s^{-1} and constant rate of 6 °C.min^{-1}.

The same test is then performed on the 20% HS sample, as shown in Fig. 7.14. Starting from melt state, the modulus values are very low, meaning that no association of HSs take place at these high temperatures. At 125 °C, a sudden increase in the modulus is observed due to the association of T4T HSs. These results are in line with the DSC results, as 20%HS samples have a crystallization temperature of 125 °C. Increase in modulus is observed until 80 °C, followed by the elastic plateau reaching the same modulus value as that of segmented PEA (see Figure 7.15). On heating, however, either sample suddenly cracks or a huge increase in normal force was observed. Cracking of the sample indicates that the sample is too brittle in nature. As compared to the segmented 20% sample, the dumbbell 20% sample shows a fast association of the HSs reaching very high storage plateau modules at low temperature. These samples are thus hard and brittle.

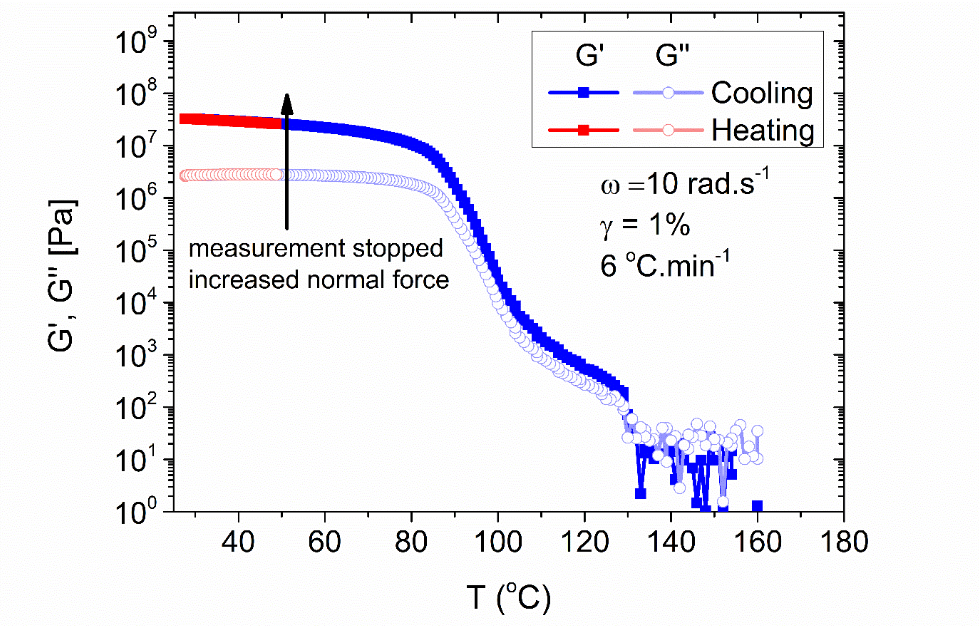

Figure 7.14: Dynamic temperature ramps of storage and loss modulus for 20%HS.

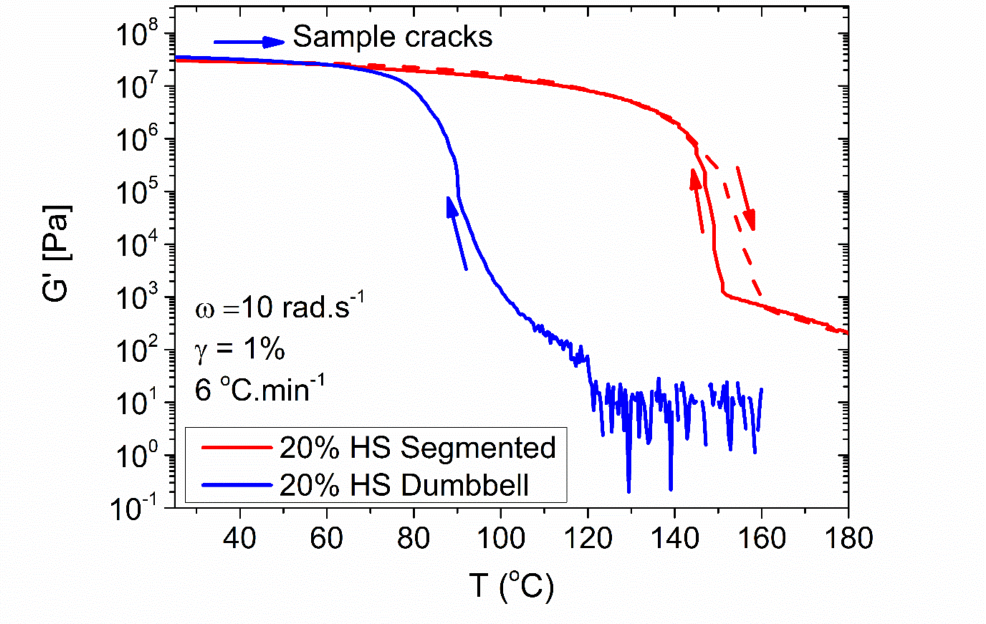

Figure 7.15: Dynamic temperature ramps of storage and loss modulus comparison for 20%HS containing segmented and dumbbell sample.

7.6 Summary

Dumbbell PEAs based on PTMO soft and T4T HSs were synthesized as mentioned in chapter 3. Thermal and viscoelastic properties of T4T end capped with 5 and 20% of HSs were studied using the DSC, FSC and rheology technique. For 20%HS sample, DSC data show a decrease in melting temperature of the dumbbell samples as compared to the segmented PEAs. FSC studies showed the formation of ribbon structures on progressive cooling, whereas amorphous morphology is obtained under fast cooling (above 200 °C.s^{-1}) just like segmented PEAs. Then isothermal measurements at intermediate temperature (T_{iso} = 90 to 50 °C) showed that only one melting transition is observed, which is isothermal time independent. Interestingly at low temperature (T_{iso} = 50 °C) formation of T4T structures were seen, which were characterized by one melting transition i.e. no formation of baby-ribbon was observed. This observation let us conclude that the dumbbell architecture provides higher chain mobility (compared to the segmented copolymers) at intermediate as well as low temperature forming the identical T4T structures having an almost same melting point. In addition, at high temperature (T_{iso} = 130 ºC), strong T4T structures can be formed, which are isothermal time-dependent and show a very high melting temperature (150 ºC). However, this requires very long waiting time in order to compensate for the low crystallization driving force. It was found that the crystallization rate for the 20%HS dumbbell sample is low as compared to the 20% segmented but does not lead to the formation of baby-ribbon at low temperature.

Viscoelastic measurements as a function of temperature, time and frequency were also studied. It was observed on temperature sweeps that the HSs in dumbbell architecture associate very fast, with only low hysteresis effect for 5%HS sample in comparison to the segmented 5%HS PEA sample. For 20%HS dumbbell sample, the association of the HSs was so fast and complete that the sample became brittle and fractured at low temperature. We attributed this effect to the short chain length, with low connectivity among the polymer chains. With this last sample, it was difficult to quantify the liquid to solid transition as the T4T structures formed were weak and broke even at low (0.1%) strain rate.

7.7 References

1) Baeza, G.P., A. Sharma, A. Louhichi, L. Imperiali, W. P. J. Appel, C. F. C. Fitie, M.P. Lettinga, E. van Ruymbeke, D. Vlassopoulos, Multiscale organization of thermoplastic elastomers with varying content of hard segments. Polymer, 2016. 107: p. 89-101.

2) Sharma, A.; G. P. Baeza, L. Imperiali, W. P.J. Appel, C. Fitie, G. Vanden Poel, E. van Ruymbeke, Fast scanning calorimetry clarifies the understanding of the complex melting and crystallization behavior of polyesteramide multi-block copolymers, accepted in Polymer Int, DOI 10.1002/pi.5713.

3) Mathot, Vincent, et al. "The Flash DSC 1, a power compensation twin-type, chip-based fast scanning calorimeter (FSC): first findings on polymers." Thermochimica Acta 522.1-2 (2011): 36-45.
4) Zhuravlev, E., and C. Schick. "Fast scanning power compensated differential scanning nano-calorimeter: 1. The device." Thermochimica Acta 505.1-2 (2010): 1-13.
5) Poel, Geert Vanden, et al. "Performance and calibration of the Flash DSC 1, a new, MEMS-based fast scanning calorimeter." Journal of thermal analysis and calorimetry 110.3 (2012): 1533-1546.
6) Schick, Christoph, and Vincent Mathot. Fast Scanning Calorimetry. Springer, 2016., chapter 18 (pp. 611-632).
7) Poel, G. V., et al. "Recommendation for temperature calibration of fast scanning calorimeters (FsCs) for sample mass and scan rate." Beuth Verlag GmbH, Berlin Adam Metal (2014) In vivo and in vitro investigations of a nanostructured coating material—a preclinical study. Int J Nanomedicine 9.1 (2011): 975-984.
8) Gaymans, R.; De Haan, J., Segmented copolymers with poly (ester amide) units of uniform length: synthesis. Polymer 1993, 34 (20), 4360-4364.
9) Van Bennekom, A.; Gaymans, R., Amide modified polybutylene terephthalate: structure and properties. Polymer 1997, 38 (3), 657-665.
10) Gaymans, R. J., Segmented Copolymers With Monodisperse Crystallizable Hard Segments: Novel Semi-Crystalline Materials. Prog Polym Sci 2011, 36 (6), 713-748.

Chapter 8: **Conclusions and Perspectives**

In this chapter, we summarise and present the decisive outcomes of this thesis.

As we know, Thermoplastic elastomers (TPEs) are an interesting class of segmented copolymers, which exhibit the properties of thermoplastic and elastomers. This dual property of TPEs leads to excellent mechanical and physical properties, while keeping the thermo-reversibility of the hard phase domains, thus providing an alternative material for conventional rubbers from both recycling and ease of processing point of view. The commercial growth of TPEs is continuously increasing owing to the wide range of applications in consumer products used in day-to-day life.

In this work, we focused on polyesteramide (PEA), which is one of the most interesting classes of TPEs. These materials can be engineered to obtain specific properties depending on the applications due to wide choice of soft and HSs. From literature it was clear, that the dispersity and unit length of the HS plays important role in deciding the thermal, mechanical and viscoelastic properties of the copolymer. Therefore, in order to obtain enhanced properties, pure monodisperse T4T di-amide HS were synthesized, which has unit length of 2.1 nm (see chapter 4), close to the optimum length of 2nm for obtaining high phase separation. Furthermore, PTMO SS was used in the copolymer synthesis due to its properties like flexibility due to low T_g, good hydrolytic stability and elastomeric properties at low temperatures. The segmented copolymers with almost equal molar masses were synthesized, although the concentrations of T4T HSs were systematically varied (0, 5, 10, 15 and 20wt%) so that the final properties of polymers are independent of the molar masses. Dumbbell PEA copolymers with same HS concentration were also synthesized.

Thus, these 'model TPEs' were synthesized in order to allow a systematic study of the influence of important parameters (HS density, temperature, time, HS position) on their final properties.

The DSC measurements revealed a strong increase of the terminal melting point as a function of HSs concentration (Figure 3.7), due to increase in number of hydrogen bonding groups. The melting transition were found to be broad and complex. In contrary, the solvent casted sample showed better HSs organization, as sharp melting transitions were observed instead of broad and complex (Figure 4.2). These measurements thus confirmed that the PEA samples exhibit different T4T crystal structures, which strongly depend on the processing conditions as high-temperature properties are related to HSs (see chapter 4). These ones were further studied by FSC measurements, which allows a better control of the processing parameter like high heating and cooling rates to explore the variety of phases likely to exist in PEAs (see chapter 5). In particular, we showed that the progressive cooling from the melt results in formation of T4T crystallites in homogenous way forming ribbon structures. These ribbon-structured crystallites thus formed exhibit high melting point, resulting into good mechanical properties (Figure 5.4). However, fast cooling leads to the formation of smaller and metastable baby-ribbon structure, characterized by low melting temperature. FSC data also allowed us to illustrate the importance of polymer chain mobility and isothermal time effect on development of T4T structures. The isothermal measurements around *Tc* and *Tc+10* °C confirm the better T4T HS crystal formation, characterized by increase in terminal melting point (figure 5.8). Therefore, depending on cooling rate, isothermal crystallization temperature and time, we could control the development of crystals (good or poor), which is important from processing point of view.

In order to understand the key factors influencing structural arrangement during crystallization of T4T HSs from chemical composition point of view, we performed WAXS measurements at the molecular scale (1 Å - 1 nm). They revealed that π-π stacking interactions in addition to the well-known H-bonds in polyamide-based systems are important and enhance the HS association (chapter 4, Table 2). SAXS experiments at length-scales (1-30 nm), showed that the T4T inter-crystallites distance decreases as a function of HS concentration. The time resolved SAXS measurements as a function of the temperature showed the presence of HS aggregates in the melt especially when the HS concentration is 20%. Based on these results, we proposed a growth mechanism of T4T HSs, which is highly dependent on the initial processing condition (Figure 4.8).

In order to understand the influence of both thermal history and sample composition on the final properties of these TPEs, we investigated their viscoelastic properties and in particular, how these last ones are influenced by the time and temperature.

To this end, oscillatory measurements were performed, applying a temperature sweep. We showed that while the storage modulus is governed by the entanglements in the melt state, the rheological properties of the copolymers are governed by the HSs at lower temperature. These ones first associate and act as cross-linkers (Figure 6.14), before forming larger T4T crystallites interacting with each other and thus, enhancing the mechanical properties of the TPEs. On heating, hysteresis was observed, as stronger crystallites melts at higher temperature. With the help of a statistical model, we could show that the sharpness of the transition from liquid-like to solid-like properties was related to the HS concentration, with a special emphasis on the role of dangling ends in this process and on the entanglements trapped between HSs (Figure 6.10). In particular, we showed how a larger concentration of HSs enhances the probability of SS to be trapped in the elastic network. Thanks to large amplitude oscillatory shear (LAOS) strain tests, we could study the reversibility of the network under large flow, and how temperature affects the corresponding sample properties. In particular, we showed that partial disentanglement of the network takes place under cycles of shear deformation, as after a large shear deformation, the chains do not have time to re-entangle before being trapped again between associated HSs. Large flow at even lower temperature, results in the change of the sample state, induced by the reorganization of the crystallites in order to adapt to the flow. As for the partial disentanglement, this order transition has a large effect on the final properties of the sample (Figure 6.17).

To sum it up, results show that the final properties of the samples like high-temperature stability, temperature independent plateau modulus, or improved low-temperature flexibility are strongly dependent on the association of HSs, which is largely influenced by the chemical composition, HS density, SS entanglements, thermal history, cooling conditions (fast or slow) and external parameters like time and temperature. Based on these conclusions, dumbbell PEAs comprising of PTMO soft and T4T HSs were synthesized. The idea was to change the polymer chain architecture but keeping the T4T concentration equal to the one in segmented PEAs. Therefore, obtained copolymers, end-capped with 3, 5 and 20% HSs, having different molar masses were studied in comparison with the segmented PEAs (chapter 3, Table 9). Thermal and viscoelastic properties were studied using the DSC, FSC and rheology technique (see chapter 7). For 20%HS sample, DSC show the lowering of the melting temperature of dumbbell samples as compared to segmented PEAs. This was not foreseen as we expected better organization of HSs due to more chain freedom considering the HSs are located at the chain end and can diffuse easily to form stable and perfect crystals. However, the melting point was difficult to determine for 3 and 5% HS samples. Hence, FSC studies were performed, the effect of isothermal time and temperature were same as observed for segmented PEAs, except at low temperature (T_{iso}=50 °C) formation of T4T structures were seen, which were characterized by one melting transition i.e. no formation of baby-ribbon took place (Figure 7.7). This observation let us conclude that the enhanced mobility of the dumbbell architecture at intermediate and low temperature allows the formation of identical T4T structures (whatever

T), having an almost identical melting point. Thus, this study allowed us to confirm the large role of chain mobility in the formation of the crystallites.

In addition, at high temperature (around 130 ºC), long waiting times allowed the formation of strong T4T structures characterized by a high melting temperature of 150 ºC (Figure 7.8). The fact that the crystallization rate for 20%HS dumbbell sample is low as compared to the 20% segmented TPE allowed us to highlight the influence of chain mobility in the crystallization process.

Viscoelastic measurements as a function of temperature, time and frequency were also studied for these samples. It was concluded from temperature sweep tests that the HSs in dumbbell architecture associate very fast, leading to a very weak hysteresis 5%HS sample in comparison to the segmented 5%HS TPE sample. For 20%HS dumbbell sample, the association of the HSs was so fast and complete that the sample became brittle and fractured at low temperature (Figure 7.15). This behaviour was attributed to the effect of short chain length, with low connectivity among the polymer chains. The liquid to solid transition in 5% sample was quick and led to the formation of stable crystallites at low temperature. However, it was difficult to observe liquid to solid transition for 20%HS sample as the T4T structures formed were weak and broke even at low (0.1%) strain rate.

As a final remark, the structure property relationship of PEAs explains how the final properties of PEAs strongly depend on their microstructure, which is largely influenced by various parameters such as phase separation, hydrogen bonding, crystallization or π-π stacking, processing process, thermal history as well as by the density of HS. In the direction of understanding the relationship between these parameters and the final properties of the TPEs, we analyzed ‘model’ PEAs (segmented or dumbbell), which provided us with clear and new insights about the role of thermal history, chain mobility and HS density on the formation of the crystallites and consequently, on the final properties of the TPEs. Therefore, this study brings new tools to better control on the final properties of PEAs, needed in the applications.

Thesis Acknowledgments

At the end of the thesis, Firstly, I would say thanks to my supervisor Prof. Evelyne van Ruymbeke to guide me well throughout the research work from finding the results to thesis title's selection. Your immense knowledge, motivation, and patience have given me more power and spirit to excel in research writing. I enjoyed working on TPEs in industrial as well as academic environment. Besides this your continuous support throughout my Ph.D., related research and expertise in rheology are unforgettable. Apart from research your guidance, advice and insightful suggestions have been always standing along with me, which helped me a lot to come across the hurdles and make my way till the end of the thesis.

I would especially like to thank, team DSM: Dr. Carel Fitié, Dr. Wilco Appel and Dr. Luna Imperiali for providing me an opportunity to join their research team as a Ph.D. researcher. Thanks a lot for providing access to the lab and other research facilities. It was a pleasure to work at DSM in the best work environment. I want to thank Wilco Appel for helping me out with the synthesis and characterization of TPEs. Your guidance and inputs really helped me a lot in progressing throughout my Ph.D., you have been a source of inspiration for me when it comes to the research. I also enjoyed the company of the other colleagues from the polyester lab and would like to take this opportunity to thank them. I want to mention the name of Peter, Stein, and Rob for their timely help. Besides, this many thanks to Dr. Luigi Balzano for being my coach at DSM. I am very grateful to Dr. Poel-vanden Geert for introducing and helping me with FSC measurements on my sample.

Your assistance and valuable insights on manuscript writing was huge, which resulted in an article. Actually, I want to thank all the co-authors, without you people it won't have been possible. I also want to express my thank to Pascal Van Velthem at UClouvain for preparing the FSC samples for me and being always available for other timely help.

I would like to express my heartiest gratitude to all the jury members Jacques Devaux, Charles-André Fustin, Jean-François Gohy, Pavlik Lettinga, Guilhem Baeza, Wilco Appel, Carel Fitié and Evelyne Van Ruymbeke for reviewing my work and your insightful comments and encouragement. These constructive comments have really improved the quality of this thesis.

My colleagues from rheology group, thank you guys, for healthy discussions, suggestion and your help whenever I needed. It means a lot for me, I especially want to mention the names of Taisir, Laurence, Sina, Hamid, Flanco, and Yanzhao. I also want to thank Nicky, Aurore, Rose-Anne, and Anne for helping me with the administrative work.

At last, A special thanks to my family. Words cannot express how grateful I am to my mother, and father for all of the sacrifices that you've made on my behalf. I would like to dedicate this thesis to my Parents, family members and well-wishers as your love, blessings, and support helped me to sustained thus far. I would like to thank my beloved wife, Ruchika for always being there for me, your enormous support and confidence will surely, make me a very successful person one day. I would also like to thank all of my friends who supported me throughout my thesis to achieve my goals.